



## THÈSE

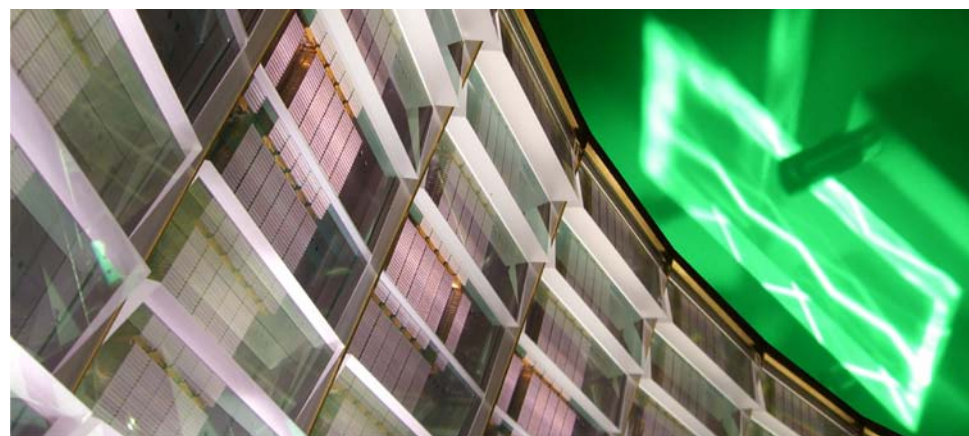
pour obtenir le grade de  
**DOCTEUR de l'ÉCOLE POLYTECHNIQUE**  
Spécialité : Physique

présentée par  
**Daniel ALBACH**

Titre de la thèse :

*Amplified Spontaneous Emission and Thermal Management  
on a High Average-Power Diode-Pumped Solid-State Laser*

*The Lucia Laser System*



soutenue le 28 Avril 2010 devant le jury composé de :

MM. A. BAYRAMIAN	
J.-C. CHANTELOUP	
J. HEIN	
J. KAWANAKA	
Y. LUTZ	Rapporteur
R. MONCORGÉ	Rapporteur
E. ROSENCHER	Président du jury
C. SAUTERET	Directeur de thèse



# Acknowledgments

At this point I would like to take the opportunity to thank all the persons involved in this thesis work throughout the almost four magnificent years, which are now behind me. It was an exceptional experience and I'm very grateful to have had such a possibility to join the LULI.

This thesis would have not been possible without the help of Mathias SIEBOLD who introduced me to the Lucia project after I finished my diploma thesis at Jena. I'm especially thankful for the intense and fruitful exchange with Mathias within the last years concerning various smaller and larger problems and discussions, especially amplifier and oscillator architecture.

The work described in this thesis was performed in collaboration between the LULI and the ISL. At this point I would like to express gratitude to the director of the LULI Francois AMIRANOFF and the responsible persons at the ISL, especially Antoine HIRTH and Yves LUTZ for the kind introduction at the LULI and ISL.

I wish to express special thanks to the head of the Lucia team, Jean-Christophe CHANTELOUP, who always gave the necessary confidence and support needed to accomplish this work and kindly introduced me to the group. Many personal occasions and fruitful discussions gave the impulse to find the right track for this work as well some distraction, when work seemed to be completely overloaded.

Special esteem goes to Christian SAUTERET, who superbly found the right words to further amplify my efforts to understand the physical problems and opened my mind for alternative approaches. He gave a great backup as a very good teacher and I am happy to have had the chance to be his last PhD student.

The Lucia team gave always the possibilities for intense and interesting discussions and I would like to thank at this point all the current and former members of the team, in particular: Gilbert BOURDET, Philippe HOLLANDER, Antonio LU-CIANETTI, Mikayel ARZANKANTSYAN, Thierry NOVO, Pascal PIATTI, Francois ASSEMAT, Stephanie LeMOAL and especially Sofiane BAHBAH.

I am pleased to thank one particular team-member, Bernard VINCENT and his family. Without their support many things would have been much more difficult (and less funny). I would like to thank especially his wife Brigitte for introducing me to French cuisine, the French poetry and chansons as well as the many special words and expressions otherwise hidden to me. I am especially grateful to be such deeply integrated into the family, which gave me a special support during the years passed.

Especially for the introduction to ASE and thermal problems I would like to express my gratitude to Geoffroy Le TOUZÉ, in particular for the major help concerning the simulation of the wavefront deformation.

I would like to thank Emmanuel ROSENCHER as the president of my PhD thesis committee as well as Yves LUTZ and Richard MONCORGÉ who took the position and the work as reviewers. My gratitude goes in the same manner to Andrew BAYRAMIAN, Joachim HEIN, Junji KAWANKA and Christian SAUTERET for their participation as committee members.

For their collaboration as industrial partners a special thanks is attributed to Hubert ÄHLING and Jürgen ORTMANN at AMTRON, Jörg NEUKUM, Sandra AHLERT, Roland VENOHR and Timo MATTERN at DILAS for their swift solutions for various technical problems as well as the industrial part of the construction of the Lucia laser system. Thanks to Narine ANANYAN and the many workers at LASERAYIN TEKHNIKA for the necessary laser crystals, especially in this size and quality.

The very good ambiance and the kind reception at the LULI made it possible for me to work on this thesis and I would like to express my thanks to all the members of the LULI I met within the recent years. Their steady help for smaller and larger problems and the integration into the collective gave a lot of confidence to me.

I'm thankful for the support of my family – from the beginning of my study at Jena until the very end. Without their support this whole voyage would have been impossible.

# Contents

<b>Introduction</b>	<b>1</b>
<b>1. Delivering High Energy at High Repetition Rate: A Different Paradigm</b>	<b>5</b>
1.1. The way to the Laser . . . . .	5
1.2. Laser classification . . . . .	7
1.2.1. 3-Level, Quasi-3-Level and 4-Level-Lasers . . . . .	7
1.2.2. Laser gain media . . . . .	9
1.2.3. Semiconductor Lasers . . . . .	14
1.3. Efficiency considerations . . . . .	16
1.4. Energy storage . . . . .	18
1.4.1. Energy storage and extraction . . . . .	18
1.4.2. Thermal constraints for energy storage . . . . .	24
1.5. Power and Intensity Limitations . . . . .	26
1.6. Overcoming the limitations – Gain medium selection for DPSSL . . .	29
1.7. Repetition-rate applications . . . . .	36
1.7.1. DPSSL and (OP)CPA . . . . .	36
1.7.2. Laser Fusion . . . . .	38
1.7.3. State of the Art . . . . .	41
<b>2. The Lucia Laser System</b>	<b>45</b>
2.1. Overview . . . . .	45
2.2. Oscillator . . . . .	46
2.3. Preamplification Stage . . . . .	52
2.4. Beam Shaping . . . . .	57
2.5. Main Amplifier . . . . .	65
2.5.1. Laser Diode Array . . . . .	65
2.5.2. Light Concentration System (LCS) . . . . .	67
2.5.3. Laser head . . . . .	75

---

<b>3. Amplified Spontaneous Emission Management</b>	<b>79</b>
3.1. Motivation . . . . .	79
3.2. Introduction . . . . .	79
3.2.1. ASE flux estimation in the one-dimensional, monochromatic case . . . . .	80
3.2.2. ASE intensity contrast at the end of a laser chain . . . . .	81
3.2.3. ASE flux estimations in Two and Three Dimensions . . . . .	83
3.2.4. Life time modifier $M_{ASE}$ . . . . .	84
3.3. Numerical Simulation of ASE . . . . .	85
3.3.1. ASE Simulation in 2D . . . . .	86
3.3.2. ASE Simulation in quasi-3D . . . . .	89
3.3.3. ASE in three dimensions . . . . .	92
3.4. Experimental Benchmark . . . . .	93
3.5. Parasitic oscillations . . . . .	102
3.6. Application on the Lucia Amplifier . . . . .	110
3.7. Conclusion . . . . .	119
<b>4. Thermal Management</b>	<b>121</b>
4.1. Motivation . . . . .	121
4.2. Introduction . . . . .	121
4.2.1. Heat generation . . . . .	121
4.2.2. Thermal conductivity . . . . .	123
4.2.3. Heat transport . . . . .	126
4.2.4. Radial temperature distribution . . . . .	130
4.3. Estimation of the Lucia laser head cooling capacity . . . . .	133
4.4. Thermally induced wavefront deformation . . . . .	140
4.4.1. Basic Model . . . . .	142
4.4.2. Thermal performance of the laser head . . . . .	144
4.4.3. Numerical estimation of the gain medium deformation . . . . .	152
4.5. Thermally induced depolarization . . . . .	157
4.5.1. Stress induced birefringence . . . . .	157
4.5.2. Intrinsic birefringence . . . . .	161
4.5.3. Thermally introduced birefringence on the Lucia laser head .	163
4.6. Conclusion . . . . .	168

<b>5. Lucia Amplifier Performance</b>	<b>171</b>
5.1. Motivation . . . . .	171
5.2. Lucia amplifier performance estimation . . . . .	171
5.3. Energy extraction . . . . .	176
5.4. Perspectives . . . . .	183
5.4.1. Static Astigmatism Correction . . . . .	183
5.4.2. Doping variation along the pump axis . . . . .	185
5.4.3. Ceramic laser gain media . . . . .	188
<b>6. Conclusion</b>	<b>191</b>
<b>A. Annex</b>	<b>195</b>
A.1. Variable Doping Distribution . . . . .	195
A.1.1. Pump $\leftrightarrow$ Excitation Relationship . . . . .	195
A.1.2. Doping distribution in transmission case . . . . .	196
A.1.3. Gain profile for internal reflection . . . . .	197
A.2. Linfords Formula . . . . .	200
A.3. The Quasi-Three-Level-System Yb <sup>3+</sup> :YAG . . . . .	203
<b>B. Tables</b>	<b>205</b>
<b>List of Figures</b>	<b>205</b>
<b>List of Tables</b>	<b>211</b>
<b>Bibliography</b>	<b>213</b>

## Abbreviations

AR	–	Anti-Reflection
$AR_L$	–	Aspect Ratio
ASE	–	Amplified Spontaneous Emission
BC	–	Boundary Condition
CCD	–	Charge Coupled Device
CPA	–	Chirped Pulse Amplification
cw	–	continuous wave
DP	–	Delaunay Prism
DPL	–	Diode-Pumped Laser
DPSSL	–	Diode-Pumped Solid-State Laser
FAC	–	Fast Axis Collimator
FD	–	Finite Difference
FWHM	–	Full Width Half Maximum
HR	–	High-Reflection
JP	–	Jet-Plate
LCS	–	Light Concentration System
LDA	–	Laser Diode Array
LIDT	–	Laser Induced Damage Threshold
LOI	–	Line Of Interest
OPA	–	Optical Parametric Amplification
OPCPA	–	Optical Parametric Chirped Pulse Amplification
PC	–	Pockels Cell
qcw	–	quasi-continuous wave
SAC	–	Slow Axis Collimator
TFP	–	Thin Film Polarizer
TIR	–	Total Internal Reflection
VCSEL	–	Vertical-Cavity Surface-Emitting Laser

## List of Symbols

$\alpha, \alpha_T$	-	absorption coefficient [ $\text{m}^{-1}$ ], expansion coefficient [ $\text{K}^{-1}$ ]
$a$	-	distance, length [m]
$a_0$	-	maximum of the normalized vector potential of the laser pulse [ $\text{W}^{-1/2}$ ]
$A$	-	surface [ $\text{m}^2$ ]
$A_{ij}$	-	Einstens coefficients for spontaneous emission [ $\text{s}^{-1}$ ]
$\beta$	-	relative excitation value [1]
$B, \mathbf{B}$	-	B–Integral [rad], dielectric impermeability tensor [1]
$c, c_P$	-	speed of light [ $\text{m s}^{-1}$ ], heat capacity [ $\text{J m}^{-3} \text{K}^{-1}$ ]
$c_d, c_n$	-	doping concentration [at.%], distance of jet–plate holes [m]
$C_{\text{bunch}}$	-	electron bunch charge [C]
$\emptyset$	-	pinhole diameter [m]
$d, D$	-	length [m], thickness [m]
$\delta, \Delta\delta$	-	optical path [m], phase shift [1]
$e$	-	Euler number [1]
$\epsilon, \boldsymbol{\epsilon}$	-	interatomic distance increase [1], dielectric tensor [1]
$E, \mathbf{E}, \mathfrak{E}$	-	energy [J], elastic modulus [Pa], electric field amplitude [ $\text{V m}^{-1}$ ]
$\Phi$	-	photon density [ $\text{m}^{-3}$ ]
$f_i, f$	-	thermal population of an energy level [1], focal length [m]
$F$	-	energy density [ $\text{J m}^{-2}$ ]
$\gamma$	-	scaling factor [1]
$g, g_0$	-	amplification factor [ $\text{cm}^{-1}$ ], small-signal gain [ $\text{cm}^{-1}$ ]
$g_{ij}(\nu), g(\nu)$	-	line–shape function [s]
$G$	-	energetic gain [1]
$\eta, \eta_h$	-	efficiency [1], heating parameter [1]
$\vartheta, \theta, \Theta$	-	angle [°]
$\Theta_D$	-	Debye temperature [K]
$h$	-	Planck constant [Js]
$h$	-	heat exchange coefficient [ $\text{W m}^{-2} \text{K}^{-1}$ ]
$H$	-	height [m]
$I$	-	intensity [ $\text{W m}^{-2}$ ]
$k$	-	heat conductivity [ $\text{W m}^{-1} \text{K}^{-1}$ ]
$k_B$	-	Boltzmann constant [ $\text{J K}^{-1}$ ]
$K_c$	-	fracture toughness [ $\text{Pa m}^{1/2}$ ]
$\kappa$	-	geometry dependent scaling parameter [1]
$\lambda, \Delta\lambda$	-	wavelength [m], bandwidth [m]

$L$	–	characteristic length [m]
$\Lambda$	–	multiplier of the diffraction limit [1]
$M_{ASE}$	–	life time modifier [1]
$M$	–	molar mass [ $\text{kg mol}^{-1}$ ]
$\mu$	–	reduced mass [ $\text{kg mol}^{-1}$ ]
$\nu, \Delta\nu, \nu_p$	–	frequency [ $\text{s}^{-1}$ ], bandwidth [ $\text{s}^{-1}$ ], Poisson ratio [1]
$n_0, n_2$	–	index of refraction [1], non-linear index of refraction [ $\text{m}^2 \text{W}^{-1}$ ]
$\hat{n}, \Delta\hat{n}$	–	population density [ $\text{m}^{-3}$ ], population density difference [ $\text{m}^{-3}$ ]
$N$	–	number [1]
$Nu, Pr, Re$	–	Nusselt number [1], Prandtl number [1], Reynolds number [1]
$\Omega$	–	solid angle [sradiant]
$\omega$	–	pump rate [ $\text{s}^{-1}$ ]
$\pi$	–	Archimedes constant [1]
$\pi_{ijkl}$	–	piezo-optical coefficients [1]
$P$	–	power [ $\text{W s}^{-1}$ ]
$\psi, \varphi, \varsigma$	–	angle [ $^\circ$ ]
$r$	–	radius [m]
$R_S$	–	thermal shock parameter [ $\text{W m}^{-1}$ ]
$R$	–	reflectivity [1], radius [m]
$\rho$	–	density [ $\text{kg m}^{-3}$ ]
$\sigma, \boldsymbol{\sigma}$	–	cross section [ $\text{cm}^2$ ], stress [Pa]
$t$	–	time [s]
$T, \Delta T$	–	temperature [K], temperature difference [K]
$\tau$	–	life time [s]
$V$	–	volume [ $\text{m}^3$ ]
$w$	–	beam diameter [m]
$x, y, z$	–	coordinates [m]
$z_{ijk}$	–	electro-optical coefficients [1]
$cr, crit$	–	related to critical values
$beam, SF$	–	related to beam parameter, beam self-focusing
$\Delta T, R_S$	–	related to temperature difference, thermal shock parameter
$tot$	–	related to total amount
$min, max$	–	related to minimum value, maximum value
$i,j,k,l$	–	related to index
$st, sp, ASE$	–	related to stimulated, spontaneous, ASE emission
$R, \Theta$	–	related to radial variable, tangential variable

# Introduction

Fifty years ago, an outstanding invention was about to revolutionize our daily life – the laser (*light amplification by stimulated emission of radiation*). It is one of the acronyms associated with the dawn of the technological era in the 20th century. Ranging from the extent of a grain of salt to the size of several football fields, and covering the electromagnetic spectrum from X-rays to the Far-Infrared, this invention gave birth to a complete new world of scientific development and applications.

The first successful realization of the predictions made by Schawlow and Townes in 1958 resulted in the ruby laser in 1960 by Maiman. Like most inventions, the laser was considered as a ‘device waiting for a job’ in the beginning.

Today, many parts of our daily life are in direct contact with lasers or laser-processed products. Applications range from cutting and welding materials for cars, airplanes and ships down to nanometer scale lithography for microelectronics. Besides industrial applications, these light sources are used for medical treatment and help to understand fundamental physical laws.

Laser-plasma interaction is currently one of the most fruitful fields in scientific research. Probably the most spectacular application of a laser system would be the fulfillment of a long time dream: the exploitation of the stellar energy production under controlled conditions.

The next decades will see the generation of energy by thermonuclear fusion. Whether a future power plant will rely on magnetic fusion or inertial (laser) fusion is not yet clear. But from this demonstration to a full-scale, efficient power plant, still many technological steps are required and a wide field of physics has to be explored. Intense research in plasma physics and laser development is therefore necessary.

The main french national civil pole in research activities on warm and dense plasma physics is the *Laboratoire pour l'Utilisation des Laser Intenses* (LULI). It is a joint research unit and is supported by the *Centre National de la Recherche Scientifique* (CNRS), the *Commissariat à l'Energie Atomique*, the *Ecole Polytechnique* and the *Université Paris VI*.

Operating state-of-the-art laser technology has always been a necessity for the LULI to fulfill its mission of exploring forefront plasma physics. LULI launched the program Lucia in the early 2000's. This program is a scientific project dedicated to the exploration of an emerging laser physics field: the so-called *Diode-Pumped Solid-State Laser* (DPSSL). At the turn of the millennium, a conjunction of two majors breakthrough in laser technology triggered the rise of high average-power DPSSL.

Firstly, performances and costs of diode lasers became compatible with laser programs at a laboratory scale. Secondly, transparent laser-grade quality ceramics reached maturity. Together they give credibility to Mega-Joule scale, high average-power laser programs like HiPER (*High Power laser Energy Research*).

Lucia, together with Mercury (LLNL, USA), Halna (ILE, Japan) and Polaris (FSU Jena, Germany), is among the handful of DPSSL laser programs currently working throughout the world.

The first three of the mentioned programs aim at a similar point of operation which is around 100 joules in the near infrared with a repetition rate of 10 hertz for  $\sim 10$  nanoseconds long pulses. Such an energetic goal can be regarded as relatively modest, compared to thousand times higher requirements for an inertial fusion power plant working with hundreds of kilojoules. Depending on the finally selected architecture to efficiently couple that energy into a nuclear fuel pellet, the individual beam energy requirement might be in the order of a few kilojoules. The Lucia final energetic goal should then be considered as a 1/10 scale unit.

Lucia is mainly funded by the local administrative body *Région Ile-de-France* and the *Ministère de la Recherche et de l'Enseignement Supérieur*. CNRS, *Ecole Polytechnique* and *Délégation Générale à l'Armement* are also among key supporting partners. The thesis work described in this document was funded by the *Institut Franco-Allemand de Recherches de Saint-Louis* (ISL), a bi-national scientific institution established by the Federal Republic of Germany and the French Republic.

When building a laser like Lucia, aiming at average powers in the kilowatt regime with pulses of tens of Joules, key aspects to be addressed are optical elements integration management, *Amplified Spontaneous Emission* (ASE) and thermal effects.

The first point was extensively explored in a first phase of the Lucia program (2003–2006). It took advantage of research performed within the *Laser Mega Joule* program in the field of *Laser Induced Damage Threshold* of optical elements and dielectric coatings.

The work performed within the context of this thesis focuses on ASE and thermal management. It takes place within an energetic milestone fixed at 10 joules and a repetition rate of 2 hertz. This document is therefore structured around the following five chapters:

Chapter 1, entitled “Delivering High Energy at High Repetition Rate: A Different Paradigm” introduces the basic principles underlying this research work. In conjunction with the fiftieth anniversary of the invention of the laser, a short historical introduction opens the chapter. The following sections depict the general context and identify the main obstacles for high average-power laser systems. Solutions are indicated as well as applications for rep-rated laser systems. The relevant obstacles and their solutions are then discussed in more detail in following chapters.

Chapter 2, entitled “The Lucia Laser System” describes all five stages of the Lucia laser. Of special interest is the Lucia main amplifier, as this stage of the laser chain is extensively studied in the following chapters.

Chapter 3, entitled “Amplified Spontaneous Emission Management” describes a comprehensive theoretical and experimental study of ASE. Starting from one-dimensional models, the complexity is further increased up to a three dimensional model. This model is benchmarked to an extensive experimental study of ASE control solutions explored in the laboratory.

Chapter 4, entitled “Thermal Management” analyses the heat generation and heat transport in the context of the Lucia main amplifier stage. It demonstrates the capability of the developed laser head cooling approach to perform a satisfying thermal management by the presentation of experimental results of wavefront and birefringence measurements. Further, it introduces a simplified one-dimensional model of gain medium deformation which is benchmarked against a fully three-dimensional analysis of the laser gain medium.

Chapter 5 entitled “Lucia Amplifier Performance” explores the energetic potential of the Lucia main amplifier. An experimental campaign aiming on energy extraction showed the performance and limitation of the current amplifier setup. Solutions for a further improvement is given as well as perspectives.

Finally, a conclusion closes this thesis, proposing a scaling approach for higher average-power DPSSL extraction designs.



# 1. Delivering High Energy at High Repetition Rate: A Different Paradigm

The aim of this chapter is to introduce the basic principles underlying the research work depicted in this thesis, setting up its general context. Most of the points addressed here are discussed more in detail in the following chapters.

After a brief historical overview, a discussion of the laser gain medium types follows. Then, fundamental efficiency considerations are discussed in a general view as well as problems arising from energy storage, peak power and intensity limitations. How Diode-Pumped Solid-State Lasers (DPSSL) might overcome these issues will thereby be discussed briefly. A short review for possible applications is given, as well as a presentation of state of the art DPSSL programs currently explored throughout the world. A conclusion summarizes this chapter.

## 1.1. The way to the Laser

In the year 1900, Max Planck (1858–1947) introduced the idea of an energy quantum in his famous 'Strahlungsgesetz' (law of radiation) with the use of the, at that time unpopular, theory introduced by Ludwig Boltzmann (1844–1906). Within the time of the birth of the quantum-theory, Albert Einstein (1879–1955) postulated in 1916 the existence of a 'reverse process of absorption' [1]<sup>1</sup>.

The proof of such a stimulated emission has been shown on Neon in 1928 by Hans Kopfermann (1895–1963) and Rudolf Ladenburg (1882–1952) [2]. In the meantime Gilbert N. Lewis (1875–1946) created the word 'photon' in 1926 [3]. The idea to build an optical generator based on stimulated emission was proposed by Valentin A. Fabrikant (1907–1991) in his PhD-thesis in 1940. He basically offered to use a gas discharge to produce a significant higher population in the excited state compared to the Boltzmann-distribution. He supposed that the energy would be transferred by collisions of the second kind. More than twenty years later this technique was used in the first gas lasers. However, neither his doctorate work in 1940 nor his

---

<sup>1</sup>First publication in 'Mitteilungen der Physikalischen Gesellschaft Zürich. Nr. 18, 1916'

soviet patent issued in 1951<sup>2</sup> could be considered to be known to the international scientific community, as it was de facto unknown even to the soviet researchers. Another important step towards the laser was the observation and understanding of the 'optical pumping' between the discrete atomic energy levels<sup>3</sup> by Alfred Kastler (1902–1984) in 1950 [4].

Without paying attention to it, Felix Bloch (1905–1983) found the experimental proof of the inversion of population, while working on nuclear resonances in 1946 and shortly after this, Edward M. Purcell (1912–1997) and his co-worker Robert V. Pound (1919–) introduced the concept of a 'negative temperature' explaining their experimental results [5]. A population inversion can be interpreted as such a 'negative temperature', as the probability of a population in a higher energy state is therefore higher compared to the population probability in the lower energy state. No attention was paid at that time, that in connection with a microwave cavity or waveguide, coherent amplification by stimulated emission might have been achieved. Such a device was proposed by Weber (1919–2000) in 1952<sup>4</sup>, however, he was more interested in an amplifier than in an oscillator and therefore didn't discuss the impact of a feedback.

Shortly after that, Charles H. Townes (1915–) and his co-workers successfully demonstrated the first MASER (Microwave Amplification by Stimulated Emission of Radiation) in 1954 [6]. Simultaneously and independently Nikolai G. Basov (1922–2001) and Alexander M. Prokhorov (1911–2002) demonstrated the Maser in the Soviet Union. The extension from the microwaves to the infrared and to the optical region was proposed by C. H. Townes together with Arthur L. Schawlow (1921–1999) in December 1958 [7].

Gordon Gould (1920–2005) encountered Townes at the Columbia University and while he was working on his PhD-thesis wrote in a notebook for the first time a new acronym – LASER (Light Amplification by Stimulated Emission of Radiation). While Gould held his ideas secret, not to spoil possible patents, the theoretical paper from Schawlow and Townes started a world-wide race for the first 'optical maser'. Finally on May 16, 1960, Theodore H. Maiman (1927–2007) built the first working laser – the ruby laser [8].

---

<sup>2</sup>The title of the patent was 'A method for the amplification of electromagnetic radiation (ultraviolet, visible, infrared and radio waves) characterized by the fact that the amplified radiation is made to pass through a medium that by means of auxiliary radiation or by other means generates an excess concentration with respect to the equilibrium concentration of atoms, other particles, or systems at upper energy levels corresponding to excited states'

<sup>3</sup>These discrete atomic energy levels were found in 1913–14 by James Franck (1882–1964) and Gustav Hertz (1887–1975).

<sup>4</sup>Electron Tube Research Conference, Ottawa

## 1.2. Laser classification

The acronym laser describes the physical mechanism behind the representation as a machine. We get amplification through stimulated emission of photons with the same energy and the same polarization as the incident photons. This gives the striking features of the laser beam. However, the acronym does not explicitly refer to the most important class of lasers, the oscillator. In fact every laser system starts with an oscillator and may posses several amplifiers afterwards, helping to further amplify the energy output initially generated.

The very basic principle allowing amplification is the preparation of population inversion. As it can be shown, in a simple two-level system such an inversion cannot be achieved directly. For the sake of clarity, let us consider the most simple representations of energy level systems – the three-level-laser and the four-level-laser. The first laser, the ruby-laser, was a three-level-laser and, as we will see, had to be pumped quite hard to achieve a positive gain for the circulating photons. A special type of lasers can be operated without population inversion [9], however it is a very special case and will not be discussed in the context of this thesis and will be excluded from the following discussions.

### 1.2.1. 3–Level, Quasi–3–Level and 4–Level–Lasers

Pumping real laser materials usually involves a complicated energy level system, making modeling rather complex. Simplified models on the other side give a reasonably good understanding of the basic relationships and general behaviors of such systems.

Laser emission can only be achieved if the upper laser level exhibits a higher population density than the terminal laser level – an inversion is then created. Classically two different laser models are discussed - the three-level laser and the four-level laser. Simplified examples of these schemes are shown in Figure 1.1. In this short explanation we neglect all cross relaxations and the interaction with energy levels outside the described ones and approximate the energy bands to be discrete energy levels.

**Four-level system** If the energy levels for the pump and the laser emission are energetically sufficiently separated, one speaks of a four-level system. Ions in the lower pump level (referred as  $|0\rangle$  in Figure 1.1) are excited into the energetic higher pump level  $|3\rangle$  with a pump rate  $w_P$ . Between the upper pump level  $|3\rangle$  and the upper laser level  $|2\rangle$  occurs an energy transfer which might be radiative or

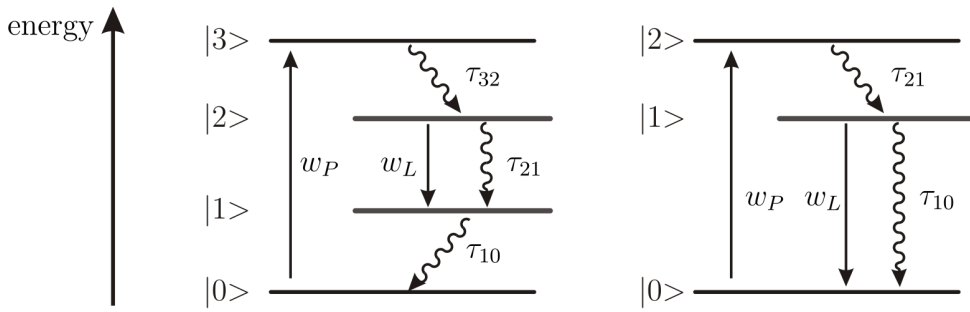


**Figure 1.1.:** Simplified 4-level (left) and 3-level (right) system. The 3-level system shown has the energy split for the upper laser state, a similar system with a energetic split in the lower laser level. A quasi-3-level system is a variation of the 4-level-case, where  $\Delta E_{10}$  and/or  $\Delta E_{32}$  is in the order of  $kT$  ( $k$  the Boltzmann constant and  $T$  the temperature).

nonradiative. This transfer can be characterized by a lifetime  $\tau_{32}$  describing the rate for the increase of population for the upper laser level. The upper laser level has a fluorescence lifetime  $\tau_{21}$  leading to a depopulation into the lower laser level emitting a photon. Moreover, this transition can be used to add photons coherently to a photon flux with a rate  $w_L$  by stimulated emission. The lower laser level  $|1\rangle$  is again connected to the lower pump level by a lifetime  $\tau_{01}$ . Let us mention that the inverse process connected with  $w_L$  is not generally excluded. We only get a gain by stimulated emission, if the population in the upper laser state is higher than the population in the lower laser state - an inversion is achieved.

In this case of a four-level system we supposed that the corresponding energy levels are such far (speaking in terms of energy) that they are not thermally populated. The energy level separation  $\Delta E$  should therefore be larger than  $kT$ , where  $k$  is Boltzmann constant and  $T$  the temperature<sup>5</sup>.

**Three-level system** In the degenerated case where an energy level of the laser emission fuses together with a corresponding pumping level we obtain the three-level laser system. Two cases can occur: coincidence of the upper laser and upper pump level, or the lower laser and the lower pump level. Figure 1.1 (right) illustrates such a simplified three-level system scheme, where the lower laser and lower pump level are the same which makes it more difficult to achieve inversion, as at least half of the ions have to be excited into the upper laser state. Therefore one has to apply a high pump rate  $w_P$  and use a material exhibiting a long fluorescence lifetime  $\tau_f = \tau_{10}$  while the transition  $\tau_{21}$  should be very fast.

<sup>5</sup>In the case of an ambient temperature of 300 K, the energy is  $E \approx 1/40 \text{ eV} \approx 200 \text{ cm}^{-1}$ .

**Quasi–three–level system** An intermediate case also exists, where the energetic separation  $\Delta E$  between the laser and pump level are in the order of  $\approx kT$ . In this case both levels are significantly influenced by the Boltzmann statistics. Despite this scheme is more similar to the four–level case, it is often called quasi–three–level system with respect of the population of the laser level. Consequently the laser performance depends on the temperature of the laser gain medium in this case.

### 1.2.2. Laser gain media

Taking a closer look on the transition from the upper laser state  $i$  to the lower laser state  $j$ , one defines the stimulated emission cross section  $\sigma_{ij}$  with the lifetime  $\tau_{ij}$  and the line shape function  $g_{ij}(\nu)$  for a given frequency  $\nu$  as [10]:

$$\sigma_{ij}(\nu) = \frac{c^2}{8\pi \nu^2} \frac{g_{ij}(\nu)}{\tau_{ij}} \quad (1.2.1)$$

Equation 1.2.1 gives the fundamental connection between the main parameters for each given gain material. The physical representation of this gain medium depends on the application and envisaged properties. Indeed, every kind of existing state of matter can be used to build a laser. An extensive collection can be found in [11]. A very natural classification of the laser gain media is the physical state of the gain medium, which might be gaseous, liquid or solid. We will discuss briefly the main three classes – gas, liquids (dyes) and solid state laser gain media in the following.

It should be mentioned, that in the X–ray domain, plasma lasers exist as well as FELs (Free Electron Lasers). They are not discussed here.

#### 1.2.2.1. Gas Lasers

A very intuitive laser gain medium is gas. The main advantage of gas is that it automatically adapts its volume to its host cavity. It can flow through the laser device and can be very quickly refreshed as well. Also it might transport a high amount of heat out of the device. A very low density of gas can generate very stable laser sources with well defined spectral properties. The output spectrum can be shifted by the use of isotopes, e.g. in the case of a hydrogen/deuterium fluoride chemical laser, where the output is shifted from  $2.7\text{ }\mu\text{m}$  to about  $3.8\text{ }\mu\text{m}$ . [12]

The lifetime of the excited state is usually in the order of  $10^{-9} - 10^{-7}\text{ s}$ , but can span up to seconds for specific types of lasers. The spectral line width is usually rather small compared to other laser types (see Table 1.1) and dominated by broadening mechanisms as collision and Doppler broadening. Gaseous laser gain media show emission line widths in the MHz to the GHz–range, which implies in

Equation 1.2.1 (together with a relatively short lifetime of the upper laser state in the case of electronic transitions) a high emission cross section of up to  $10^{-12} \text{ cm}^2$ . These huge emission cross sections have to be evaluated relatively, as the gas pressure is usually in the order of  $\approx 1 \text{ Torr}$ <sup>6</sup> implying a low density of the active medium.

Despite the first laser demonstrated was a solid state laser, the highest significance was given to the gas laser, as they can produce high-power cw laser sources (in the IR especially the CO<sub>2</sub>-laser [13]) and therefore dominated the industrial applications for many years and made up most of the market. Historically the He–Ne–Laser was the second laser to be demonstrated experimentally in the IR (1.15 μm) [14] and now is more known to its emission wavelength in the visible at 632.8 nm.

As there is no need to produce specific laser gain media sizes for a gas, scaling of a gas laser can easily be achieved. Applications demanding high peak and cw powers like welding and cutting (CO<sub>2</sub>-laser) and photolithography (excimer and exiplex lasers as ArF and KrF-lasers, due to their short wavelength) are therefore predestinated applications.

A drawback of gas lasers is usually the absence of a broad bandwidth for the absorption cross section, making it difficult to pump them optically, i.e. by the use of flash lamps. The proposition to use a gas discharge is more adapted to the excitation mechanisms. Most gas lasers use gas discharge performed by different methods. A collection reviewing the different excitation mechanisms can be found in [12].

An alternative approach can be done for the Atomic Iodine Laser (AIL), where the excitation is done using photolysis, as well as for the Chemical Oxygen Iodine Laser (COIL) using a chemical reaction to reach the excitation needed. Applications requiring a very rugged design, high power combined with a minimum of infrastructure are particularly well suited for chemical or combustion lasers.

---

<sup>6</sup>1 Torr is equivalent to 101.325 /760 Pa  $\approx$  133.3 Pa

### 1.2.2.2. Dye Lasers

After the invention of the laser, the question arose if there was any possibility for a widely tunable laser source. Such a laser relies on an organic dye (usually in a liquid phase) as the gain medium. Dye lasers were first reported by Sorokin and Lankard in 1966 [15] and almost simultaneously by Schäfer [16]. Dyes exhibit broad absorption and emission cross sections and are consequently gain media of choice for lasers requiring broad wavelength tunability or for ultra-short pulse generation [17]. Organic dye lasers were the first tunable lasers covering a large spectral range from the near-infrared to the ultraviolet [17].

The lifetime of the upper laser state is usually in the order of a few nanoseconds and the emission spectrum is broad, resulting in a emission cross section, not as large as for gas lasers<sup>7</sup>, but typically much larger compared to solid state laser gain media (see Table 1.1). Most laser dyes are pumped using relatively short pump wavelengths, such as Argon-ion ( $\text{Ar}^+$ ) laser, excimer lasers or frequency-double/tripled/quadrupled solid state lasers, reducing greatly the efficiency of this type of laser material. Certain laser dyes can be pumped with flash lamps or laser diodes.

With its large emission cross section (see e.g. Table 1.1) becomes the small-signal gain (the definition of the small-signal gain is given Section 1.4) fairly high (up to  $10^3 \text{ cm}^{-1}$ ). A frequently used geometry is a dye-jet running trough the focus of an intracavity laser beam (pump beam diameter in the order of  $\approx 10 \mu\text{m}$ ). For large volumes, flash lamp pumping might be considered.

Dye lasers suffer from certain disadvantages. Most notably, solvents and dyes are often toxic or carcinogen. A solvent frequently used is DMSO (dimethylsulfoxide), which greatly accelerates the transport of laser dyes into the skin, making the handling of these liquids even more problematic. Another practical problem is the trapping of the molecule in the triplet state. By this, a quenching agent might be added and the dye exchanged into a reservoir. Due to these drawbacks, most of the dye-lasers are nowadays replaced by solid-state lasers, except when certain wavelengths are demanded, which are difficult to achieve otherwise.

Recent progress in the field of dye lasers tend to use more solid-state-like materials, where organic laser dyes are incorporated into plastics or sol-gel [18, 19].

---

<sup>7</sup>The active center density is much higher in a dye compared to typical gaseous gain media. This compensates the smaller cross section.

### 1.2.2.3. Solid State Lasers

The third major type is the Solid State Laser. It can be classified by its

1. Host material, which might be a crystal, a glass or a ceramic, defining the mechanical, thermal and optical characteristics.
2. Activator/Doping ion with its energy levels leading to the lasers characteristic spectral properties.

The combination of host material and activator ion defines the specification the laser material can offer. Sufficiently sharp fluorescence lines, a strong emission cross section, a high quantum efficiency for the laser transition and good optical properties are demanded on one side. On the other side, good pumping characteristics, i.e. the availability of usable pump bands, the achievable doping density and the possibility to produce the gain medium in the requested size are often important. Such characteristics are usually provided by crystals, ceramics and glasses containing transition metals, rare earths or actinides as activator ions.

Compared to the other laser gain medium types, solid-state gain media can combine the broad emission bandwidth (in the order of THz in the NIR/IR) with lifetimes in the order of  $10^{-6} - 10^{-3}$  s. Resulting out of Equation 1.2.1, emission cross sections are typically much smaller compared to gaseous or liquid gain media, in the order of  $10^{-19} - 10^{-21}$  cm<sup>2</sup>. A comparison of several solid-state gain media can be found in Table 1.1.

Glasses are host matrices of choice when reproducible manufacturing in large sizes and quantity is requested with a high optical quality. Due to the absence of a well defined crystalline field emission spectra are broader compared to their crystalline counterparts. As an example, Table 1.1 shows the comparison between trivalent Nd-doped Glass and Yttrium-Aluminum-Garnet (YAG).

Certain glasses, especially phosphate and fluoride phosphate glasses, show a small index of refraction leading to a small nonlinear index of refraction [20, 21]. The main drawback is the low thermal conductivity of glasses compared to crystals restricting the applications to laser systems with a low average power.

A crystalline host matrix carries a high order of structure and is characterized by its crystallographic axes. Uni- and biaxial crystals are of great use for the applications in non-linear optics as e.g. frequency-conversion etc. [22]. As a laser gain medium, this feature can be used in certain cases since the emission cross section is different for propagation directions along the different crystallographic axes. Compared to glasses, crystals remain typically small in diameter (up to tens of centimeters) and usually show a higher nonlinear index of refraction [21].

laser quality ceramics combine the large size of glass and the good thermal properties of crystals. This host matrix family consists of small crystallites, which are sintered together under high pressure with the help of additives[23]. The optical and thermo-mechanical properties are almost similar to crystals. Other advantages are the possibility to adjust the spatial distribution of the doping centers, as it can improve the laser performance by adjusting the heat deposition [24] or gain management.

As activators, actinides, transition metals and rare earths are of interest. The only successful use of an actinide is trivalent uranium ( $U^{3+}$ ). It was used in the first 4-level laser [25] and, shortly later, used in the first Diode-Pumped Solid State Laser (DPSSL)[26]. Both systems used crystalline Calcium Fluoride ( $CaF_2$ ) as the host matrix. The major objection against the use of actinides is their radioactivity.

Transition metals show a strong dependency on the host, valence electrons are not shielded by outer electron shells [10]. Of special interest are divalent Chromium ( $Cr^{2+}$ ), trivalent Titanium ( $Ti^{3+}$ ) and tetravalent Chromium ( $Cr^{4+}$ ) as they exhibit a very broad emission cross section due to vibrational-electronic broadening in certain hosts. A fairly large overview for Chromium doped lasers in the infra-red spectral region can be found in [27]. Of special interest is  $Ti^{3+}$ -doped  $Al_2O_3$  (often called Titanium-Sapphire, Ti:Sa or TiSa) as it has an exceptional broad emission bandwidth in the visible and near infrared [28]. Using Kerr-Lens-Modelocking, ultra-short laser pulses are generated [29] and is nowadays one of the most important laser source for ultra-short laser pulses.

In the case of rare earths as activator, the valence electrons are shielded by the outer electron shells and by this the spectral behavior is not as strongly affected by the host as it is in the case of transition metal doped laser gain media. Rare earths are naturally good candidates for laser operation as they show sharp spectral lines throughout the near infrared and infrared. Neodymium doped glasses and crystals (especially YAG [35]) are important for high-power laser systems operating in the NIR as they show a reasonable long lifetime of the upper laser state. The terminal laser state is well above the lower pump level and therefore exhibits interesting properties for cw and pulsed operation. Holmium, Erbium and Thulium are of interest as they work in the infrared, especially in the eye-safe region. Ytterbium doped laser gain media show an exceptional long fluorescence lifetime (in the order of  $\approx 1\text{ ms}$ ) and a simple energy level system. Due to its simple energy level system, only a few pump-bands are available which is not favorable for flash-lamp pumping. With the upcoming laser diodes as pump sources, Yb-doped laser gain media gained in interest as they are good candidates for efficient high-power laser systems [36, 37].

Laser medium	type	$\lambda$ (μm)	$\sigma_{ij}$ (cm <sup>2</sup> )	$\tau_f$	$\Delta\nu$ (GHz)	Ref.
HeNe	gas	0.6328	$1 \times 10^{-13}$	1.4 μs	1.5	[12]
CO <sub>2</sub>	gas	10.6	$3 \times 10^{-18}$	2.9 s	0.06	[12]
KrF	gas	0.248	$0.6 - 2.7 \times 10^{-16}$	7–10 ns	1,000	[30, 31]
Ar <sup>+</sup>	gas	0.515	$3 \times 10^{-12}$	6 ns	3.5	[32]
AIL	gas	0.76–1.36	$7.5 \times 10^{-18}$	0.2–1.7 s	0.025–0.25	[12]
Rhodamine 6G	dye	0.56–0.64	$2 \times 10^{-16}$	3.3 ns	5,000	[32]
Coumarin 120	dye	0.43–0.46	$1 \times 10^{-16}$	5 ns	6,000	[33]
DACH	dye	0.49	$0.4 - 1 \times 10^{-16}$	2.8 ns	15,000	[34]
Ruby	solid	0.694	$4 \times 10^{-20}$	3 ms	330	[10]
Tm <sup>3+</sup> :YAG	solid	1.87–2.16	$2 \times 10^{-21}$	10 ms	25,000	[10]
Nd <sup>3+</sup> :YAG	solid	1.064	$4 \times 10^{-19}$	230 μs	120	[10]
Nd <sup>3+</sup> :Glass	solid	1.057	$3 \times 10^{-20}$	300 μs	3,000	[10]
Ti <sup>3+</sup> :Sa	solid	0.66–1.18	$3 \times 10^{-19}$	3.2 μs	100,000	[10]
Yb <sup>3+</sup> :YAG	solid	1.03	$2.1 \times 10^{-20}$	950 μs	2,000	[10]

Table 1.1.: Properties of the some selected laser materials

### 1.2.3. Semiconductor Lasers

Shortly after the first laser, semiconductor lasers were demonstrated [38]. Lasers relying on a semiconductor can be pumped using a driving current through a p–n junction. As most of the semiconductor lasers are indeed pumped in such a way, other pump techniques, like optically pumped semiconductor lasers, are omitted in this context. The optical cavity is formed by the cleaved edges, as semiconductor materials have a high index of refraction (in the order of  $n_0 \approx 3$ ) and consequently show a high reflectivity at the boundary to air/vacuum (more than 40 %).

In the following we will call semiconductor lasers with a current–carrying p–n junction *laser diodes*.

The evolution of such devices was slow at the beginning, as laser diodes could not take advantage of the (already) mature silicon technology. Direct band gap materials are needed to emit photons (compound semiconductors were developed possessing a similar band gap structure). They were limited to operate at cryogenic temperatures with short pulses and with a low efficiency. Nevertheless, even under such conditions, laser diodes were used to pump one of the first solid–state laser [26].

With the invention of the heterostructure (multiple semiconductor layers replacing the simple p–n junction) in 1969 [39], cw operation became possible. The threshold current was further reduced by the use of quantum wells [40].

Laser diodes cover a wide spectral region from the visible/NIR spectral region for InGaN/GaN (405 – 530 nm), InGaP (630 – 690 nm) and GaAs (730 – 980 nm) to the IR for InP–structures (1200 – 1700 nm) and InGaAsSb around 2000 nm.

The attractiveness of the narrow emission spectra of laser diodes compared to flash lamps make them highly efficient pump sources of choice for solid state–laser gain media, especially those doped with rare–earths. For instance, Ytterbium doped gain media show narrow single absorption lines, which would otherwise be difficult to pump without the narrow emission of laser diodes.

High–power laser diodes usually consist of several single emitters arranged on one semiconductor chip (called *bar*). Several of such bars can be stacked together (forming the so–called *stack*). The density of the laser emitters per bar and stack (fill factor) depends on the heat deposition into the heat sink. Quasi–continuous emission (qcw) with pulses in the order of milliseconds and repetition rates in the order of 1 – 10 Hz allow high fill factors up to 90%.

Current state of the art laser diode bars emit between peak powers between 200 and 400 W (for an emission wavelength near 940 nm and pulse lengths of 1 ms) for driving currents of up to 300 A. The conversion efficiency from current into laser light emission is 60–70%. Laser diode stack emission can be considered non–coherent due to the high amount of independent laser light emitters. The geometrical arrangement of the cavity leads to two different spatial laser emission divergences. A so–called *fast axis* emission perpendicular to the large extend of the laser diode bar shows a divergence in the order of  $\sim 40^\circ$ , while along the perpendicular direction (so–called *slow axis*) the divergence is in the order of  $\sim 10^\circ$ . Fast axis collimation using cylindrical lenses with sub–millimetric focal lengths and high numerical aperture reduce this divergence to  $\sim 1^\circ$ .

The rather low beam quality of laser diodes, compared to other laser sources, makes concentration of these light sources more complicated. Tapered laser diodes offer a better beam quality, which is interesting for smaller pumped areas [41].

Besides the beam quality, the drift of the emission wavelength with temperature and age of the laser diode stack is a problem for laser gain media with narrow absorption cross sections. Volume Bragg gratings can be used to drastically reduce the temperature shift by a factor of  $\sim 30$  [42].

Vertical–Cavity Surface–Emitting Lasers (VCSELs) [43] show a better beam quality compared to the edge–emitters but are limited to their output power since their operating principle relies on the large extends as emitting surface. Therefore, a high quality cavity is needed in order to prevent transverse lasing. Nevertheless, VCSEL are interesting candidates as laser diode pump sources.

### 1.3. Efficiency considerations

An important factor of a laser is its efficiency, namely the electrical-to-optical efficiency  $\eta_{e-o}$ . Some authors refer to the optical-to-optical efficiency  $\eta_{o-o}$ , which excludes the generation and transport of the pump energy and therefore the pump source efficiency  $\eta_{PS}$  and the transport efficiency  $\eta_T$ .

For the optical-to-optical efficiency of an amplifier, one might define it as the fraction of extracted energy density  $F_{out}$  compared to the injected energy density  $F_{inj}$ :

$$\eta_{o-o} = \frac{F_{out}}{F_{inj}} \quad (1.3.1)$$

The optical efficiency on its own is characterized in two contributions:

1. energy storage
2. extraction of energy

Most prominent for the energy storage is the Stokes parameter  $\eta_S = \lambda_P / \lambda_L$  describing the difference in energy for a pump and laser photon. Pump photons striking the gain material get subsequently absorbed with a fraction  $\eta_A$  and are transferred into the upper laser state with a quantum efficiency  $\eta_Q$  which is mostly influenced by auxiliary fluorescence lines and upconversion. The upper laser state has a limited fluorescence lifetime  $\tau_f$ . In the case of a pump duration  $\tau_P$  in the order of the lifetime  $\tau_f$ , a certain amount  $1 - \eta_L$  is converted into Spontaneous Emission (SE) which generates in an inverted gain medium Amplified Spontaneous Emission (ASE) affecting the efficiency by a factor  $\eta_{ASE}$ .

Energy extraction is closely related to the beam overlap  $\eta_{BO}$  and the extraction efficiency  $\eta_E$ . Achieving a high value for the beam overlap strongly depends on the pump geometry and subsequently alters the pump transport efficiency  $\eta_T$ , which includes beam shaping for the pump, too. Therefore a better optical-optical efficiency can result in a lower overall electrical-optical efficiency. The extraction efficiency  $\eta_E$  however can be defined as the extracted energy in the spatial beam distribution compared to the stored energy within the spatial beam shape.

$$\eta_{e-o} = \eta_{PS} \eta_T \underbrace{\eta_S \eta_A \eta_Q \eta_L \eta_{ASE} \eta_{BO} \eta_E}_{\eta_{o-o}} \quad (1.3.2)$$

$\eta_{PS}$  : Pump source efficiency

$\eta_T$  : Pump transport efficiency

$\eta_S$  : Stockes parameter

- $\eta_A$  : Absorbed fraction of the pump
- $\eta_Q$  : Quantum efficiency
- $\eta_L$  : Storage efficiency due to  $\tau_f$
- $\eta_{ASE}$  : ASE losses
- $\eta_{BO}$  : Beam overlap
- $\eta_E$  : Extraction efficiency

Table 1.2 compares two laser system examples, namely a flash lamp pumped Nd<sup>3+</sup>:YAG laser and a diode pumped Yb<sup>3+</sup>:YAG laser system. The major draw back of a flash lamp pumped system is the little use of the emission spectrum. If spectral lines of the pump emission correspond to a usable absorption band of the laser medium, efficiencies can reach up to 20% [10], otherwise it is typically in the order of a few percent.

The emission has no preferred direction - flash lamps emit in the full solid angle, which makes it more difficult to concentrate the whole emission on the laser gain medium. Laser diodes show a much narrower emission bandwidth and their emission can be well directed. However they are restricted to certain wavelengths. It can be seen in Table 1.2 that the storage efficiency  $\eta_L$  has a strong impact on the overall efficiency. As it will be discussed in Section 1.4, one can improve the storage

Efficiency	remarks	Nd <sup>3+</sup> :YAG	Yb <sup>3+</sup> :YAG
	pump source	flash-lamp	diode
$\eta_{PS}$	driver	0.7	0.7
	conversion	0.5	0.6
	usable emission	0.2	1
$\eta_T$		0.7	0.95
$\eta_S$		0.76	0.91
$\eta_A$		0.95	0.95
$\eta_Q$		0.85	0.93
$\eta_L$	$\tau_f = \tau_P$	0.63	0.63
$\eta_{ASE}$		1	1
$\eta_{BO}$		0.9	0.9
$\eta_{o-o}/\eta_E$		0.24	0.43
$\eta_{e-o}/\eta_E$		0.02	0.18

**Table 1.2.:** Comparison between flash lamp pumped Nd<sup>3+</sup>:YAG and diode-pumped Yb<sup>3+</sup>:YAG without considering the extraction efficiency.

efficiency by applying a shorter pump duration. However to achieve the same injected energy within a shorter period of time requires a higher pump intensity. This can be achieved with e.g. higher driving currents for the flash lamps/ laser diodes or a higher number of pump sources. The first one is limited by the damage threshold of the pump device and its lifetime, the second is connected with a higher capital investment.

## 1.4. Energy storage

Before extracting energy with a laser pulse/beam, it has to be efficiently and safely stored. In this section, limiting factors for energy storage, due to Amplified Spontaneous Emission (ASE) on one side and thermal limitations on the other side, are briefly discussed.

### 1.4.1. Energy storage and extraction

The coupled rate equations for the population inversion  $\hat{n}$  and the photon flux  $\Phi$  under amplification, neglecting fluorescence, can be written to be [10]:

$$\frac{\partial \hat{n}}{\partial t} = -\gamma \hat{n} c \sigma \Phi \quad (1.4.1)$$

$$\frac{\partial \Phi}{\partial t} = c \hat{n} \sigma \Phi - \frac{\partial \Phi}{\partial z} c \quad (1.4.2)$$

where  $\gamma$  is 1 for a 4-level system and 2 for a three-level system,  $c$  the speed of light in the medium of refractive index  $n_0$  ( $c = c_0/n_0$ ) and  $\sigma$  the cross section of the active medium. A solution can be derived according to the estimations done by Frantz and Nodvik [44]. The amplified photon density  $\Phi(z, t)$  is given for a initial photon density  $\Phi_0$  to be:

$$\frac{\Phi(z, t)}{\Phi_0} = \{1 - [1 - \exp(-\sigma \hat{n} z)] \exp[-\gamma \sigma \Phi_0 c (t - z/c)]\}^{-1}. \quad (1.4.3)$$

A square pulse of duration  $\tau_p$  sees an energy gain  $G$  in a gain medium of length  $l$ :

$$G = \frac{1}{c \gamma \sigma \Phi_0 \tau_p} \ln \{1 + [\exp(\gamma \sigma \Phi_0 \tau_p c) - 1] \exp(\sigma \hat{n} l)\} \quad (1.4.4)$$

This expression is connected to not directly measurable variables. Therefore we define the incoming energy density  $F_{in}$  to be:

$$F_{in} = c \Phi_0 \tau_p h \nu \quad (1.4.5)$$

where  $h$  is Planck's constant and  $\nu$  the laser frequency. The resulting combination of variables in expression 1.4.4 can be interpreted to be a characteristic value for the

laser gain material - the so-called saturation fluence  $F_{sat}$  [ $\text{J cm}^{-2}$ ]:

$$F_{sat} = \frac{h\nu}{\gamma\sigma} \quad (1.4.6)$$

Two other important variables can be defined out of this relation, namely the small-signal gain  $g_0$  and the non-saturated energetic gain  $G$ :

$$g_0 = \sigma\hat{n} \quad (1.4.7)$$

$$G = \exp(\sigma\hat{n}l) \quad (1.4.8)$$

Replacing  $F_{in}$ ,  $F_{sat}$  and  $G$  into Equation 1.4.4 leads to a more physically accessible formula:

$$G = \frac{F_{sat}}{F_{in}} \ln \left\{ 1 + \left[ \exp \left( \frac{F_{in}}{F_{sat}} \right) - 1 \right] G_0 \right\}. \quad (1.4.9)$$

The cross section  $\sigma$  used in Equation 1.4.6 is the spectroscopic cross section and is by this not always directly accessible. Therefore it is more convenient to define the experimental cross section as a material parameter. Equation 1.4.6 reduces with  $\sigma_e = \gamma\sigma$  to

$$F_{sat} = \frac{h\nu}{\sigma_e}. \quad (1.4.10)$$

As discussed in the previous section, storage efficiency due to limited lifetime of the upper laser state (without extraction) is an important factor for laser amplifiers. We can derive it as a solution of the differential equation:

$$\frac{d\hat{n}}{dt} = \alpha \frac{I_P}{h\nu} - \frac{\hat{n}}{\tau_f} \quad (1.4.11)$$

under the estimation of a non-saturated linear absorption coefficient  $\alpha$  [ $\text{cm}^{-1}$ ], a constant pump intensity  $I_P$  [ $\text{W cm}^{-2}$ ] and a fluorescence lifetime  $\tau_f$  [s]. Dividing this result by the total absorbed energy  $\alpha I_P / (h\nu) \tau_P$ , one yields:

$$\eta_L = \frac{1 - \exp \{-\tau_P/\tau_f\}}{\tau_P/\tau_f} \quad (1.4.12)$$

This formula shows, that for a given fluorescence lifetime  $\tau_f$ , a longer pump duration results in a lower pump efficiency. Consequently, short pump durations are preferred. Shorter pump durations, however imply, with the same energy in the pump pulse, a higher pump intensity. This makes it more difficult to build such pump devices.

In this approach, the only source for the loss of population is the spontaneous emission (SE). The very basic principle of a laser implies its amplification due to the positive gain at the fluorescence lines. Such spontaneously emitted photons traveling

through the gain medium will see amplification on its own and further depopulate the inversion – so-called Amplified Spontaneous Emission (ASE). Quite early in the laser development it was understood, that ASE is an important factor for a laser installation [45, 46] and is still an important field of research [47, 48, 49].

ASE action depopulates the local excited activator ions as it can be interpreted as a locally, time-dependent fluorescence correction factor to the lifetime  $\tau_f^* = \tau_f/M_{ASE}$ . In a first rough approximation, such a lifetime correction factor  $M_{ASE}$  can be approximated to be  $M_{ASE} \approx \exp\{\sigma_e \hat{n} L\}$ , where  $L$  is the characteristic dimension of the system. A more detailed discussion on this subject follows in Chapter 3. Equation 1.4.11 has then to be modified to:

$$\frac{d\hat{n}}{dt} = \alpha \frac{I_P}{h\nu} - \frac{\hat{n}}{\tau_f} \cdot M_{ASE} \quad (1.4.13)$$

Again we have to mention that this approximation is fairly simple and will not hold true if ASE becomes important. A strong deexcitation due to ASE leads to a non-uniform gain distribution within the gain medium and a significantly spatially varying  $M_{ASE}$ . The estimated impact obtained from  $M_{ASE}$  is then exaggerated.

Equation 1.4.13 is consequently approximated to be:

$$\frac{d\hat{n}}{dt} = \alpha \frac{I_P}{h\nu} - \frac{\hat{n}}{\tau_f} \cdot \exp(C\hat{n}) \quad (1.4.14)$$

where the constant  $C$  is given by  $C = \sigma_e L$ . The resulting efficiency  $\eta_{Leff}$  is by this given by

$$\eta_{Leff} = \eta_L \eta_{ASE}. \quad (1.4.15)$$

Relation 1.4.14 can be solved numerically and the efficiency  $\eta_{Leff}$  is shown in Figure 1.2 for values of  $C$  varying between 0 and 10.

It is of major interest to derive an estimation when ASE related effects become dominant. As it will be shown in Chapter 3, the ASE-flux in the monochromatic case is expressed as:

$$\Phi_{ASE}(r_0) = \frac{1}{4\pi} \frac{1}{\tau_f} \int_V \frac{\hat{n}(r)}{|\rho(r, r_0)|^2} \cdot G_{r \rightarrow r_0} dV \quad (1.4.16)$$

where  $\rho(r, r_0)$  is the distance between the point of observation  $r_0$  and the position of the integration variable  $r$ . With the assumption of uniform excitation and a non-saturated gain, we can simplify Equation 1.4.16 to:

$$\Phi_{ASE} = \frac{1}{4\pi} \frac{\hat{n}}{\tau_f} \int_V \frac{1}{|\rho(r, r_0)|^2} \cdot \exp\{g_0 \rho(r, r_0)\} dV \quad (1.4.17)$$

Limiting for a given geometry one can derive two cases:

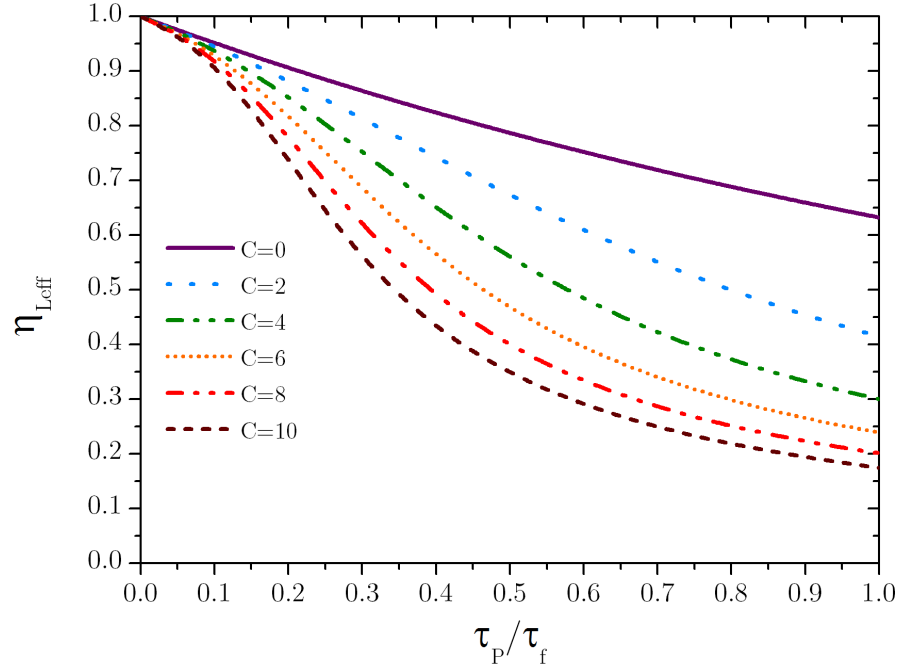


**Figure 1.2.:** Storage efficiency as a function of the pump duration  $\tau_P$ , the fluorescence lifetime  $\tau_f$  and the factor  $C = \sigma_e L$  characterizing the influence of ASE

- The ASE-fluence gets in the order of the saturation fluence  $F_{\text{sat}}$  and ASE significantly depopulates the stored energy in the case of an absence of parasitic oscillations.
- The product of the average gain and the gain medium internal surface reflectivity exceeds one reaching the oscillation threshold.

In the case of 4-level-system the relations  $g_0 = \sigma_e \hat{n}$ ,  $F_{\text{sat}} = h\nu/\sigma_e$  and  $\Phi_{\text{ASE}} \tau_f h\nu = F_{\text{ASE}}$  transform Equation 1.4.17 to:

$$\frac{F_{\text{ASE}}}{F_{\text{sat}}} = \frac{g_0}{4\pi} \int_V \frac{1}{|\rho(r, r_0)|^2} \cdot \exp\{g_0 \rho(r, r_0)\} dV \quad (1.4.18)$$

In order to estimate the oscillation threshold for a given geometry, one can define a product  $g_0 L$  of the small-signal gain  $g_0$  and a characteristic length  $L$ . For a thin disc this length would be the disc diameter and for a pen-shape like rod the length of the rod. We can define a threshold for the parasitic oscillations, when the gain  $\exp(g_0 L)$  is larger than the losses introduced at the extremities of the gain medium, i.e. absorbing cladding and surface reflectivity. With an effective reflectivity  $R^*$  characterizing the losses, one derives:

$$g_0 L < -\ln(R^*) \quad (1.4.19)$$

Typical values for the surface reflectivity are  $R^* = 1\%$  (AR coatings),<sup>8</sup>  $R^* = 4\%$ <sup>8</sup> and  $R^* = 9\%$ <sup>9</sup> yielding  $g_0 L \approx 4.6$ ,  $g_0 L \approx 3.2$  and  $g_0 L \approx 2.4$  respectively. This certainly restricts the usable dimension of a laser gain medium. Of special interest for scaling is the critical volume  $V_{cr}$ . The volume of a gain medium can be expressed in terms of the characteristic length to be  $V \propto L^3$ . Using Equation 1.4.19 gives:

$$V_{cr} \propto \kappa g_0^{-3} \quad (1.4.20)$$

where  $\kappa$  depends on the given condition and geometry. Equation 1.4.18 shall now be solved for a given gain medium geometry and small signal gain  $g_0$  in the case of  $F_{ASE}/F_{sat} = 1$ . The numerical result for the observation in the center of the gain medium with a homogeneous small signal gain ( $g_0 = \text{const.}$ ) is shown in Figure 1.3(a).

It should be noted that the derived value only leads to a rough approximation. Equation 1.4.18 is only fully satisfied in the case of  $F_{ASE} \ll F_{sat}$  as the gain is taken to be strictly exponential. Consequently the values shown in Figure 1.3(a) and (b) lead to a value below which the design of the laser gain medium is not dominated by ASE or parasitic oscillations, while a design point well above these estimations can become critical to issues connected to ASE and parasitic oscillations.

Different geometries scale slightly different in terms of the critical volume. Rods are slightly inferior compared to the thin disk in terms of energy storage in this case, but as the extraction is typically in the direction of the characteristic length, they are superior in the energetic gain  $G$ .

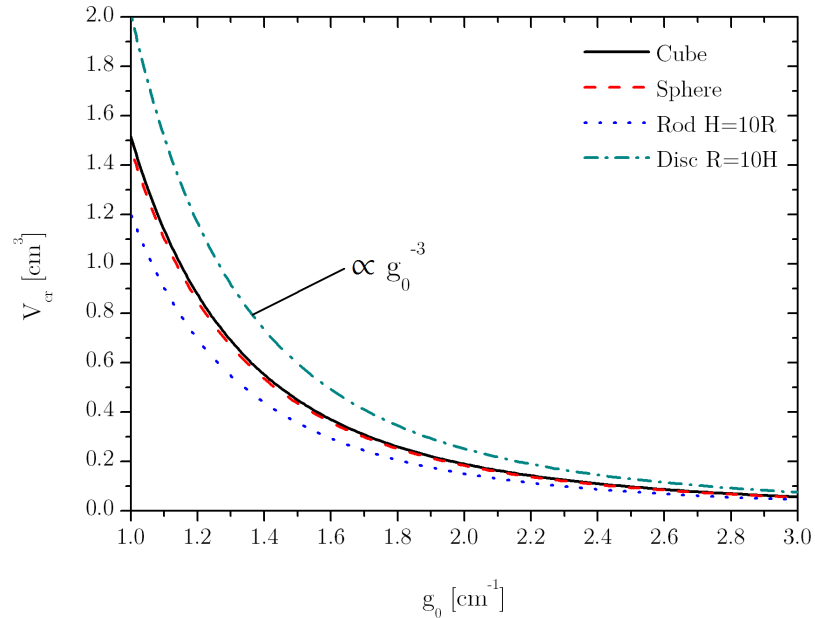
Figure 1.3(b) shows a comparison between the results of Equation 1.4.18 and 1.4.19 in the case of thin cylinder (the height is 1/10 of the radius). In this case, the critical radius  $R_{cr}$  is shown as a function of the small signal gain  $g_0$ . As comparison, the limit imposed by the surface reflectivity is plotted for different values. The main result is that the surface reflectivity plays an important role, if it is not suppressed. ASE depopulation will be the limiting factor if  $g_0 L > 4$  and parasitic oscillations are suppressed.

Beside the impact within the laser gain medium itself, the propagation of ASE in a laser amplifier chain decreases the laser system performance, especially the energy and temporal intensity contrast. ASE photons traveling under the restricted solid angle  $\Delta\Omega$  can reach the saturation fluence  $F_{sat}$  on the last amplifier stages. As an approximation for the ASE fluence  $F_{ASE}$  at the end of a laser chain the following

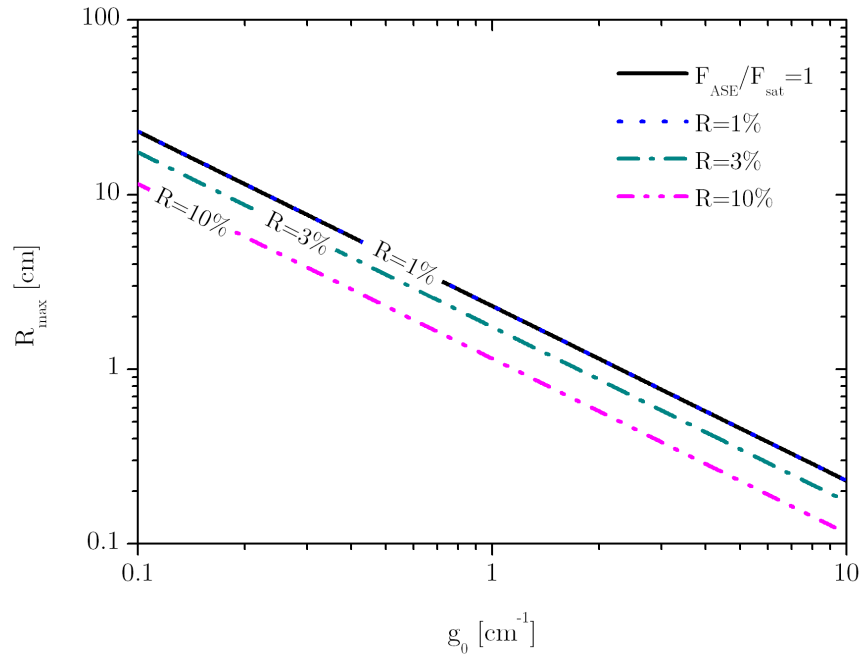
---

<sup>8</sup>This corresponds to the reflectivity of glass with  $n_0 = 1.5$  under normal incidence against air.

<sup>9</sup>This corresponds to the reflectivity of YAG with  $n_0 = 1.83$  against air under normal incidence.



(a) The critical volume  $V_{crit}$  as a function of  $g_0$  for different geometries below which strong ASE losses are prevented.



(b) The critical radius  $R_{crit}$  of a disk with a height  $H$  in the case  $R = 10H$  (Equation 1.4.18) and the corresponding limit for a given surface reflectivity (Equation 1.4.19)

**Figure 1.3.: Estimation of the critical volume  $V_{crit}$  as a function of  $g_0$  for different geometries (a), below which the condition  $F_{ASE} \ll F_{sat}$  is satisfied and therefore the working point is preferred. The critical radius  $R_{crit}$  for a disc with  $R = 10H$  (b) is compared to the corresponding values for different surface reflectivities.**

expression can be used [50, 51]:

$$F_{ASE} \approx \Delta\nu_{ASE} \Delta\Omega \Delta t_{ASE} \frac{hc_0 n_0^2}{\ln(2)\lambda^3} \frac{G}{\ln(G)} \quad (1.4.21)$$

where  $\Delta\nu_{ASE}$  is the ASE bandwidth,  $\Delta t_{ASE}$  is the duration of the ASE,  $h$  Planck's constant,  $c_0$  the speed of light in vacuum,  $n_0$  the refractive index of the amplifying medium,  $\lambda$  the emission wavelength and  $G$  the total energetic gain of the laser beam line. As an approximation for the spectral width of the ASE  $\Delta\nu_{ASE}$  one might use the relation for the spectral gain narrowing [52]:

$$\frac{1}{(\Delta\lambda_{out})^2} = \frac{\ln(G)}{(\Delta\lambda_g)^2} + \frac{1}{(\Delta\lambda_{in})^2} \quad (1.4.22)$$

where  $\Delta\lambda_{in}$  is the initial bandwidth,  $\Delta\lambda_g$  the bandwidth of the amplifying medium and  $\Delta\lambda_{out}$  the resulting bandwidth. Corresponding spectral shapes are approximated to be Gaussian. Translated into the bandwidth for the ASE  $\Delta\nu_{ASE}$  starting out of the noise gives approximatively:

$$\Delta\nu_{ASE} \approx \frac{\Delta\nu}{\sqrt{\ln(G)}} \quad (1.4.23)$$

wherein  $\Delta\nu$  is the gain medium bandwidth. A similar expression for the duration of the ASE can be found [51]:

$$\Delta t_{ASE} \approx \frac{\tau_{Pump}}{\sqrt{\ln(G)}} \quad (1.4.24)$$

where  $\tau_{Pump}$  is the pump pulse duration.

## 1.4.2. Thermal constraints for energy storage

Another limitation connected to the pump action comes out of the materials properties. When a solid state laser material is exposed to a certain value of stress it can deform or it fractures, if the limit of the strength of the material is reached. A non-uniform heating results in a non-uniform expansion and therefore leads to stress in the bulk material. The robustness of a laser material to a thermal shock is characterized by its thermal shock parameter [53]

$$R_S = \frac{k(1 - \nu_p)}{\alpha_T E} \sigma_{max} \quad (1.4.25)$$

where  $k$  [ $\text{W m}^{-1} \text{K}^{-1}$ ] is the thermal conductivity,  $\nu_p$  the Poisson ratio,  $\alpha_T$  [ $\text{K}^{-1}$ ] the thermal expansion coefficient,  $E$  [Pa] the modulus of elasticity and  $\sigma_{max}$  [Pa] is the maximum surface stress a material can resist. The value for the maximum

allowable surface stress is strongly related to surface quality, especially the fracture depth. Taking into account this consideration, a more general estimation is done by defining the allowable surface stress as [54]:

$$\sigma_{max} = \frac{YK_c}{\sqrt{a}} \quad (1.4.26)$$

where  $Y$  is a geometry factor near to unity, the fracture toughness  $K_c$  [ $\text{Pa m}^{1/2}$ ] and  $a$  [m] the depth of the largest flaw. The maximum allowable surface stress is a function of the maximum flaw and the material can be characterized by its thermal shock resistance  $R'_S$ :

$$R'_S = R_S \sqrt{a} \quad (1.4.27)$$

if the fracture depth is known. The polishing quality and the polishing materials are consequently key factors [55]. Estimation for the requested surface preparation quality and surface treatment quality can be given. A significant increase for the thermal shock parameter was achieved by improving polishing techniques [56, 57, 58].

One has to understand, that due to the statistical nature of the occurrence of surface and volume defects, the thermal shock parameter  $R_S$  will likely be reduced with an increasing size of the active medium. This is an important factor for scaling the active medium.

While pumping the active material, a fraction  $P_h = \eta_h P$  of the incident pump power  $P$  is converted into heat. The fraction of the absorbed energy, which is transformed into heat  $\eta_h$  depends on the laser and material parameters [59]. If the heat-generated stress exceeds the elastic modulus, fracture is imminent. A thermal shock limited pump power  $P_{R_S}$  can be defined as [60, 61]:

$$P_{R_S} = \frac{3R_S L^2}{\eta_h D}, \quad (1.4.28)$$

where  $L$  is the width of the pumped region,  $D$  the thickness of the gain medium. The assumption is that the slab is uniformly heated, is insulated on one side and  $D \ll L$ . In the case of a slab cooled on both lateral sides,  $P_{R_S}$  is four times larger. Besides the physical destruction of the laser material, generated heat affects the laser performance (e.g. a temperature dependent gain, stress induced birefringence, thermal lensing etc.). Considering a critical temperature difference  $\Delta T_{max}$  (compared to the initial temperature), a temperature difference limited pump power  $P_{\Delta T_{max}}$  might be defined as [60]:

$$P_{\Delta T_{max}} = \frac{2kL^2}{\eta_h D} \Delta T_{max} \quad (1.4.29)$$

Again a uniform heating was assumed and in the case of a cooling applied to both lateral surfaces, the allowable pump power is four times larger.

## 1.5. Power and Intensity Limitations

In the previous section we discussed the limitations due to the energy storage in a gain material used as an amplifier. Energy extraction brings limitations as well. If a laser beam is kept at a low intensity, it introduces no deterioration in a material. With increasing intensity reversible effects occur and finally non-reversible changes are generated. The physical origins of these changes are manifold, like a rise in temperature, strain, stress and the whole world of non linear effects. Nevertheless the interaction of the electrical field component of the laser pulse with the electrons in the conduction band of the solid state material is always the bias of the destruction mechanisms.

Two main classes of mechanisms lead to laser induced damage. Thermal processes, arising from the absorption of laser energy, is the first type and applies typically for cw, long-pulses (pulse duration  $\gg 10$  ps) and an operation at high repetition rates. Absorbed energy is transported into the lattice of the solid-state material resulting in local heating and therefore melting, softening or decomposition lead to laser induced damage. Because thermal conduction limits the heat deposition, the Laser Induced Damage Threshold (LIDT) fluence goes with  $F_{LIDT} \propto \tau_P^{0.4-0.5}$  in the range from 0.1 – 100 ns [62].

The second type of processes is a dielectric breakdown, where the electric field strength is strong enough to generate free electrons. The initial electron density (so-called seed) gets amplified by avalanche processes until it reaches a density of  $\approx 10^{18} \text{ cm}^{-3}$  where dielectric breakdown occurs [63]. For short laser pulses (pulse lengths  $\ll 10$  ps), the initial seed-electron density can be increased by multi-photon ionization. In this temporal regime absorption centers in the material are not dominant anymore [64], no direct correlation between the absorption and the damage threshold can be found.

Dielectric coatings are a very sensitive interface and by this of particular interest for the LIDT. Recent years showed a steady improvement in LIDT for those coatings. Inclusions within the coating layers can lead to the destruction of the dielectric coating itself. The density and nature of these inclusions significantly influence the laser damage threshold [65]. Minor ablations can lead to diffraction centers damaging preceding optical elements or can lead to bulk damage.

For high intensity pulses, the index of refraction  $n$  becomes dependent of the local intensity  $I$ :

$$n = n_0 + n_2 \cdot I \quad (1.5.1)$$

where  $n_2$  is the nonlinear index of refraction of a material. One of the effects is that the material becomes an optical element on its own, potentially compensating the natural diffraction. A power can be derived for the moment the diffraction by the beam propagation gets compensated by the intensity related non-linear lens effect and trapping the beam [66]. This power is called critical power  $P_{cr}$  and is given for a top-hat intensity distribution to be [67]:

$$P_{cr} \simeq \frac{\pi(0.61)^2 \lambda_0^2}{8n_0 n_2}. \quad (1.5.2)$$

The critical power  $P_{cr}$  is slightly different for different spatial profiles. However, the correction factor is close to 1 [67] and by this neglected in this context. Values for the nonlinear refractive index are often given in the CGS unit system ( $\gamma$  [esu]) and has to be transformed into the nonlinear refractive index in the SI unit system ( $n_2$  [ $\text{cm}^2 \text{W}^{-1}$ ]) using the relation  $n_2 = 4\pi\gamma/(c_0 n_0)$ . If the power is larger than the critical power ( $P \gtrsim P_{cr}$ ), whole beam self focusing after a distance  $z_{sf}$  is expected [67]:

$$z_{sf} = \frac{2n_0 w_0^2}{\lambda_0} \frac{1}{\sqrt{P/P_{crit} - 1}} \quad (1.5.3)$$

where  $w_0$  is a characteristic beam radius (in the approximation of a Gaussian beam profile it would be the half-width for the intensity at  $I/I_0 = 1/e^2$ ). Usually the material is not thick enough to generate a whole beam self focusing. Nevertheless a nonlinear lens is generated with a focal length  $f_{NL}$ . If the pulse crosses a thin layer with a thickness  $D$ , the focal length can be given as [10]:

$$f_{NL} \approx \frac{w_0^2}{4n_2 I_0 D}. \quad (1.5.4)$$

Again, one should consider, that the focal length is dependent from the spatial profile.

If the power is considerably larger than the critical power ( $P > P_{cr}$ ), small amplitude modulations in the spatial profile grow faster compared to the whole beam auto-focalization. The beam profile breaks up into small filaments, the so-called small-scale self-focusing occurs [68]. A threshold power similar to those of Equation 1.5.2 depends of the initial uniformity of the beam profile. Smooth beams will have higher thresholds compared to strongly modulated beam profiles. Moreover, these modulations can be acquired by bulk imperfections of the optical materials encountered during the propagation in the laser system.

Considering a randomly modulated uniform beam profile, a specific spatial frequency can be found where the modulation grows at maximum. The corresponding power is of the same order of magnitude as the critical power. During propagation, the ripples in the spatial profile grow at maximum in intensity [69]:

$$I = I_0 e^{2B} \quad (1.5.5)$$

where  $B$  is the beam break-up integral. An exponential growth of the spatial modulation is hereby estimated. The break-up integral is defined as the non-linear component of the spatial phase integrated over the beam trajectory:

$$B = \frac{2\pi}{\lambda_0} \int_0^D n_2 I(z) dz \quad (1.5.6)$$

where  $D$  is the length of the passed material. If not controlled by spatial filtering, the beam can break up into a number of filaments each containing the critical power.

Moreover, the output energy density of a laser system is limited by a given acceptable B-Integral  $B_{max}$ . In the case of a non-saturated gain,  $g_0 = \ln(G)/D$  and  $F_{in} \ll F_{out}$  Equation 1.5.6 is solved to get:

$$F_{out} \leq \frac{B_{max} \lambda_0 \ln(G) \tau_P}{2 \pi n_2 D}. \quad (1.5.7)$$

We can filter the spatial frequencies corresponding to the B-Integral  $B$  by the means of spatial filtering. Those have to obey certain rules regarding the design of filtering itself, especially the pinhole diameter  $\emptyset$  and the focal length  $f$ . The angular scale inhomogeneities growing with the maximum increment are [50, 69]:

$$\Theta_{max} = \left( \frac{2n_2}{n_0} I \right)^{1/2}. \quad (1.5.8)$$

In the far-field (i.e. in the focal plane of a spatial filter) spatial frequencies according to Equation 1.5.8 can be observed and filtered out by a pinhole located in the focal plane of a lens with a focal length  $f$ , if one satisfies

$$\Theta_{max} > \frac{\emptyset}{2f}. \quad (1.5.9)$$

Using Equation 1.5.7 we can estimate the necessary pinhole diameter to cancel a previously built-up B-Integral to be:

$$\emptyset < 2f \left( \frac{B_{max} \lambda_0 \ln(G)}{n_0 \pi D} \right)^{1/2}. \quad (1.5.10)$$

Typically a  $\Lambda$ -times diffraction limited pinhole is chosen, where the diffraction limit for a given Gaussian beam with a  $1/e^2$ -radius is  $w_f = \lambda f / (\pi w_0)$ . Therefore we can only cancel down to the spatial frequencies corresponding to the B-Integral  $B_{min}$ :

$$B_{min} > \Lambda^2 \cdot \frac{\lambda_0 n_0 D}{w_0^2 \pi \ln(G)}. \quad (1.5.11)$$

## 1.6. Overcoming the limitations – Gain medium selection for DPSSL

As described in the latter sections, depending on the parameters of the laser systems, various limitations occur, mainly in terms of repetition rate, energy, power and laser damage threshold. Every laser system to be build is then somehow limited according to its foreseen application. With the uprising of the first laser systems in the early 60's, laser damage threshold on/in the laser gain material and optics triggered the exploration of techniques to circumvent these issues. Shorter pulses with more energy require a higher laser damage threshold of all optical surfaces and volumes. Surpassing this limit was finally achieved using a technique called "Chirped Pulse Amplification" (CPA) [70] allowing a significant increase for the amplification of short pulses. The laser energy is nowadays limited by the LIDT of the pulse compression system.

On the other hand, large laser systems are limited in a more trivial way: their thermal management and efficiency. Large scale laser systems show typically efficiencies in the range of 1–0.1% as discussed in Section 1.3. This is acceptable for low-repetition rate applications (several shots per day up to several shots per hour), but becomes a problem if applications demand several shots per second. Average power consumption is a problem in this case, as for a kW-average power laser the injected power would be in the MW-range. Moreover, most of the injected energy would be transformed into heat resulting in a potentially vast cooling effort.

The key to the solution is an increase in efficiency. One solution is a Diode-Pumped Laser (DPL), as laser diodes combine a good e–o efficiency and a sharp emission spectrum compared to e.g. the emission of a flash lamp. The difficulty is that the output power of semiconductor laser emitter is rather small. Nonetheless, packaging several emitters to a bar leads to output powers in the order of 200–300 W per bar. Several bars can be stacked together and form a laser diode stack with a power in the order of 3–6 kW per stack with a surface of typically a few square centimeter. High-power laser diode stacks show an e–o efficiency of currently up to 70% under laboratory conditions and more than 60% for mass produced stacks. The rapid increase of available power and efficiency within the last decade will bring available efficiencies of 70% on the market for the next generation of laser diode stacks.

But even with an efficiency of 70%, 30% of the injected energy would be converted into heat. We define at this point the duty–cycle as the fraction of time in which the laser diodes are activated compared to the time of a period duration (i.e. the time

between the beginning of two successive pulses). For a duty–cycle higher than 10%, aggressive cooling is needed which can be achieved by water–cooling the laser diode stack with micro–channel coolers. Lower duty cycles relax this demand leading to much simpler cooling solutions.

State of the art laser diode stacks are driven with current up to 300 A, typically 150 A, and a voltage per bar of 2–4 V. Drivers delivering such currents have a rise time  $\tau_{10-90}$  in the order of 10  $\mu$ s. The falling time is in the same order. Pulses are by this limited to an order of magnitude of  $\tau_P \gtrsim 100 \mu\text{s}$ .

A suitable laser gain medium should therefore offer a lifetime of at least 100  $\mu\text{s}$ , a suitable pump band matching the laser diode emission and desired working wavelength, a low nonlinear index of refraction  $n_2$ , a high thermal conductivity, a sufficiently large absorption cross section, a saturation fluence less than the LIDT but large enough not to be limited by ASE. Unfortunately such an all–in–one gain medium suitable for every purpose doesn’t exist.

The fluorescence lifetime demand eliminates right away the gaseous and liquid gain media as their lifetimes are typically too short or the line width too small as discussed in Section 1.2.2. Solid–state materials are most adapted to these demands which is the reason why most of the diode pumped laser systems are Diode–Pumped Solid–State Lasers (DPSSL).

Let us now give a brief overview over a selected number of gain media and discuss their selection with respect to DPSSL requirements.

Equation 1.2.1 describes the relationship of the four gain media parameters

- the stimulated emission cross section  $\sigma_{ij} = \sigma_e$
- the line shape function  $g(\nu)$
- the frequency  $\nu$
- the fluorescence lifetime  $\tau_{ij} = \tau_f$

where by fixing three of those, a maximum performance for the fourth parameter is consequently defined. This section is dedicated to the derivation of the gain media parameters suitable for Diode Pumped Solid State Lasers.

In the case of a Gaussian broadening, the line shape function is given at the FWHM as [10]:

$$g(\nu) = \frac{2}{\Delta\nu} \left( \frac{\ln 2}{\pi} \right)^{1/2}. \quad (1.6.1)$$

This yields together with Equation 1.2.1:

$$\sigma_e = \frac{c_0^2}{8\pi\nu^2} \frac{1}{n_0^2} \frac{1}{\tau_f} \frac{2}{\Delta\nu} \left( \frac{\ln 2}{\pi} \right)^{1/2}. \quad (1.6.2)$$

Selecting the appropriate laser material strongly depends on the intended laser parameters. Laser systems operating in the picosecond (ps) and femtosecond (fs) range require large spectral bandwidths ranging from a few to several hundred nanometers. In contrast, pulses in the order of nanoseconds (ns) are manageable using laser gain media with a considerably smaller bandwidth. The relation between bandwidth and transform-limited pulse duration  $t_{min}$  [s] is expressed as:

$$t_{min}\Delta\nu \leq K \quad (1.6.3)$$

where  $K$  is a factor depending on the spectral shape of the pulse. As an example, a Gaussian shaped spectrum leads to  $K = 2 \ln 2/\pi \approx 0.441$  [32]. Transform limited pulses will show a minimum FWHM  $t_{min}$  of

$$t_{min} \leq \frac{\lambda^2 K}{c_0 \Delta\lambda} \quad (1.6.4)$$

where  $\lambda$  is the central wavelength and  $\Delta\lambda$  the FWHM bandwidth. Figure 1.4 shows the necessary bandwidth for different pulse durations  $t_{min}$  in a spectral range varying between 500 and 1500 nm.

Using Equation 1.6.3 in 1.6.2 with the definition of the saturation fluence 1.4.10 gives [71]:

$$\frac{\tau_f}{t_{min}F_{sat}} = \frac{\lambda^3}{8\pi n_0^2 hc} \left( \frac{\pi}{\ln 2} \right)^{1/2} \quad (1.6.5)$$

which describes the maximum performance achievable out of a solid-state laser material. With a wavelength of  $\lambda = 1 \mu\text{m}$ , a fluorescence lifetime of  $\tau_f = 100 \mu\text{s}$  and an index of refraction of  $n_0 = 1.5$  we get  $t_{min}F_{sat} \approx 5.3 \times 10^{-14} \text{ J cm}^{-2} \text{ s}$ . Ideally, a saturation fluence not larger than  $10 \text{ J cm}^{-2}$  would then allow diode-pumped fs-laser systems. Nonetheless, such an ideal material has to be found.

Figure 1.5 displays a number of various laser gain materials doped either with Nd, Yb or a transition metal. Most of the Nd-doped materials are limited by

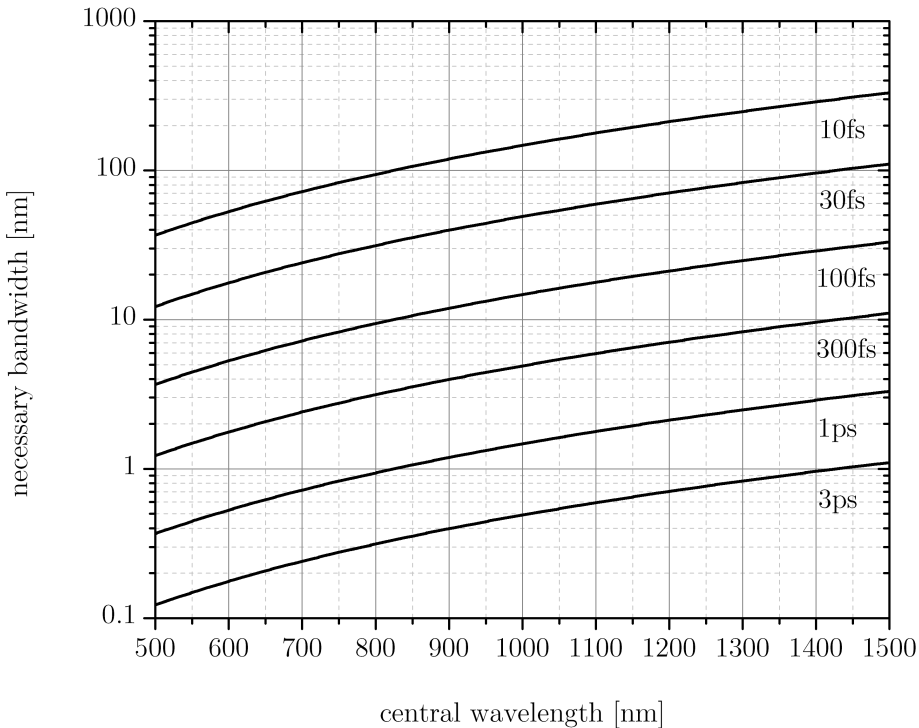


**Figure 1.4.:** Necessary bandwidths for selected pulse durations as a function of the central wavelength according to Equation 1.6.4

their low saturation fluence most of the transition metal doped materials show short fluorescence lifetimes. On the other hand, most of the Yb-doped materials show a high saturation fluence and a long fluorescence lifetime which makes energy storage more easy, but energy extraction becomes more difficult, as LIDT issues become more important.

The available bandwidths for selected materials are shown in Figure 1.6. In high-energy laser chains is the overall energetic gain  $G$  in the order of  $10^6 - 10^9$ , which increases in combination with Equation 1.4.22 the need for the available bandwidth approximately by a factor of  $\approx \sqrt{\ln G} \approx 4-5$ . As most of the laser materials work at laser wavelengths close to  $\approx 1 \mu\text{m}$ , satisfying a bandwidth of  $\approx 1 \text{ nm}$  for 1 ps pulses would require to rely on a gain medium with at least a spectral bandwidth of  $> 6 \text{ nm}$ . However, as in certain cases different laser materials can be combined to achieve a larger amplification spectrum (e.g. fluoride and phosphate glasses near 1057 nm) and a spectral shaping can be applied, restrictions can be somehow softened.

Thermal effects play an important role for high-power laser systems and therefore we are interested in a material exhibiting good thermal characteristics, especially the thermal conductivity  $k$  and the thermal shock parameter  $R_S$ . As shown in Equation 1.4.25, a linear relation between both parameters exists. Figure 1.7 shows,

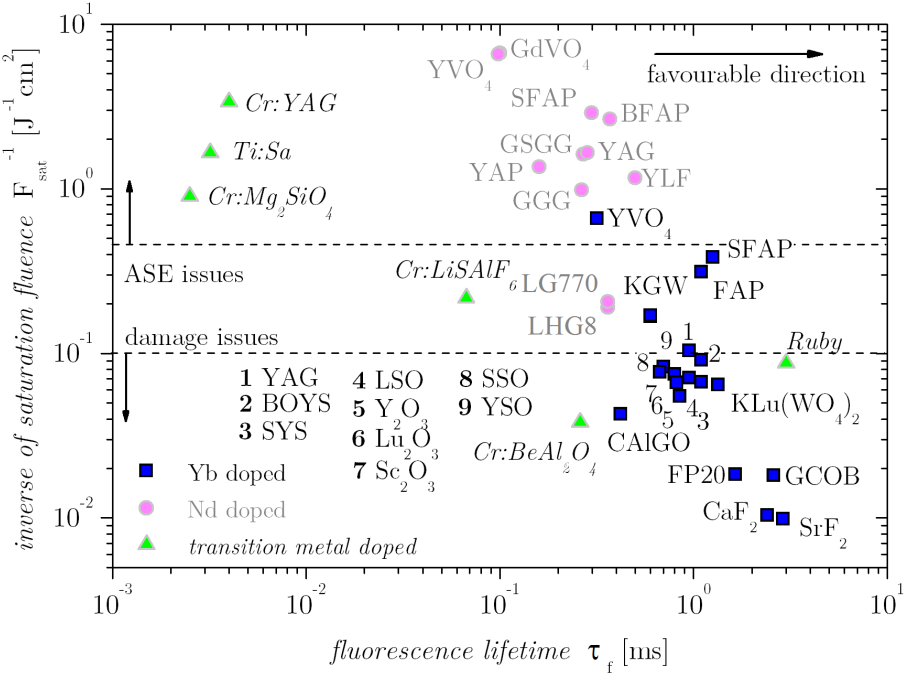


**Figure 1.5.:** Fluorescence lifetime (horizontal axis) and saturation fluence (vertical axis) overview over several laser gain materials, according to [71] and Table B.2.

for selected laser materials, the thermal shock parameter as a function of the thermal conductivity. Clearly one identifies the low thermal conductivity of glasses on one side and the high thermal conductivity for crystalline hosts, especially sapphire ( $\text{Al}_2\text{O}_3$ ). One has to take into account, that the fracture toughness depends strongly on the preparation of the samples [56, 54]. A significant increase can be found, resulting in an increase of the thermal shock resistance of up to one order of one magnitude (see GSCG and strengthened GSCG in Figure 1.7).

Recalling the significance of the nonlinear index of refraction  $n_2$ , another interesting way of classifying laser gain media for high-peak power laser systems is shown in Figure 1.8, where the product  $2\pi n_2 F_{sat}$  for a given pulse length of 1 ns at a wavelength of 1  $\mu\text{m}$  as a function of the critical power  $P_{cr}$  is shown. The first parameter represents the B-integral susceptibility of a laser material. If a laser pulse with a given pulse length  $\tau$  propagates with the saturation fluence  $F_{sat}$  in a laser amplifier, which might take place in the final passes within the laser amplifier, the accumulated B-Integral between the spatial filtering will be  $B \approx 2\pi n_2 F_{sat}/(\lambda\tau)DG$ , where  $D$  is the trajectory length in the gain medium and  $G$  the integrated energetic gain in this pass.

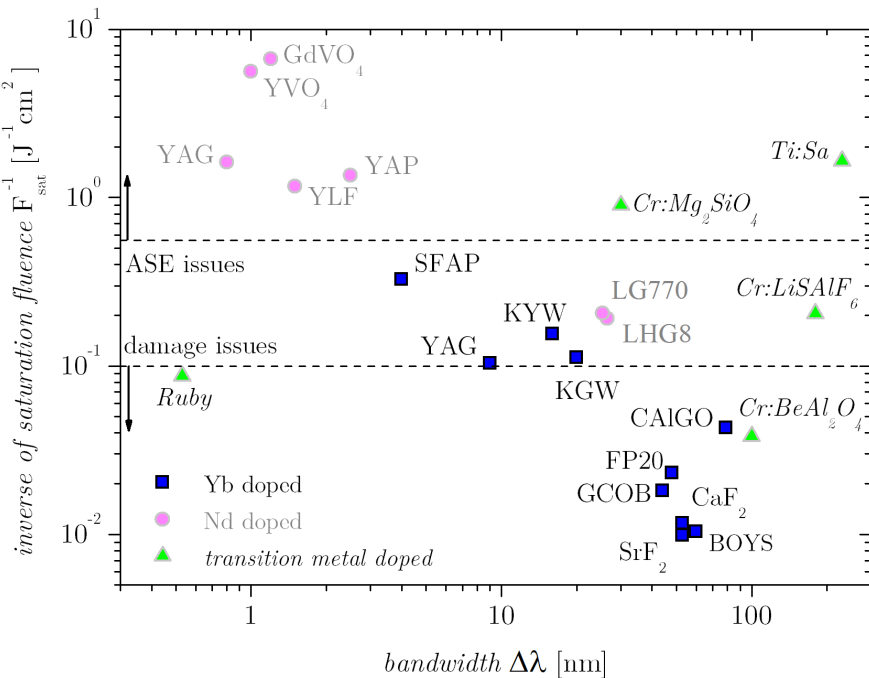


**Figure 1.6.:** Bandwidth versus saturation fluence for a selection of prominent laser materials, according to [71] and Table B.2.

By this, the traveled length in the amplifier  $D$  is restricted by a maximum allowable break-up integral  $B_{max}$ . The laser material performance for high-peak-power amplification is restricted by this parameter, as typically tens of centimeters of gain material has to be encountered before the spatial frequencies are filtered out and a catastrophic beam breakup is avoided. We have therefore a natural restriction for the amplifier sections in its last passes affecting the available gain in the early amplification passes, i.e. less material thickness is allowed to use, less gain being then achieved in the last amplification stage.

At this point one has also to consider, that not every gain medium can be produced with a sufficiently good optical quality in large sizes. Glass gain media were subject to a steady increase in available size and quality – especially Nd-doped glasses designated to the large high-energy systems [72]. Using standard glass fabrication techniques huge laser glass slabs were produced. For crystals this is more problematic and they are restricted to typical usable extensions ranging from 5 cm to 50 cm depending on the technique used. Currently transparent ceramics are of interest for future laser applications. They are currently mostly restricted to the cubic lattice system, like YAG and CaF<sub>2</sub>.

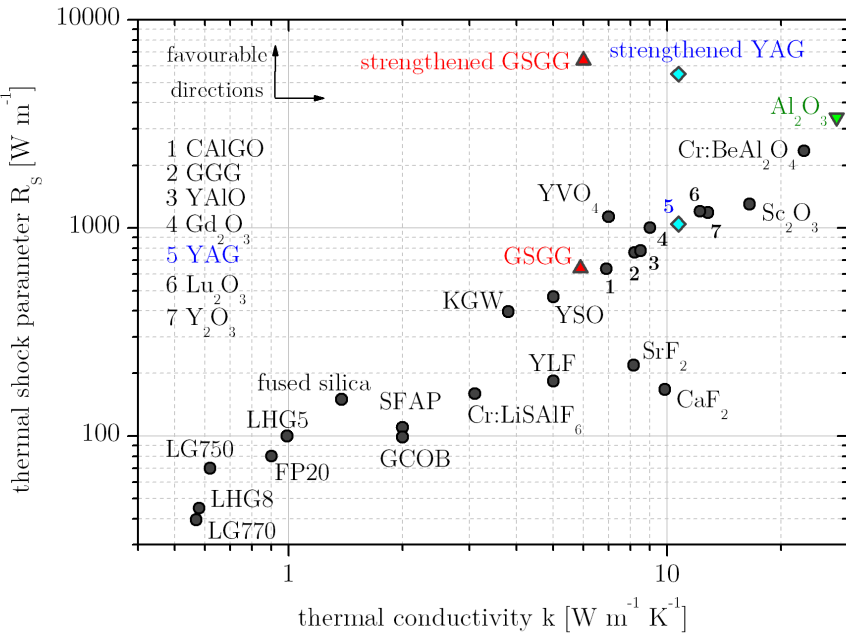


**Figure 1.7.:** Thermal shock parameter  $R_S$  as a function of the heat conductivity  $k$  for various materials at room temperature.  $R_S$  can be improved through specific preparation techniques e.g. for GSGG (red triangles) and YAG (blue diamonds). The data is given in Table B.2.

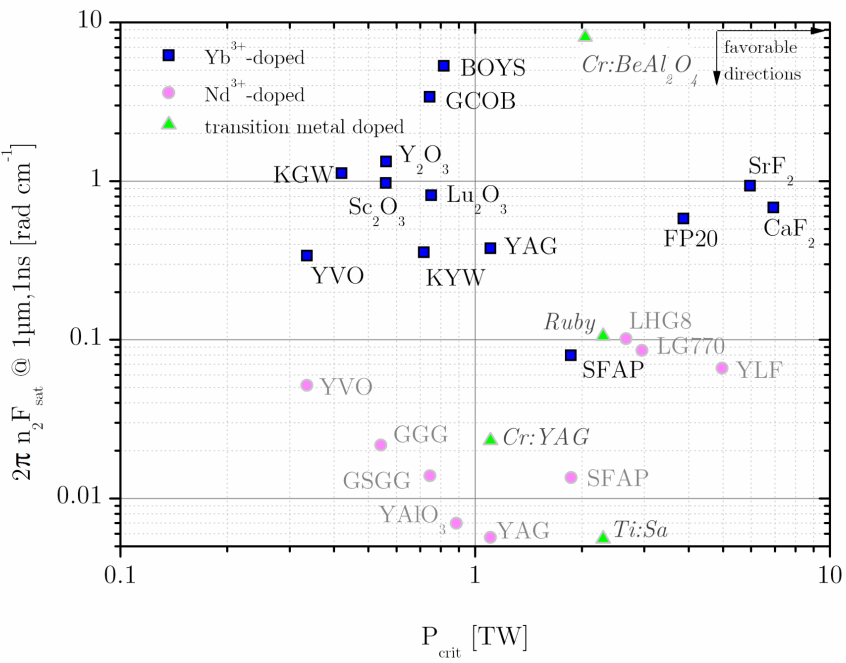


**Figure 1.8.:** Integral B susceptibility versus the critical power for  $1\text{ ns}$  pulses for various gain media. The data is given in Table B.2.

## 1.7. Repetition-rate applications

A classification of repetition-rate laser systems can, for example, be performed according to the envisioned applications

- Direct use of the laser system. The laser parameters must then fit specific application requirements.
- Indirect use, where the laser system acts as a pump source: the laser parameters must then satisfy pump requirements.

Interest in DPSSL is mainly related to efficiency on one side and the low thermal effects allowing high repetition rate operation on the other.

Recent years showed major steps in development of high-field physics using high-intense, ultra-short laser pulses. This opened the way for interesting applications, especially in the acceleration of electrons and ions on very short distances, allowing compact accelerators with outstanding particle pulse durations. One prominent future application is the generation of ion beams for cancer treatment, where conventional acceleration techniques result in large-scale machines, not suited for the common use e.g. in hospitals.

Another important application may be the thermonuclear fusion using lasers, a field known as IFE (Inertial Fusion Energy). Different fusion schemes need different lasers and different parameters.

This section summarizes the demand for such laser systems in terms of energy and pulse properties. When requested very basic discussions of the physical background and the related physical problems are derived.

### 1.7.1. DPSSL and (OP)CPA

After a certain period of stagnation in terms of short pulse duration, Chirped Pulse Amplification (CPA) [70] gave a major boost for the available peak power. Driving the development further in terms of available peak intensity will only be realizable with an increase in energy for pulses in the fs-regime coupled to a tight control of beam focusability through adaptive optics [73, 74].

A typical critical power for laser gain media is in the order of  $1 - 3 \text{ TW}$  (see Figure 1.8) and pulses are usually stretched to the order of a few nanoseconds. Energies up to the order of kilojoules are by this possible. Exawatts of laser power ( $10^{18} \text{ W}$ ) are potentially feasible if an appropriate bandwidth, an amplifying gain medium with a sufficient large diameter and a compression of the amplified, stretched pulses can be

achieved. In this extreme case it gets increasingly complicated to compensate the accumulated phase [75] and to control the intensity and energy contrast of such a laser system.

The choice whether one or more amplifying stages of the laser system should be realized as a DPSSL or if the DPSSL should act as a pump source, depends on the necessary bandwidth. As discussed in the previous section, gain media available for pumping by laser diodes have a bandwidth which is significantly less than 100 nm. As those laser systems work in the NIR near 1 μm pulses shorter than ≈ 30 fs are not easily accessible. Shorter pulses are only available if combinations of different gain media are used in the amplifier chain or in the case the DPSSL acts as a pump for a Ti:Sa CPA laser system or for an OPCPA (Optical Parametric Chirped Pulse Amplification).

OPCPA combines the Optical Parametric Amplification (OPA) [76] with the CPA concept. The gain medium in an OPCPA system is replaced with a non-linear crystal and the transfer between the pump (i.e. generated by the DPSSL) bases on non-linear wave mixing. The main advantage is a large available bandwidth for ultra-short pulses [77]. Despite the absence of ASE, we have unfortunately Optical Parametric Noise and Parametric Fluorescence as contrast-limiting effects [78]. The efficiency of OPCPA systems varies typically between 20 – 30% [79, 80].

If the DPSSL is chosen to act as a pump source for the corresponding laser system, conversion and extraction efficiency of the pump system has to be taken into account separately, which leads to a global 10 – 20% efficiency.

The electron acceleration by laser interaction is mainly defined by the maximum of the normalized vector potential of the laser pulse  $a_0$  [81]:

$$a_0 \simeq 8.6 \times 10^{-10} \lambda_L I_L^{1/2} \quad (1.7.1)$$

where  $\lambda_L$  [μm] is the laser wavelength and  $I_L$  [W cm<sup>-2</sup>] is the laser intensity at the laser focus. Relativistic effects become important if  $a_0 \geq 1$ , therefore for a wavelength of  $\lambda = 1$  μm for intensities  $I_L \geq 1.36 \times 10^{18}$  W cm<sup>-2</sup>. Current laser system achieve peak intensities of up to  $I_L \approx 10^{20}$  W cm<sup>-2</sup> consequently  $a_0 \approx 10$ . The peak electric field strengths reach  $E_{peak}^{elec}$  [TV m<sup>-1</sup>]  $\approx 3.2 a_0 / \lambda$  [μm]. The electron motion becomes relativistic and the laser–plasma interaction becomes nonlinear. As the magnetic component of the Lorentz force will create a component in the laser light propagation direction, electrons get accelerated. A good overview over the theory of laser–driven plasma–based electron accelerators can be found in [81].

Electron energies of up to 1 GeV have been demonstrated so far [82]. Laser systems used are table–top sized and show powers in the order of 50 TW with pulse durations

between  $30 - 50$  fs. The electron energy scales in respect to the laser power  $P_L$  as  $E_e \propto P_L^{1/3}$  and, concerning the electron bunch charge, we get  $C_{bunch} \propto P_L^{1/2}$  [83]. High electron energies in the order of a few GeV with charges in the order of 1 nC requires a laser of the petawatt-class with pulse durations in the order of 100 fs or less [83].

Generating proton beams is currently only accessible via a secondary effect as the protons are 1836 times less susceptible to acceleration than electrons due to their higher mass. Typical laser pulses show an ASE pedestal and potential pre-pulses which generates a plasma if the high-intense laser pulse hits a target (i.e. a metal foil). As this heating generates electrons and their mean free path is long enough to travel through the target material, a strong charge separation is generated tearing positively charged ions and protons along their path [84, 83]. Using microstructured targets, one can favor a defined energy range and quasi-monoenergetic proton beams are possible [85].

Using proton beams for cancer treatment would need energies in the order of 100 – 200 MeV as well as a sufficient repetition rate (i.e. 1 Hz). Such laser systems would have peak powers in the order of  $P_L \approx 1 - 2$  PW [83] and demand a good temporal contrast (pre-pulses e.g. should not show intensities of more than  $10^{14}$  W cm $^{-2}$ ).

### 1.7.2. Laser Fusion

Shortly after the first Q-switched lasers were demonstrated, the idea to create a laser pulse intense enough to ignite DT (Deuterium–Tritium) fuel came into mind. Such thermonuclear burn gives access to a rather clean source of energy, when considering the relatively short lifetime of associated nuclear wastes.

The first approach is historically the Inertial Confinement Fusion (ICF) triggered by laser impact (laser fusion). A fuel capsule is imploded by a laser-driven expanding plasma (corona) on its surface such that certain values of core temperature and density are achieved. They must obey the Lawson criterion [86]. A major breakthrough to achieve those compression factors is an isentropic compression using laser pulse shaping on nanosecond time scale [87]. Those pulses have a pulse shape in the form of

$$P(t) \propto \frac{1}{|t - t_0|^\beta} \quad (1.7.2)$$

where  $\beta$  is  $\approx 2$ . In special cases  $\beta = 2$  can be shown explicitly [88]. This scheme can be called Central Ignition (CI) as the hot spot, where the thermonuclear burn

starts, is situated in the center.<sup>10</sup> In this regime, two routes are conceivable:

- direct drive with a directly laser-irradiated capsule
- indirect drive where the laser energy is first converted into X-rays with help of a small Hohlraum target surrounding the capsule

Direct drive is somehow unfavorable as it implies high demands for the spatial uniformity of the laser light of the target. A nonuniform pump distribution would give rise to hydrodynamic instabilities which inhibit compression, thus more driver energy is required. Expanding plasma has a critical density and light entering the plasma front will be reflected at the critical electron density  $n_{cr} = \omega_L^2 \epsilon_0 m_e / e^2$ . Usually the laser wavelength is converted to the third harmonic increasing significantly the penetration.

The conversion to X-rays on the other hand smears the intensity variations out, the irradiation is more homogeneous, and allows a much better penetration. However, an indirect driven target is much more complicated and this conversion has its own limited efficiency. The energy requirement for such a pulse [87] is in the order of

$$E_{ICF} = 1 - 2 \text{ MJ} \quad @ \quad 3\omega, 5 \text{ ns} \quad (1.7.3)$$

With a conversion efficiency of about 50% from the NIR to the UV wavelength, the energy at  $\omega$  must be then approximatly 4 MJ. In the case of a glass laser chain, peak powers of 3 – 4 TW are reasonable taking into account critical power limitations. Consequently about 200 laser lines are necessary.<sup>11</sup>

To overcome the strong demand on the compression energy the concept of Fast Ignition (FI) was proposed in 1994 [89]. The thermonuclear fuel is pre-compressed using spherical implosion [90] and then ignited near the center of the compressed fuel using a heating event<sup>12</sup>. This has the advantage that less laser power and energy is needed for compression. The triggering event near the compressed core might be electrons or ions injected from an external source or an ultra-intense laser pulse generating the hot electrons. Once the burn started, a burn wave propagates through the whole fuel.

---

<sup>10</sup>The overall process is somewhat similar to a Diesel combustion engine.

<sup>11</sup>In the case of a material using a lower critical power, the number of laser lines has to be adjusted consequently.

<sup>12</sup>As the CI is compared with a Diesel engine, one might understand the FI as a gasoline combustion engine.

In the case of a high-energy, ultra-intense laser pulse, the requested laser energy  $E_L^{ig}$  is [91]:

$$E_L^{ig} \geq 93 \left( \frac{\rho}{300 \text{ g/cm}^3} \right)^{-0.9} \left[ \frac{f_R \lambda_{ig}}{0.5 \mu\text{m}} \frac{0.25}{\eta_{ig}} \right]^2 \text{ kJ} \quad (1.7.4)$$

where  $\rho$  is the fuel density,  $f_R$  is a parameter close to unity,  $\lambda_{ig}$  the ignition pulse wavelength and  $\eta_{ig}$  the amount of laser energy transferred to the compression fuel through hot electrons. The laser pulse has consequently an energy in the order of 100 kJ. Typical estimated pulse durations are in the order of 10 ps. The compression pulse shows a similar shaping compared to the ICF case but with an energy of only  $\approx 180$  kJ.

Again, the compression pulse must be converted to the third harmonic implying an efficiency of about 50%. About 400 kJ are by this needed resulting in at least 20 laser lines, which is a factor of 10 less than for CI. The main problem lies in the short pulse part, as those powers need the application of CPA. The problem of LIDT of gratings, grating size and grating separation favor large bandwidth pulses [92]. Using the same type of laser lines for the ignition pulse, another (at least) 10 laser lines are necessary. However those beams have to be combined within a restricted angle from one side onto the compressed thermonuclear fuel.

A relatively new concept of FI is Shock Ignition (SI) [93, 94]. The ignition is generated through an additional hydrodynamic laser-generated shock. The overall concept is close to the CI combined with additional laser pulses generating the shock. This combines the relatively relaxed requirements for the compression (slow but efficient compression) with an all-optical approach, free of an additional particle source. This shock is generated by a “spiked” pulse at the end of the nanosecond compression pulse<sup>13</sup>. The total laser energy is less than for the standard CI.

This scheme uses only 50 – 75 kJ in a 300 – 500 ps [90]. If a temporal substructure within the sub-ns pulse is demanded, stretching and compression of the pulses is necessary. If the hurdle of a temporal shaping could be overcome, a CPA part could be avoided.

The main advantages of SI compared to FI is that the beam spot sizes are concentrated uniformly on the (spherical) fuel capsule. However, detailed calculations for peak power, B-Integral, etc. are necessary to assess more informations about the maximum achievable performance of appropriate laser lines for FI and SI.

---

<sup>13</sup>As CI has its analogon in the Diesel engine, the FI as the gasoline engine, the SI can be understood as a low-pressure Diesel engine, whose cylinders shrink abruptly at maximum compression to finally initiate the burn.

The HiPER (High Power laser Energy Research) project currently favors a  $\sim 10$  Hz repetition rate Shock Ignition scheme. LULI is strongly involved in this pan-European program in terms of Laser–matter interaction as well as Laser–development through the Lucia laser system. In the next section, DPSSL facilities throughout the world are described.

### 1.7.3. State of the Art

Project	Mercury	HALNA	GENBU	POLARIS	PFS
Location	USA	Japan	Japan	Germany	Germany
Application	IFE/Ti:Sa	IFE	IFE	CPA	OPCPA
Gain medium	Yb:S–FAP	Nd:Glass	Yb:YAG	Yb:Glass	Yb:YAG
Pulse energy [J]	55(100)	21.3(100)	0.22(1000)	12(150)	2.9( $4 \times 12$ )
Pulse duration [ns]	14	9	10	2	6(2)
Repetition rate [Hz]	10	10	100	0.05	1(10)
Center wavelength [nm]	1050	1050	1030	1030	1030
Pump Wavelength [nm]	899	808	940	940	940
o–o efficiency [%]	12	12	30	5	9

**Table 1.3.:** Comparison between the different DPSSL laser systems worldwide [95]. Target characteristics are given in parenthesis.

Throughout the world, a limited number of High–Energy–Class Diode Pumped Solid–State Lasers (HEC–DPSSL) are currently under construction, mainly situated in USA, Europe and Japan. Those systems can be divided into two groups of lasers according to their application. As mentioned before, the application drives the required characteristics of those laser system, swiftly speaking of the repetition rate, pulse duration, pulse energy and restrictions to the amplifying material.

One one side there are efficiency–oriented ns–lasers mainly dedicated to the field of IFE and on the other side the laser systems dedicated to (OP)CPA applications. Table 1.3 summarizes the current point of development of those systems.

**POLARIS** The POLARIS (Petawatt Optical Laser Amplifier for Radiation Intensive experimentS) system is the only direct–diode–pumped fs–laser in this overview. The laser gain material is Yb:FP–glass offering a sufficient wide gain bandwidth to support pulses in the order of 100 fs. It relies on the CPA–technique being structured according to an oscillator–stretcher–amplifiers–compressor architecture. As the gain medium is glass, a high repetition rate such as 10 Hz can not be reached. The target

pulse energy after compressor is 150 J at a repetition rate of 0.05 Hz. Combined with a pulse duration of 150 fs, a 1 PW laser system would be realized. Within the amplifier, the pulse is stretched to 2 ns, gets subsequently amplified within five amplifier stages (the last contains 240 laser diode modules with 6 J at 940 nm each) and is recompressed using a tiled grating compressor [96].

Current operation is at 10 J which results in a 60 TW laser system.

**Petawatt Field Synthesizer** The Petawatt Field Synthesizer (PFS) is an OPCPA laser system aiming at few-cycle laser pulses ( $\sim 5$  fs) with energies above 3 J and repetition rate of 10 Hz [97]. The pump source is a DPSSL laser system with four laser arms each delivering 12 J at 1030 nm. The pump laser is a CPA on its own and produces frequency-doubled  $\approx 6$  J with pulse durations of 1 – 10 ps.

A portion of the pulse used in the OPCPA part is used to generate the seed for the pump laser part ensuring the synchronization. Currently about 3 J have been shown on the pump laser part [98].

**MERCURY** The first 100J-class DPSSL program developed and yet showing the highest performance is the MERCURY project [99, 100]. The system uses two main amplifiers in a image-relayed four-pass setup. Each of the amplifier heads hosts seven thin slabs and is cooled using a turbulent He-gas flow. The gas flows between the slabs with a low Mach number ( $\approx 0.1$ ) and ensures an efficient cooling. The gain medium is Yb<sup>3+</sup> doped S-FAP [101] pumped from both sides along extraction direction.

The achieved output energy is  $\approx 55$  J at a repetition rate of 10 Hz. It has shown that such systems can work stable for a long time ( $> 2 \times 10^5$  shots have been shown so far). In the same time an efficient frequency conversion at a high average power has been shown. Dedicated applications range from scaling for laser fusion beam lines to Ti:Sa pumping for ultra-short laser pulses.

**HALNA** The Japanese HALNA (High Average-power Laser for Nuclear Fusion Application) [102] system relies on a zig-zag amplifier design to generate in the final layout 10 ns pulses with 100 J at a repetition rate of 10 Hz. The beam travels under Total Internal Reflection (TIR) within the gain medium. Despite it is intended to work at a high average power, a Nd<sup>3+</sup> doped glass was chosen. The strong deformation of the glass under pumping is partially compensated by an electrical heating of the the not pumped periphery. A low beam quality is inherent to the zig-zag slab geometry used. Due to the choice of the dopant, pump pulse duration is in the order of  $\sim 200$   $\mu$ s. Nevertheless more than 21 J were achieved at 10 Hz [103].

Favored applications for such beams are surface treatment applications. Experiences drawn out of this program are a vital input for cryogenic approaches for a better beam quality which are currently under study by this group.

**GENBU** The most ambitious project in the context of this section is the GENBU (Generation of ENergetic Beam Ultimate) laser. It is designed as a CPA laser system comprising two optically synchronized laser lines. One laser line will be dedicated to a cryogenic Yb<sup>3+</sup>:YAG laser system in an active mirror scheme with a pulse energy of 1 kJ, pulse durations 10 – 100 ps and repetition rates of up to 100 Hz [104].

A part of this laser light is frequency converted and used as the pump pulse of the ultra-short, ultra-intense OPCPA laser line. Large bandwidths support pulse durations down to  $\sim 5$  fs with pulse energies of up to 10 J and a repetition rate of up to 100 Hz.

The current development is in the first stages of the GENBU laser system demonstrating 1 J with a repetition rate of 100 Hz [105].



## 2. The Lucia Laser System

### 2.1. Overview

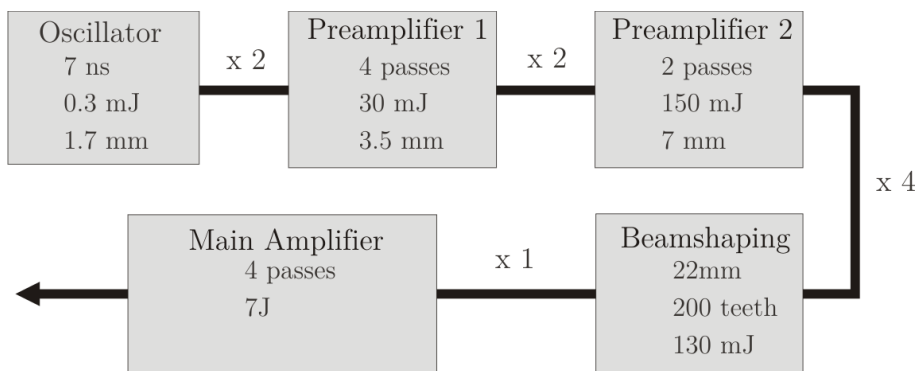


**Figure 2.1.:** Schematic overview over the Lucia laser system.

The Lucia laser system is a DPSSL program aiming at a 100 J, 10 Hz (i.e. a kW average power) laser pulse train. A pulse duration around 10 ns is targeted. The whole system relies on Yb<sup>3+</sup>:YAG as its gain medium and thereby the wavelength will be 1030 nm.

This thesis is situated within the context of the first 10 J milestone for laser operation at a repetition rate close to 2 Hz and a pulse duration of  $\leq 10$  ns.

Figure 2.1 shows the layout of the laser system as a sketch. An oscillator generates the initial pulses which are amplified in the two stage pre-amplifier system to a sub-J level. Successive magnification and a beam shaping section using a serrated aperture magnifies the beam to a diameter of 22 mm. The main amplifier stage boosts the energy to the 10 J level in four passes before the laser pulse leaves the laser system.

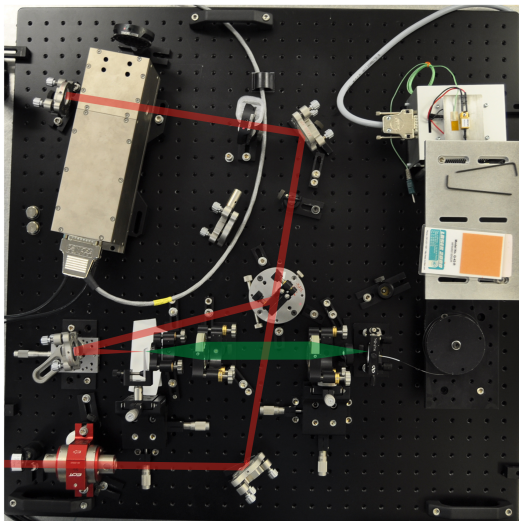
A short description of every stage of the Lucia laser system is given within this chapter. The following section describes the oscillator followed by the pre-amplification stage. The final two sections are dedicated to the beam shaping and finally the description of the main amplifier.

## 2.2. Oscillator

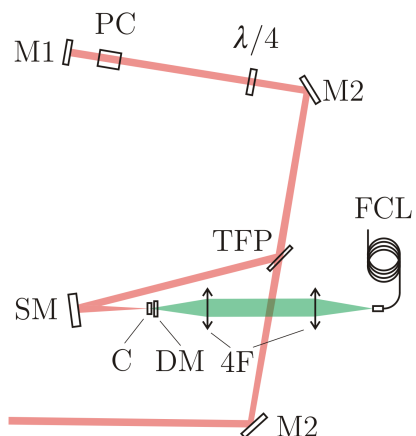
The setup of the developed oscillator is shown in Figure 2.2(b). It relies on cavity dumping although it is not driven with a high-repetition rate in contrast to typical cavity dumped systems. The repetition rate ranges from single-shot up to 10Hz, which makes the system more to a regenerative amplifier used as an oscillator. Pulse creation can be considered through several steps:

1. pumping the gain medium hosted in a lossy cavity, which is similar to the Q-switching operation.
2. establishing a low loss (high quality) cavity whereas the energy is stored inside the cavity
3. the pulse is coupled out at a speed only related to the cavity length and the switching speed.

The main advantage is that the pulse duration relies only on the cavity length and the switching time of the outcoupling. Such a system has been demonstrated to work in the mJ-level as well as in regenerative amplifier configuration[106].



(a) Oscillator operating setup



(b) Oscillator setup sketch

**Figure 2.2.:** Setup sketches for the oscillator, (a) operating setup, (b) sketch of the setup. M1 0° mirror, M2 45° mirror,  $\lambda/4$  wave plate, PC Pockels Cell, TFP Thin Film Polarizer, SM Spherical Mirror, C Yb:YAG Crystal, DM dichroic mirror, 4F 4-f imaging system of the pump, FCL Fiber-Coupled Laser Diode

The pump source is a fiber-coupled laser diode (LUMICS GmbH) tuned to the zero-line of Yb<sup>3+</sup>:YAG (970 nm) with a cw power of up to 10 W at 12 A, while the laser diode driver (OSTECH GmbH) is restricted to 8 A. The fiber has a diameter of 150 µm with a numerical aperture of 0.22. The emission of laser diode transported to the fiber tip is imaged using two lenses with a focal length of 75 mm forming a classic 4f afocal imaging system onto the gain medium (C). A 3 mm thick, 10 at.% doped Yb<sup>3+</sup>:YAG crystal is used as the gain medium. Both sides are Anti-Reflection (AR) coated for pump and laser emission wavelengths.

As depicted in Figure 2.2, the resonator is composed of a dichroitic mirror (DM) (AR for the pump at 970 nm and HR for the laser emission at 1030 nm), a spherical mirror (SM) of focal length of 100 mm, a thin film polarizer (TFP), a bending mirror (M2), a  $\lambda/4$ -wave plate, the Pockels Cell (PC) and the final cavity end mirror (M1). The SM is slightly tilted, which introduces astigmatism. In the pulsed regime a repetition rate of up to 10 Hz is achievable. Due to the small pumping spot of approximately 150 µm, the oscillator is limited by the LIDT of the gain medium coating.

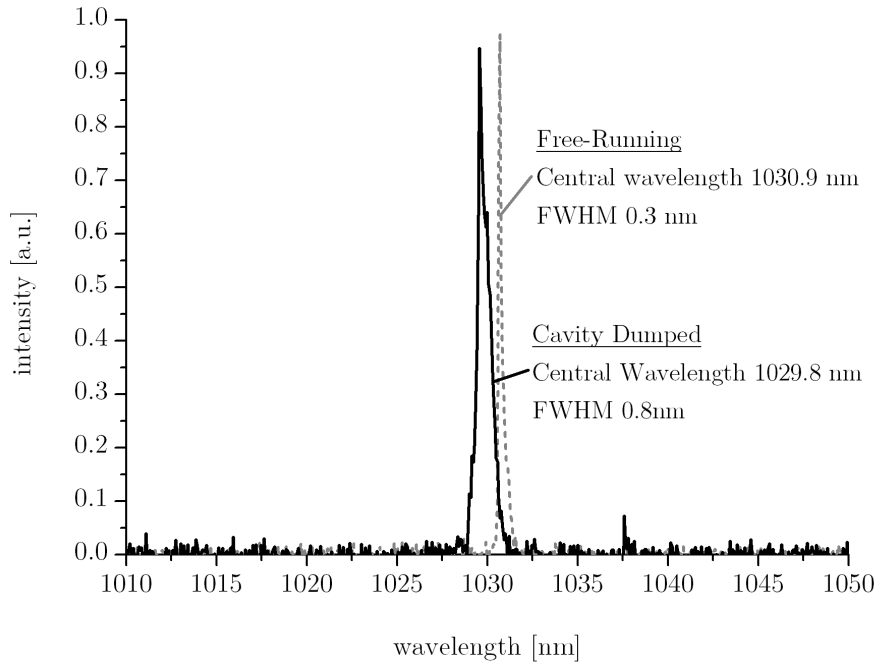
The DKDP<sup>1</sup> Pockels Cell is driven by a high-voltage driver (built by Bergmann GmbH) with an adjustable tension around 3.4 kV.

The pump duration is 1.3 ms. Approximately 10 % of the pump light is transmitted and only  $\approx 55$  % of the energy is stored according to Equation 1.4.12. Working in the free-running regime where no cavity dumping is applied, allows a narrow output spectrum with a FWHM of only 0.3 nm, whereas in the cavity dumped case the spectral width rises to 0.8 nm (see Figure 2.3). Simultaneously, the output spectrum shifts from almost 1031 nm to approximately 1030 nm. This behavior is explained in Figure 2.3(b). While in the free-running regime the laser oscillation starts at the point where the intracavity gain overwhelms the losses, the excitation of the laser gain medium stays low. This is opposite to the case, where the cavity dumping is applied – the relative excitation value  $\beta = \hat{n}/\hat{n}_{tot}$  is higher, therefore the emission wavelength shifts to smaller values, as in the case of Yb:YAG, the wavelength with the maximum gain is dependent from the excitation.

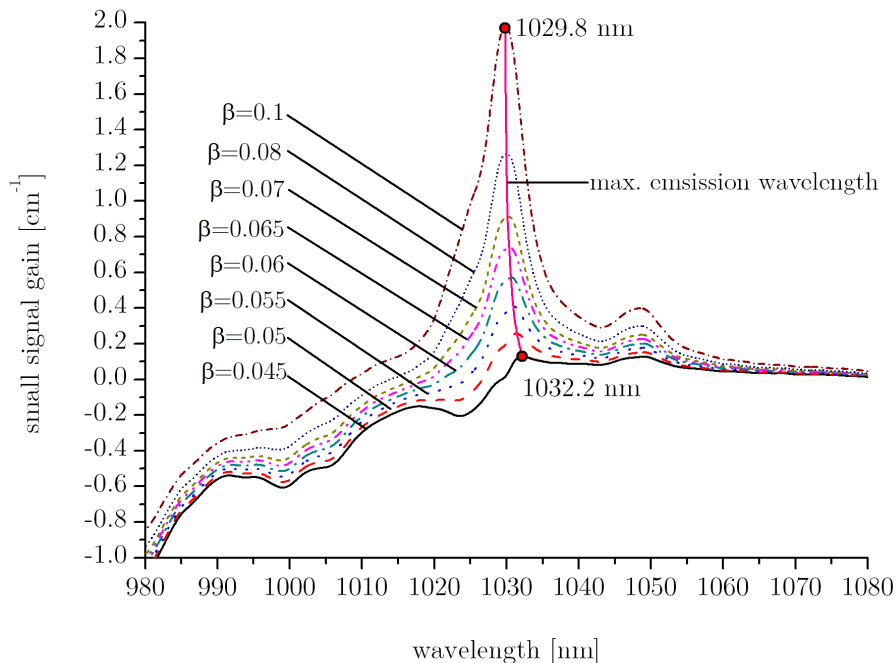
The pulse energy as a function of the stored energy within the Yb:YAG crystal is shown in Figure 2.4(a) for three different repetition rates, namely 1 Hz, 3 Hz and 10 Hz. A decrease in available output energy is observed, as the gain is depending from the temperature. A higher average power introduces a higher temperature within the gain medium.

---

<sup>1</sup>more than 98 % Deuterium



(a) Oscillator spectra in the free-running and cavity dumped regime.



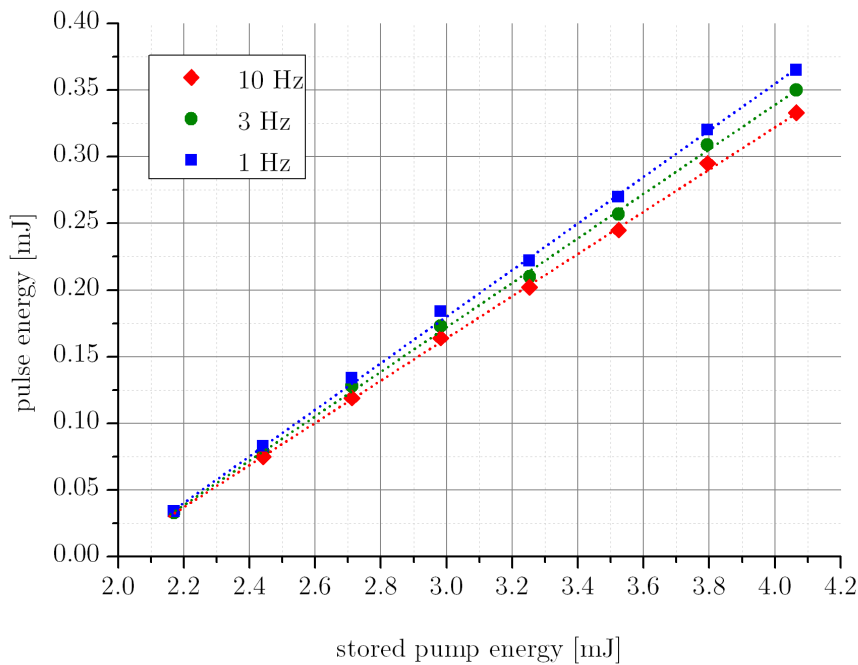
(b) Oscillator wavelength shift explanation

**Figure 2.3.:** Spectra for the free-running and the cavity dumped operation of the oscillator are shown in (a). The maximum gain wavelength varies with the excitation value  $\beta = \hat{n}/\hat{n}_{not}$  (b) and therefore the output wavelength of the oscillator shifts.

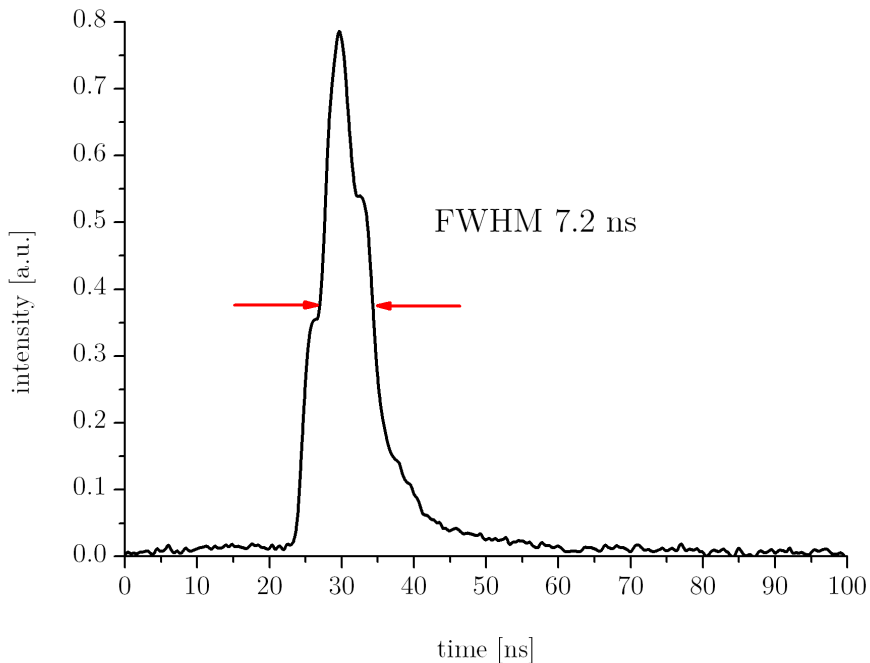
As the optical length of the cavity divided by  $c$  is approximately 5 ns and the fall time of the Pockels–Cell is approximately 5 ns too, a resulting pulse duration of approximately 7.2 ns is found. The temporal pulse form is displayed in Figure 2.4(b).

The spatial beam profile is Gaussian in the near field as it is shown in Figure 2.5(a). Due to the slight off-axis use of the spherical mirror, an astigmatism can be found in the far field (Figure 2.5(b)).

Oscillator protection from unwanted reflections is performed with a Faraday isolator (more than 30 dB extinction ratio). Consequently the polarization is turned by 45°.

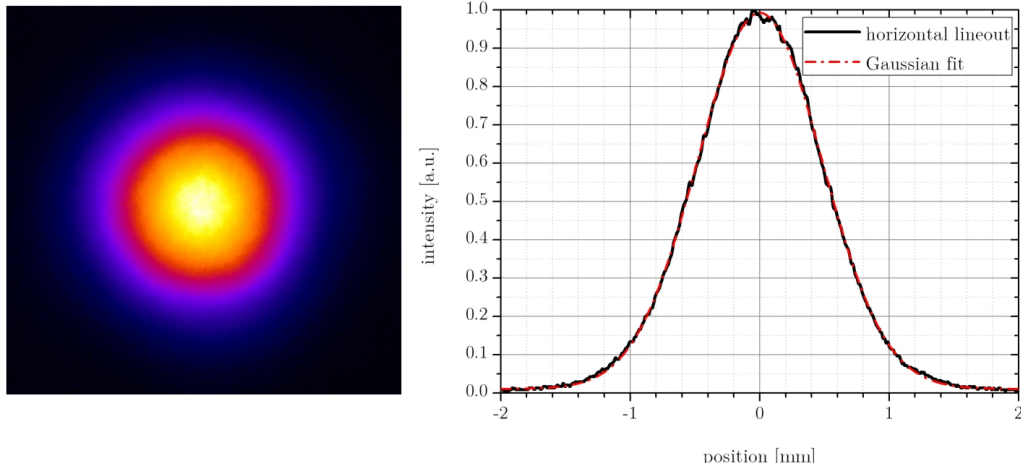


(a) Oscillator energy as a function of stored pump energy for three different repetition rates

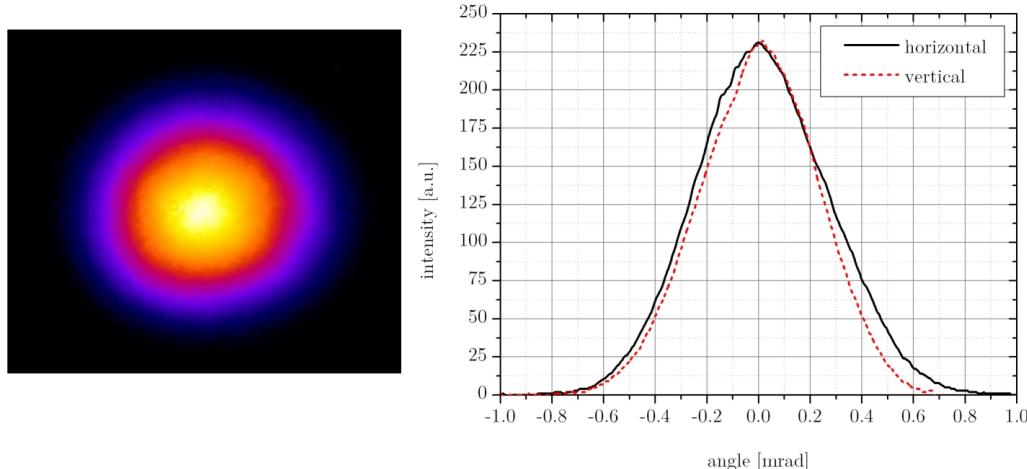


(b) Oscillator temporal pulse shape

**Figure 2.4.:** Energy characteristics of the oscillator, (a) shows the pulse energy as a function of the stored energy and (b) the temporal pulse shape.



(a) Oscillator near field transverse intensity distribution (left), with horizontal lineout (right). As comparison, a Gaussian fit is given.



(b) Oscillator near field transverse intensity distribution (left), with horizontal and vertical lineout (right).

**Figure 2.5.:** Output beam shape of the operating oscillator, (a) shows the near field of the laser pulse, (b) the far field. Lineouts are given.

## 2.3. Preamplification Stage

Coming from the oscillator, the pulse is directed to a pre-amplifier stage. After encountering a Faraday isolator, a magnifying imaging 4f system is used to increase the beam diameter from 1.3 mm to 2.7 mm.

Pre-amplification is performed in 2 steps. A first stage based on four angular multiplexed passes increases the pulse energy from  $\approx 0.3\text{ mJ}$  up to  $170\text{ mJ}$ . The typical point of operation is an output energy of  $30\text{ mJ}$ . A second stage increases the pulse energy in two passes from  $30\text{ mJ}$  to  $\approx 150\text{ mJ}$ . Both stages rely on image relay to keep the intensity distribution from one step to the next one. The first preamplifier pumping head relies on a 3 kW laser diode stack manufactured by DILAS whose emission is concentrated using a spherical lens and a pair of concentration mirrors.

The achievable pump intensity is  $20\text{ kW cm}^{-2}$  on a spot size of  $3.3\text{ mm} \times 3.8\text{ mm}$ . The pump duration is set to 1ms and the emission spectrum tuned to 940 nm by adjusting the water temperature of the laser diode stack. The laser gain medium is a 3.2 mm thick Yb:YAG crystal AR coated for both the pump and emission wavelength on the front surface and HR coated on the back side, where the internal reflection occurs.

Each pass shows a maximum non saturated gain of up to 6. A magnifying telescope between the two amplifiers adapts the pump spot size.

The second pre-amplifier is built according to the same design, with a pump spot size is of  $7.5\text{ mm} \times 10.5\text{ mm}$ . Instead of one single laser diode stack, 4 identical laser diode stacks are used for the pumping head, resulting in a comparable pump intensity.

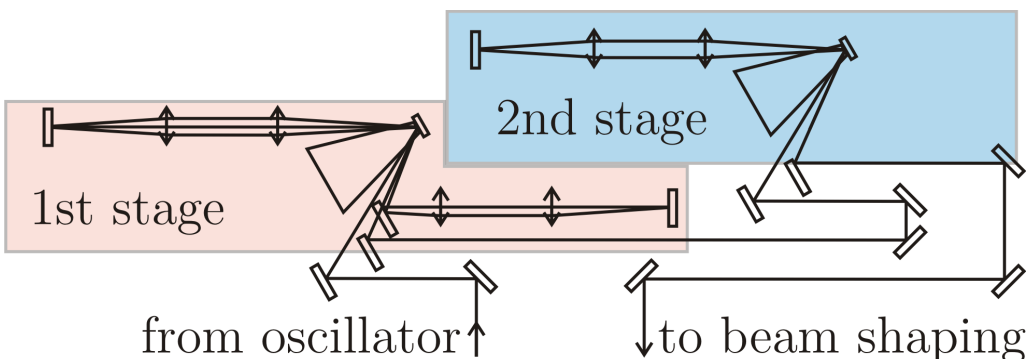


**Figure 2.6.:** Preamplifier sketch.

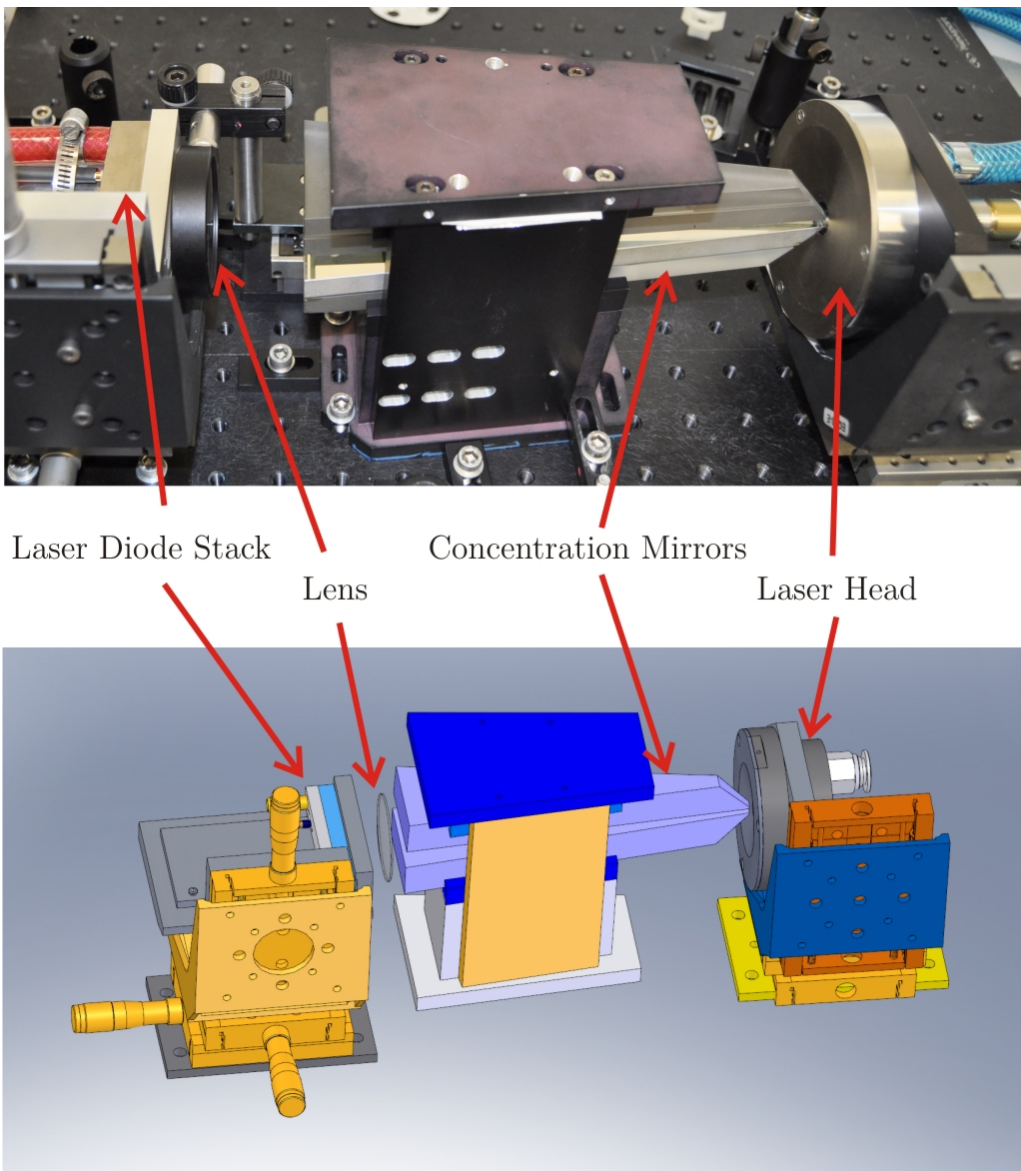


**Figure 2.7.:** Setup of the first preamplifier laser head.

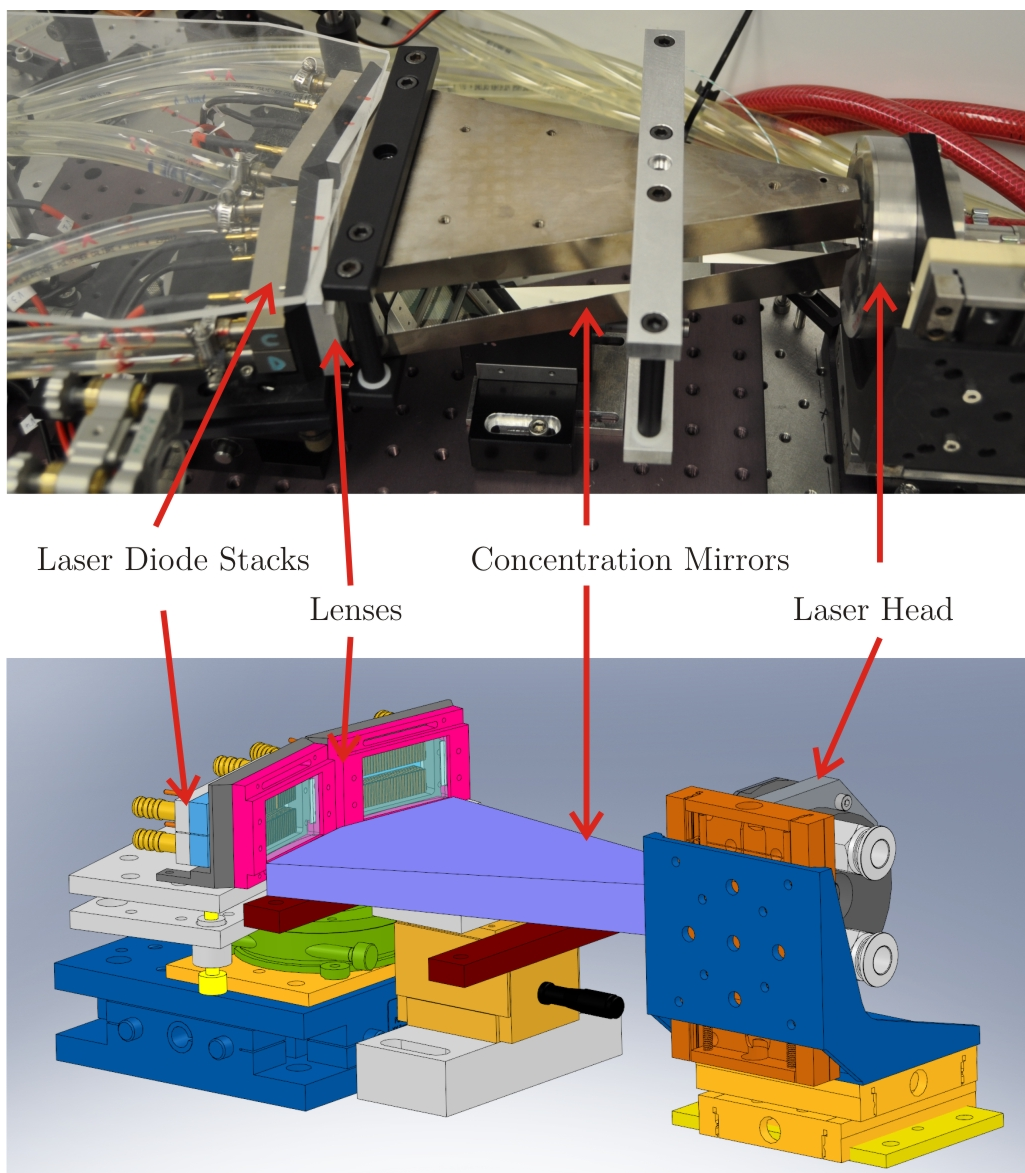


**Figure 2.8.:** Setup of the second preamplifier laser head.

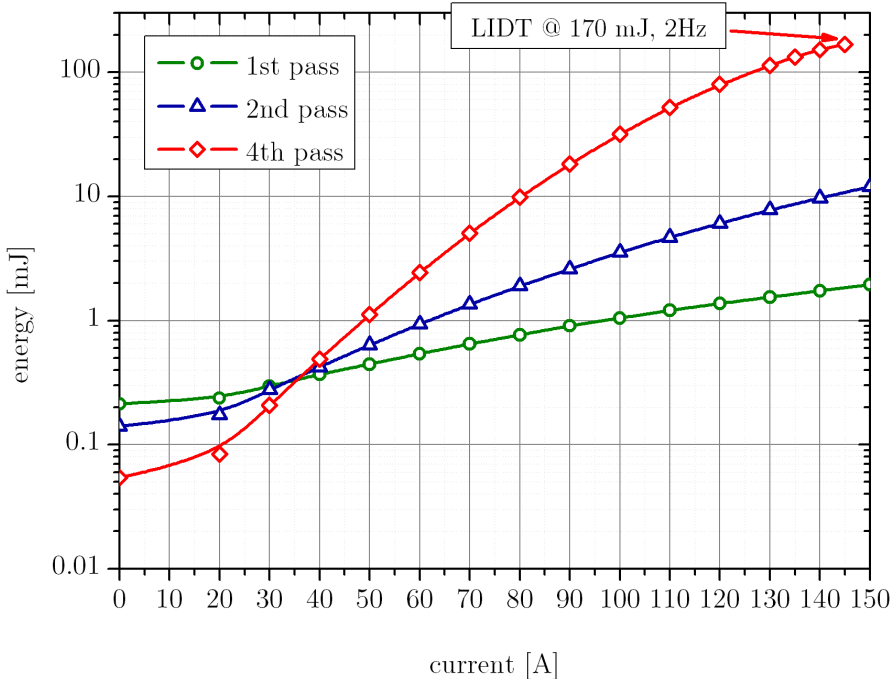


**Figure 2.9.:** Output energy after one, two and four passes in the first preamplifier. Input energy was 0.34 mJ. Lens damage occurred to the magnifying telescope after the preamplifier.

While in the first amplifier four round trips take place, only two passes are realized in the second amplifier in order to take LIDT considerations into account.

Due to a ten times lower thermal load, emission wavelength is shifted  $\approx 6$  nm towards smaller wavelengths when the laser diode stacks operate at 1 Hz instead of their nominal 10 Hz repetition rate design point. Taking into account a measured thermal shift of 0.3 nm/K for the laser diode stack peak emission wavelength, an increase of 18 K for the cooling water was requested (43 °C instead of 25 °C).

The extraction scheme used in the amplifier heads is the active mirror scheme. A simplified overview of the three main pumping schemes is shown in Figure 2.10, where single side pumping, counter-propagating pumping and the active mirror scheme is illustrated.

Graph 2.9 shows the experimental results for the extracted energy in the case of an injection of 0.34 mJ after one, two and finally four passes at 2 Hz. A maximum energy level of 170 mJ was achieved, limited by the LIDT of the transport optics between the first and second pre-amplifier. The maximum achieved total gain within this amplifier setup is  $\sim 500$  at a repetition rate of 2 Hz.

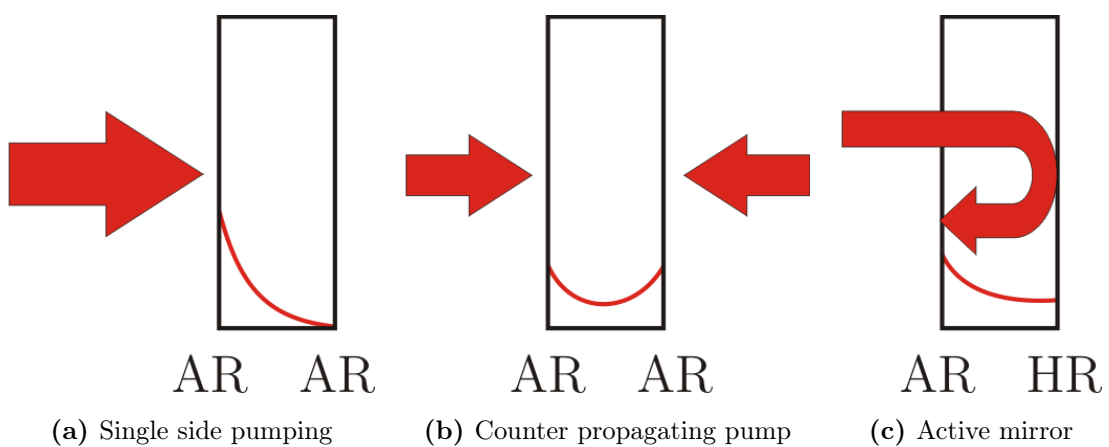


**Figure 2.10.:** Description of the three major pumping schemes. The most common pumping geometry is shown in (a) where the pump is incident from one side only resulting in a strongly varying gain profile (indicated by the small red curve). An improvement is the counter propagating pumping scheme (b) and especially the active mirror scheme (c) used in the Lucia amplifiers.

## 2.4. Beam Shaping

Getting an efficient energy extraction in amplifier systems implies to satisfy several constraints. For instance it is desirable to have a sufficient high fluence of the laser pulse to achieve saturation, or a sufficient amount of round trips in the amplifying medium, to efficiently extract stored energy.

Also, as shown in Table 1.2 the beam overlap plays an important role in terms of efficiency. Pump and extraction area should indeed match as much as possible. Satisfying these specific requirements often implies tight adjustment of pump light delivery optics, laser head mechanical mount and extraction optics. Minimizing the presence of edges, which ultimately generate diffraction, along the extraction beam path becomes therefore very difficult.

This is especially true at the Lucia amplifier head, where four concentration mirrors and a circular mask are in close contact with the laser head. The available space for the extraction beam path is very narrow. Figure 2.11 depicts the laser head assembly with the concentration mirrors and mask.

Performing a multi-pass extraction in such an environment with a Gaussian beam would clearly generate diffraction ripples on both the extraction beam phase and intensity profile and consequently put extraction optics at risk. It is therefore requested to adjust the intensity transverse distribution.

To perform this task an intermediate beam shaping stage is implemented after pre-amplification.

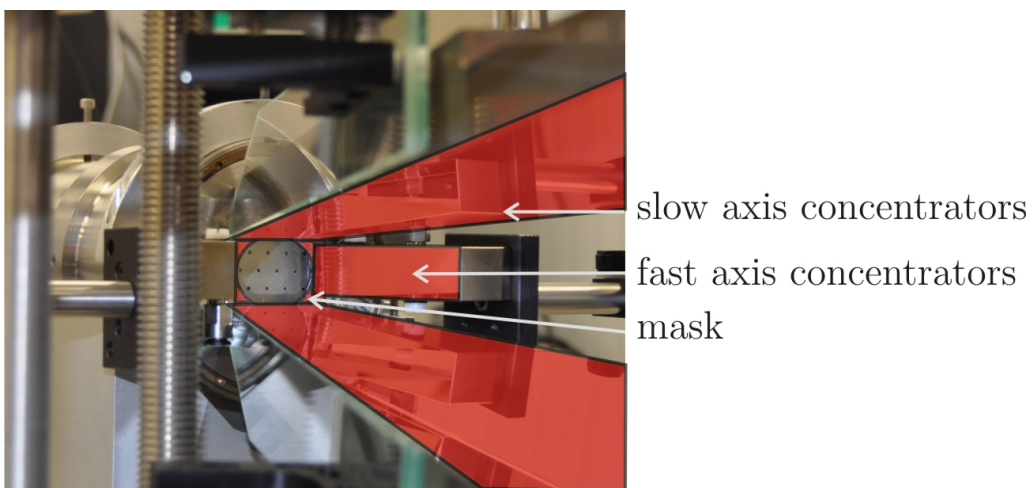


**Figure 2.11.:** View from extraction direction at the main amplifier. The slow axis and fast axis concentration mirrors and the mask are potential sources of diffraction for the extraction beam.

We might rely on two distinct approaches – at first a transformation of the laser beam transverse energy distribution with, for instance telescopes based on aspherical lenses [107] or apodizers using phase plates manipulating the laser output or the laser beam focus [108, 109]. A more common approach for high power laser systems is the sculpting of the laser beam shape by the means of soft diaphragms [69] or a serrated aperture[110]. This is the approach selected for Lucia: the use of a serrated aperture combined with a spatial filtering performing apodization (swiftly speaking apodizers), first introduced by Trenholme et. al. on the NOVA laser system in 1978 [110]. An example of such a serrated aperture is shown in Figure 2.12.

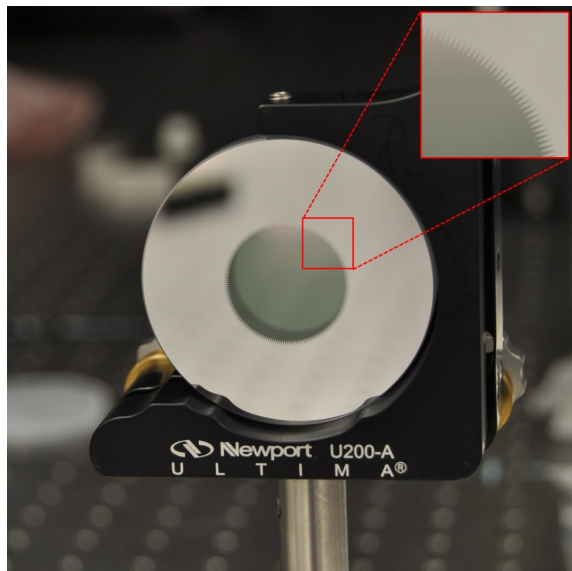


**Figure 2.12.:** The apodizer used in the Lucia laser is a chrome mask applied onto a substrate (anti-reflection coated). The fine tooth structure is illustrated in a magnified inset.

The name apodization derives from the greek  $\alpha$  (to take away) and  $\rho\delta\omega\varsigma$  (foot), literally meaning ‘taking the foot away’ or more illustrative ‘cutting the feet’. Coming out of the signal theory, the term found its way to optical applications referring to an action which changes the intensity distribution in the near field.

The serrated aperture cuts the unwanted peripheral parts of the beam. Teeth at the outer boundaries of this intensity filter are used to get a defined slope at the edges. Since it introduces sharp edges, this will generate high spatial frequencies leading to a strongly disturbed beam shape with hot spots at the outer edges after free propagation. Consequently, the serrated aperture needs to work together with a subsequent spatial filtering. The filtering function has to be designed in a manner,

that the spatial frequencies in the direction perpendicular to the teeth are cut out, but the intensity variation parallel to the teeth is conserved.

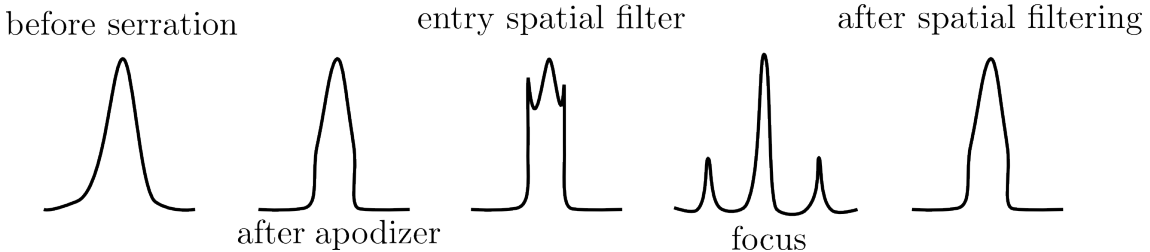


**Figure 2.13.:** Apodizer setup general

The shape of the teeth used impacts the slope at the edges of the resulting beam. Size and slope are by this important in terms of transmission and the resulting beam shape. The most intuitive shape is the triangular tooth. However, applications demanding a proper slope demand a well defined transmission function and by this a well defined tooth pattern.

As mentioned before, such a beam-shaping device consists of a serrated aperture coupled to a spatial filtering. The object and image plane positions of such an arrangement are related as follows:

$$L_1 \frac{f_2}{f_1} + L_2 \frac{f_1}{f_2} = f_1 + f_2 \quad (2.4.1)$$

where  $L_1$  is the distance from the image plane to the first lens,  $L_2$  the distance from the second lens to the object plane. The lenses have focal lengths of  $f_1$  and  $f_2$  respectively. Both lenses are separated by  $f_1 + f_2$ , therefore describing the image relay technique forming an image from one plane to the next one, while conserving phase and intensity. A special type would be the classical 4f-assembly when  $L_1 = L_2 = f_1 = f_2$ .

Considering a lens as a Fourier operator, estimating the impact of the applied filtering function can be done by generating the 2D-Fourier transform of the electric field amplitude distribution with the specific serration pattern. Then, multiplying the result in the Fourier space with the diaphragm function and finally applying an inverse 2D Fourier transformation to get the resulting beam shape after filtering.

The base length of the teeth is  $L$  and their height  $H$  (see Figure 2.14). The teeth consequently introduce a period  $H$  in radial and  $L$  in tangential direction. After passing the serrated aperture, it is the task of the spatial filtering function to eliminate the tangential modulation in the focal plane.

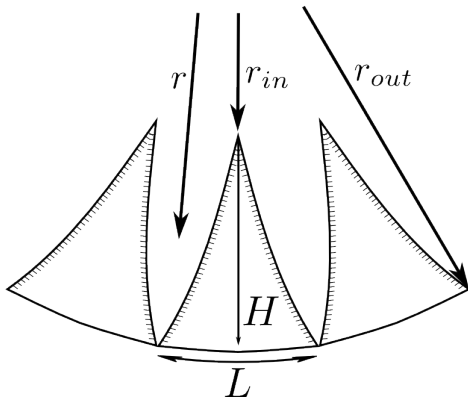


**Figure 2.14.:** Apodizer teeth design sketch

Let us consider the separation  $u$  in the Fourier-space introduced by a period  $L$  and a lens with a focus  $f$ . We know that the spatial frequency  $k_L = 1/L$  yields:

$$\frac{1}{L} = \frac{u}{\lambda f} \quad (2.4.2)$$

$$u = \frac{\lambda f}{L} \quad (2.4.3)$$

We will see diffraction rings according to the radial and tangential spatial frequency which should be sufficiently separated. Consequently the tangential pattern should carry a higher spatial frequency – the teeth have to be higher than wide. As a rule of thumb, the relationship between the height  $H$  and teeth width  $L$  should be at least

$$\frac{H}{L} \gtrsim 3. \quad (2.4.4)$$

The Number of teeth is determined by the allowable height  $H$  and Equation 2.4.4. Figure 2.15 gives an illustrative example of a circular aperture with an outer radius of  $r_{out} = 10$  mm and  $N = 80$  as the number of teeth. As one can easily estimate, we do not completely fulfill Equation 2.4.4. The amount of teeth needed is given by:

$$N \gtrsim \frac{6\pi r_{out}}{H} \quad (2.4.5)$$

The pinhole diameter  $\emptyset$  filtering the serration pattern should then be smaller than:

$$\emptyset < \frac{6\lambda f}{H}. \quad (2.4.6)$$

The realization of the teeth pattern is subject to different approaches, which might be:

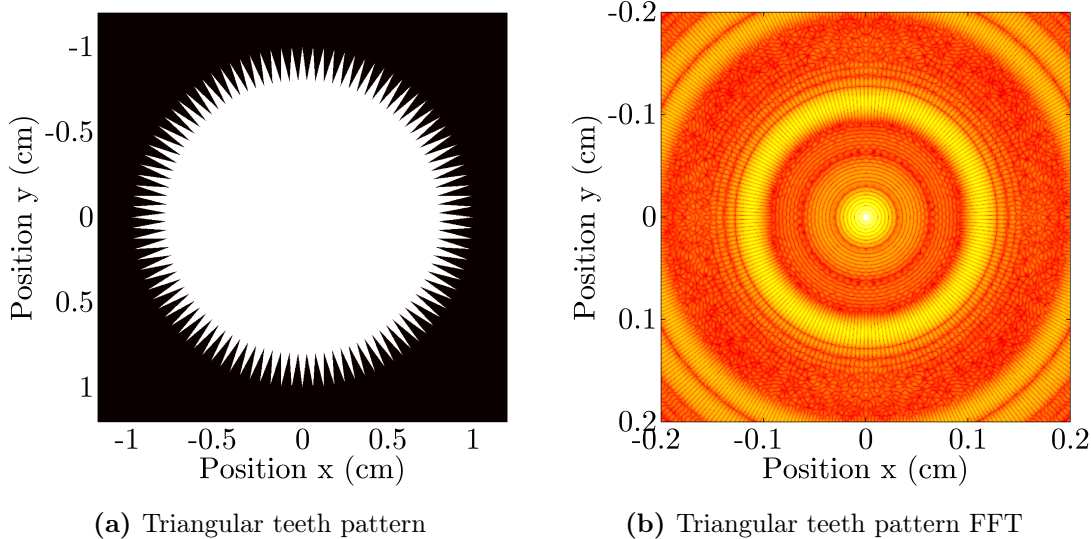


**Figure 2.15.:** Triangular teeth pattern example with  $80, f=1\text{m}$ ,  $633\text{nm}$  teeth (a) and its distribution in the focal plane (b)

1. Direct writing of the serration pattern: laser cut metallic sheet or a metal vapor deposition with the appropriate pattern. These techniques are well known, but suffer from laser induced damage due to the nature of metals.
2. Another possibility would be a double-sided anti-reflection coated bulk material [111]. The serration pattern is introduced by destroying partially the AR-coating using a laser or sand-dusting. Mixing Fresnel reflection and scattering may give a durable high-power apodizer. Unfortunately getting edge profile of quality might be difficult when using sand-dusting in respect to the brittleness of the coating material. fs-laser surface damage would be preferred for the sake of precision but will severely impact the speed of writing the serration pattern.
3. An alternative would be to write small bubbles within the material implying Mie-scattering for spheres with a diameter of approximately the same size as the wavelength. This has the advantage to use commercially available techniques. Randomly distributed spheres within the serration pattern should give a quite homogeneous extinction profile probably superior to the sand-dusting technique. As this is not tested until now (not know by the author), this might be a very attractive alternative, as the writing is widely commercially available.

Apodization with serrated apertures is performed on the Lucia laser system for the last amplifying stage boosting the energy from the  $100\text{ mJ}$ -level to the  $\text{J}$ -level.

The beam radius is set for the beam shaping section to be  $r_{out} = 11$  mm and the tooth height is set to be  $H = 1$  mm. According to Equation 2.4.5 the requested number of teeth would be  $N \gtrsim 200$ . The wavelength being  $\lambda = 1030$  nm and the focal length  $f = 1$  m, the pinhole diameter (according to Equation 2.4.6) needs then to be  $D \lesssim 6$  mm.

Figure 2.16 simulates the apodizer setup used on Lucia. Figure 2.16(a) depicts the image teeth pattern used and Figure 2.16(b) shows the intensity distribution in log-scale in the Fourier-plane (focal length is 1 m). Filtering the high spatial frequencies is done using a 5.6 mm diameter diaphragm. The resulting intensity distribution is shown in Figure 2.16(c).

A serrated aperture was manufactured by IMTAG with an external radius  $r_{out} = 11$  mm, 200 teeth and a tooth height of  $H = 1$  mm. The triangular teeth are structured on a Chromium mask on a double-sided AR coated, laser quality BK7-substrate.

Testing these predictions was one of the main interests of an experimental verification. The impact of the serration pattern is shown in Figure 2.17. Starting with an initial beam shape depicted in Figure 2.17(a), the serrated aperture is inserted into the beam, showing the serration pattern in Figure 2.17(b) when observed in the corresponding image plane. Filtering the diffraction pattern (shown in Figure 2.18) results in the defined beam border as depicted in Figure 2.17(c).

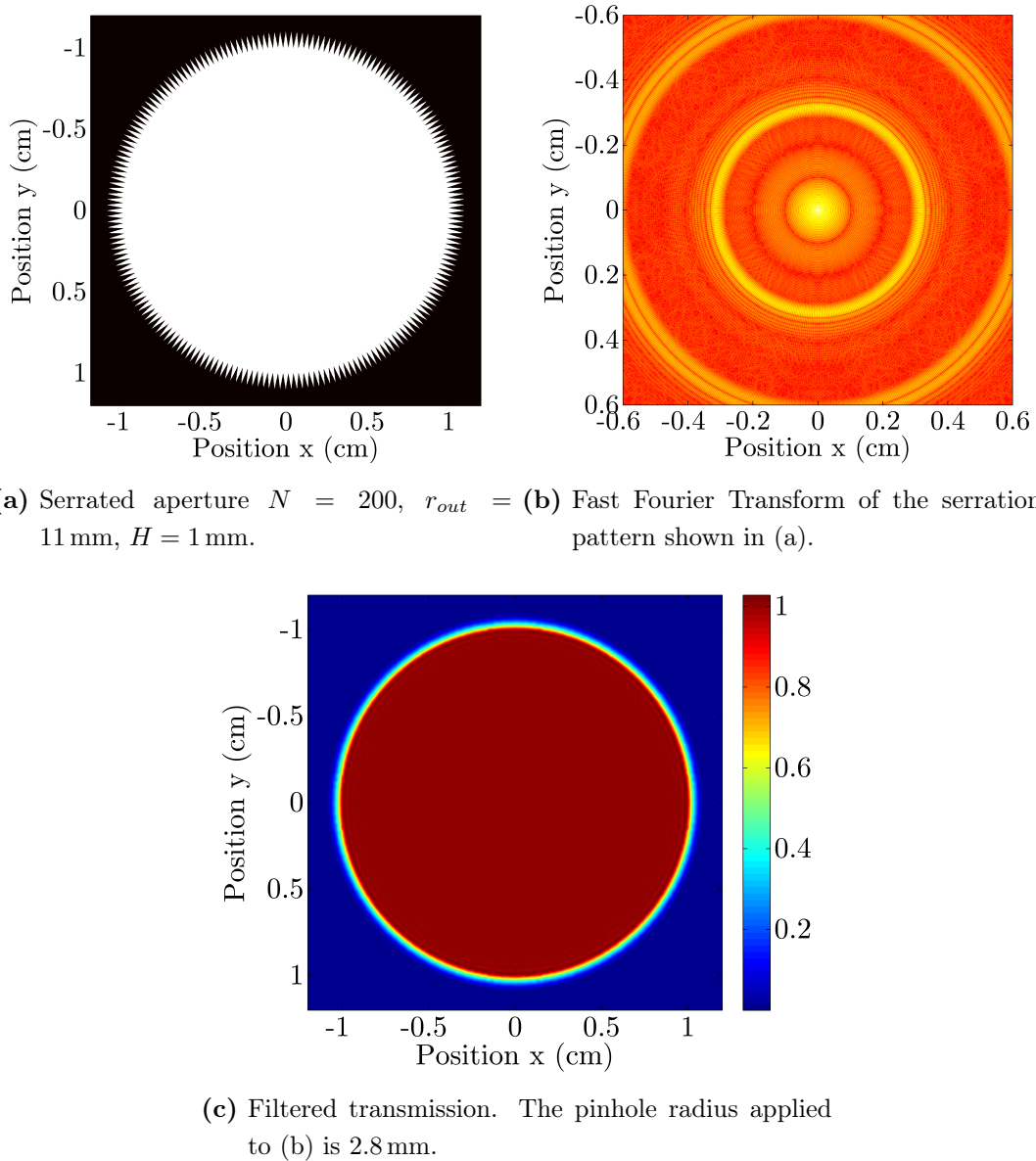
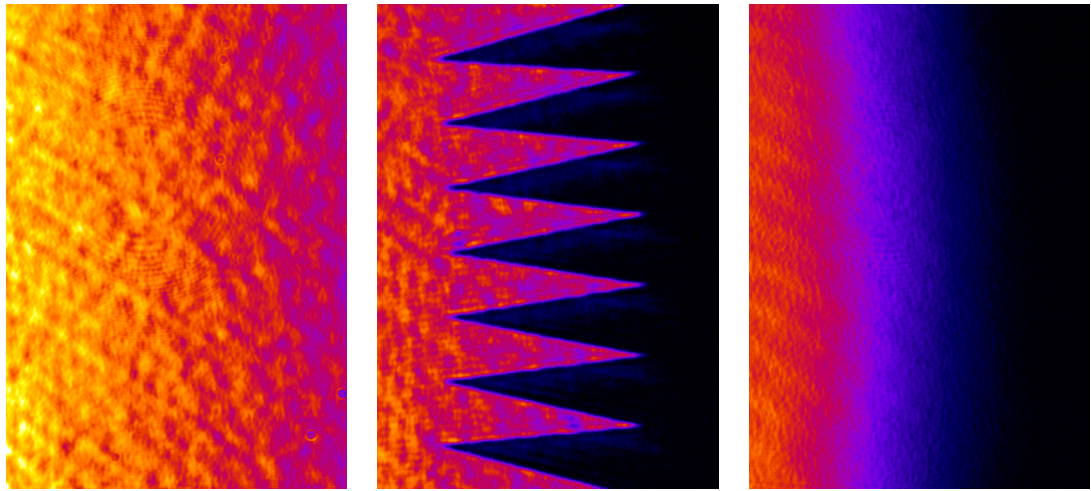


**Figure 2.16.:** Simulation of the serrated aperture action on a beam of constant transverse energy distribution. The configuration corresponds to the actually used serrated aperture. The serration pattern is shown (a), while a zoom in the focal plane is shown in (b). The resulting beam shape is illustrated in (c).



(a) Initial intensity distribution    (b) With serrated aperture    (c) With serrated aperture and filtered

**Figure 2.17.:** The impact of the serration pattern on the initial beam shape (a) in the image plane is shown in (b). Filtering the appropriate spatial frequencies generates a smooth edge (c).

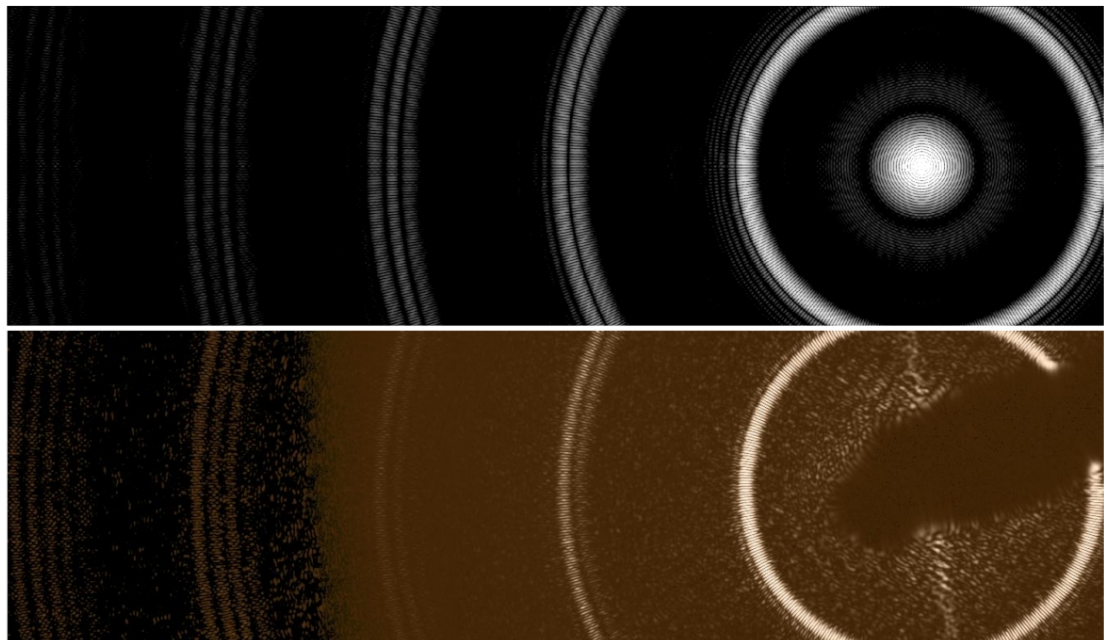


**Figure 2.18.:** The upper image shows, in logarithmic scale, a fraction of the calculated intensity distribution observed in the focal plane of a serrated aperture with  $N = 200$ ,  $r_{out} = 11 \text{ mm}$ ,  $H = 1 \text{ mm}$ . The lower image depicts a stitched intensity distribution made with different filters with the experimental apodizer, tested with a collimated He-Ne (633 nm) laser. The central intensity lobe is blocked. A good agreement is found.

## 2.5. Main Amplifier

After preamplifying the pulse generated by the oscillator to the level of  $\approx 200\text{ mJ}$  and shaping the beam, a last amplification step is performed in a single amplifier with four passes. This laser amplifier is made of three major components as depicted in Figure 2.19 and 2.22:

1. The laser diode array housing up to 88 laser diode stacks.
2. The Light Concentration System (LCS) consisting of a set of prisms and concentration mirrors.
3. The laser head with its laser gain medium.

Each of these elements will be discussed in the following sections.

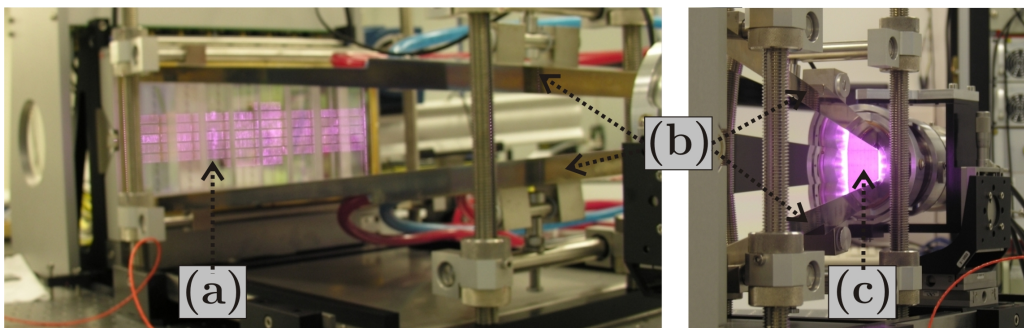


**Figure 2.19.:** Overview of the main amplifier. The laser diode array housing up to 88 stacks with the multiplexing prisms is shown on the left (a), the large concentration mirrors (b) and the laser head (c).

### 2.5.1. Laser Diode Array

The Laser Diode Array (LDA) can host 88 laser diode stacks distributed in eleven rows and eight columns. Each of the laser diode stacks (manufactured by DILAS) has a nominal peak power of 3 kW at 130 A with a typical emission duration of 1 ms, therefore the LDA can emit 264 kW when fully populated.

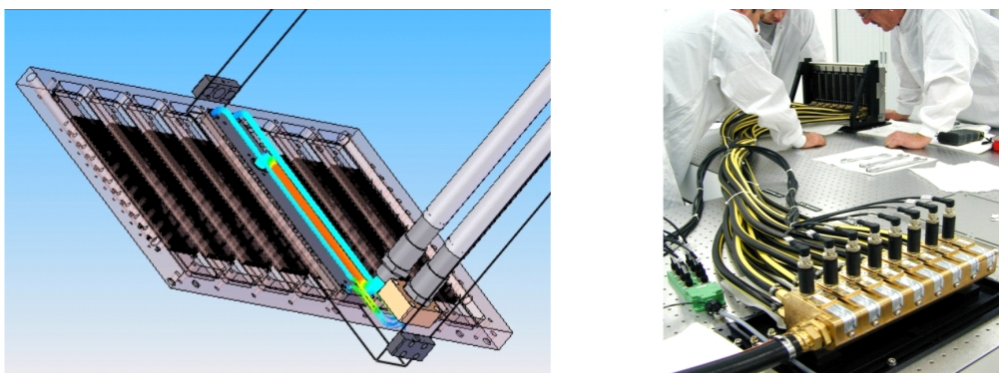
Each current source supplies up to four laser diode stacks with driving currents up to 150 A at a duty cycle of one percent (nominally 1 ms at a repetition rate of 10 Hz). Under such conditions, no aggressive cooling is necessary for the stacks and consequently no micro-channel cooling is required, improving the overall reliability of the laser diode stacks (corrosion is an inherent risk with micro-channels). Although

every column has its own cooling water entry, all eight columns are connected to only one cooling unit (see Figure 2.20). Such a cooling approach leads to a robust and simple cooling architecture but does not allow an individual water temperature adjustment for each laser diode stack. In order to do so, we rely on the so-called bias current.

Applying a constant current besides the pulsed driving current on the laser diode stacks introduces an additional thermal load. This results in a higher average temperature of the laser diode junction and leads to a spectral shift similar to what can be obtained when changing the cooling water temperature. The dc current applied is well below the laser emission threshold (about 15 A). The average shift for the laser diode stacks used in the Lucia project is  $\approx 0.12 \text{ nm/A}$ . Current drivers (AMTRON GmbH) offer up to 1 A with a 5 mA accuracy, giving the possibility to precisely adjust the emission wavelength over a 12 nm range.

This technique allowed us to relax the constraints on the laser bar sorting procedure (wavelength selection) and greatly decreased the overall cost of our stacks.

As stated in Section 2.3, a change from single-shot condition to an operation at 10 Hz introduces a shift of  $\approx 6 \text{ nm}$  in central emission wavelength. While it was possible to adjust this shift for the first pre-amplifier by raising the water temperature by 18 K, a similar shift if achieved for each stack individually on the LDA. Figure 2.21 illustrates the impact of the bias current on the spectrum of 30 laser diode stacks in single-shot operation.



water flow visualization

water distribution unit

**Figure 2.20.:** Water distribution and cooling of the individual LDA columns. The water arrives from one cooling unit and is split up into eight channels using a water distribution unit (right). On the LDA, all channels are separately and simultaneously cooled to improve cooling homogeneity (right).

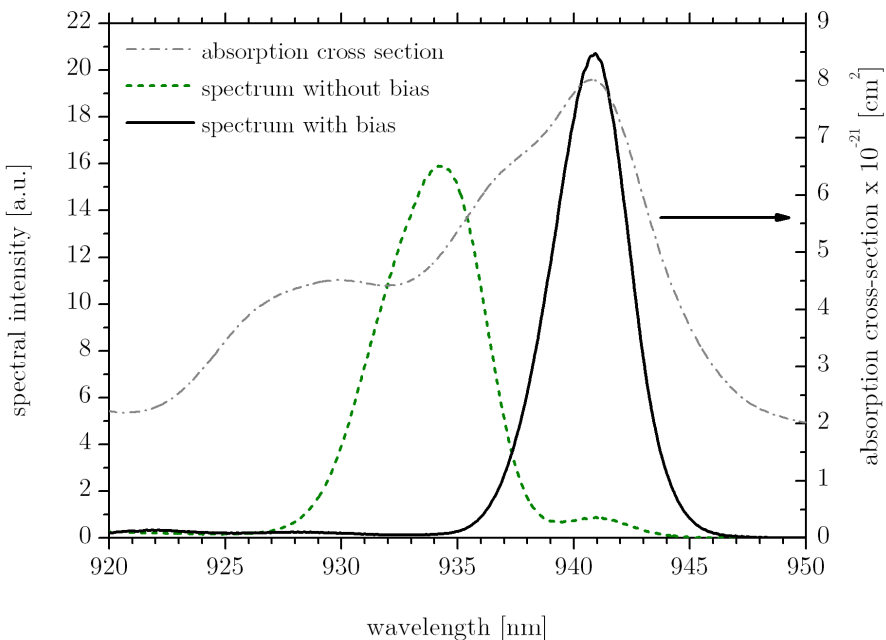


**Figure 2.21.:** Impact of the bias current on the emission spectra of the laser diode array. The emission of 30 stacks operated at 0.1 Hz and 130 A can be compared with (bold) and without (green) optimized bias current. The absorption cross section of Yb:YAG is shown as reference (right scale).

## 2.5.2. Light Concentration System (LCS)

Concentrating the light emitted by the LDA onto the gain medium is performed with refractive and reflective optics. In order to superimpose at the laser head the light emitted by each of the eight columns of the the LDA, a set of eight prisms is placed right in front of the laser diode stacks (see Figure 2.22)

Performing such an angular multiplexing is made possible along the horizontal direction thanks to the collimation (divergence  $< 1^\circ$ ) achieved by stack micro-lensing. The resulting depths of focus is compatible with the relatively small thickness of the gain medium ( $< 1 \text{ cm}$ ). The impact of the horizontal multiplexing can be seen in Figure 2.23.

The large concentration mirrors used to concentrate the laser diode emission in the slow axis direction are made out of aluminum, polished and silver coated. A protective layer is applied to avoid oxidation of the silver and offers the possibility to clean the mirrors. Taking into account the reflectivity of silver ( $< 98\%$  for the considered angle, polarization and wavelength) and the total average power to be

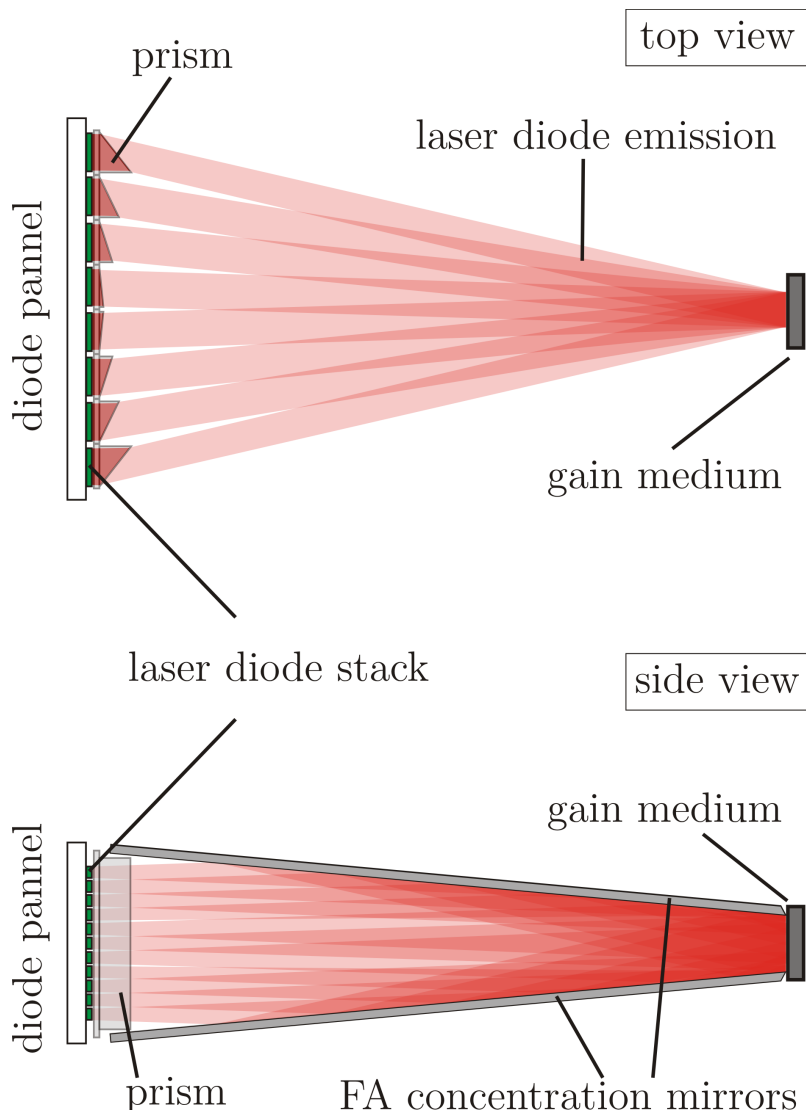


**Figure 2.22.:** LCS sketch. The stacks mounted on the diode panel are horizontally multiplexed by the use of prisms. The slow axis emission concentration is done using two large silver-coated mirrors.



**Figure 2.23.:** Horizontal multiplexing of the laser diode emission using the prisms. Only two laser diode stacks in one row are activated. The distance between the diffusive screen and the laser diode stacks increases from the left to the right.

concentrated, these mirrors are actively cooled. The length of the large mirrors is 617 mm. Due to the inclination of the mirrors one finds the superposition of the laser diode emission approximately at 630 mm after the prisms plane.

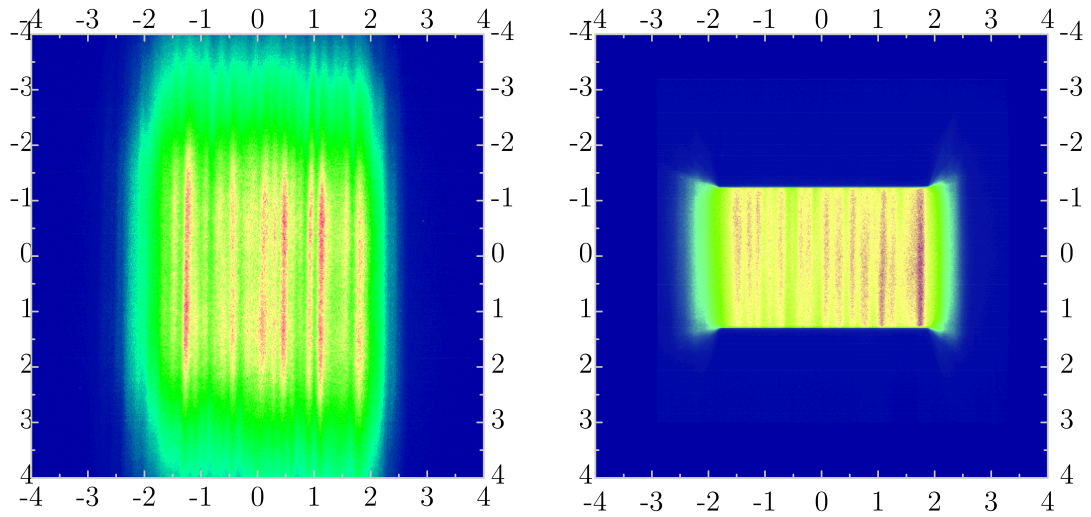
Figure 2.24(a) shows the reconstructed composite laser light distribution in the plane of superposition without the action of the large concentration mirrors for 30 stacks, while Figure 2.24(b) depicts the intensity distribution with the mirrors forming a clear aperture of 26 mm and 41 stacks installed. The transmission within a row is basically not affected by the stacks horizontal position. This is not the case for different vertical positions.

The more distant from the LDA central position (marked as '0' in Figure 2.25), the higher the losses experienced by this stack will be. With a total of eleven rows on the LDA, six different positions can be identified – from the center ('0') to the most upper/lower ('5') position. Consequently positions most far away from the center will suffer more losses. An overview of the transmission of the LCS calculated out of a ray tracing analysis compared to experimental results is shown in Figure 2.25.

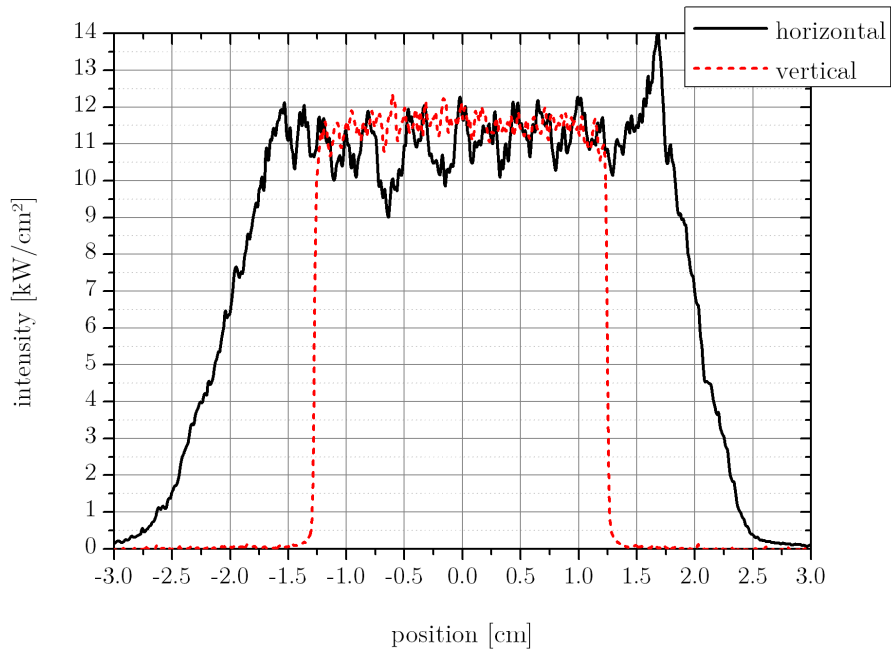
The homogeneity of the pump spot is also of importance. Assuming a gain modulation period  $a_g$ , a beam propagation under an angle  $\psi$  within a gain medium with a thickness  $D$ , minimum modulation for the extracted beam in the case of a constant gain distribution along the z-axis (see Figure 2.26) is achieved if

$$a_g = 2D \tan(\psi). \quad (2.5.1)$$

For a non-constant gain profile along the z-axis, this relation loses its validity since the integrated gain along the beam paths is not compensated after the reflection on the HR surface anymore. We have then to integrate along the beam path (we



(a) Pump distribution without concentration mirrors, 30 stacks.  
 (b) Pump distribution with concentration mirrors, 41 stacks.



(c) Intensity lineouts in vertical and horizontal direction for 130 A, single shot, 41 stacks.

**Figure 2.24.:** Illustration of the role of LCS on the pump light distribution. Figure (a) shows the pump light distribution without the concentration mirrors and (b) with slow axis (SA) concentration mirrors. A central horizontal and vertical intensity line out of (b) is given in (c).

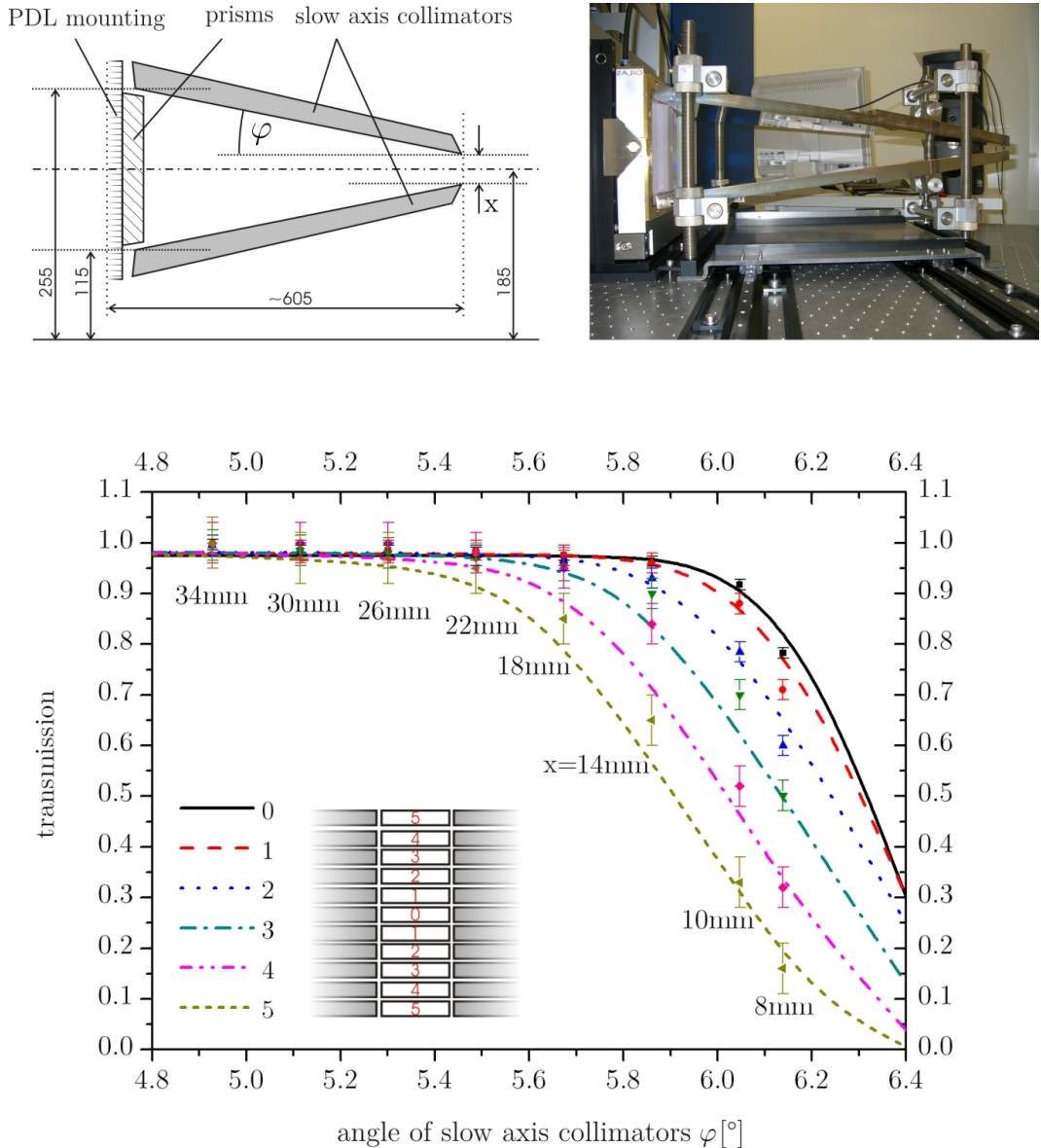


**Figure 2.25.:** The transmission of the concentration system using large mirrors depends on the half-angle  $\varphi$  of the mirrors (given in  $^{\circ}$ ) which is coupled to its aperture  $x$  (given in mm). While for apertures of up to 26 mm the transmission for each row is approximately the same  $\approx 98\%$ , narrow concentrated setups show very different transmission factors for different vertical positions. If one reduces the aperture to 18 mm by adjusting the angle to  $\approx 5.7^{\circ}$ , then the transmission drops for the most outer stacks (rows '5') to approximately 80%.

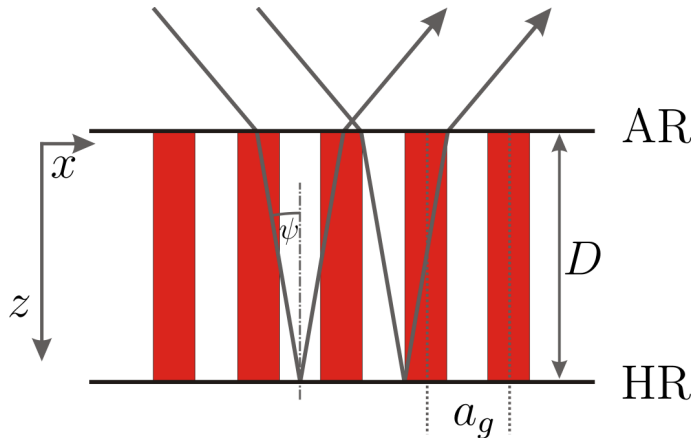


**Figure 2.26.:** Beam trajectory in a pumped gain medium with a modulated gain (along the  $x$ -axis) profile. The front surface is anti–reflection (AR) coated, while the back side is highly reflective (HR). The beam is incident from the top, along a direction close to the  $z$ -axis. The internal angle of reflection is  $\psi$ , the modulation period  $a_g$  and the thickness of the gain medium  $D$ .

(neglect interference effects). Let us consider the gain variation as a cosine–pattern perpendicular to the pump direction (i.e. the  $x$ –direction)

$$f_{mod}(x) = a \cos(x) + b \quad (2.5.2)$$

where  $a$  and  $b$  are constants defining the modulation depth and offset. In the direction of the pump–propagation ( $z$ –axis), an exponential and a constant distribution are discussed with:

$$h_{mod}(z) = \begin{cases} 1 & \text{constant distribution} \\ \exp(\ln(\kappa)z) & \text{exponential distribution} \end{cases} \quad (2.5.3)$$

where  $\kappa$  is the exponential drop at the HR surface (e.g. the gain drops down to 50 %). The distribution function  $\Upsilon(x, y)$  of the small signal gain  $g_0$  is then

$$\Upsilon(x, z) = g_0 f_{mod}(x) h_{mod}(z). \quad (2.5.4)$$

The solution for the gain  $G$  is found by integrating along the beam trajectory  $C$ :

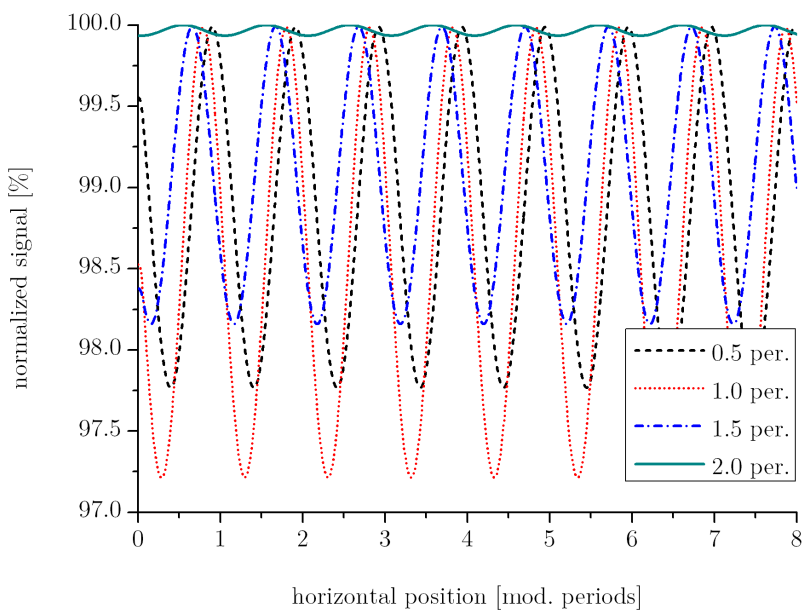
$$G = \exp \left[ \int_C \Upsilon(x, z) ds \right] \quad (2.5.5)$$

The curve  $C$  can be approximated as a straight propagating under the angle  $\psi$  towards the surface and from where it is reflected.

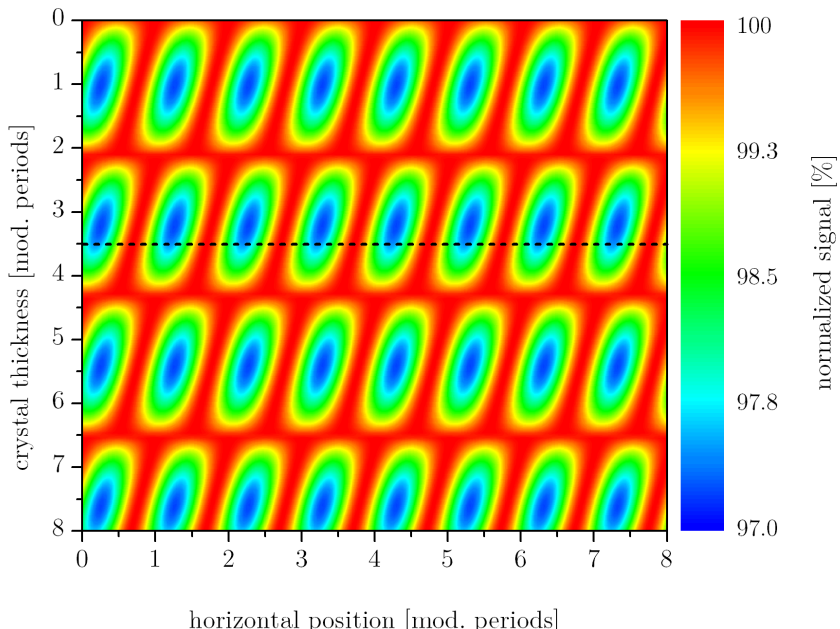
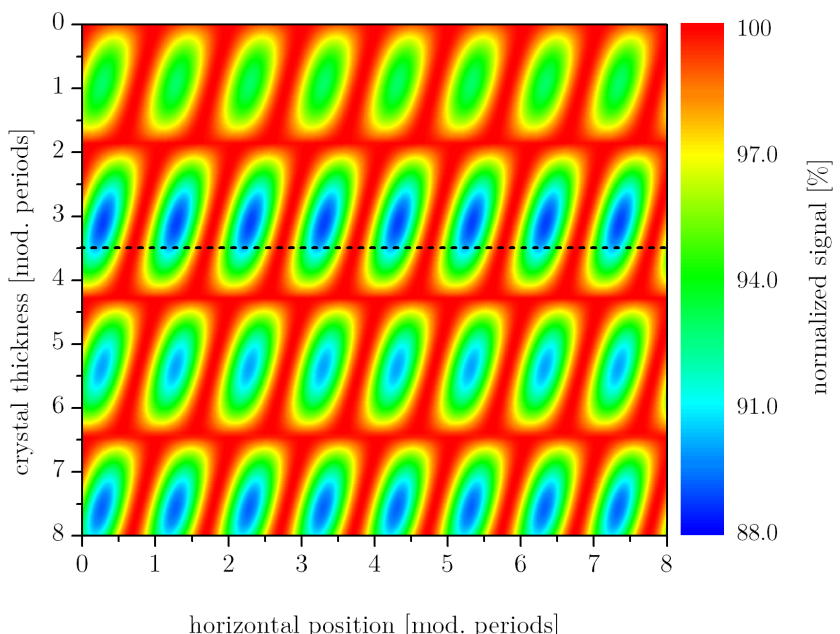
Typical modulations are in the order of  $\pm 10\%$  in intensity, as shown in Figure 2.24(c). The parameters used for the numerical analysis are then  $a = 0.1$ ,  $b = 1$ . To stay consistent with the experimental data, the small signal gain is chosen for the different thicknesses in such a way that the overall gain  $G$  is 4 (see Figure 3.31). In the case of an exponential drop with the penetration depth, the value for  $\kappa$  is set to be  $\kappa = 0.5/D$ , where  $D$  is the thickness of the active mirror. The propagation angle is  $\psi = 13^\circ$  and the backside exhibits a perfect reflectivity ( $R = 1$ ).

Figure 2.27 shows the resulting modulation imprint of a constant gain distribution along the z-axis for four different thicknesses varying between half and twice the modulation period. One sees that, with the proper choice of thickness, a significant reduction in modulation can be achieved. The optimum thickness for the given parameters is given by Equation 2.5.1, giving  $D/a_g = 1/(2 \tan \psi) \approx 2.1$  in the case of  $\psi = 13^\circ$ . Figure 2.27 shows a weak modulation for a ratio close to 2 (solid line).

An overview over the periodicity as a function of the gain medium thickness for a given angle is shown in Figure 2.28. A comparison between the case of a constant distribution along the z-axis (a) and an exponential decay in the z-axis (b) shows, that in the case of an exponential distribution the periodicity is altered as well as the



**Figure 2.27.:** Modulation example for internal propagation under an angle of  $13^\circ$ . The parameters are  $a = 0.1$ ,  $b = 1$ ,  $\kappa = 0.5/D$ . The horizontal position is given in modulation periods and the thickness varies between 0.5 and 2 periods.

(a) sine pattern,  $a = 0.1$ ,  $b = 1$ , constant in z(b) sine pattern,  $a = 0.1$ ,  $b = 1$ , constant in z, exponential in z ( $\kappa = 0.5/D$ )

**Figure 2.28.:** Impact of the gain medium thickness on the modulation of an amplified beam in the active mirror scheme. The dotted line defines the working point (thickness of the gain medium) in the case of the Lucia amplifier.

modulation is increased from a maximum value of 3 % to 12 % in the cases observed.

The pump system used on Lucia amplifiers generates a modulation period of about 2 mm combined with a crystal thickness of 7 mm. Overall the system is obviously not optimized to minimize modulations, as the working point is rather unfavorable (3.5 periods). For future gain medium optimizations, the results derived above should be taken into consideration.

### 2.5.3. Laser head

The laser head assembly holds the laser gain medium and ensures the cooling of the active mirror. In the active mirror scheme, the back and front surfaces offer the largest interaction areas when compared to the lateral faces. As water absorbs strongly outside of the visible spectrum [112], only one side can be cooled (see Figure 2.10). Active cooling is achieved by water circulation on the back side, while the pump and extraction is incident on the front. Cooling the active medium on the backside can be only efficient, if the heat exchange coefficient  $h$  is sufficiently high. This can be estimated by the use of relation 4.2.14 (introduced in Section 4.2.3) for the active mirror case.

$$T(z) = \underbrace{\frac{\dot{q}}{2k} (D^2 - z^2)}_{T_1} + \underbrace{\frac{1}{h} \dot{q} D}_{T_2} + T_\infty \quad (2.5.6)$$

where  $z$  is the pumping direction,  $T$  [K] the temperature,  $\dot{q}$  [W/cm<sup>3</sup>] is the volumetric heat production,  $k$  [W/m/K] the thermal conductivity,  $h$  [W/m<sup>2</sup>/K] the heat exchange coefficient and  $T_\infty$  [K] the coolant temperature.

Term  $T_1$  in Equation 2.5.6 is the only one contributing to the global thermal gradient. The contributions  $T_2$  and  $T_\infty$  are responsible for the average offset temperature. For a given  $\dot{q}$ , minimizing the thermal gradient can then be achieved by increasing  $k$ . Since  $k$  is strongly dependent of the temperature, it is desirable to minimize  $T_2$  and  $T_\infty$  as much as possible.

Representative values for the Lucia laser system are an area  $A_P = 10\text{ cm}^2$ , a gain medium thickness  $D = 1\text{ cm}$ , an average incident power  $P_P \approx 260\text{ W}$ , a fraction of the stored energy transformed into heat  $\eta_h \approx 0.1$ , a thermal conductivity  $k \approx 0.07\text{ W/cm/K}$  and a cooling water temperature of  $T_\infty = 285\text{ K}$ .

We get,  $T_1 \approx 20\text{ K}$  and  $T_2 \approx 2.6/h\text{ K}$ . If we want e.g. minimizing  $T_2$  to one tenth of  $T_1$ ,  $h$  should exceed a value of  $h > 1.4\text{ W/cm}^2/\text{K}$  or  $h > 14.000\text{ W/m}^2/\text{K}$ .

Figure 2.29 gives three examples how water cooling could be achieved. Classically a single water jet is used impinging on the cooled surface as shown in Figure 2.29(a). This technique is usable for small diameters, as the water throughput is typically in

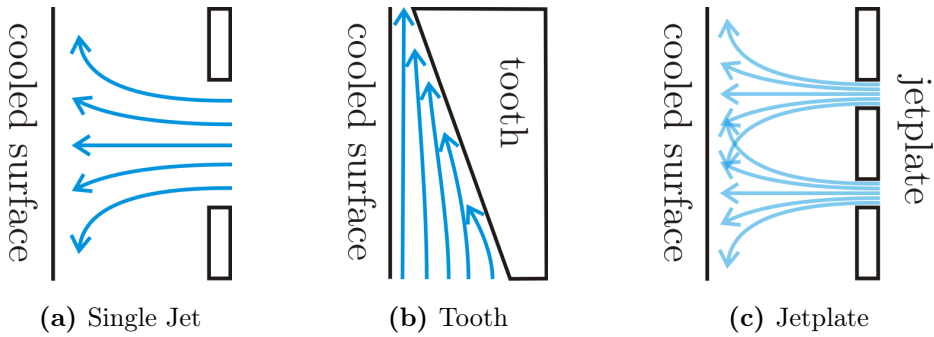


**Figure 2.29.:** Comparison of the different cooling setup possibilities.

the order of 10 l/min for a surface of 1 cm<sup>2</sup>. As the surface scales with the square of the diameter, this technique is not usable for large laser disks due to the need of large water pumps.

A different method is to use a lateral streaming coolant which is confined using a narrowing channel (e.g. a tooth as indicated in Figure 2.29(b)). Besides the fact it introduces potentially a pressure and an unfavorable transverse temperature gradient, an experimental demonstration at the pre-amplifier level was not considered successful.

As a third possibility, a so-called jet-plate is shown in Figure 2.29(c). It basically consists of a regular assembly of holes, where water is pushed through from behind. As the water is forced through the small holes, strongly turbulent water jets will form. The resulting heat exchange coefficient map will be, however, strongly depending on the position of the holes, their respective diameter and shape. A strong modulation of the heat exchange coefficient is expected, if the surface is close to the jet-plate. Roughly speaking, each jet forms an interaction similar to the single jet case and consequently a large surface can be efficiently cooled.

The laser head developed and built within this thesis is sketched in Figure 2.30. Water enters the assembly from the back and enters a cylinder (relaxation chamber). At the end is the pierced plate whose distance to the gain medium can be adjusted by moving the whole cylinder.

The water pump delivers a nominal pressure of 2.5 bar with a flow of 14 l/min, which is sufficient to generate a heat exchange coefficient of more than  $h_{exp} > 15.000 \text{ W/m}^2/\text{K}$  with a 39 holes (1.4 mm diameter each) plate (see Figure 2.31). The whole assembly is shown in Figure 2.32.

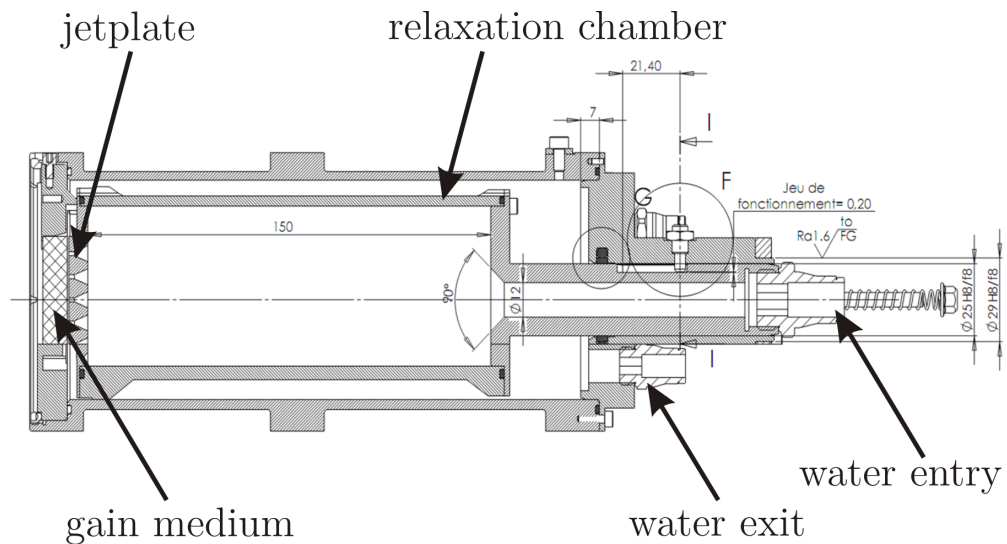


**Figure 2.30.:** Cooling head assembly



**Figure 2.31.:** Manufactured jet-plate with 39 holes, shown from the water inlet side.

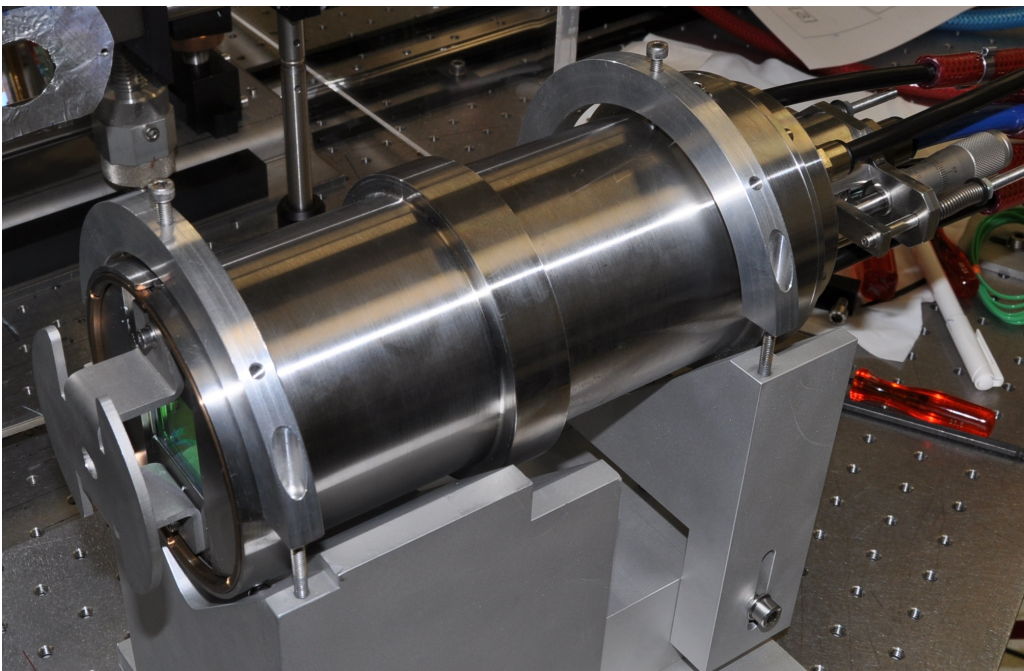


**Figure 2.32.:** Laser head assembly on top of its massive, stable mount. A protection cover is fixed on the crystal holder.

# 3. Amplified Spontaneous Emission Management

## 3.1. Motivation

A spontaneously emitted photon (Spontaneous Emission, SE) traveling through the gain medium (from which it originated) will experience amplification, ultimately leading to a depopulation of the gain medium. This process is called Amplified Spontaneous Emission (ASE). ASE is unavoidable as it is inherent to the fundamental origin of every laser. Keeping the impact of the ASE at a minimum, so it doesn't significantly impact the laser performance, is one of the main requirements for the successful realization of an amplifying system. Besides the impact of pure ASE, a feedback from the outer boundaries can easily introduce parasitic lasing.

As it will be shown in this chapter, the scaling of laser gain media is not an easy task to achieve, if we don't abide by a specific set of constraints. Basic models are derived as well as a three dimensional numerical analysis. The numerical results are benchmarked against experimental results gathered from the main amplifier stage. Finally, an experimental campaign to explore several solutions to avoid parasitic oscillations is described in the last section.

## 3.2. Introduction

During pumping, and while being below threshold for parasitic lasing, three major physical phenomena will impact the population density  $\hat{n}$  in the upper laser state. The pump action takes place followed by the unavoidable losses due to the radiative lifetime of the upper laser state and, third, the influence of the ASE. These actions are respectively represented as the three terms on the right hand side of the following equation:

$$\frac{d\hat{n}}{dt} = \left. \frac{d\hat{n}}{dt} \right|_P - \left. \frac{d\hat{n}}{dt} \right|_{SE} - \left. \frac{d\hat{n}}{dt} \right|_{ASE}. \quad (3.2.1)$$

For the two first ones (the pump and the spontaneous emission), the change in the population density of the upper laser state is written as:

$$\frac{d\hat{n}}{dt} \Big|_P = \int_{\lambda} g_0 \cdot \frac{I_P}{h\nu_P} d\lambda \quad (3.2.2)$$

$$\frac{d\hat{n}}{dt} \Big|_{SE} = \frac{\hat{n}}{\tau_f} \quad (3.2.3)$$

with  $I_P$  the spectral pump intensity [ $\text{W}/\text{cm}^2/\text{nm}$ ],  $h$  Planck's constant,  $\nu_P$  the frequency of the pump light,  $\lambda$  the spectral wavelength and  $g_0$  the small signal gain at the corresponding wavelength.

The origin of the deexcitation is the photon flux throughout the crystal traveling across the position under observation. The SE becomes ASE and acts as an auxiliary pump term. It can be written in the same way.

$$\frac{d\hat{n}}{dt} \Big|_{ASE} = \int_{\lambda} g_0 \cdot \Phi_{ASE} d\lambda \quad (3.2.4)$$

where  $\Phi_{ASE}$  [ $1/\text{cm}^2/\text{nm}/\text{s}$ ] is the ASE flux.

### 3.2.1. ASE flux estimation in the one-dimensional, monochromatic case

Determining the factor  $\Phi_{ASE}$  can be done according to Figure 3.1 [113]. The gain medium should be uniformly excited with the density in the upper laser state  $\hat{n}$ . We express the fraction of the photon density  $d\Phi$  out of the infinitesimal interval  $dx$  after traveling the distance  $x$  to be:

$$d\Phi_{ASE} = \frac{\hat{n}}{2\tau_f} e^{g_0 x} dx \quad (3.2.5)$$

where  $\tau_f$  is the lifetime of the upper state. Equation 3.2.5 is true under the estimation that the amplification is not saturated. The factor  $1/2$  appears, because

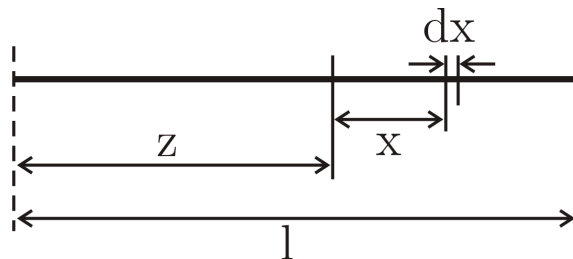


**Figure 3.1.:** Description of the variables used in the 1D, monochromatic estimation of  $\Phi_{ASE}$

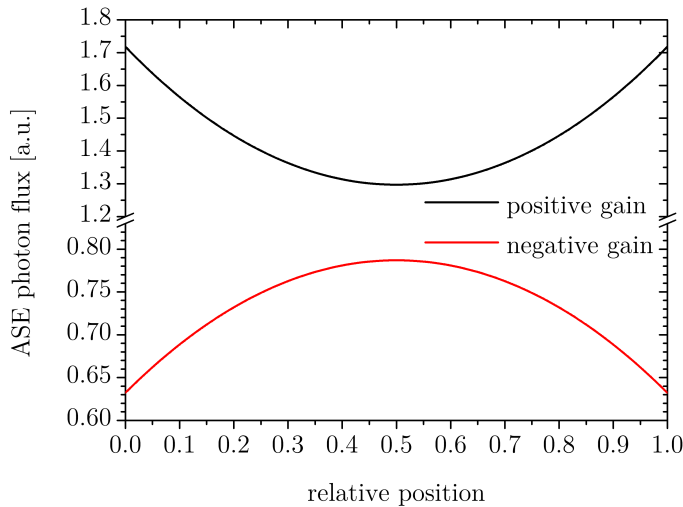


**Figure 3.2.:** Distribution of the ASE-flux in a 1D gain medium for  $g_0 = \pm 1 \text{ cm}^{-1}$

half of the emission can be emitted in the positive or negative direction. Equation 3.2.5 is integrated the following way:

$$\Phi_{ASE}(z) = \frac{\hat{n}}{2\tau_f} \left[ \int_0^z e^{g_0 x} dx - \int_z^l e^{g_0(l-x)} dx \right] \quad (3.2.6)$$

which finally gives

$$\Phi_{ASE}(z) = \frac{\hat{n}}{2g_0\tau_f} [e^{g_0 z} + e^{g_0(l-z)} - 2] \quad (3.2.7)$$

Figure 3.2 compares the solution of Equation 3.2.7 in the case of a positive ( $g_0 = 1 \text{ cm}^{-1}$ ) and a negative gain ( $g_0 = -1 \text{ cm}^{-1}$ ) for  $l = 1 \text{ cm}$  and  $\hat{n}/\tau_f = 1$ . In a system showing absorption we get a negatively shaped curve for the ASE-flux. This is the case of a system showing reabsorption at the emission wavelength. A positive gain will deplete mostly the most outer edges of the pumped area.

### 3.2.2. ASE intensity contrast at the end of a laser chain

Considering a pencil shaped geometry, a well-known approximation is the relationship derived by Linford [46]. This relationship is of special interest for approximations in a laser chain. References [114, 115] give generalizations of the approach for this type of geometry. Let us then derive Linfords formalism.

The approach is very similar to the one described in Figure 3.1 with the difference that the pure 1D configuration is replaced by a pencil-like geometry characterized

by a high Aspect Ratio ( $AR_L$ )<sup>1</sup>. Also, unlike the preceding case, the emission is not monochromatic but possesses a line shape function  $g(\nu)$ .

As one might not expect a very different interpretation inside the cylinder in terms of physics, we will restrict ourselves to the interesting case of the output ASE flux. This is particularly interesting for a laser chain. Applying a similar strategy as in Equation 3.2.6, the ASE distribution within the cylindrical gain medium can be obtained.

Besides the integration over the length, an integration covering the spectral distribution and the solid angle for the interesting point must be performed. Consequently the differential appears to be three-dimensional:

$$d^3\Phi_{ASE} = \frac{\hat{n}}{\tau_f} \frac{d\Omega}{4\pi} g(\nu) G d\nu dx \quad (3.2.8)$$

The solution for this problem is found in Section A.2. With the definition of the ASE intensity at the central frequency  $\nu_0$ ,  $I_{ASE} = \Phi_{ASE} h\nu_0$  and the saturation intensity  $I_{sat} = h\nu_0 / [\tau_f \sigma(\nu_0)]$ , we derive out of Equation A.2.18

$$I_{ASE} = I_{sat} \frac{\Omega}{4\pi} \frac{\Delta\nu_{st}}{\Delta\nu_{sp}} \frac{(e^{g_0 z} - 1)^{3/2}}{(g_0 z e^{g_0 z})^{1/2}} \quad (3.2.9)$$

where the FWHM widths of the stimulated emission cross section is  $\Delta\nu_{st}$  and spontaneous emission cross section  $\Delta\nu_{sp}$ .

As the amplification is strong, and using the expression for the energetic gain  $G(z) = \exp(g_0 z)$ , Equation 3.2.9 reduces to:

$$I_{ASE} = I_{sat} \frac{\Omega}{4\pi} \frac{\Delta\nu_{st}}{\Delta\nu_{sp}} \frac{G(z)}{\sqrt{\ln(G(z))}} \quad (3.2.10)$$

In good estimation we can take the stimulated and spontaneous emission linewidths to be the same and we get:

$$I_{ASE} = I_{sat} \frac{\Omega}{4\pi} \frac{G(z)}{\sqrt{\ln(G(z))}} \quad (3.2.11)$$

This relationship is useful for estimating the ASE intensity at the end of an amplifier chain. With the knowledge of the total gain of the laser chain, the material properties and the solid angle, limited by spatial filters pinhole aperture, intensity contrast of the laser pulse against the ASE pedestal can be estimated.

---

<sup>1</sup>The  $AR_L$  is defined as the length in extraction direction divided by the typical size of the gain medium cross section (diameter in the case of a rod or disc).

### 3.2.3. ASE flux estimations in Two and Three Dimensions

The very first requirement when calculating the ASE flux within/outside the laser gain medium is to estimate the solid angle. The two previous paragraphs avoided this problem with the use of a mere one or quasi-one dimensional analysis. This task is not so easy to fulfill, if a two or three-dimensional computation with a more complex geometry is of interest.

Writing the ASE flux at a position  $\vec{r}_0$  in the most general way leads to the following expression:

$$\Phi_{ASE}(\vec{r}_0) = \frac{1}{\Omega_f^s} \int \cdots \int \frac{\hat{n}(\vec{r})}{\tau_f} g(\lambda) G_{\vec{r} \rightarrow \vec{r}_0} d\vec{r} d\lambda d\Omega \quad (3.2.12)$$

where  $\Omega_f^s$  is the full solid angle depending on the dimension  $s = 1, 2, 3$  of the given geometry,  $\hat{n}$  the excitation of the upper laser state,  $\tau_f$  the fluorescence lifetime,  $g(\lambda)$  the spectral distribution of the spontaneous emission and  $G_{\vec{r} \rightarrow \vec{r}_0}$  the gain over the trajectory. This can be solved as the line integral between the point of integration and the point of observation. The full solid angle in  $s$  dimensions is given as

$$\Omega_f^s = \frac{2\pi^{s/2}}{\Gamma\left(\frac{s}{2}\right)} \quad (3.2.13)$$

where  $\Gamma$  is the Gamma-function. For a one dimensional problem,  $\Omega_f^1 = 2$ , for a two dimensional problem  $\Omega_f^2 = 2\pi$  rad and in three dimensions  $\Omega_f^3 = 4\pi$  sr. The line shape function  $g(\lambda)$  is approximated as:

$$g(\lambda) = \frac{\sigma_e(\lambda)}{\int_0^\infty \sigma_e(\lambda) d\lambda} \quad (3.2.14)$$

Numerically it is rather difficult to integrate over the solid angle for an arbitrary geometry. It can be simplified in the way, that the infinitesimal element  $d\vec{r}d\Omega$  describes a small volume element and is replaced by  $d^s V / |\rho(\vec{r}, \vec{r}_0)|^{s-1}$ , where  $\rho(\vec{r}, \vec{r}_0)$  is the distance a ray has to travel until it reaches the point of observation.

The most simple case is the one dimensional evaluation. Equation 3.2.12 reduces to:

$$\Phi_{ASE}(z_0) = \frac{1}{2} \iint \frac{\hat{n}(z)}{\tau_f} g(\lambda) G_{z \rightarrow z_0} dz d\lambda \quad (3.2.15)$$

which leads to the expression 3.2.5 in the monochromatic case of a uniform excitation coupled with a non saturated gain. The limits for the integration are given in such a way that the whole (one dimensional) volume contributes to the ASE flux at the position  $z_0$ .

The two dimensional interpretation of the ASE flux is consequently written as

$$\Phi_{ASE}(\vec{r}_0) = \frac{1}{2\pi} \iint \frac{\hat{n}(\vec{r})}{\tau_f |\rho(\vec{r}, \vec{r}_0)|} g(\lambda) G_{\vec{r} \rightarrow \vec{r}_0} da d\lambda \quad (3.2.16)$$

where  $da$  indicates the surface element. The integration has to be performed over the whole surface. In the same way an expression for the three dimensional ASE flux is derived as:

$$\Phi_{ASE}(\vec{r}_0) = \frac{1}{4\pi} \iint \frac{\hat{n}(\vec{r})}{\tau_f |\rho(\vec{r}, \vec{r}_0)|^2} g(\lambda) G_{\vec{r} \rightarrow \vec{r}_0} dV d\lambda \quad (3.2.17)$$

This expression is very similar to the expressions found in the literature [116]. The amplification is, in good approximation, exponential and will by this rapidly overcome the  $1/\rho^2$  loss in intensity along the propagation in the gain medium. This recalls the result given in Equation 3.2.7 in a more general context.

### 3.2.4. Life time modifier $M_{ASE}$

ASE reduces the local population in the upper laser state, which is indicated by the third term in Equation 3.2.1. One can also see the action of ASE as a local reevaluation of the fluorescence lifetime. We introduce a lifetime modifier  $M_{ASE}$  quantifying the impact of ASE. Equation 3.2.1 can thus be rewritten as:

$$\frac{d\hat{n}}{dt} = \frac{d\hat{n}}{dt} \Big|_P - \frac{d\hat{n}}{dt} \Big|_{SE} \cdot M_{ASE}. \quad (3.2.18)$$

In the quasi three level scheme (relevant in the  $\text{Yb}^{3+}\text{:YAG}$  context of this thesis) the small signal gain  $g_0$  is defined with the cross sections for emission and absorption  $\sigma_e$  and  $\sigma_a$ :

$$g_0 = [\hat{n}(\sigma_a + \sigma_e) - \sigma_a \cdot \hat{n}_{tot}]. \quad (3.2.19)$$

From the point of view the absorbed light, the sign of the small signal gain is inversed.

For the lifetime modifier  $M_{ASE}$ , one gets using Equation 3.2.1, 3.2.4 and 3.2.19 the following relationship:

$$M_{ASE} = 1 + \tau_f \int_{\lambda} \left[ \sigma_a \left( 1 - \frac{\hat{n}_{tot}}{\hat{n}} \right) + \sigma_e \right] \Phi_{ASE} d\lambda. \quad (3.2.20)$$

From this point, an interesting relationship between the maximum achievable inversion density and  $M_{ASE}$  can be derived for a quasi three level system. It is the limiting case for the energy storage, as the depletion by the ASE gets such strong that the pump action is equalized (left and right hand side of 3.2.18 will become

zero for a given  $M_{ASE}$ ). The left hand side of 3.2.18 should be zero and by this consequently:

$$\frac{d\hat{n}}{dt} \Big|_P = \frac{d\hat{n}}{dt} \Big|_{SE} \cdot M_{ASE} \quad (3.2.21)$$

Simplifying further towards a monochromatic approach and stating that the emission cross section for the pump might be much smaller than the absorption cross section and, in conjunction with Equation 3.2.19 and the definition  $I_{sat,P} = h\nu_P/(\sigma_a\tau_f)$ , this yields:

$$\beta_{max} = \frac{I_P}{I_{sat,P}M_{ASE} + I_P} \quad (3.2.22)$$

where we set  $\beta = \hat{n}/\hat{n}_{tot}$ . Using this relationship gives the possibility to estimate the maximum excitation by calculating the fluorescence lifetime modifier. Computing the energy distribution in the absence of ASE and deriving the mapping of  $M_{ASE}$  will bring up a  $\beta_{max}$  distribution. A comparison between the maximum and the estimated value can give an indication, whether ASE is important or not. Another interesting result is, that in the case of a quasi three level system, the maximum  $\beta_{max}$  is limited to 0.5 if a pump intensity satisfying  $I_P = I_{sat,P}$  is applied.

### 3.3. Numerical Simulation of ASE

The purpose of this section is to present the numerical approach developed from the relationships derived in the previous sections. Computing the transverse ASE flux  $\Phi_{ASE}$  will be the main interest. The last sections treated the one dimensional case.

We will start with a two dimensional estimation, followed by a quasi-three dimensional estimation of the lifetime modifier  $M_{ASE}$ , finally resulting in a three dimensional model, accompanied by a experimental benchmarking. The expected gain distribution within the Lucia main amplifier head will be discussed.

The used 2D geometries are shown in Figure 3.3. The pumping and extraction scheme is that of an active mirror. Pump and extraction are along the direction of the z-axis. The material is homogeneously doped and pumped uniformly over its surface  $A = L_xL_y$ . Within the calculations several options are available for the surface properties. The most simplest one is the approximation of a perfect translucent/absorptive surface, even neglecting total internal reflection (TIR). This condition means, that any ASE encountering a gain medium surface is considered as lost. This rule is applied to all the following calculations.

The emission spectrum is taken monochromatic, as the material studied is Yb<sup>3+</sup> doped YAG. It has a considerably narrow emission cross section compared to other

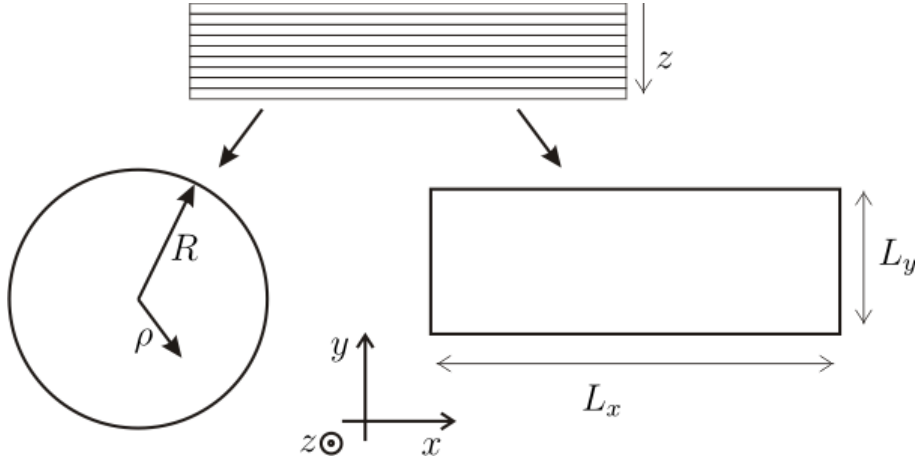


**Figure 3.3.:** Sketches for the two dimensional and quasi–three dimensional ASE flux estimations. The gain medium is sliced into several layers in  $z$ –direction. In the  $x$ – $y$  plane, a circular or rectangular geometry can be used.

laser gain material and with the exponential behavior of the amplification process, SE will become rapidly narrow enough justifying this estimation.

### 3.3.1. ASE Simulation in 2D

Let us recall the relationship between the ASE flux at a given position and the geometry in two dimensions:

$$\Phi_{ASE}(\vec{r}_0) = \frac{1}{2\pi} \iint \frac{\hat{n}(\vec{r})}{\tau_f |\rho(\vec{r}, \vec{r}_0)|} g(\lambda) G_{\vec{r} \rightarrow \vec{r}_0} da d\lambda \quad (3.3.1)$$

Considering a monochromatic approach, this expression is reduced to:

$$\Phi_{ASE}(\vec{r}_0) = \frac{1}{2\pi} \int \frac{\hat{n}(\vec{r})}{\tau_f |\rho(\vec{r}, \vec{r}_0)|} G_{\vec{r} \rightarrow \vec{r}_0} da \quad (3.3.2)$$

An interesting information is the distribution of the ASE impact within the gain medium. Simplifying the numerical estimation, a rectangular two dimensional gain medium is taken as an example.

Covering an area of extension  $L_x$  and  $L_y$ , integral 3.3.2 reduces with the estimation of a non saturated gain and a homogeneous distribution of the small signal gain to:

$$\Phi_{ASE}(x_0, y_0) \cong \frac{1}{2\pi} \int_0^{L_x} \int_0^{L_y} \frac{\hat{n}}{\tau_f} \frac{\exp\{g_0 \sqrt{(x - x_0)^2 + (y - y_0)^2}\}}{\sqrt{(x - x_0)^2 + (y - y_0)^2}} dx dy \quad (3.3.3)$$

where the small signal gain  $g_0$  can be defined as given in Equation 3.2.19. When solved,  $M_{ASE}$  can be calculated. However, Equation 3.3.3 has still to be solved. One

possibility is to use a Monte-Carlo (MC) approach. Using a uniformly distributed random generator (e.g. the Mersenne Twister [117]) generating  $N$  random numbers  $x_i$  and  $y_i$  within the interval  $[0,1]$  for the positions in  $x$  and  $y$  Equation 3.3.3 will be transformed into

$$\Phi_{ASE}(x_0, y_0) \cong \frac{L_x L_y}{2\pi N} \sum_{i=1}^N \frac{\hat{n}}{\tau_f} \frac{\exp\{g_0 \sqrt{(x_i L_x - x_0)^2 + (y_i L_y - y_0)^2}\}}{\sqrt{(x_i L_x - x_0)^2 + (y_i L_y - y_0)^2}} \quad (3.3.4)$$

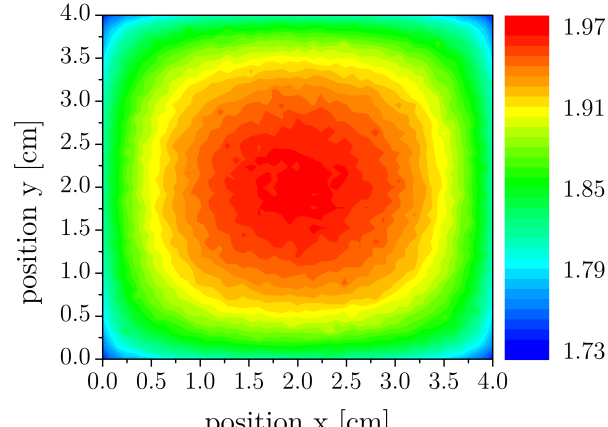
As example for such a MC calculation, a  $4\text{ cm} \times 4\text{ cm}$   $\text{Yb}^{3+}\text{-YAG}$  slab is studied in Figure 3.4. Initially the population inversion was set to a constant level in each case, resulting in a small gain coefficient of  $0.3\text{ cm}^{-1}$  (a),  $0.5\text{ cm}^{-1}$  (b) and  $1.0\text{ cm}^{-1}$  (c).

While in the first example (Figure 3.4(a)) the depopulation in the center of the two-dimensional slice is at maximum, a more and more important influence towards the outer parts of the pumped region is revealed, when  $g_0$  is increased to 0.5 (see Figure 3.4(b)).

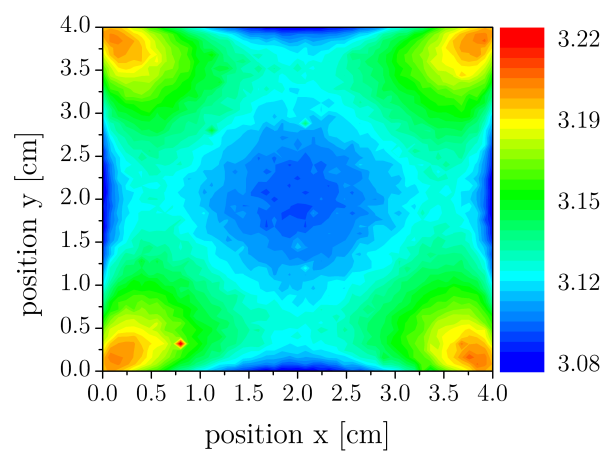
This can be interpreted as follows. With a small gain, the amplification stays low and by this, the local influence plays the major role (Figure 3.4(a)). With a rising gain, the exponential product between length and gain dominates, resulting in a depopulation of the outer parts. This behavior is somehow similar to the one dimensional case discussed in Section 3.2, but occurs now even for the case of a non absorbing gain medium. The lifetime modifier  $M_{ASE}$  is in this case in the order  $\approx 2$  (Figure 3.4(b)).

Stronger pumping leads to the case, where the exponential gain overwhelms the effects described and a stronger depopulation appears in the outer edges of the gain medium resulting in a higher value for the modifier  $M_{ASE} \approx 3$  (Figure 3.4(b)).

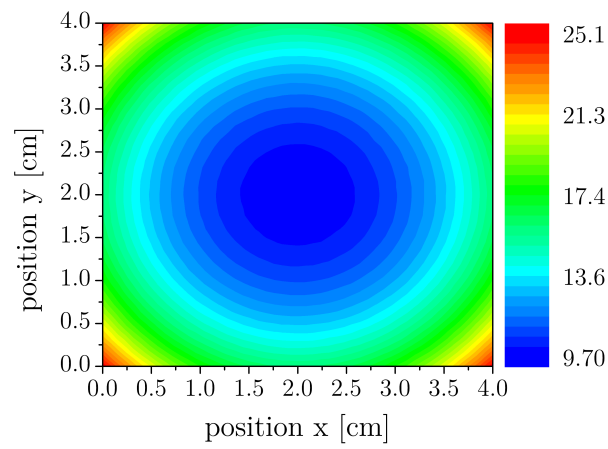
A further increase in pump power and thereby in gain will mainly deplete the areas most far away from the center. One finds himself in the situation, where storage efficiency in the center is such strongly reduced, that an efficient energy storage is not possible anymore (Figure 3.4(c)).



(a)  $g_0 = 0.3 \text{ cm}^{-1}$  2D example,  $M_{ASE}$



(b)  $g_0 = 0.5 \text{ cm}^{-1}$  2D example,  $M_{ASE}$



(c)  $g_0 = 1.0 \text{ cm}^{-1}$  2D example,  $M_{ASE}$

**Figure 3.4.:**  $M_{ASE}$  distribution for different homogeneous  $g_0$

### 3.3.2. ASE Simulation in quasi-3D

As long as the product of the small signal gain and the characteristic length of the pumped gain medium is low ( $g_0 L \ll 4$ ), we might estimate the distribution of  $M_{ASE}$  to be uniform. We can therefore calculate for each slice the impact of ASE and solve Equation 3.2.18.

We estimate the gain medium to be circular (polar coordinates) and set the point of observation in the center. Moreover, the gain distribution should be uniform within each of those slices and therefore the excitation  $\hat{n} = const$ . Consequently, after integration, Equation 3.3.2 becomes:

$$\Phi_{ASE}(0) = \frac{\hat{n}}{\tau_f g_0} [\exp(g_0 R) - 1] \quad (3.3.5)$$

where  $R$  is the radius of the gain medium.

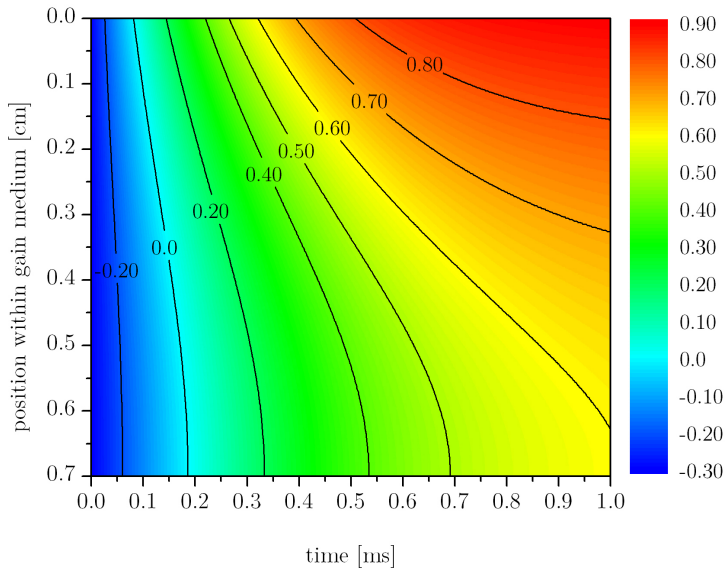
Using Equation 3.2.20 describing the lifetime modifier, Equation 3.2.18 is reduced to:

$$\frac{d\hat{n}}{dt} = \frac{d\hat{n}}{dt}\Big|_P - \frac{\hat{n}}{\tau} \cdot \exp(g_0 R) \quad (3.3.6)$$

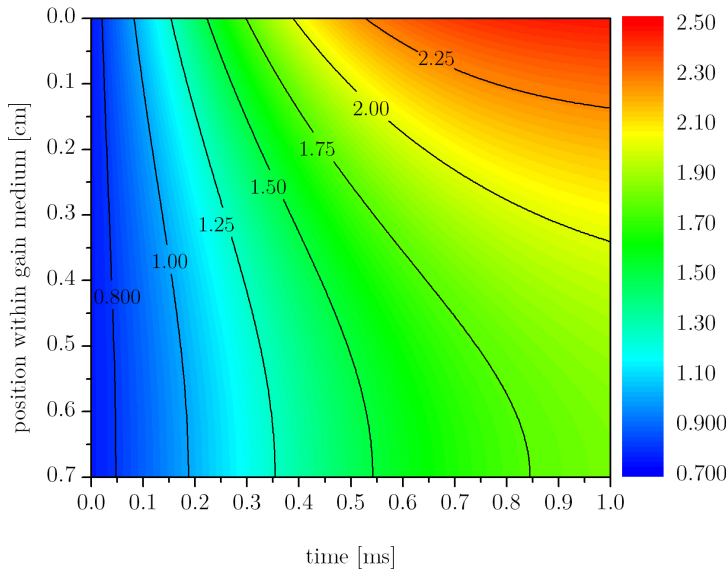
This expression is now solved numerically along the pump axis ( $z$ ). The model separates the transverse ASE from the pump action and consequently a one dimensional gain distribution with a two dimensional estimation for the ASE is derived. The model will be by this somewhat overestimating, as the gain distribution will not be uniform anymore as soon as ASE becomes important.

Figure 3.5 shows the compiled result for an 7 mm thick, 2 at.% Yb<sup>3+</sup> doped YAG circular disk with a radius of 1 cm. As already discussed, the pump and ASE action is treated quasi-three dimensional. Figure 3.5(a) shows the evolution of the local small signal gain as a function of the time and position within the gain medium and Figure 3.5(b) shows the corresponding  $M_{ASE}$ .

Integrating along the  $z$ -axis gives access to  $G$  along the extraction direction. For different dimensions of the gain medium, the evolution of the gain distribution will be differently affected, which is shown in Figure 3.6. The larger the lateral size, the stronger the transverse ASE, the less effective the energy storage. Values of  $M_{ASE}$  larger than  $\approx 2$  lead to a significant reduction of energy storage and gain. This value is reached for pump durations between 300  $\mu$ s and 400  $\mu$ s for gain medium layers located in the vicinity of the pumped front surface. Further pumping will not generate significantly more gain, but creates more ASE and by this more undesired



(a)  $g_0$  1D example, 2at.%, 7 mm thickness,  $15 \text{ kW/cm}^2$ ,  $R = 1 \text{ cm}$



(b)  $M_{ASE}$  1D example, 2at.%, 7 mm thickness,  $15 \text{ kW/cm}^2$ ,  $R = 1 \text{ cm}$

**Figure 3.5.:**  $g_0$  and  $M_{ASE}$  evolution during the 1 ms long pump process arriving along the vertical axis from top to bottom. For instance, after 0.4 ms of pump duration,  $M_{ASE} \approx 2$  in the vicinity of the entering surface ( $z=0$ ), meaning the effective lifetime of the  $\text{Yb}^{3+}$  ions in the upper laser state is half of its nominal ( $\sim 1 \text{ ms}$ ) value.

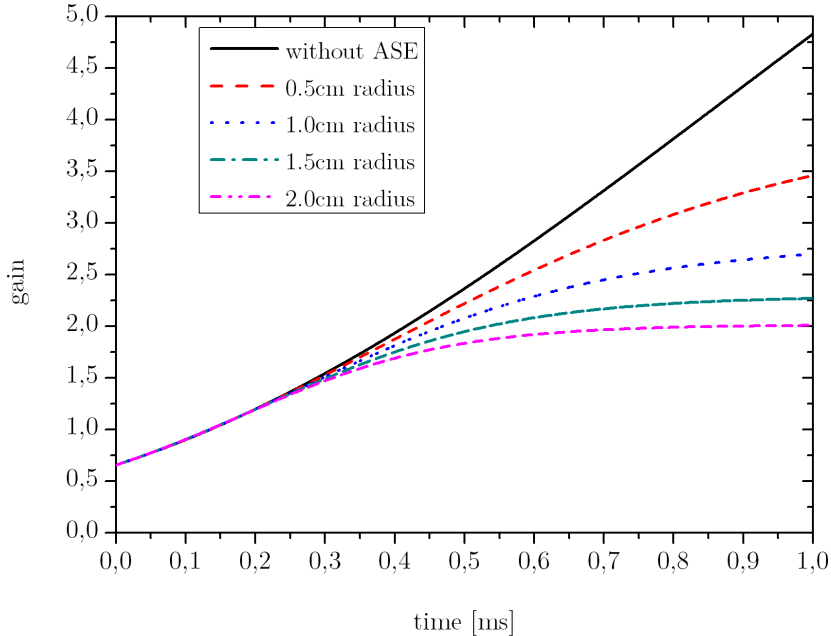


**Figure 3.6.:** Impact of increasing transverse size on the gain evolution during pumping for a 2 at.%, 7 mm thick  $\text{Yb}^{3+}$ :YAG gain medium.

effects like heat generation. Ultimately this leads to the case, where the maximum  $\beta$  derived by Equation 3.2.22 is reached.

It should be noted, that the impact of ASE is overestimated. In the case of a lateral extend very large compared to the thickness of the gain medium (thin disc case), coupled with a homogeneous gain distribution, the approximations applied to this model would be in good agreement to the physical model. In the case discussed above this is not true. The lateral extend is in the same order of magnitude as the gain medium thickness and therefore SE will travel significantly through the differently pumped “layers”. Consequently exists besides the transverse ASE an inter-layer crossing effect, which has to be taken into account. This reduces the ASE impact and therefore a significant overestimation of the ASE takes place in the simple model derived above.

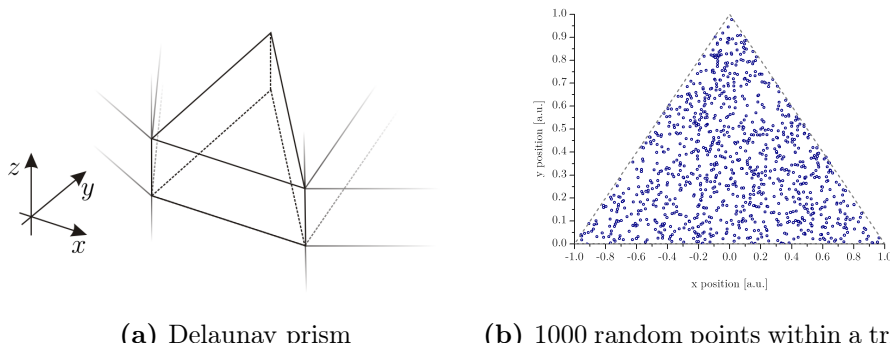
In order to estimate the impact of such an effect, a full three-dimensional simulation is necessary. Such a model is the content of the next section with the emphasis on its experimental validation.

### 3.3.3. ASE in three dimensions

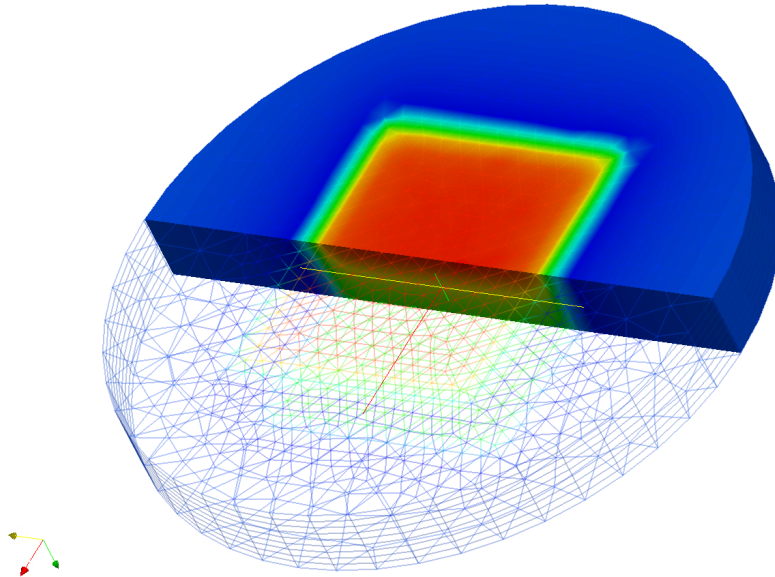
In the three dimensional case, the gain distribution is not taken to be uniform anymore. A ray tracing is necessary to evaluate the gain during the propagation throughout the gain medium. The surfaces are kept to be perfectly absorptive here as well. Pumping is decoupled from the ASE propagation process and can be implemented using an independent ray tracing model or an one dimensional evaluation. The gain medium itself is split into a 2D mesh using Delaunay triangulation. The third dimension is spanned using a linear extrusion in several layers. This simplifies the generation of a random position within the gain medium and the ray tracing code on its own.

Figure 3.7(a) displays a sketch of such a combination of Delaunay triangulation and linear extrusion, a so-called Delaunay Prism (DP). The main simplification for the generation of the random position is, that the generation of the random position within each DP is split into the position within the triangle and a position along the z-axis. Barycentric coordinates are used to get the position within the triangle. The interval for the sampling is  $(0, 1)$ . Such a sampling with 1000 points within a triangle is shown in Figure 3.7(b) using the Matlab `rand()` routine (option Mersenne Twister). The average number of rays per node (during a simulation step) is in the order of  $10^4$  to  $10^5$  which typically results for 5000 nodes in 50 to 500 million rays observed per propagation time step.

Figure 3.8 depicts an example data representation with mesh and volume representation of the small signal gain distribution for a circular gain medium with a rectangular pumped region. Within the pumped region, the grid is almost two times more dense compared to the not pumped periphery.



**Figure 3.7.:** Delaunay prism with a random distribution example



**Figure 3.8.:** Three dimensional example for a rectangular pumped zone within a circular crystal. The meshing is adapted to the rectangular geometry within the pumped region. For visualization, half of the data is shown as a grid.

### 3.4. Experimental Benchmark

In order to evaluate the ability of the developed code to accurately model experimentally observed ASE effects, a series of laboratory test cases were studied with low and high  $g_0 L$  products.

The pump source is the partially filled Laser Diode Array (LDA), i.e. 30 stacks, emitting within 1 ms an energy of 90 J in total. This energy is concentrated onto a surface of 40 mm  $\times$  10 mm, where the average intensity can be adjusted up to 18 kW cm $^{-2}$ .

As the experimental setup is based on a transmission scheme, the crystals cannot be cooled, requiring to operate the LDA in a single shot mode. The laser diode emission is tuned to 940 nm at its peak to fit the absorption cross section. Such spectral adjustment of the laser emission relies on the use of a bias current (Section 2.5.1) and allows to work under the same spectral conditions as for the design point of the laser diodes (usually at 1 % duty cycle). Recorded spectra for the whole LDA are shown for three different currents in Figure 3.9. As reference, the absorption cross section of Yb $^{3+}$ :YAG is shown in the image as well.

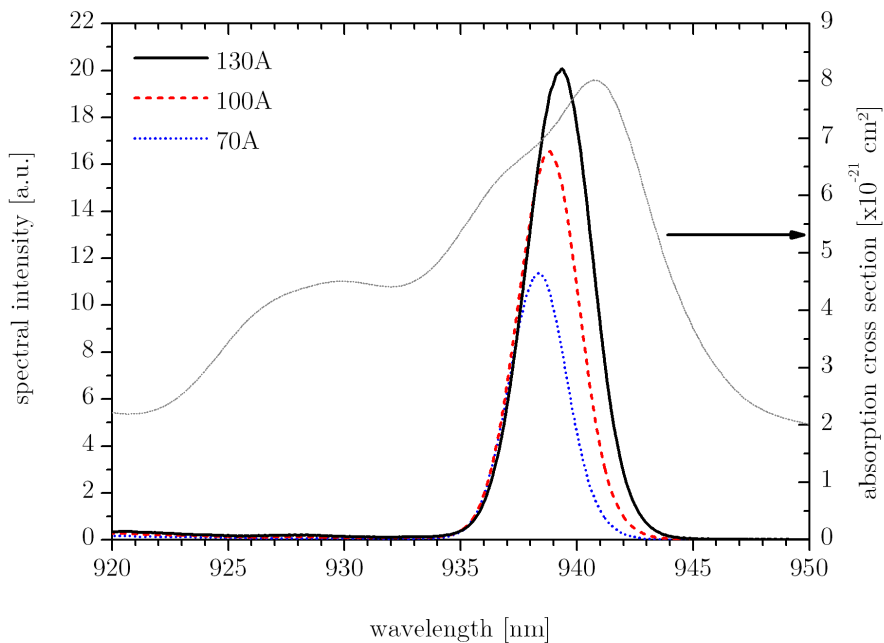


**Figure 3.9.:** Pump spectra observed for the single shot experiments. Each of the 30 stacks is spectrally tuned to its optimum working wavelength using the bias current.

As depicted in Figure 3.10 the emission of the pump laser (pink rectangle) enters from the front along the z-axis. The material is supposedly homogeneously doped and pumped more or less uniformly over its surface (see Figure 3.10 (right)). Gain probing is performed under an angle of incidence of  $24^\circ$  (i.e. the assumed extraction direction of the final amplifier layout) using a fiber-coupled cw laser source emitting at 1030 nm. The temporal evolution of the gain is recorded at several points of a central horizontal line, the Line Of Interest (LOI). While recording the amplified signal, and with the knowledge of the transmission of the crystals as well as the fluorescence light captured by the detector, the integrated gain can be deduced. The temporal evolution of this signal gives a limited, but sufficient insight about the processes within the gain medium during the pumping action.

In total, 7 different mm-thick  $\text{Yb}^{3+}\text{-YAG}$  slabs were under observation. Their doping concentration varied between 1 at.% and 10 at.% and their thicknesses between 1 mm and 6 mm. The thin lateral surfaces are not polished attempting to damp retro-reflections and also wedged under  $37^\circ$  introducing auxiliar losses through Fresnel reflection. The large faces (normal to the z-axis) have an anti-reflection coating with reflectivities below 0.5 % for pump and probing wavelength.

With a one dimensional code, the small signal gain distribution along the pump

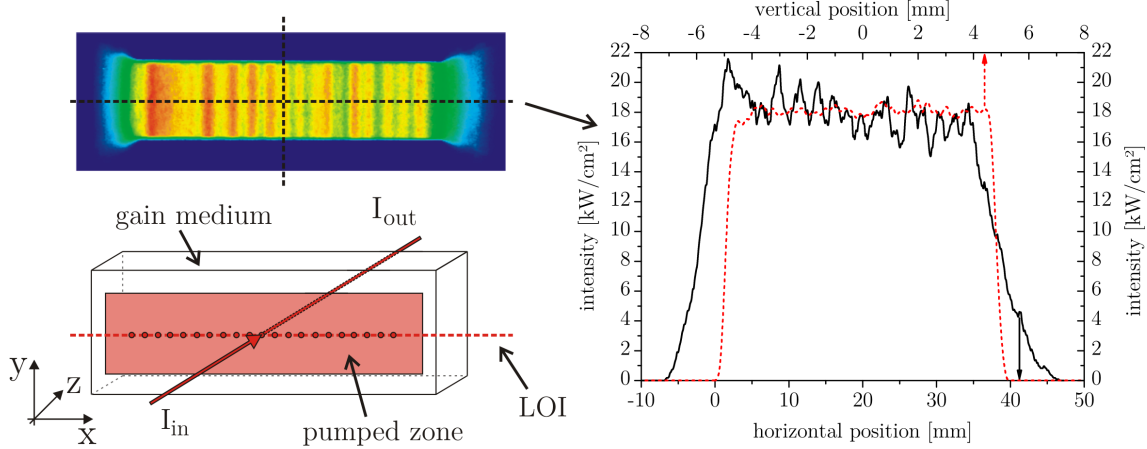


**Figure 3.10.:** ASE experiment setup. The top horizontal scale refers to the vertical lineout of the depicted 2D pump profile (top left).

axis (i.e.  $z$ ) is evaluated and, therefore, with the known geometry, a maximum  $g_0L$  calculated. Within these preliminary results two different groups are identified – the crystal series with low doping (1 at.%) showing a  $g_0L$  up to 4 and the other crystals with a huge small signal gain (5 and 10 at.% doping). Consequently the first set ( $2 < g_0L < 4$ ) is expected to reveal less impact from ASE and parasitic lasing than the second one. Let us mention, that cases with a large  $g_0L$  are often discussed in literature, however under strong estimations [46].

With the estimation of a monochromatic model for the pump and SE, the emission and absorption cross sections are set as follows:

- absorption cross section for pump wavelength  $\sigma_{a,P} = 0.7 \times 10^{-20} \text{ cm}^2$
- emission cross section for pump wavelength  $\sigma_{e,P} = 0.22 \times 10^{-20} \text{ cm}^2$
- absorption cross section for SE wavelength  $\sigma_{a,P} = 0.11 \times 10^{-20} \text{ cm}^2$
- emission cross section for SE wavelength  $\sigma_{e,P} = 0.4 \times 10^{-20} \text{ cm}^2$

Doping	$g_0L$ at $10 \text{ kW cm}^{-2}$	$g_0L$ at $14 \text{ kW cm}^{-2}$	$g_0L$ at $18 \text{ kW cm}^{-2}$
1 at.%	2	3	4
5 at.%	8	13	16
10 at.%	17	25	33

**Table 3.1.:** Maximum  $g_0L$  assuming a uniform pump distribution of 10, 14 and  $18 \text{ kW cm}^{-2}$  and a transverse size of  $L = 40 \text{ mm}$ . ASE is neglected during pumping.

Since the setup works in transmission, samples characterized by identical product of the doping concentration  $c_d$  and the thickness of the gain medium  $D$  will behave similarly without ASE. Consequently in this case a classification can be done concerning the product of  $c_dD$ . As one might expect, such classification will not be relevant anymore with different  $g_0L$  factors.

To illustrate this effect one case is depicted in Figure 3.11, where two different Yb<sup>3+</sup>:YAG crystals with the same  $c_dD$  are simulated with the numerical model derived in the previous section. The doping is 1 at.% and a thickness of 30 mm in the low gain case and a doping of 10 at.% with a thickness of 3 mm in the high gain case. For both slabs the [doping concentration  $\times$  thickness] ( $c_dD$ ) is then equal to 30 at.% mm. The pump power was taken to be uniformly distributed with an intensity of 14 kW cm<sup>-2</sup> on the 4 cm  $\times$  1 cm surface for 1 ms. Results are depicted in Figure 3.11.

We focus the interpretation on the central horizontal LOI out of the 2D gain maps, since this line will be probed experimentally later on. Figure 3.11 (a) shows the result for the low gain case. The LOI shows a gain distribution with a positive curvature, indicating a higher expected gain in the outer periphery of the gain medium. Concerning the high gain case, a lower gain in the outer periphery is expected, showing a negative curvature on the LOI. The origin is already discussed in Section 3.3.1. Although the same factor  $c_dD$  would yield the same gain neglecting ASE, this cannot be taken to be true in the case of the high  $g_0L$  anymore. Finally it is interesting, that the 1 at.% case shows a higher gain in transmission compared to the 10 at.% example (max values are 1.56 vs. 1.2).

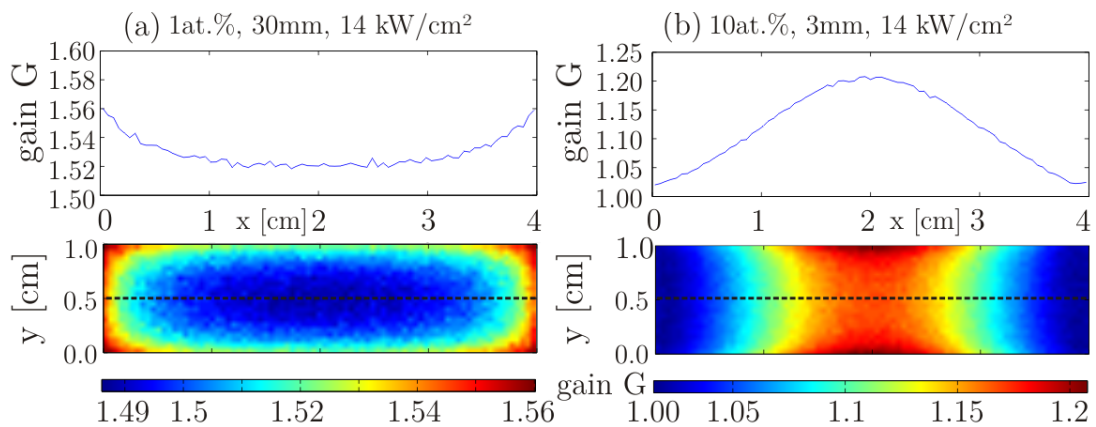


**Figure 3.11.:** ASE experiment examples simulation. The integrated gain along the z-axis  $G$  is shown as a map and as a horizontal lineout.

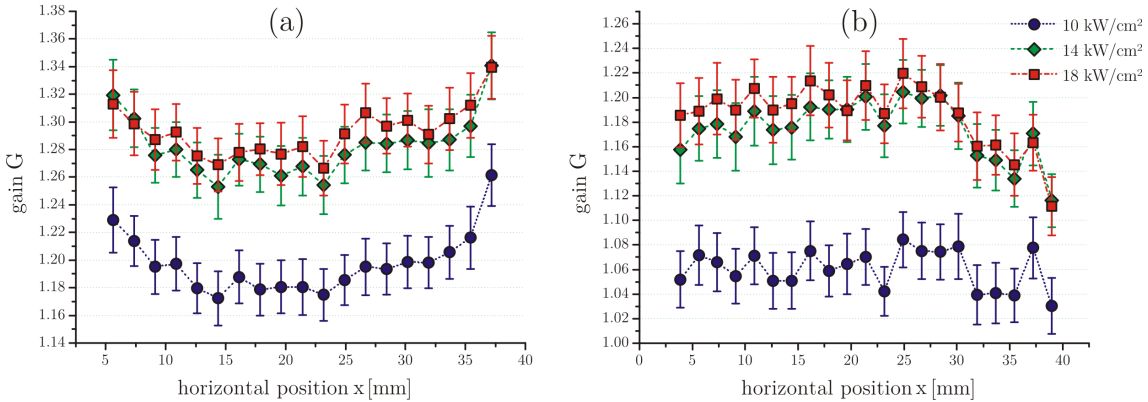


**Figure 3.12.:** Experimental gain distributions for a  $\text{Yb}^{3+}\text{:YAG}$  crystal doped at 1 at.% (a) and 10 at.% pumped at 10 (blue circle), 14 (green upright box) and  $18 \text{ kW cm}^{-2}$  (red box). The gain corresponds to the horizontal line out in the center of the pumped region.

Three intensities were used in the experiment:  $10, 14$  and  $18 \text{ kW cm}^{-2}$  respectively. The transverse gain probing is performed using an  $80 \text{ mW}$  cw fibre-coupled laser at  $1030 \text{ nm}$ . The angle of incidence is  $24^\circ$ . Measuring the temporal evolution of the transmitted signal and knowing the transmission without pumping, will lead to  $G$ .

From this point we will concentrate on two experimental cases: a crystal doped at 1 at.% with a thickness of 5 mm and a crystal with a doping of 10 at.% with a thickness of 3 mm. These two examples correspond to a low transverse gain factor  $g_0L$  (1 at.%) and a large  $g_0L$  (10 at.%) on the one hand and a factor  $c_dD = 0.5$  (1 at.%) and a  $c_dD = 3$  (10 at.%) on the other hand.

Figure 3.12 shows the measured gain distribution along the central horizontal line (LOI). Figure 3.12(a) depicts the lateral gain distribution in the case of a doping level of 1 at.%, 5 mm thickness after 1 ms pumping. The average  $g_0L$  would be 2, 3 and 4 for the intensities of 10, 14 and  $18 \text{ kW cm}^{-2}$  (see table 3.1) without taking ASE into account. A positive curvature is revealed, resulting in a higher gain on the outer edges of the probed gain medium. For a small  $g_0L$ , the local effects are dominant, leaving less population in the central region, as already discussed in part 3.

Examination of the gain distribution in the case of a higher factors of  $g_0L$  can be seen in Figure 3.12(b). While neglecting ASE, the values of  $g_0L$  would be 17, 25 and 33 after 1 ms respectively (see Table 3.1), and a strong influence of ASE is expected. Such high values for the factor  $g_0L$  will never be achieved, thus the small signal gain will be restricted to much smaller values. The resulting gain will be strongly reduced compared to the ideal (non-ASE) case and the gain distribution

will change as well. In this high gain case (large  $g_0L$ ) SE gets strongly amplified resulting in a stronger depopulation at the edges, resulting in a negative curvature shown in Figure 3.12(b). The maximum gain dropped by  $\approx 10\%$  compared to the low gain case.

Each point in Figure 3.12 corresponds to a single measurement using a photodiode allowing a sub- $\mu\text{s}$  temporal resolution. Figure 3.13 shows the recorded temporal evolution for both the high and low gain cases for the three pump intensities and for the three different localizations along the LOI.

In the case of a low doping concentration (Figure 3.13(a) (b) and(c) with 1 at.%, 5 mm thick crystal) the central gain ( $x = 21.4\text{ mm}$ ) stays always below the gain recorded for lateral locations ( $x = 5.5\text{ mm}$  and  $37\text{ mm}$ ). The gain temporal evolution in graphs (a) and (c) at pumping intensities of  $18\text{ kW cm}^{-2}$  reveals a drop before the end of pumping 1 ms, whereas a saturation is observed for the central position (b). At about 0.6 ms after the pump started, the gain reaches its maximum in each of the three cases. In the remaining 0.4 ms, the impact of ASE will differ with respect of the position. We have to remind that the crystal has a  $c_dD = 0.5$ , therefore we will still see even a significant amplification close to the back surface of the crystal (see sketch in Figure 3.10). As the photons under internal reflection will see an amplification which gets stronger and stronger with the ongoing pumping, the depopulation due to ASE will increase on the vicinity of the edges much stronger compared to the center. This leads to the decreasing gain at the edges and a saturation in the center after 0.6 ms. Pump intensities superior to  $14\text{ kW cm}^{-2}$  show saturation.

Let us now consider the temporal gain evolution for the crystal doped at 10 at.% in Figure 3.13(d)–3.13(f). Due to a higher reabsorption, almost one third of the pump will be used to bleach out the reabsorption. As the intensity distribution of the pump drops almost exponentially with the penetration depth, the populated parts will suffer from ASE, while the backside is still absorbing. An intensity of  $10\text{ kW cm}^{-2}$  doesn't show saturation, but is again influenced by ASE. Stronger pump intensities show saturation near the end of the pump duration of 1 ms.

Figure 3.14 shows for the 7 different examined crystals at pump intensities of  $10\text{ kW cm}^{-2}$  (a),  $14\text{ kW cm}^{-2}$  (b) and  $18\text{ kW cm}^{-2}$  (c) the resulting average gain calculated along the LOI in transmission compared to the simulation. While in the small gain example (1 at.% with a low  $g_0L$ , i.e. below 4) the expected gain fits quite well with the experimental results, we observe for large values of  $g_0L$  a strong deviation, especially in the case of a high doping.

In the case of  $10\text{ kW cm}^{-2}$ , measured values for a large  $c_dD$  are in relatively good agreement with the simulation. As the pump is weak compared to the examples

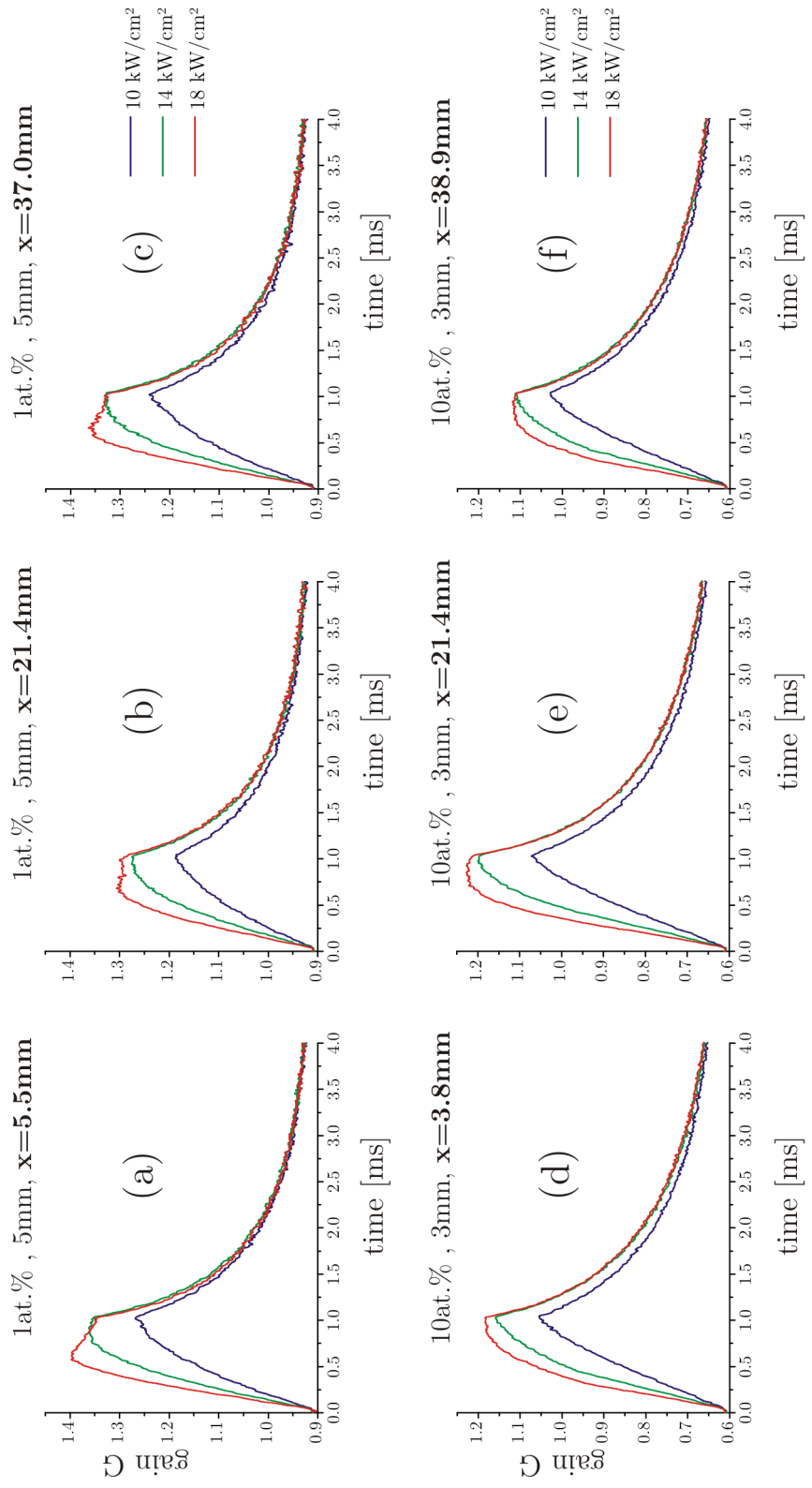


**Figure 3.13:** The upper row shows the temporal evolution during pumping in the case of a 1 at.% doped, 5 mm thick crystal for the most lateral left (a), central (b) and the most lateral right (c) measured points in the case of 10 (blue), 14 (green) and 18 kW cm<sup>-2</sup> (red). The lower row displays the same measurement in the case of a 10 at.% doped, 3 mm thick crystal. The horizontal axis shows the time after pump begin in ms, while the vertical axis shows the measured gain. The pump duration was 1 ms.

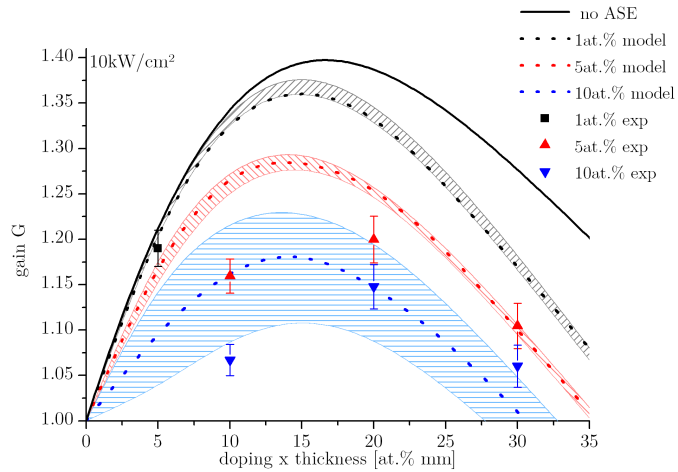
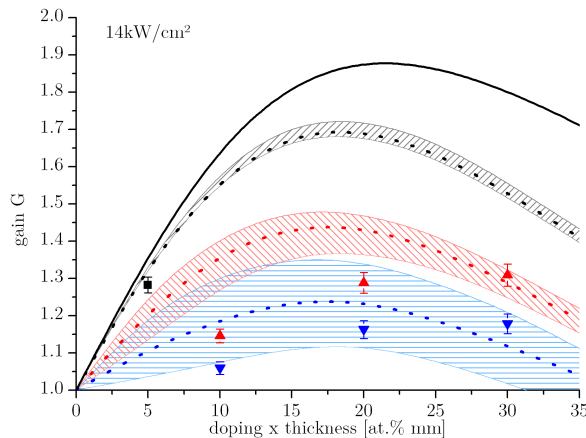
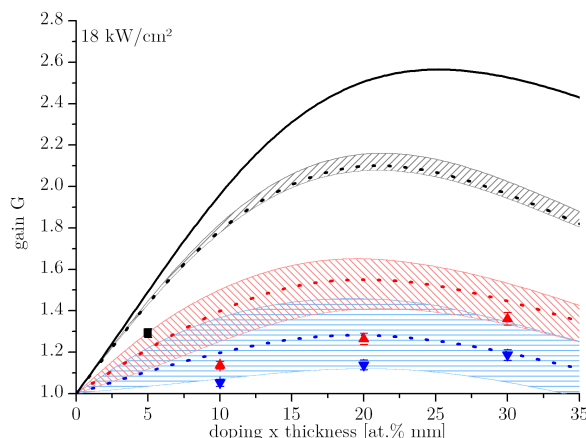
shown in (b) and (c), the trend of the gain as a function of the factor  $c_d D$  stays close to the expectations. It is obvious in the cases of high  $g_0 L$  and a small  $c_d D$ , that the deviation is significant. The thicker the crystal, the closer we get to the model, the less important are the internal reflections.

Even higher pump intensities will further increase the gain and the influence of ASE as well. This can be clearly seen while comparing Figure 3.14(a) with 3.14(b): as the gain increases with increasing pump intensity, the more the measurements deviate from the model. The impact can be dramatically seen in (c). While in (a) the evolution of the gain as a function of  $c_d D$  shows a curvature for the distribution of the measured points, this feature evolves into a linear behavior in (c). The 5 at.% doped crystal with a high  $c_d D$  ( $c_d D = 3$ ) shows at  $18 \text{ kW cm}^{-2}$  the same performance as a crystal of 1 at.%.

We have to keep in mind that the crystal is too thin compared to the optimal thickness. We can expect a far superior performance for a gain medium with a low doping and an increased thickness.

This again shows that a low factor  $g_0 L$  should be preferred while designing an amplifier gain medium. However, such a low doping results in a higher demand of material, the gain medium becomes more thick and the thermal management might become more complicated. Different cooling approaches are potentially needed, if a high average-power of the laser system is demanded.

As the loss due to ASE can be accounted using the developed three dimensional code, a potential exterior feedback resulting in parasitic oscillations should be taken into account as well. However such computations including parasitic oscillations are not within the context of this discussion, as working close to such oscillations must be avoided. Threshold conditions are discussed in the next section.

(a) Simulation and experimental results for  $10 \text{ kW cm}^{-2}$ (b) Simulation and experimental results for  $14 \text{ kW cm}^{-2}$ (c) Simulation and experimental results for  $18 \text{ kW cm}^{-2}$ 

**Figure 3.14.:** Overall comparison between simulation and experiment of ASE. Shaded areas indicate the range between the maximum/minimum values within the LOI.

### 3.5. Parasitic oscillations

The model described to this point neglects internal reflections for simplicity reasons. Unfortunately this does not stand true for a real application. There are indeed two different additional sources contributing to gain depletion within a gain medium. First, surfaces show a non null reflectivity, enabling thus the SE photons to travel a longer path due to internal reflections – the ASE might become stronger than it is estimated until this point. Second, photons can get trapped in closed paths as well as a feedback from the outer periphery can create parasitic oscillations within the gain medium. The first one is mainly affected by the coatings applied and the geometry used. Feedback relies on the properties of the surfaces, especially the preparation of the boundary, as well as on the conditions how the gain medium is mounted. Figure 3.15 shows TIR within a  $\text{Yb}^{3+}$  doped YAG slab. Injected on the lower right of the picture, a cw signal at 1030 nm travels to the other side of the crystal and gets partially reflected although the prisms outer faces were wedged and grounded.

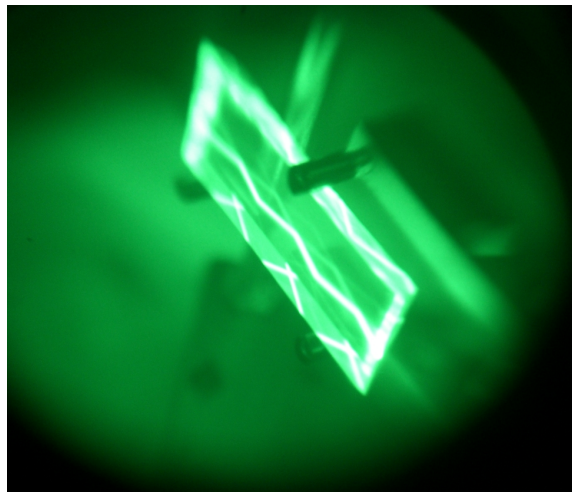


**Figure 3.15.:** Internal reflection in a slab

A gain medium will show in average one or more total internal reflections, if the Aspect Ratio ( $AR_L$ ) is less than:

$$AR_L = \frac{\sqrt{n_1^2 - n_2^2}}{n_2} \quad (3.5.1)$$

where  $n_1$  is the index of refraction of the gain medium and  $n_2$  the index of refraction of the surrounding medium. In our example, the refractive indexes are  $n_1 \approx 1.82$  and

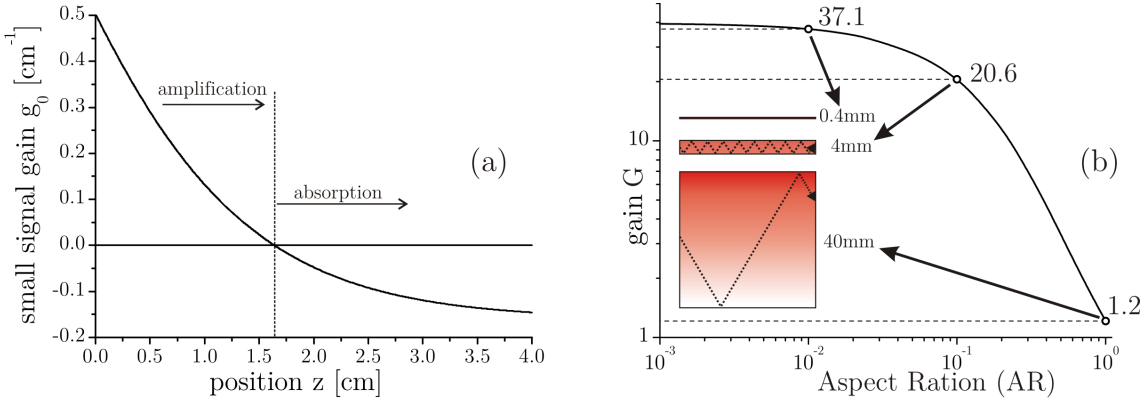


**Figure 3.16.:** Impact of the aspect ratio

$n_2 \approx 1$  at 1  $\mu\text{m}$ , consequently  $AR_L \approx 1.5$ . Materials with a lower  $n_1$  are therefore more preferred for constructing thin amplifiers.

Recalling the pump geometry used in the last section (single-side pumped gain medium used in transmission), its small signal gain distribution is, in a quasi-three level scheme, associated with a specific thickness  $z_{opt}$ , before reabsorption becomes imminent (see e.g. Figure 3.16). Increasing the gain medium thickness will increase the overall gain on the extraction wavelength until  $z_{opt}$  is reached. Models neglecting the ASE and internal reflection will by this show a decreasing energetic gain with a further increasing thickness. As an example, a one dimensional model neglecting ASE shows in Figure 3.16(a) the small signal gain distribution along the pump axis for a 4 cm thick Yb<sup>3+</sup>:YAG doped at 1 at.% pump for 1 ms at 10 kW cm<sup>-2</sup>. An optimum thickness is found to be  $z_{opt} \approx 1.7$  cm. Pure transverse ASE will consequently see an integrated energetic gain throughout the 4 cm long propagation of  $\approx 7.4$ .

Considering now SE confined by the internal reflections, the total energetic gain for photons traveling through the gain medium will depend on the thickness of the gain medium itself. Under the estimation of a transverse size of 4 cm, one can calculate the average energetic gain under TIR for this case as a function of the thickness of the slab. The result depicted in Figure 3.16(b) considers three separate  $AR_L$ . For an  $AR_L$  of 1 (4 cm thickness), the photons suffer from the reabsorption, as the thickness is significantly larger than  $z_{opt}$ . An  $AR_L$  of 0.1 (4 mm thickness) however results in a gain of  $\approx 21$  and a photon experiences under an AR of 0.01 a gain of  $\approx 37$ . Overall the gain is converging in this case to a value of 39.4. Very thin disks will by this suffer from an increased ASE impact due to TIR. If the AR is  $\approx 0.3$  the same gain compared to the pure transverse ASE ( $\sim 7.4$ ) case can be found.

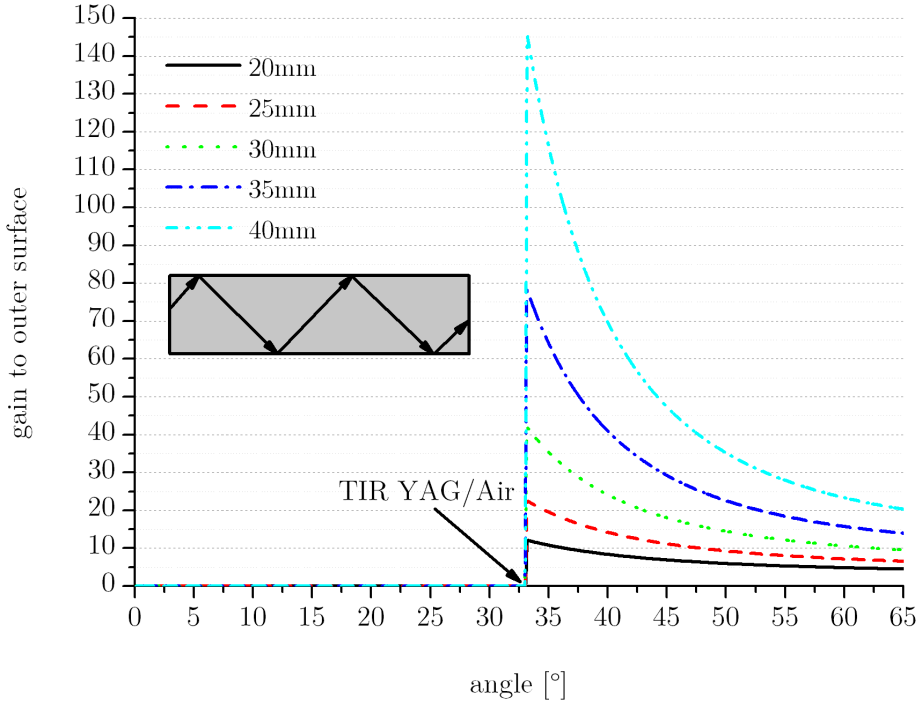


**Figure 3.17.:** Gain for SE neglecting ASE for 7 mm thick Yb:YAG crystal pumped at  $10 \text{ kW cm}^{-2}$ .

This result should now be applied to the dimensions used in the case of the Lucia main amplifier head. As discussed, even a moderate gain along the extraction direction can lead to strong amplification in the most disadvantageous directions. The gain integrated along optical paths set at different angles within a 7 mm thick 2 at.% doped  $\text{Yb}^{3+}:\text{YAG}$  slab pumped at  $10 \text{ kW cm}^{-2}$  is of interest in Figure 3.17. Surfaces are considered to be not coated on any surface. Indeed, the average reflectivity between a HR ( $> 99\%$ ) and AR ( $< 1\%$ ) coating is approximately the reflectivity found for  $\text{Yb}^{3+}:\text{YAG}$  against air ( $\approx 8.5\%$ ).

This graph illustrates, for different pumped areas, the respective gain as a function of the propagation angle. It shows clearly, that the gain under TIR ( $\theta \gtrsim 33^\circ$ ) is most important. Large pumped zones (lengths beyond 30 mm) are not beneficial at all in this example. Indeed, the gain obtained near TIR for a 40 mm large pumped area is so strong  $\sim 145$ , that a simple reflection on an uncoated surface would not be enough to suppress parasitic oscillations anymore.

Of special interest are closed paths within a specific geometry, as SE can get trapped. In a cylindrical geometry closed paths are well known and have the shape of stars. Such an example is shown in Figure 3.18 depicting a star with nine teeth

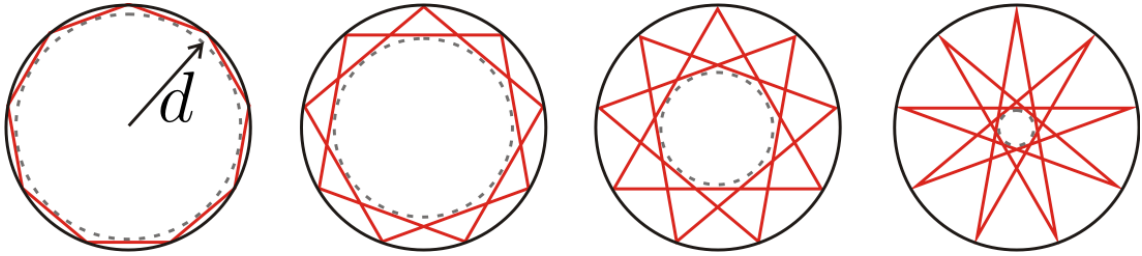


**Figure 3.18.:** Closed paths within a circle and not crossed inner circle of radius  $d$ .

with its four different variants. With an arbitrary point of origin, such stars will generate inner, not crossed circles of radius  $d$  (dotted line in Figure 3.18).

The most simplest case is a centered circular homogeneously pumped region within a circular gain medium. A general sketch of this problem is found in Figure 3.19. Every closed path is defined by its radius  $d$ . One can then define the length  $s_2$  traveled within the pumped area. The reflectivity on the peripheral surfaces is related by the angle of incidence  $\eta$ .

The total traveled distance between two reflections is  $s_1$ :

$$s_1 = 2\sqrt{r_1^2 - d^2} \quad (3.5.2)$$

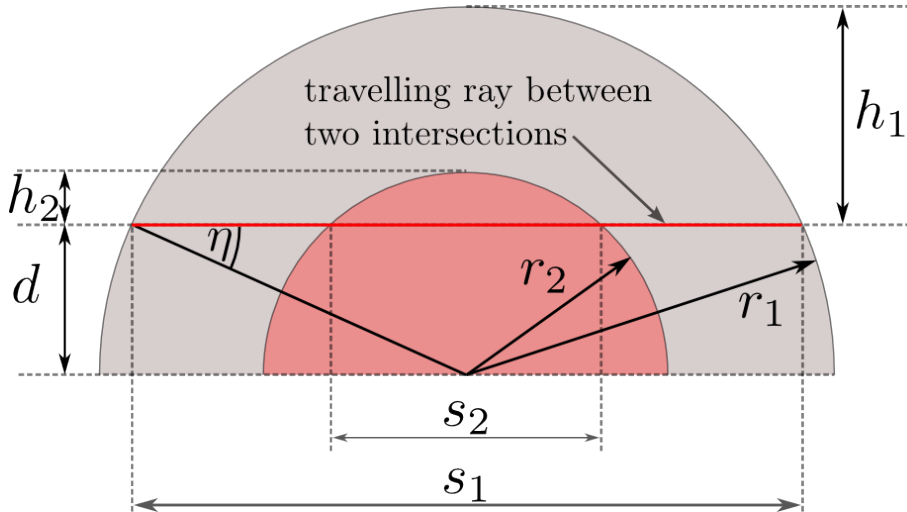
where  $i = 1, 2$ . Within the length  $s_2$  amplification occurs while within the distance  $s_1 - s_2$  ASE can be absorbed, if an absorbing material is used. This might be not pumped  $\text{Yb}^{3+}$  doped YAG on its own as it absorbs at 1030 nm at ambient temperatures as well as an absorbing cladding (e.g.  $\text{Cr}^{4+}\text{:YAG}$ ). In this geometry the incident angle on the outer boundary is given by the angle  $\eta$ :

$$\eta = \arcsin\left(\frac{d}{r_1}\right) \quad (3.5.3)$$

However as the angle  $\eta$  will approach, with increasing  $d$ , the critical angle of Total Internal Reflection (TIR)  $\eta_c = \arcsin(n_1/n_2)$ , where  $n_1$  is the index of refraction of the external medium and  $n_2$  the index of the gain medium, a maximum radius  $r_{2,max}$  is given with the condition  $\eta = \eta_c$  (Figure 3.19):

$$r_{2,max} < \frac{n_1}{n_2} r_1 \quad (3.5.4)$$

The consequence is that surfaces larger than described by radius of  $r_{2,max}$  very likely become a subject of closed ray traces under TIR and by this parasitic oscillations. These modes traveling under such angles are usually called lossless modes [116].

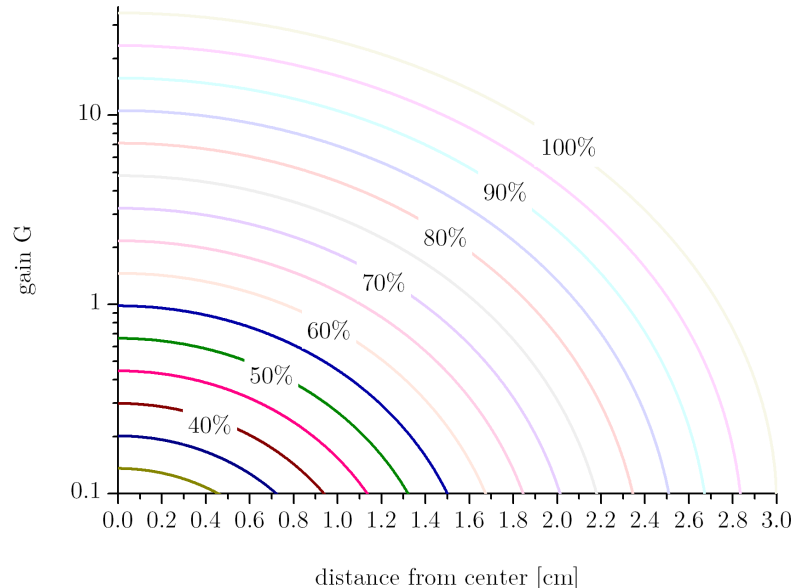
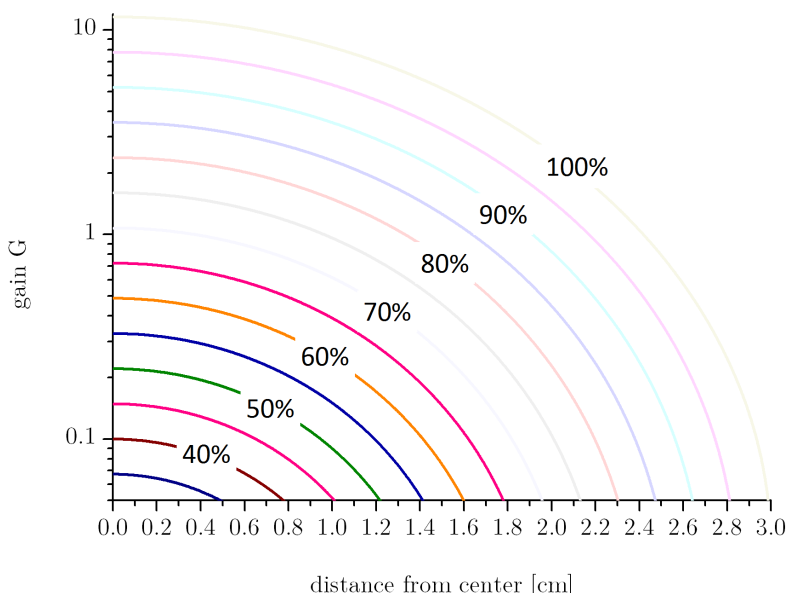


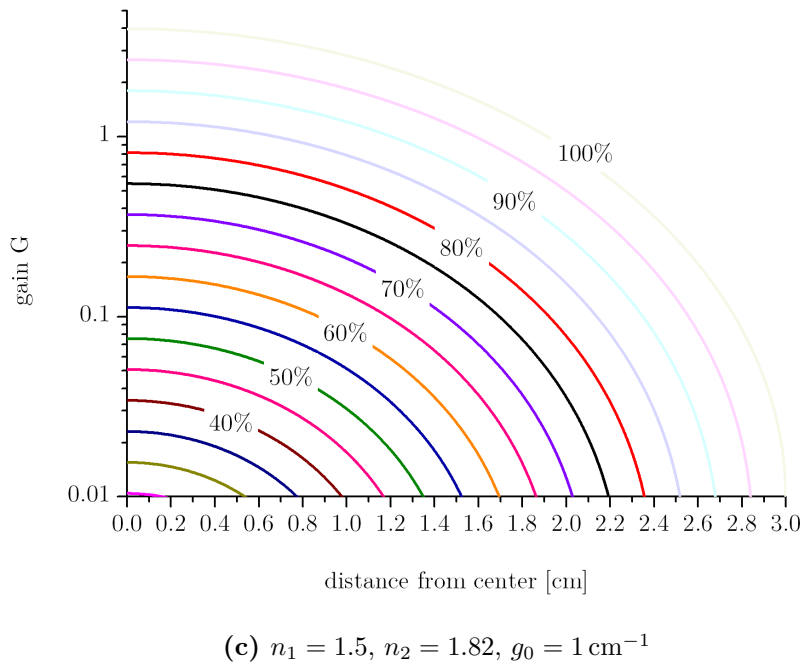
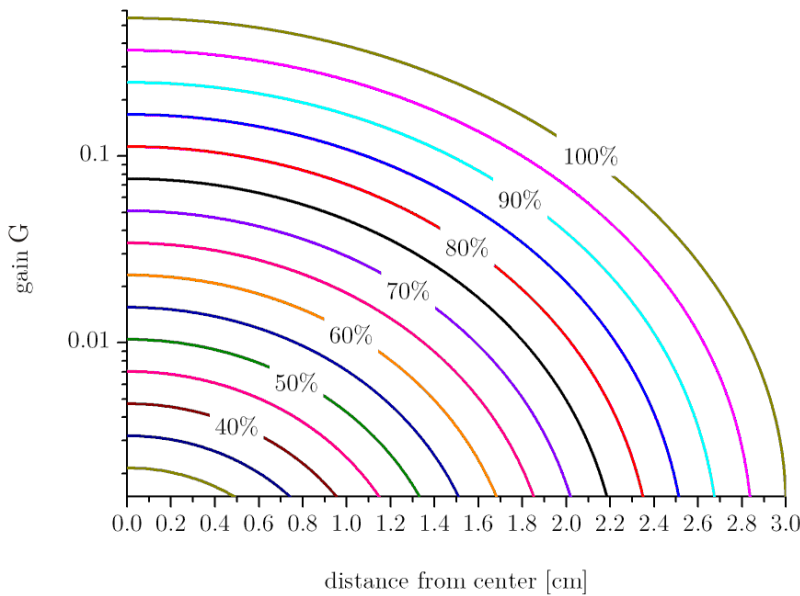
**Figure 3.19.:** A pumped circular region (red) located in the center of a circular gain medium (grey).

In first order, the amplification and absorption process will be exponential on its own and the reflectivity is governed by the Fresnel reflectivity. Parasitic oscillations will quickly become polarized, maximizing the experienced gain. Consequently a first-order approximation with a Fresnel reflectivity for s-polarized (transversal electric, TE) light is most appropriate. This reflectivity however is strongly influenced by the index of the external material. Thus, index-matching can dramatically improve the threshold for parasitic lasing.

Figure 3.20 shows a compilation of four different index matching combinations for a 2 at.% doped  $\text{Yb}^{3+}$ :YAG crystal at room temperature with an index of refraction of the external medium ranging from 1 to 1.7. The small signal gain  $g_0$  within the pumped area is equal to  $1 \text{ cm}^{-1}$ . The crystal diameter is  $2r_1 = 60 \text{ mm}$  and the radius of the pumped inner circle varies between 0 and 100 % of the outer radius. The curves of graphs 3.20 (a)–(d) show the gain as a function of the parameter  $d$  (horizontal axis) for given radii (normalized to the outer radius ( $r_2/r_1$  in %)) of the pumped region. The increment is 5 % for each curve. The pastel-colored lines indicate gain conditions above 1 per pass including reabsorption and reflection-losses. Special attention should be given on the logarithmic scale for the gain.

In the case of air as index matching material (Figure 3.21(a)), one observes a maximum pumped area defined by a radius of  $r_2 = 0.55 r_1 = 1.65 \text{ cm}$  (corresponding to  $g_0 L = 0.55 \times 1 \times 6 \approx 3.3$ ). This corresponds to the maximum allowable radius  $r_{2,max} \approx 1.64 \text{ cm}$ . Replacing the external material (air) with another medium

(a)  $n_1 = 1, n_2 = 1.82, g_0 = 1 \text{ cm}^{-1}$ (b)  $n_1 = 1.33, n_2 = 1.82, g_0 = 1 \text{ cm}^{-1}$


 (c)  $n_1 = 1.5, n_2 = 1.82, g_0 = 1 \text{ cm}^{-1}$ 

 (d)  $n_1 = 1.7, n_2 = 1.82, g_0 = 1 \text{ cm}^{-1}$ 

**Figure 3.20.:** Gain  $G$  (vertical axis in log-scale) per pass in the pumped region vs. the distance from the center (horizontal axis) as a function of the index matching liquid ( $n_1$ ), reabsorption is taken into account. The diameter of the  $\text{Yb}^{3+}:\text{YAG}$  crystal is 60 mm. The diameter of the pumped zone is given by the lines in 5 % steps.

showing a higher index of refraction, e.g. water ( $n_1 \approx 1.33$ , Figure 3.21(b)), implies this time, that about  $\approx 69\%$  of the total diameter can be covered, before a gain of 1 occurs between each reflection. In this case  $r_{2,max}/r_1$  is  $\approx 73\%$  therefore transverse oscillations are more likely to occur than oscillations due to closed paths.

A further increase in refractive index of the matching material to  $n_1 = 1.5$  (Figure 3.20(c)) shows a  $r_{2,max}/r_1 = 82\%$ . Again, a very similar value compared (in this two dimensional example) is found for pure transverse oscillations ( $\approx 82\%$ ). Index matching media with an even higher index of 1.7 (see Figure 3.20(d)) allows almost the whole surface to be used as pumped surface.

The factor of acceptable  $g_0L$  for closed paths rises to values of up to  $g_0L \approx 0.82 \times 1 \times 6 \approx 5.5$ . Despite in such a case the parasitic oscillation for this special type of modes might be suppressed, ASE will strongly deplete the gain medium as well as feedback from the outer limitations (e.g. the gain medium mount) might generate a sufficiently strong feedback generating oscillations within the gain medium. The estimation of these effects are more complicated to estimate and are often only accessible to experimental observations.

In summary the following is deduced:

- In the active mirror scheme, the emission confined by TIR within the gain medium can quickly become the main source of parasitic oscillations.
- Lossless modes must be avoided. For each specific geometry of the gain medium, the pumped area should be adjusted in such a way that closed paths don't experience a gain superior to 1.

### 3.6. Application on the Lucia Amplifier

The Lucia main amplifier head hosts a 60 mm diameter  $\text{Yb}^{3+}$ :YAG crystal doped at 2 at.% (grown by Laserayin) in an active mirror architecture. A thickness of 7 mm leads to an aspect ratio of  $AR_L \approx 0.12$ . On one side an antireflective coating is applied while on the other side a highly reflective coating is applied on the central part (35 mm diameter, see Figure 3.21). As the YAG of the non-coated periphery on the HR coated surface is in direct contact with water, ASE can be minimized due to a better coupling of the SE into the water. The gain medium is then mounted into the assembly as it is shown in Figure 3.22.

At the crystal periphery exists a cavity confining emitted SE and ASE to prevent a full back reflection into the gain medium itself. The cavity on its own can be filled with different index matching liquids (using a special sealed retaining ring), however usually filled with water entering through the holes in the standard mount.

The area to be pumped with the light coming from the Laser Diode Array

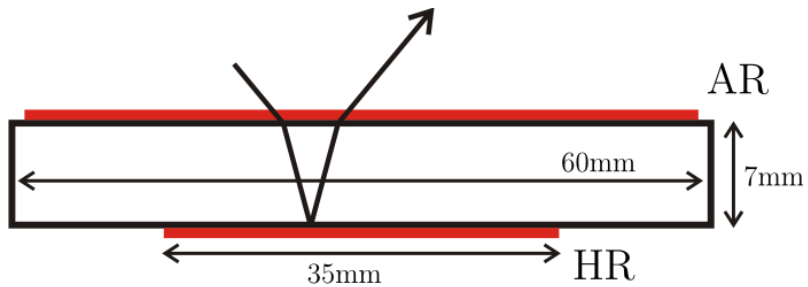


**Figure 3.21.:** Sketch of the coatings applied on the 60 mm active mirrors. The crystals are doped at 2 at.%.

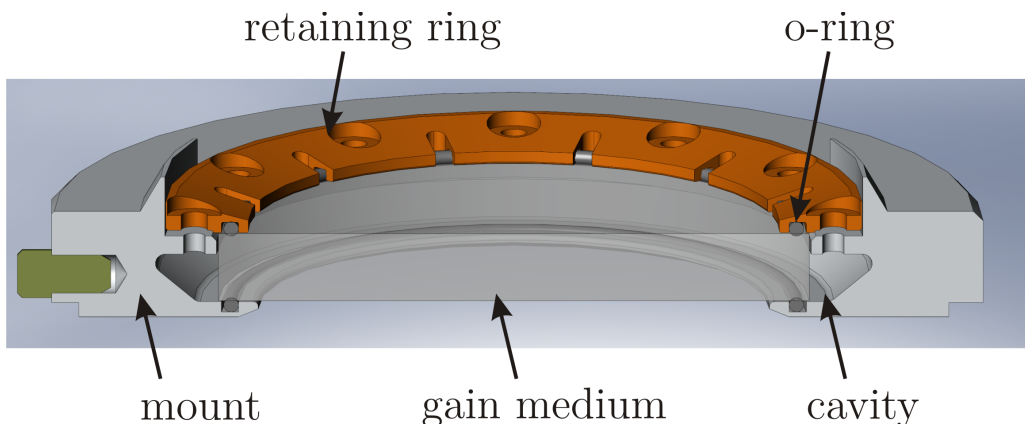


**Figure 3.22.:** CAD view (half cut) of the mount for the 60 mm crystals. The pump direction in this image is from below and the water cooled side is on top.

(LDA) is illuminated through the AR coated side (see Figure 3.21) with intensities ranging from  $11.5 \text{ kW cm}^{-2}$  for large pumped surfaces ( $2.6 \text{ cm} \times 3.8 \text{ cm}$ ) and up to  $16.5 \text{ kW cm}^{-2}$  in the case of a reduced circular zone (diameter of 30 mm).

The initial experimental pump distribution is shown in Figure 3.23. With a driving current of 130 A, the average intensity is  $11.5 \text{ kW cm}^{-2}$  and can reach up to  $13 \text{ kW cm}^{-2}$  for a maximum driving current of 150 A. The gain probing is performed under the expected extraction direction with a 80 mW cw fiber coupled source at 1030 nm. The detector is a photo diode with a bandwidth of 1 GHz in conjunction with a 1 GHz, 5 GS/s oscilloscope. The simulation is performed with a super-Gaussian pump distribution of the order 20 with a FWHM of 2.6 cm in vertical and 3.8 cm in horizontal direction.

Both, calculated and measured, gain evolutions in the case of a pump intensity of  $11.5 \text{ kW cm}^{-2}$  (130 A driving current on all the laser diode stacks) can be compared in Figure 3.24. While at the beginning of the pump pulse the prediction fits rather well to the experimental results, a strong derivation appears after about 600  $\mu\text{s}$ , when the gain in the transverse direction is affected by the onset of parasitic oscillations. Further pumping does not increase the gain anymore, as the gain medium started to transversally lase on its own.

The threshold for parasitic lasing can be roughly estimated as it was discussed in the foregoing section. The origin in this case lies in the large extend of the pumped zone. We might expect the highest gain for the internal reflections for a

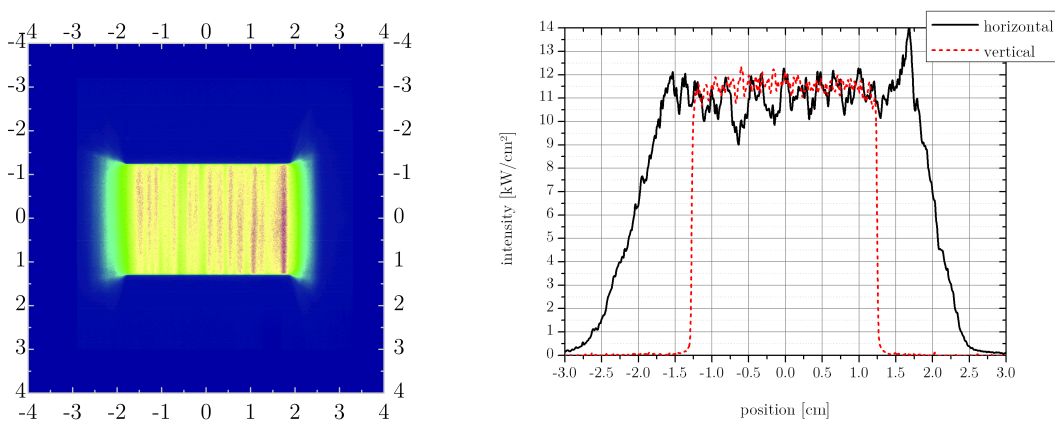


**Figure 3.23.:** 2D pump profile and horizontal and vertical lineouts at 130 A, which corresponds to an average intensity of  $11.5 \text{ kW cm}^{-2}$ .

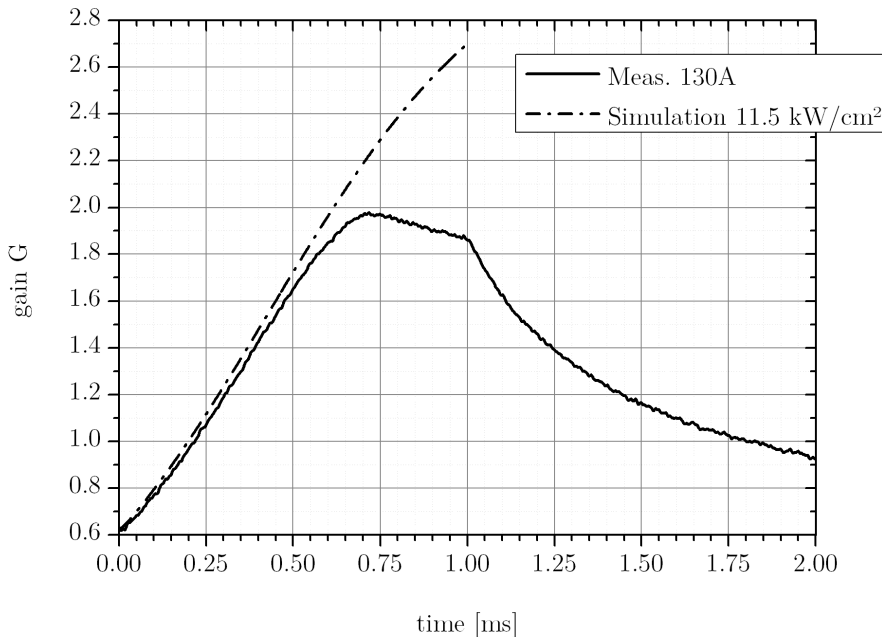


**Figure 3.24.:** Comparison between the simulation and measurement for a rectangular pump zone in a 60 mm crystal,  $11.5 \text{ kW cm}^{-2}$ . 130 A corresponds to an average pump intensity of  $11.5 \text{ kW cm}^{-2}$ .

TIR (YAG–water) propagation. The gain for a closed loop depends on the lateral surface preparation as well as the boundary conditions. Lateral surfaces should be AR coated or kept unpolished in order to reduce the direct reflection from those surfaces. Highly reflective coatings should only applied, where they are needed.

In the experimental case a highly reflective coating is applied within a diameter of 35 mm centered on the backside and the antireflective coating spans the whole front surface. At the periphery an index matching liquid can be inserted in the cavity shown in Figure 3.22. In the most simple case water is used implying a reflectivity of  $\approx 2.5\%$ . The not pumped periphery is absorbing at the emission wavelength, as  $\text{Yb}^{3+}\text{:YAG}$  exhibits reabsorption at room temperature.

To get a feeling whether the parasitic oscillations set in or not, we use the model for the TIR reflections as it is shown in Figure 3.17. The angular distribution of the gain as a function of the time is of interest (Figure 3.25). The propagation under the TIR ( $\sim 33^\circ$  at the interface YAG–air) will still see losses at the YAG–water surface (TIR  $\sim 47^\circ$ ). Consequently, the TIR angle connected to the surface YAG–water is of main importance.

Keeping in mind that the reflectivity of YAG against water under normal incidence

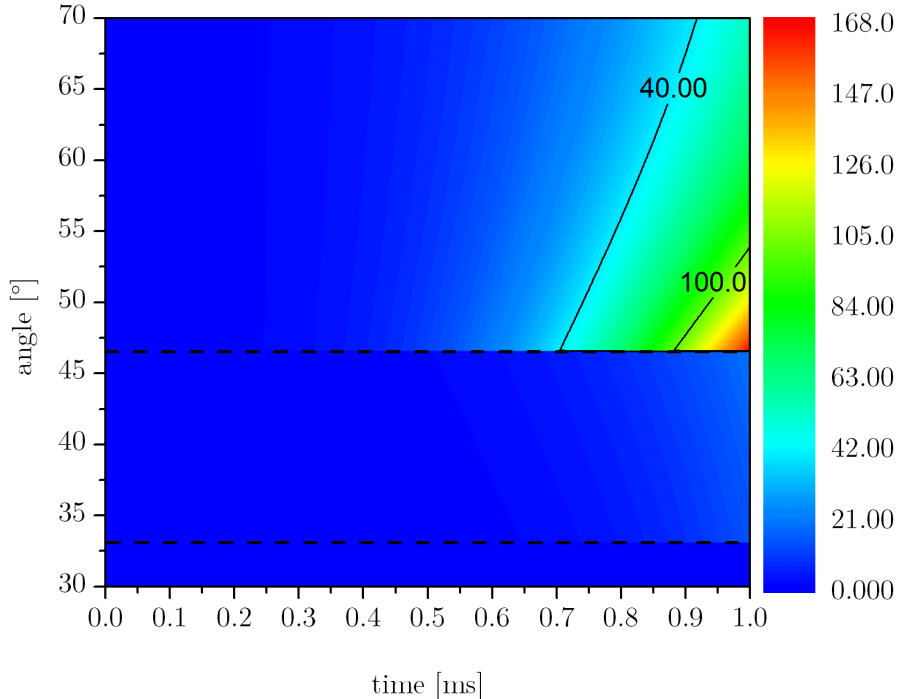


**Figure 3.25.:** Gain distribution (colorbar) for rays propagating inside the gain medium with angles of incidence on the large faces varying between  $30^\circ$  and  $70^\circ$ . The x-axis gives the time scale during the pump process and the y-axis the variation of the propagation angle. The dotted lines show the TIR angle against air  $\theta_{TIR} = 33.1^\circ$  and water  $\theta_{TIR} = 46.6^\circ$ . The contour lines at a gain of 40 and 100 are indicated (rectangular pump  $12 \text{ kW cm}^{-2}$ ).

is  $\approx 2.5\%$  a maximum overall gain of  $1/0.025 = 40$  is acceptable to avoid lasing. Considering such a threshold value, Figure 3.25 shows an onset of lasing around  $\approx 700 \mu\text{s}$  fitting the experimental value in Figure 3.24 quite well.

With an exponential growth of the amplification it is imperative to reduce the pumped area to its minimum with respect to the extraction aperture. The pump zone is reduced to a region limited by a circle of 30 mm diameter using a mask. Usable surface is reduced from  $\approx 10 \text{ cm}^2$  to  $\approx 6.5 \text{ cm}^2$ , in total resulting in 30 % of the energy wasted as it gets blocked by the mask. Additional concentration mirrors are introduced reflecting most of the lost light back into the aperture. This increases the incident intensity and therefore the local gain in the pumped area.

The optimization process is shown in Figure 3.26 while the experimental setup is illustrated in Equation 3.27. Fast axis concentration mirrors are silver coated. The mask is simply made out of an aluminum sheet. The transmission loss due to the mask and fast axis concentration is in approximately 20 %. The whole transmission

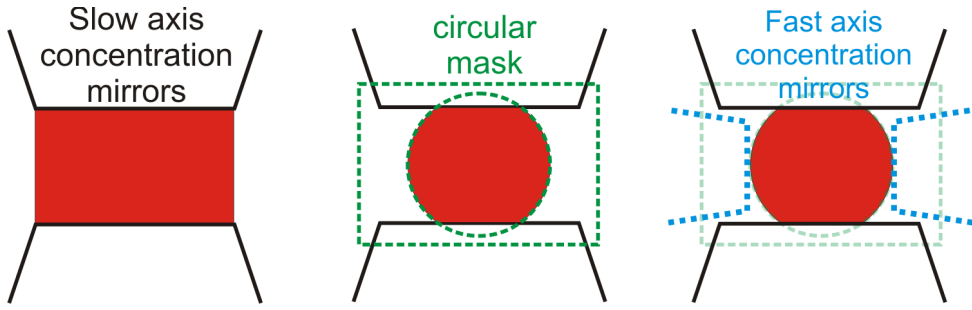


**Figure 3.26.:** Light concentration optimizations, Large concentration mirrors (slow axis concentrators, grey), circular mask (green) and fast axis concentrators (blue).

function of the pump setup drops from  $\approx 90\%$  to  $\approx 80\%$ . Despite the higher transport losses a rise in intensity of almost 30 % is found.

Compiled results are shown in Figure 3.28. Applying the mask to the pumped region suppresses effectively the parasitic oscillations and a satisfying agreement between the simulation and the experimental results is found (green curve). Recycling the pump light using the fast axis collimators (fac) brings a major improvement in gain (blue curve). However, pump durations longer than  $\approx 700\mu\text{s}$  show parasitic oscillations again.

As it was discussed already before, suppression of transverse ASE is performed by the reduction of the feedback from the lateral surfaces, especially when using index-matching. Consequently with the possibility of filling the peripheral cavity, several liquids were explored (see Table 3.2). An exhaustive collection of index matching liquids can be found [118, 47]. Unfortunately most of the index matching liquids with an index higher than 1.6 are toxic or at least irritant. Table 3.2 summarizes five cases of index matching media under observation.

The impact of the index matching liquid on the gain evolution is shown in Figure 3.29. Using no index matching liquid at all (air) a slight reduction of the maximum gain is observed. Nevertheless it does not change the overall behavior, especially not the roll-over appearing at  $\approx 700\mu\text{s}$ .

The roll-over is shifted by  $\approx 50\mu\text{s}$  using water or diiodomethane. Diiodomethane is of common use for ruby and Ti:Sa index matching as it has an index of refraction very close to the gain media in those cases.

Unfortunately diiodomethane suffers from a decomposition which results in a distinctive yellow to red coloring. On the other hand, diiodomethane and  $\alpha$ -bromo-naphthalene show a high viscosity and are by this not easily applicable in contrast to decaline or water. Moreover, those liquids (besides water) penetrate different type of rubber rings, so special care should be taken in order to prevent leakage.

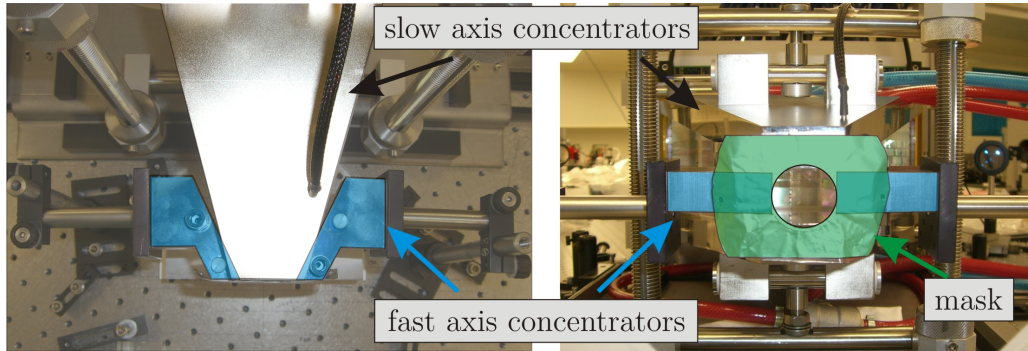


**Figure 3.27.:** Optical elements used for the light concentration optimizations (slow axis concentrators, grey), fast axis concentrators (blue) and circular mask (green).

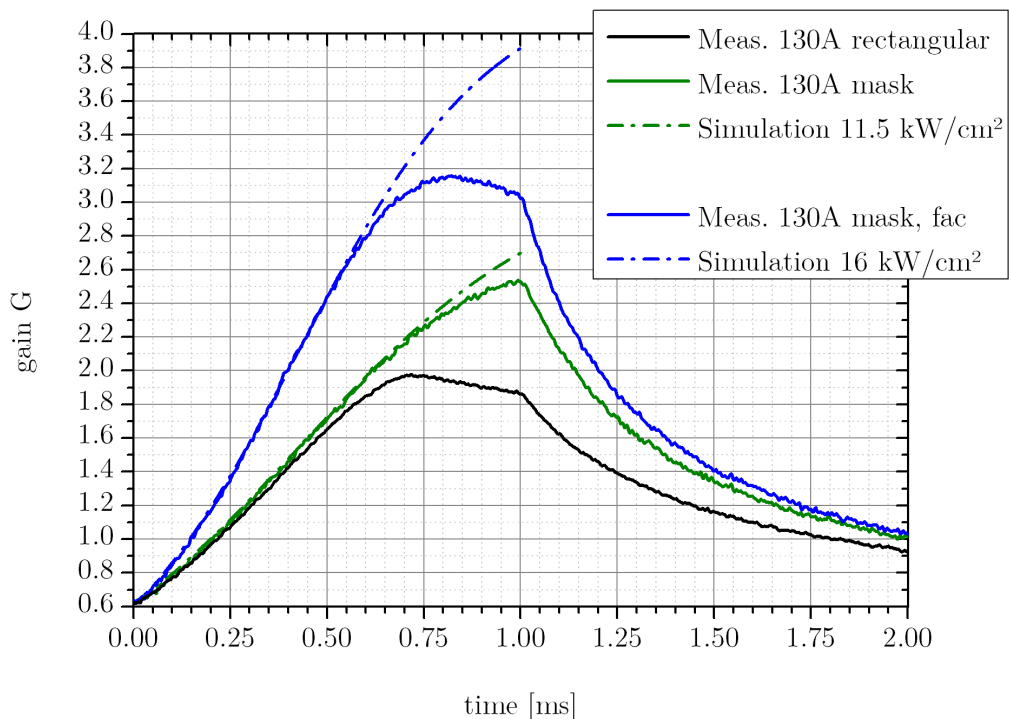


**Figure 3.28.:** Temporal gain evolution observed for three experimental pump distributions depicted in Figure 3.26.

An interesting characteristic is the absence of a difference in slope after the roll-over for most of the studied cases. The slope after the roll-over is directly related to the impact of parasitic oscillations; a different slope indicates a different feedback. Consequently a change in this feature indicates the effectiveness of the measures taken to suppress parasitic oscillations. An absence of parasitic oscillations is reached, when the roll-over vanishes.

Feedback for transverse oscillations is related to the:

- reflection at the gain medium/liquid interface.
- reflection from the external cavity back into the gain medium.

The latter one was identical for the experimental results depicted in Figure 3.29 for air and  $\alpha$ -bromonaphthalene as well for the cases of water and diiodomethane.

Only the case of a blackened (ink) cavity and decaline (orange curve) showed an important improvement over the use of water as index matching liquid. In this case gain is improved and, more interesting, exhibiting a bit different slope after the roll-over.

A reduction of the reflectivity on the outer periphery does not reveal any improvement in gain performance, whereas the reduction of the reflectivity of the gain medium holder shows an improvement. Obviously reflections from the gain medium mount are the main cause of parasitic oscillations in the studied amplifier assembly.

Another reflecting surface was also identified as a non negligible feedback for ASE: the back side of the circular (reflective) mask. The mask is made out of aluminum and is located in short distance to the AR coated top crystal surface. Aluminum has a typical reflectivity in the order of 90 %. Consequently spontaneous emission originating from the laser gain medium will be partially reflected back into the gain medium.

Liquid	$n_0$ (1 $\mu$ s)	R(0°)	remarks	Ref.
water	1.33	2.5%	absorption in the NIR	[112]
decaline	1.42	1.6%	nontoxic, solvent, low viscosity	[119]
$\alpha$ -bromonaphthalene	1.66	0.2%	high viscosity, solvent, irritant	[118, 47]
diiodomethane	1.74	0.06%	solvent, toxic, high viscosity	[118, 47, 120]
air	1.00	8.6%	gaseous	

**Table 3.2.:** Comparison between four different Index matching liquids used in the experimental studies. Air is given as reference.

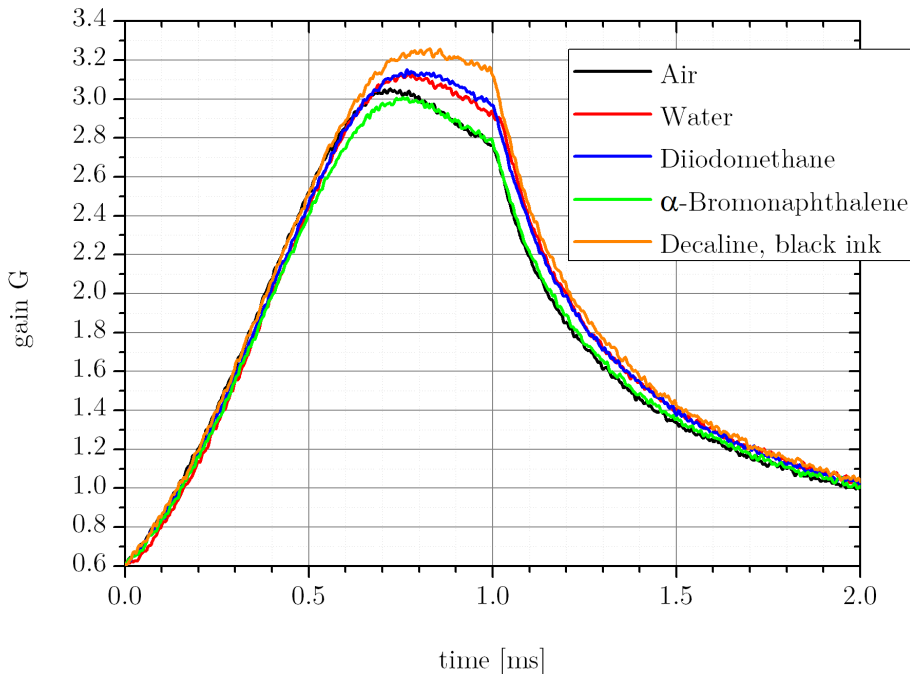


**Figure 3.29.:** Impact of the index matching liquid on the gain,  $16 \text{ kW cm}^{-2}$

To overcome these problems, the gain medium mount is modified as depicted in Figure 3.30. The surfaces are treated with black nickel, lowering significantly the reflectivity [121]. The aperture of the laser gain medium mount is reduced to 32 mm and replaces the mask. On the inner side all surfaces are blackened as well. The outer side (which is hit by the pump light) is kept untreated. Figure 3.31 shows the result of the gain measurement with the modified gain medium mount compared to the original mount design and the 3D simulation using the developed model. The roll-over vanished and the experimental results fit excellently the three dimensional prediction neglecting parasitic lasing using the developed code.

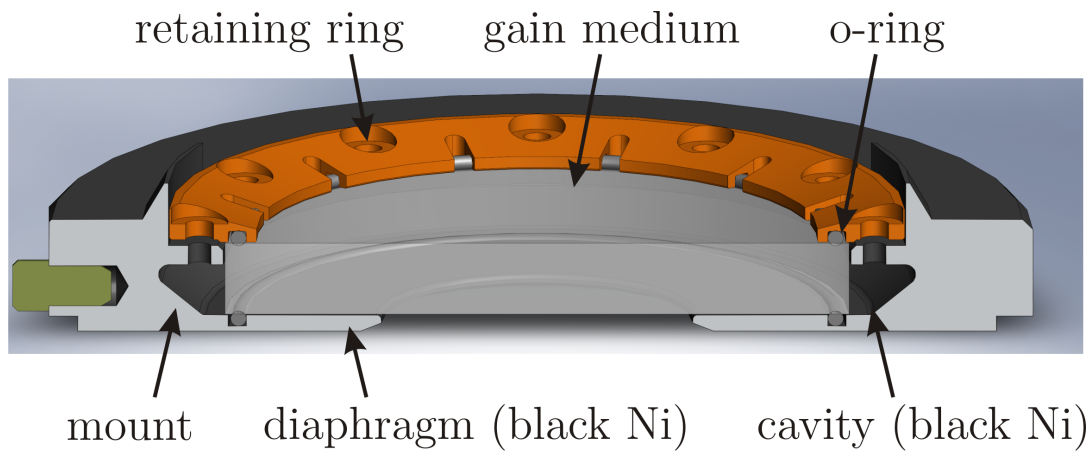


**Figure 3.30.:** Redesigned gain mount with incorporated mask and blackening.

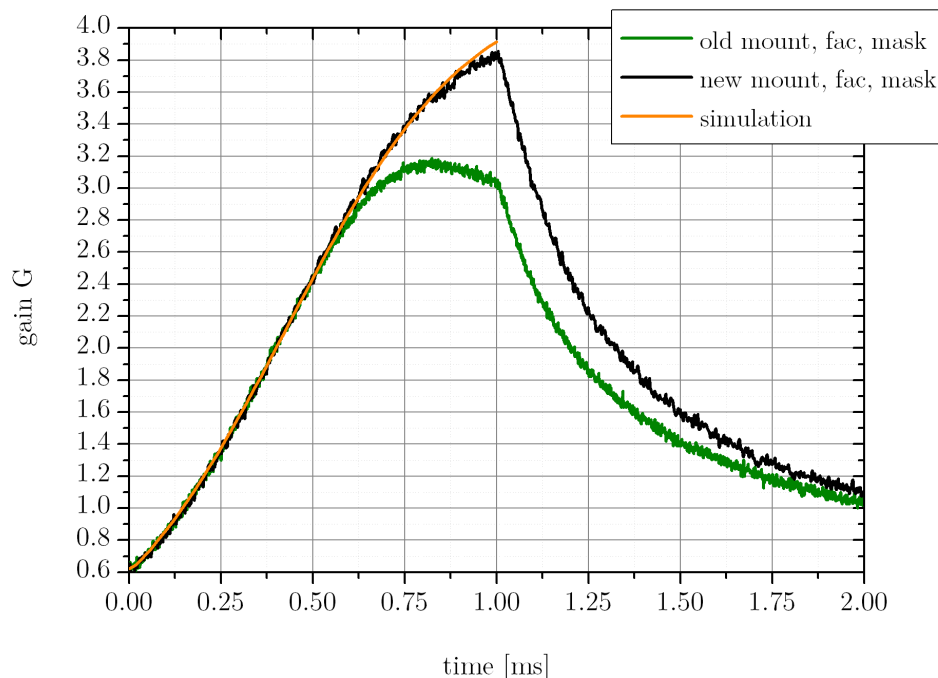


**Figure 3.31.:** Impact of the new mount and comparison to the simulation results

### 3.7. Conclusion

Amplified spontaneous emission is a fundamental limit to be very seriously analyzed, when considering laser gain media scaling. It grows exponential with the factor  $g_0 L$ ,  $g_0$  being the small-signal-gain and  $L$  a characteristic dimension of the gain medium. It will dominate other scaling parameters if this value is not kept constant or at least below a certain limit. Those limits are set by the gain depletion due to ASE or due to parasitic oscillations.

For the depopulation by ASE Equation 3.2.12 is fundamental. It is most useful when rewritten in the form of Equation 3.2.15 – 3.2.17. In the estimation of a constant small-signal gain distribution several estimations can be made.

If the ASE flux  $F_{ASE}$  reaches the saturation fluence  $F_{sat}$  in a four level system approximation, the expression

$$\frac{F_{ASE}}{F_{sat}} = \frac{g_0}{4\pi} \int_V \frac{1}{|\rho(r, r_0)|^2} \cdot \exp\{g_0 \rho(r, r_0)\} dV \quad (3.7.1)$$

was derived in the three dimensional case with  $g_0 = \sigma_e \hat{n}$ ,  $F_{sat} = h\nu/\sigma_e$  and  $\Phi_{ASE} \tau_f h\nu = F_{ASE}$ . Furthermore, we estimated the absence of saturation, which is, of course, a very strong approximation as the saturation fluence is reached. Nonetheless, such an expression gives a first order approximation, from which a critical volume can be derived:

$$V_{cr} \propto \kappa g_0^{-3} \quad (3.7.2)$$

where  $\kappa$  is a geometry dependent factor. A small collection of computed values for the available  $g_0 L$  and the factor  $\kappa$  is found in Table 3.3. Geometries with a high aspect ratio are profitable for energy storage ( $\kappa$  in the order of 2). The gain along the extraction direction is low (transverse  $g_0 L$  is 2–3, but along extraction direction it is 0.1–0.2). Low aspect ratios (rods etc.) show potentially a higher gain accompanied by a factor of  $\sim 2$  lower energy storage. This discussion is only true for reasonable aspect ratios, i.e. between 0.1 and 10. As the ASE flux is somehow overestimated, an approximate value for the ASE limit should be situated somewhere in the order of 2 to 4 for discs and larger values in the case of rods.

As one can imagine out of the values for the factor  $g_0 L$  in Table 3.3, extreme values can not be achieved even if the ASE would allow it. The amplification would generate an energetic gain of  $G \approx \exp(g_0 L)$  and  $g_0 L = 4$  it would require a reflectivity of less than 1.8 % preventing a potential parasitic lasing. This value can be reached by the use of index-matching. Nonetheless values above  $g_0 L > 4$  are not manageable at all

Geometry	Height H to Radius R	Aspect Ratio	$g_0L$	$\kappa$	typical length L
cylinder	H=2R	1	1.2	1.43	cylinder diameter
disc	H=R/10	5	2.3	1.91	disc diameter
disc	H=R/20	10	3	2.20	disc diameter
rod	H=10R	0.2	4.2	1.14	rod length
rod	H=20R	0.1	7	1.37	rod length

**Table 3.3.:** Values for  $g_0L$  and  $\kappa$  for different aspect ratios

without the aid of an absorbing cladding. For rods this is not an option, as it would introduce an absorbing element along the extraction direction.

Parasitic oscillations and lasing can be avoided by the proper analysis of the gain medium geometry:

- closed lossless paths, i.e. paths under TIR, must be avoided
- use of a material with an index of refraction close to the surrounding medium

A gain medium with an aspect ratio  $AR_L$  showing less reflections under TIR is profitable. Gain media with a high aspect ratio can be more sensitive to parasitic lasing.

The gain medium mount plays an important role too. Direct back reflection of ASE must be avoided. The use of materials with a low reflectivity for the ASE wavelength is advised.

One point of discussion was somewhat excluded: The transport of ASE from one amplifying medium to the next. This problem is observed in a simple approximation within Section 3.2. It depends on the gain medium structure and its geometry, but also on the overall extraction architecture. Spatial filtering should be used to minimize the resulting ASE flux. Cross-talk between several amplifying passes can be avoided by the proper extraction scheme.

ASE can not be avoided – however, parasitic oscillations can. ASE can only be minimized.

# 4. Thermal Management

## 4.1. Motivation

As already stated, understanding thermal mechanisms occurring within an amplifying medium is of key importance for every system based on high repetition rate. Several thermally induced effects can alter or degrade the laser system performance significantly. Consequences span from losses due to beam quality degradation, damages to the optical components to the destruction of the gain medium itself.

We will discuss the thermal management in the context of the Lucia laser system in this section. Section 4.2 will present the heat source, the role of the thermal conductivity in the heat transport and give a first estimation of the temperature distribution expected in the Lucia main amplifier case.

Then Section 4.3 will demonstrate the capacity of the developed laser head cooling approach to perform a satisfying thermal management.

Section 4.4 and 4.5 will close this chapter by describing an evaluation of our numerical model and an extensive experimental campaign aiming at qualifying the Lucia laser head in terms of wavefront management and the impact on depolarization.

## 4.2. Introduction

Overall, the thermal processes can be described as the following three steps sequence:

- heat generation
- heat transport
- induced effects (phase, polarization, . . . )

This section will thereby describe these steps in the following three subsections.

### 4.2.1. Heat generation

The heat generation is proportional to the amount of absorbed radiation. The absorbed photons at pump wavelength  $\lambda_P$  define a pump efficiency  $\eta_P$  associated with the amount of radiation available at the upper laser state. In the ideal case

this parameter is close to unity and depends on the energy level system and its corresponding branching ratio. With a finite lifetime of the upper laser state, fluorescence at the central wavelength  $\lambda_F$  or stimulated emission (i.e. extraction) at the extraction wavelength  $\lambda_L$  reduces the population inversion. The fraction of energy actually extracted through stimulated emission is given by the factor  $\eta_L$ . For fluorescence, a radiative efficiency  $\eta_R$  is introduced (related to separate losses).

Considering these three efficiencies, we write the fraction of the absorbed energy transformed into heat,  $\eta_h$ , as [59]:

$$\eta_h = 1 - \eta_P \left[ (1 - \eta_L) \eta_R \left( \frac{\lambda_P}{\lambda_F} \right) + \eta_L \left( \frac{\lambda_P}{\lambda_L} \right) \right]. \quad (4.2.1)$$

A very special case occurs when the efficiency is limited by the quantum defect  $\eta_{QD}$  ( $\eta_P = \eta_L = \eta_R = 1$ ):

$$\eta_{QD} = 1 - \frac{\lambda_P}{\lambda_L}. \quad (4.2.2)$$

Another definition is the amount of heat generated for each Watt of laser output [122]:

$$\eta_{h,LO} = \frac{\eta_h}{1 - \eta_h} \quad (4.2.3)$$

In the case of  $\text{Yb}^{3+}\text{:YAG}$  ( $\lambda_P = 0.94 \mu\text{m}$ ,  $\lambda_F \approx \lambda_L = 1.03 \mu\text{m}$ ) and in the quantum defect limited case,  $\eta_{QD} = 8.7\%$  of the absorbed power is transformed into heat while 96 mW (according to Equation 4.2.3) must be dissipated at the cold reservoir for each single Watt of laser output. In the case of  $\text{Ti:Sa}$  ( $\lambda_P = 0.532 \mu\text{m}$ ,  $\lambda_L = 0.8 \mu\text{m}$ ) 33.5 % of the absorbed energy is transformed into heat and for each W output power 500 mW are dissipated.

The quantum defect limited operation is interesting as it gives the ultimate limit in terms of laser efficiency for a given laser material. However the material properties are strongly altered if impurities and other effects are involved. As rare earth ions can experience energy exchange, an impact on the heat generation will occur. Other defects, like  $\text{OH}^-$ , color centers etc., open new decay channels as well [123]. With increasing Yb doping a stronger impact of the impurities and defects is found.

Let us now introduce the quantum efficiency  $\eta_Q$  defined as the product of pump and radiative efficiency:

$$\eta_Q = \eta_P \eta_R \quad (4.2.4)$$

Values for  $\eta_Q$  for  $\text{Yb}^{3+}\text{:YAG}$  are found experimentally to be 90 – 95% [124, 59]. Considering a value of  $\eta_Q = 0.93$  when no lasing occurs ( $\eta_L = 1$  in Equation 4.2.1) leads to  $\eta_h = 15.1\%$ , i.e. twice more heat generation than in an ideal quantum defect limited case, where  $\eta_{QD} = 8.7\%$ .

The volumetric heat production  $\dot{q}$  is consequently

$$\dot{q} = \frac{P_{abs}\eta_h}{V} \quad (4.2.5)$$

where  $P_{abs}$  is the absorbed incident pump power.

### 4.2.2. Thermal conductivity

In crystalline solid state materials phonons (lattice vibrations) are responsible for the heat transport. A perfect, infinite crystal would exhibit an infinite thermal conductivity if phonon–phonon interaction is omitted. However, such a perfect crystalline structure doesn't exist. The lattice vibrations propagate through the system and interact with each other, impurities and other defects. Those interactions lead to a loss of energy before the phonons strike the outer boundary. P. Debye (1884–1966) interpreted the phonons as vibrations in a solid box and in reference to the theory of gases the expression of the thermal conductivity  $k$  [ $\text{W m}^{-1} \text{K}^{-1}$ ]

$$k = \frac{1}{3} c_P \nu \lambda \quad (4.2.6)$$

is derived, where  $c_P$  is the heat capacity,  $\nu$  the velocity of the phonons and  $\lambda$  the mean free path. For very low temperatures, where the mean free path is mainly restricted by the sample size (or the grain size), the thermal conductivity will grow proportionally to  $\sim T^3$  since the heat capacity in the model derived by Debye (or the model derived by Einstein) carries the corresponding behavior.

To satisfy the collision theory, a phonon energy in the order of  $1/2k_B\Theta_D$  is necessary, where  $k_B$  is Boltzmann's constant and  $\Theta_D$  the Debye temperature<sup>1</sup>. For YAG values of  $\Theta_D$  varies between 505 K and 750 K [125]. Increasing the temperature leads to an exponential growth in Umklapp processes [126], decreasing the thermal conductivity.

For ambient temperatures a qualitative model determining the thermal conductivity was derived by Gaumé [127]. The thermal conductivity  $k$  is expressed as:

$$k = \frac{1}{T} \frac{A}{\gamma^2 \epsilon^3} T_{mp}^{3/2} \rho^{2/3} M^{1/3} n^{-1/3} \mu^{-2/3} \quad (4.2.7)$$

where  $T$  is the temperature,  $A$  a numerical constant,  $\gamma$  a parameter measuring the deviation to a pure harmonic behavior of chemical bonds,  $\epsilon$  the increase of the interatomic distance due to the nature of the chemical bond,  $T_{mp}$  the melting point temperature,  $\rho$  the material density,  $M$  the molar mass,  $n$  the number of atoms per formula unit and  $\mu$  the reduced mass.

---

<sup>1</sup>The Debye temperature is the corresponding reduced temperature at the Debye cut-off energy.

This expression reveals that  $k$  depends, besides the temperature, on the composition of the laser material, too. Figure 4.1 shows the thermal conductivity of YAG as a function of the grain size (ceramics) and the temperature. As comparison, a single crystal is used which is in the order of mm in size. The grain size varies between 3 and 7.5  $\mu\text{m}$  in average and shows a reduction for  $k$  in the order of a factor 10.

Figure 4.2 illustrates the impact of the doping concentration on the thermal conductivity as a function of the temperature. A maximum value for  $k$  is found around 20 K and varies by a factor of 6 if the doping concentration is increased from 1 at.% to 20 at.%.

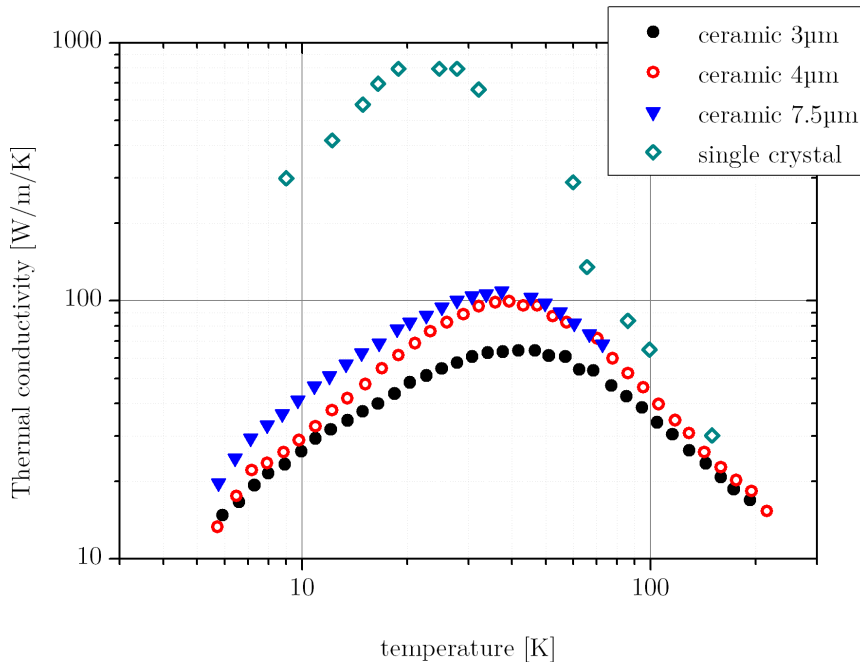


**Figure 4.1.:** Thermal conductivity of YAG as a function of grain size and temperature, after [128].

The thermal conductivity is strongly affected by the amount of defects in the crystal lattice. Consequently, changing the doping concentration affects the thermal conductivity, too. The variation of the thermal conductivity depends on the mass difference between the substituted ions. Figure 4.3 shows the variation of the thermal conductivity of  $\text{Yb}^{3+}\text{:YAG}$  at room temperature.

The value of  $k$  varies strongly with the doping concentration and shows a minimum around 30 at.%. Substituting even more  $\text{Yb}^{3+}$  for  $\text{Y}^{3+}$  will ultimately lead to

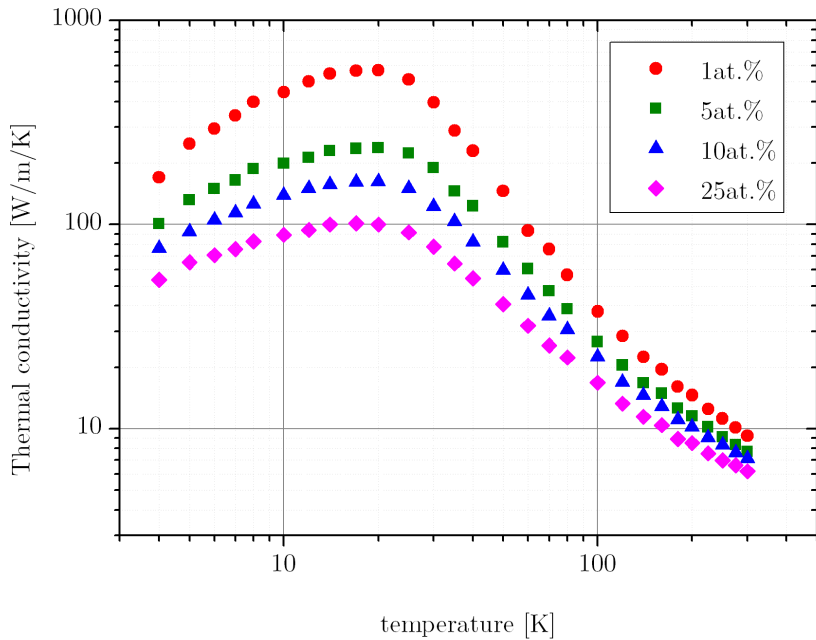


**Figure 4.2.:** Thermal conductivity of  $\text{Yb}^{3+}\text{:YAG}$  as a function of doping and temperature [129].

$\text{Yb}^{3+}\text{AG}$  instead of  $\text{Yb}^{3+} : \text{YAG}$ . By this the thermal conductivity starts rising again.

Table 4.1 displays ionic radii and molar masses of selected rare earths and as comparison, Yttrium. It shows for the case of  $\text{Yb}^{3+}\text{:YAG}$ , that the ionic radius of  $\text{Yb}^{3+}$  is smaller than  $\text{Y}^{3+}$ , but the mass significantly higher. A strong dependency of the thermal conductivity on the doping level is therefore expected. An interesting combination is a material showing for both, host and substitution, an equal ionic radius and molar mass. As an example one can mention a relatively new laser materials like  $\text{Yb}^{3+}$  doped LuAG [130].

Element	$\text{Y}^{3+}$	$\text{Yb}^{3+}$	$\text{Er}^{3+}$	$\text{Tm}^{3+}$	$\text{Lu}^{3+}$	$\text{Nd}^{3+}$	$\text{Ho}^{3+}$	Ref.
Ionic radius [pm]	90	86.8	89	88	86.1	98.3	90.1	[131]
Molar mass [ $\text{g mol}^{-1}$ ]	88.9	173	167.3	168.9	175	144.2	164.9	[132]

**Table 4.1.:** Ionic radius and molar mass of trivalent rare earths and Yttrium

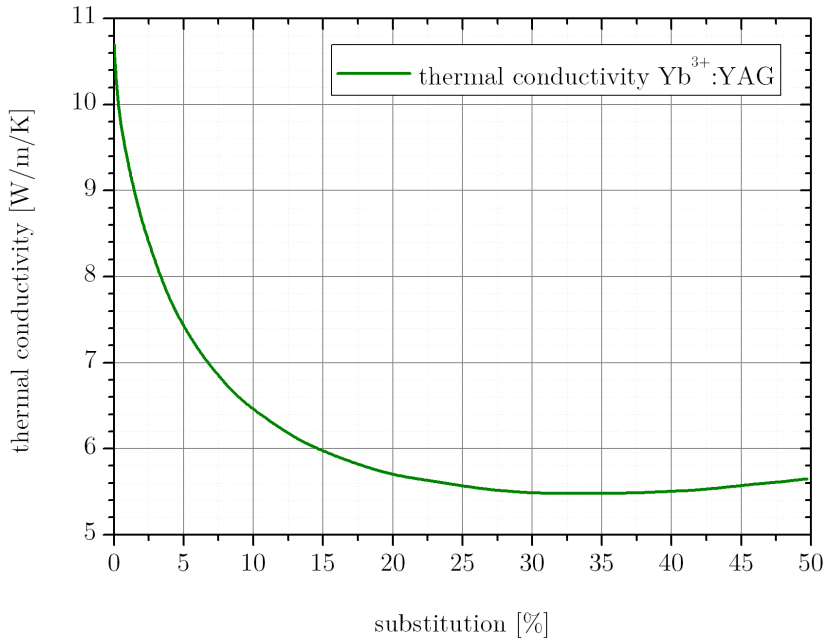


**Figure 4.3.:** Variation of the thermal conductivity of  $\text{Yb}^{3+}\text{:YAG}$  as a function of substitution, after [127]

### 4.2.3. Heat transport

The temperature distribution within a medium satisfies a parabolic partial differential equation of the Fourier type:

$$\nabla(\underline{k} \cdot \nabla T) + \dot{q} = \rho c_P \frac{\partial T}{\partial t} \quad (4.2.8)$$

with  $\underline{k}$  the thermal conductivity tensor,  $T$  the temperature field,  $\dot{q}$  the volumetric heat production,  $\rho$  the density and  $c$  the heat capacity.

In an isotropic medium becomes the thermal conductivity tensor a scalar value and Equation 4.2.8 simplifies to:

$$k \Delta T + \dot{q} = \rho c_P \frac{\partial T}{\partial t} \quad (4.2.9)$$

where  $\Delta$  is the Laplace operator. In general  $\rho$ ,  $c_P$  and  $k$  are functions of the temperature.

The solution of this partial differential equation depends on the gain medium geometry. Figure 4.4 shows the two simplified schemes for cooling a gain medium. In the case of a rod, cooling is typically applied perpendicularly to the pump and extraction direction. For top-hat pump profile in the case of a static solution with

a uniform heat generation in an infinite rod, a parabolic shape can be found in the form of [10] (polar coordinate system):

$$T(r) = T(r_0) + \left( \frac{\dot{q}}{4k} \right) (r_0^2 - r^2) \quad (4.2.10)$$

Within the context of the Lucia laser system, a thin disc approximation is more suitable. If the extension of the disc is large compared to its thickness, a one-dimensional estimation in the direction of the pump and extraction direction is valid.

Again, the volumetric heat production is taken uniform in first order approximation,  $\dot{q}(z) = const..$  The Boundary Conditions (BC) applied are that on one side an isolation is present and on the other side a boundary condition of the third kind is applied [133]. Such BC implies that the heat transported through the surface (along the surface normal) is proportional to the heat transfer coefficient  $h$  [ $\text{W m}^{-2} \text{K}^{-1}$ ] and the difference between the surface temperature  $T_S$  and the coolant temperature  $T_\infty$ . Consequently we get in the 1D case:

$$\left. \frac{\partial T}{\partial z} \right|_S = \frac{h}{k} (T_S - T_\infty) \quad (4.2.11)$$

where  $S$  stands for the position on the surface.

Solving Equation 4.2.9 for a gain medium of the thickness  $D$  with the following BCs:

$$\left. \frac{\partial T}{\partial z} \right|_{z=0} = 0 \quad (4.2.12)$$

$$\left. \frac{\partial T}{\partial z} \right|_{z=D} = \frac{h}{k} (T(D) - T_\infty) \quad (4.2.13)$$

leads to:

$$T(z) = \frac{\dot{q}}{2k} (D^2 - z^2) + \frac{1}{h} \dot{q} D + T_\infty \quad (4.2.14)$$

This reveals that the temperature is defined by three contributions. The first is, for a given  $\dot{q}$ , quadratic with the position within the medium and doesn't depend on the heat exchange on the surface. The second part is a constant throughout the medium and can be reduced with a stronger cooling effort ( $\sim 1/h$ ). Finally the strongest impact is the offset temperature defined by the coolant itself. The coolant temperature is usually limited by the dew point of moisture on cooled surfaces or phase change of the coolant.

Considering the Lucia laser system, the surface of the active medium is pumped at  $\approx 16 \text{ kW cm}^{-2}$  for 1 ms at 2 Hz. With a thickness of the active medium of  $D = 7 \text{ mm}$  and approximately  $\eta_h = 0.1$ , the heat volumetric heat production is  $\dot{q} \approx 4.6 \times 10^6 \text{ W m}^{-3}$ . The first term of Equation 4.2.14 yields  $\approx 16 \text{ K}$ , whereas the second gives  $\approx 2 \text{ K}$  for a heat exchange coefficient of  $h \approx 15.000 \text{ W m}^{-2} \text{ K}^{-1}$  and a heat conductivity of  $k \approx 7 \text{ W m}^{-1} \text{ K}^{-1}$ .

The Biot-number  $Bi$  of this arrangement is  $Bi = hD/k \approx 15$ . This indicates, that there is a strong variation in temperature between both surfaces. Selecting a thinner gain medium implies a higher doping ratio, as the energy storage and gain should be maintained. However, a higher doping results in a lower thermal conductivity and can lead to parasitic oscillations. If the cooling would be applied from both surfaces, the Biot number can be reduced by a factor of 2. This is limited by design choices.

Equation 4.2.14 gives a good first order approximation in the static case. For a transient analysis a numerical estimation is necessary. Such a code solves Equation 4.2.8 in one dimension using the implicit Finite Differential (FD) method. An introduction to FD can be found in e.g. [133].

As an application example, the characteristics of the main laser head is used in Figure 4.5. The coolant temperature is set to 286.15 K which is a typical temperature

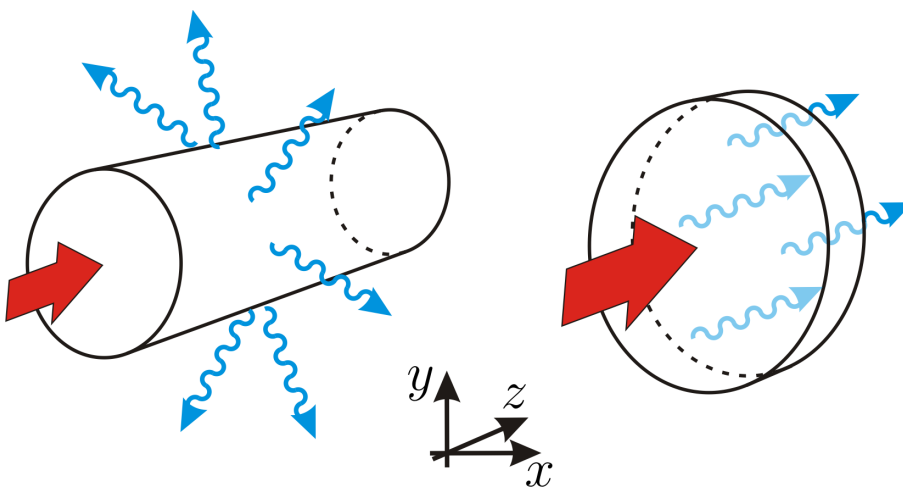
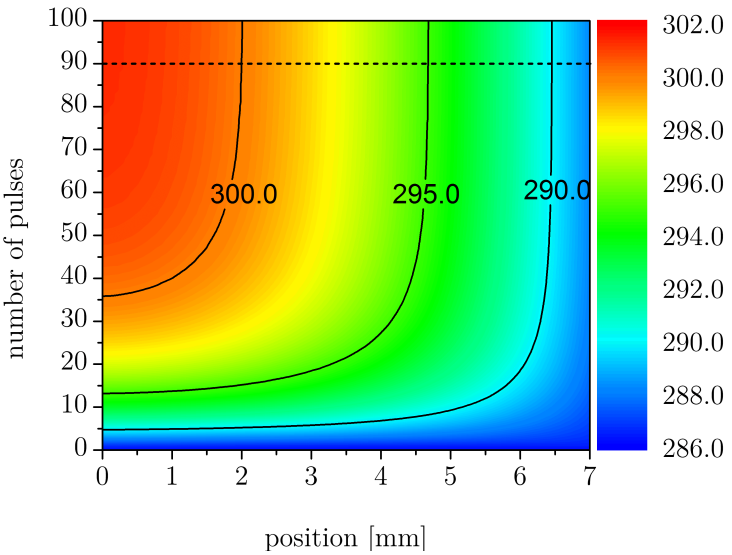
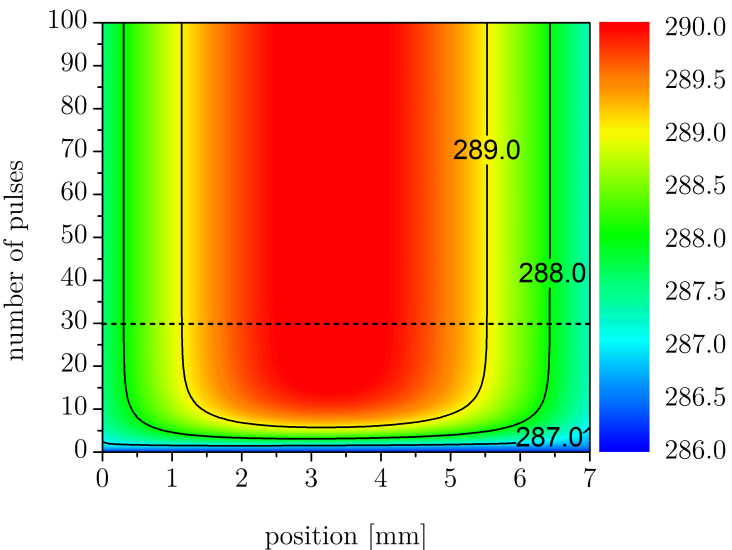


**Figure 4.4.:** Cooling scheme for a rod and for a disc. The pump pulse direction is indicated by a red arrow and the cooling is realized over the largest surfaces (indicated by blue curly arrows). In the case of a rod (left) cooling is applied on the surface perpendicular to the pump direction (z). In the case of a (thin) disc (right) the heat extraction is realized in the pump direction (in z direction along the z-axis).



(a) Heating for an 1D example, 2 at.%, 7 mm thickness,  $16 \text{ kW cm}^{-2}$ , one side isolated and one side  $h = 15.000 \text{ W m}^{-2} \text{ K}^{-1}$ , initial and coolant temperature 286.15 K



(b) Heating for an 1D example, 2 at.%, 7 mm thickness,  $16 \text{ kW cm}^{-2}$ , from both sides cooled with  $h = 15.000 \text{ W m}^{-2} \text{ K}^{-1}$ , initial and coolant temperature 286.15 K

**Figure 4.5.:** The temperature (colorbar) gradient across a 7 mm thick Yb<sup>3+</sup>:YAG crystal doped with 2 at.% is shown for a single sided cooling (a) and for a cooling applied on both sides (b). The gain medium is pumped from the left side with  $16 \text{ kW cm}^{-2}$  with 1 ms long pulses at 2 Hz. The fraction of energy converted into heat  $\eta_h$  is taken to be 10 %. The dashed lines show the pulse numbers required to reach a stationary temperature distribution.

for the laboratory setup. An aggressive cooling with a heat exchange coefficient  $h = 15.000 \text{ W m}^{-2} \text{ K}^{-1}$  is applied to the opposite side of the pump entrance (i.e. at the position at 7 mm), as shown in Figure 4.5(a), or to both sides (Figure 4.5(b)). The estimation uses a one dimensional code calculating the absorbed pump light distribution and the heat propagation within the laser gain medium during and between the pump pulses.

As an example 100 pump pulses were launched which corresponds to 50 s of operation. The simplified model derived in the previous paragraphs estimates the surface temperature to be  $\approx 304 \text{ K}$  for a completely absorbed pump pulse. However such complete absorption does not occur for the experimental case under consideration. The total pump absorption is approximately 90 %, reducing the surface temperature estimation to  $\approx 302 \text{ K}$ . If there would be any possibility to apply on both surfaces such an aggressive cooling, a reduction of 4 in peak temperature rise is achieved, as the effective thickness is reduced to its half. Figure 4.5(b) depicts this situation. The slight off-center position is given by the non-uniform heat generation due to absorption of the laser pump light coming in from the left (position 0).

#### 4.2.4. Radial temperature distribution

Up to this point we expected the lateral extend to be large compared to the thickness of the heated medium. Especially we assumed that the whole surface is pumped and consequently the system could be reduced to a one-dimensional geometry.

Let us now assume a partially pumped surface. The thin-disk theory for face-cooled rods described in [134] gives the temperature distribution in the case of a cylindrical geometry. In a cylindrical coordinate system (see Figure 4.6) Equation 4.2.8 (static problem, isotropic thermal conductivity) becomes:

$$\frac{1}{r'} \frac{\partial}{\partial r'} \left( r' \frac{\partial T'}{\partial r'} \right) + \frac{1}{4} \left( \frac{1}{D'} \right)^2 \frac{\partial^2 T'}{\partial z'^2} = \begin{cases} -\frac{4(\alpha D)e^{-\alpha Dz'}}{a'^2(1-e^{-\alpha D})}, & \text{if } r' \leq a' \\ 0, & \text{if } r' > a' \end{cases} \quad (4.2.15)$$

where the dimensionless variables are  $r' = r/b$ ,  $z' = z/D$ ,  $a' = a/b$ ,  $D' = D/2b$  and  $T' = (T - T_\infty)/(\dot{q}/(4\pi kD))$ . The sketch of the variables used is found in Figure 4.6. This problem can be solved in terms of a Fourier-Bessel series expansion for a face-cooled thin disc. Integrating along the z-axis gives the mean longitudinal temperature  $\langle T' \rangle$ , which is now only a function of the radial position  $r$ :

$$\langle T' \rangle = C_0 + \sum_{n=1}^{\infty} C_n J_0(\beta_n r) \quad (4.2.16)$$

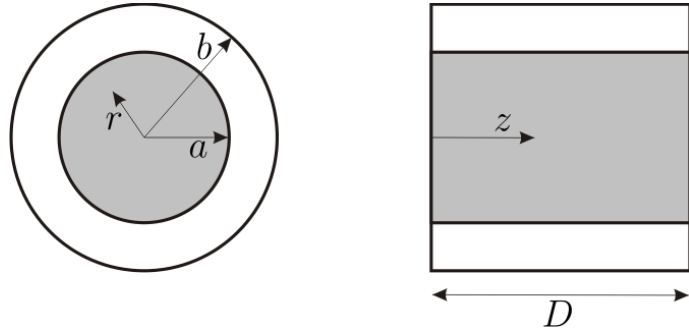


**Figure 4.6.:** Definitions for the variables used for the radial temperature distribution estimation. The thickness of the cylinder is  $D$ , the radius  $b$ , the pumped radius  $a$  and the radial position  $r$ .

where the  $\beta_n$  are the roots of  $J_1(\beta_n) = 0$ ,  $n = 1, 2, \dots, \infty$  and the coefficients  $C_n$

$$C_0 = \frac{F_0 a'^2}{(\alpha D)^2} \left( \frac{e^{-\alpha D} - 1}{\alpha D} + e^{-\alpha D} + \frac{\alpha D}{2} \right) \quad (4.2.17)$$

$$C_n = \frac{F_n}{(\chi)^2 - (\alpha D)^2} \left\{ \frac{1 - e^{-\alpha D}}{\alpha D} - \frac{e^{-\alpha D}}{\chi} \tanh(\chi) + \frac{\alpha D}{\chi^2} [\cosh(\chi) - \tanh(\chi) \sinh(\chi) - 1] \right\} \quad (4.2.18)$$

$$F_0 = 4 \frac{\alpha D}{1 - e^{-\alpha D}} (2D')^2 \quad (4.2.19)$$

$$F_n = F_0 \left[ \frac{2}{\beta_n a'} \frac{J_1(\beta_n a')}{J_0^2(\beta_n)} \right] \quad (4.2.20)$$

$$\chi = 2D' \beta_n \quad (4.2.21)$$

As an example, Equation 4.2.16 is solved for  $\alpha D = 1$ ,  $D' = 0.2$  and plotted for three different  $a'$  in Figure 4.7. The more the surface is covered by the pump, the more homogeneous is the radial temperature distribution. If the gain medium surface is only partially covered by the pump spot, a thermal lens becomes important.

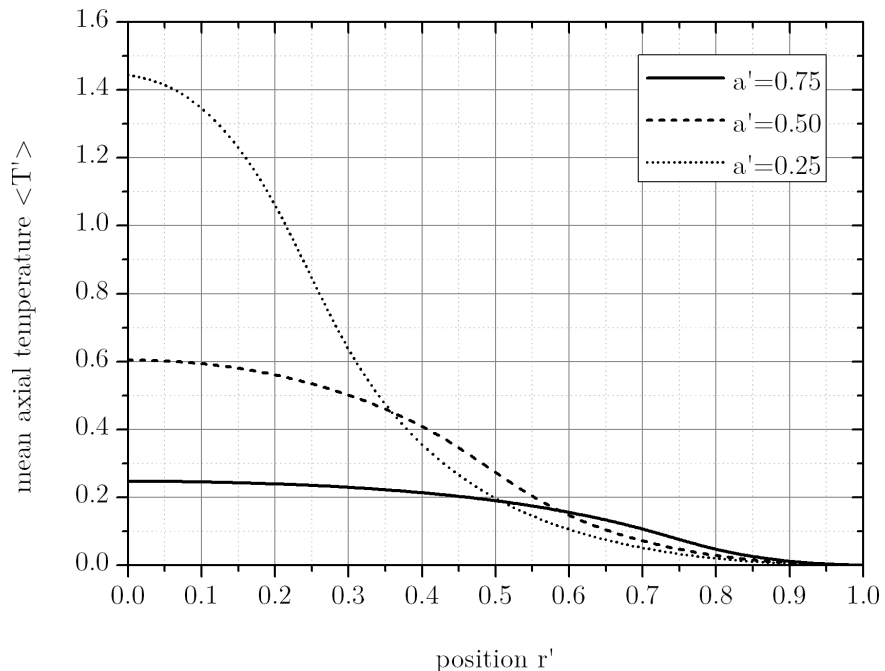


**Figure 4.7.:** The solution for Equation 4.2.16 for the dimensionless parameters  $\alpha D = 1$ ,  $D' = 0.2$ . In the case of an almost covered surface ( $a' = 0.75$ ), the temperature variation within the pumped area is low, while in the case  $a' = 0.25$  an important variation of the mean temperature distribution is found.

### 4.3. Estimation of the Lucia laser head cooling capacity

As it was discussed in the previous sections, an aggressive cooling might be necessary to gain access to a satisfying operation point with a high thermal load. In the case of the Lucia main laser amplifier, a heat exchange coefficient between  $h \approx 10.000 \text{ W m}^{-2} \text{ K}^{-1}$  and  $h \approx 20.000 \text{ W m}^{-2} \text{ K}^{-1}$  are desirable as cooling is only applied from one side of the laser gain medium. As discussed in Section 2.5.3, much higher values for  $h$  are not necessary as the heating will be dominated by the gain medium thickness  $D$  and the coolant temperature  $T_\infty$  only.

A single jet solution works well for the small-sized cooling effort in the order of up to 1 cm diameter. Achieving the same conditions would mean a quadratic scaling of the water flow, which becomes quickly not manageable anymore. An alternative is the use of a so-called jet–plate (JP). It uses an arrangement of several small jets to generate a highly turbulent regime on an extended surface.

Each hole will form its own jet and the ensemble will form a modulated flow profile close to the JP. Figure 4.8 depicts the basic operation principle of a JP.

An analytical distribution for the jet–wall interaction cannot be found, however several experimental models have been reviewed [135]. The basic parameters for the

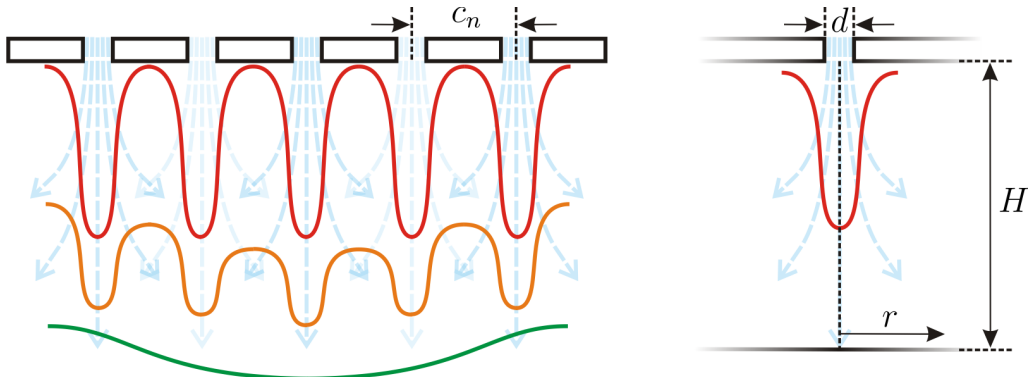


**Figure 4.8.:** The basic working principle of a JP. The water jets formed after passing a pierced plate form an overlay of several small highly turbulent jets. With increasing distance modulations will start to vanish until, for far distances, a uniform, low-turbulent flow profile is reached. An optimum working distance results from a compromise between the turbulent interaction with the surface and the requested uniformity of the flow. The distance between the jets is  $c_n$ , the jet hole diameter  $d$ , the distance to the test surface  $H$  and the radial distance from the center of a single jet  $r$ .

description are defined in Figure 4.8. According to Chang et. al. [136] the local Nusselt number ( $Nu$ ) for a single jet can be expressed in terms of the Reynolds number ( $Re$ ), the Prandtl number ( $Pr$ ), the distance between the JP and the surface  $H$  to be cooled, the jet hole diameter  $d$  and the radial coordinate starting from the center of the jet  $r$  as:

$$Nu(r) = 0.66 Re^{0.574} Pr^{0.4} \left( \frac{H}{d} \right)^{-0.106} \left[ 1 + 0.1147 \left( \frac{r}{d} \right)^{1.81} \right], \text{ for } r/d < 1.25 \quad (4.3.1)$$

$$Nu(r) = 0.7012 Re^{0.574} Pr^{0.4} \left( \frac{H}{d} \right)^{-0.106} \left( \frac{r}{d} \right)^{-0.62}, \text{ for } r/d > 1.25 \quad (4.3.2)$$

The connection between  $Nu$  and heat exchange coefficient  $h$  is  $Nu = hL_{typ}/k$  whereas  $k$  is the heat conductivity of the coolant and  $L_{typ}$  is a typical length. The Reynolds number can be expressed as  $Re = vd/\nu$  where  $v$  is the coolant velocity and  $\nu$  the viscosity of the coolant. An expression of the Prandtl number is found to be  $Pr = \nu/\alpha$  where  $\alpha$  is the thermal diffusivity of the coolant.

In the case of water jets, the Prandtl number at room temperature is  $Pr \approx 8.8$ . The JP developed for Lucia uses 39 holes  $d = 1.4$  mm in diameter and a water flow of  $\approx 14 \text{ L min}^{-1}$  which yields  $Re \approx 5,900$ .  $L_{typ}$  is, in the case of the JP,  $\approx 5$  mm. Plotting the resulting  $h$  as a function of the relative position  $r/d$  and the parameter  $H/d$  yields maximum heat exchange coefficients in the order of  $24.000 \text{ W m}^{-2} \text{ K}^{-1}$  up to  $32.000 \text{ W m}^{-2} \text{ K}^{-1}$  (Figure 4.9). It should be noted, that the jump at  $r/d = 1.25$  has no physical meaning and values around this specific value will be incorrect, since no behavior for the transition is given.

The central local minimum (at  $r/d = 0$ ) indicates a reduced water flow in the center of the impinging water jet. An incoming jet splits up into a radial distribution leaving a reduced velocity in the center (stagnation). For large distances, or a non-perpendicular impact, this behavior loses its physical meaning and a different model should be used.

In the case of a JP, the distance between the jets plays an important role, as it is found in experimental works e.g. [137, 138] and especially by Tawfek et. al. [139]. The average Nusselt number  $\overline{Nu}$  is found to be

$$\overline{Nu} = 0.453 Re^{0.691} Pr^{1/3} \left( \frac{H}{d} \right) \left( \frac{c_n}{d} \right)^{-0.38} \quad (4.3.3)$$

where  $c_n$  is the average distance between jets. One has to be aware, that this relation holds only true in the case of a sufficiently long distance between the JP and the test surface  $3 < H/d < 8$ , a Reynolds number between 3,400 and 20,000

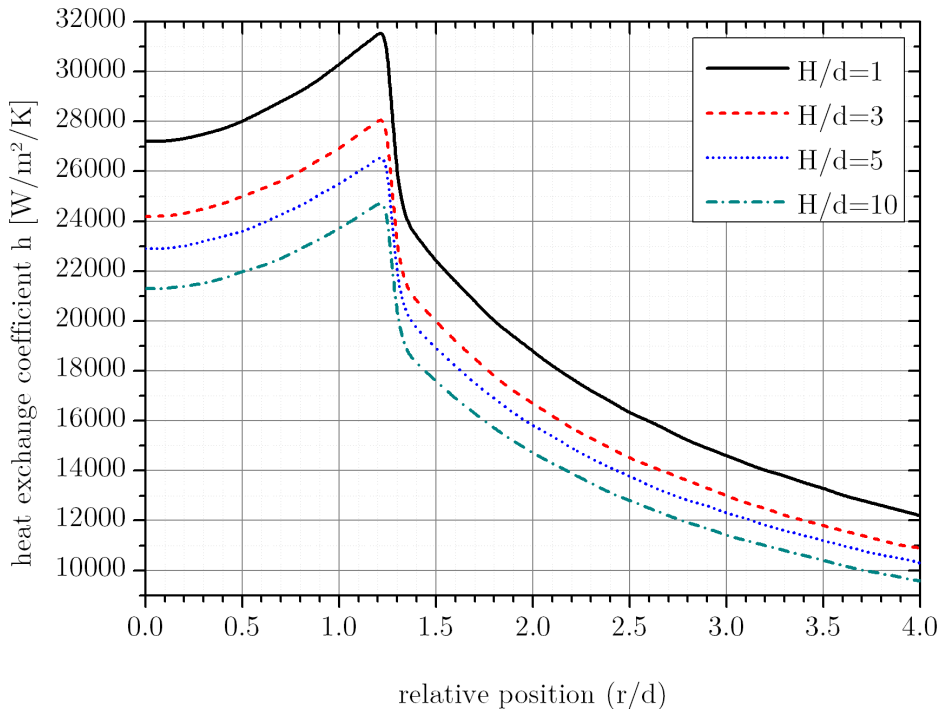


**Figure 4.9.:** Estimation of the heat exchange coefficient for one single jet. The characteristics of the jet corresponds to one of the jets on the JP used for the Lucia main laser head. A typical dimensionless distance between the exit of the jet and the surface  $H/d$  is between 3 and 5. The dimensionless position  $r/d$  has its maximum at  $r/d = 1.25$  with values varying between  $24.000 \text{ W m}^{-2} \text{ K}^{-1}$  and  $32.000 \text{ W m}^{-2} \text{ K}^{-1}$ .

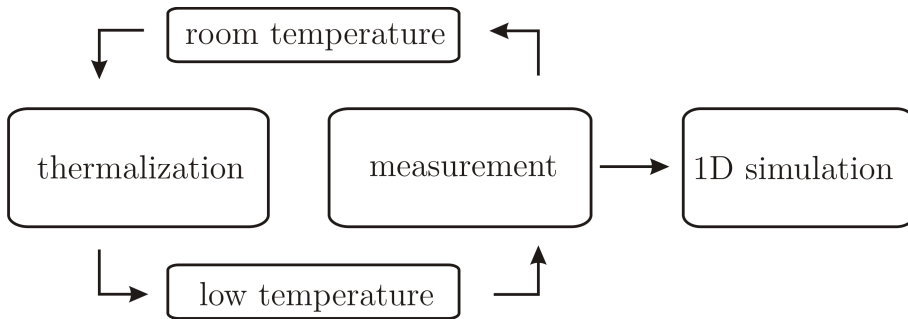


**Figure 4.10.:** Scheme of measuring the heat exchange coefficient of the Lucia laser head. The thermalized laser head is abruptly brought in contact with cold water flowing through the JP setup under the operational conditions. The temperature of the water and the surface temperature of the gain medium are measured simultaneously. the setup is brought back to room temperature and the measurement starts again for the same or a different distance of the JP to the test surface. The data of the surface temperature is compared to the result of a 1D simulation using the incoming water temperature as reference. An estimation for  $h$  is found, when the deviation between measurement and simulation is minimized.

and  $4 < c_n < 8$ . Our experimental parameters fit these requirements partially with  $c_n = 5.5$ ,  $Re \approx 5,900$  and  $0.4 < H/d < 8.2$ . Consequently for short experimental distances between JP and surface, the domain of validity of this relation will not be satisfied.

Figure 4.10 describes the experimental measurement scheme used to estimate of the heat exchange coefficient  $h$ . At first the laser head, holding a test plate, is at room temperature (the coolant as well). Using a three-way valve, the water circulation loop is abruptly changed to water coming out of a cold reservoir. The temperature of the cold water arriving at the back side of the test plate is measured using a fast external thermocouple (Type K probe 304SS, Omega Newport). The temperature evolution at the center of the isolated side (in contact to air) of the test plate is simultaneously measured using a fast response, self-adhesive thermocouple (SA1XL-KI-SRTC, Omega Newport). The test plate is maintained in its mount using silicone. Finally the temperature of the whole system is heated back to room temperature. Figure 4.11 shows a sketch of the experimental setup. This sequence is repeated several times for each  $H$ .

The result of each measurement sequence is then simulated using the data collected from the internal thermocouple (measuring the water temperature) with the 1D heat transport code, which was used in the previous section. Adjusting the

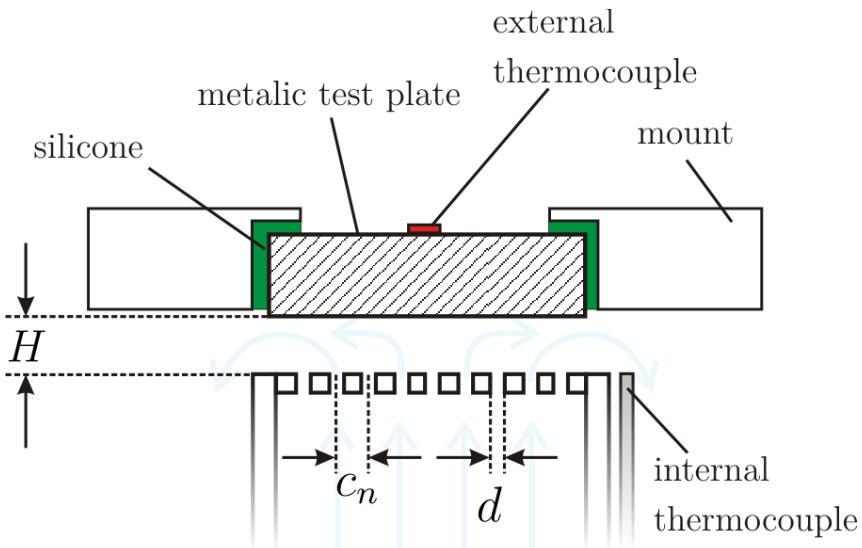


**Figure 4.11.:** Schematic view of the experimental setup used for the estimation of  $h$ . The surface temperature evolution of a metallic test plate is recorded as a function of the distance  $H$ . The temperature of the cooling liquid is measured using an internal thermocouple.

heat exchange coefficient within the simulation, a minimum deviation between the measurement and the simulation is found, which gives an estimate for the heat exchange coefficient for a given  $H$ . For each measured  $H$  the evaluated value for  $h$  is displayed in Figure 4.12.

The maximum value for the heat exchange coefficient is found at a distance near  $H = 3.5$  mm with a value of  $(16,500 \pm 1,000)$  W m $^{-2}$  K $^{-1}$ . As comparison the estimation out of the Tawfek model is shown in the graph too. For distances shorter than 3.5 mm, a decrease in  $h$  is experimentally observed. Cross flow between the neighboring jets becomes more important as it gets harder to evacuate the water flowing in with a reduced distance  $H$ . For large distances, the flow profile smooths out, but becomes less turbulent, thus for large distances  $z$ ,  $h$  drops significantly. In the following,  $h = 15,000$  W m $^{-2}$  K $^{-1}$  is used for simulations.

The impinging water jets generate a cross flow which might block water between the jets. Such an effect is visualized in Figure 4.13. Additional air is injected into the laser head and forms small bubbles within the circulating water. They gather in zones with a low velocity parallel to the surface, preferably in zones between the jets. This indicates somehow the water velocity pattern on the cooled side of the laser gain medium.

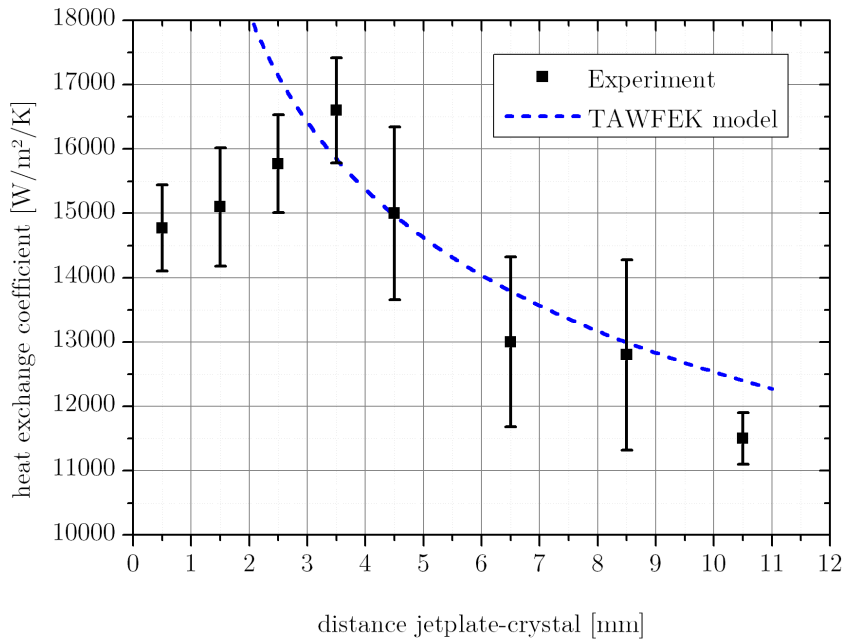


**Figure 4.12.:** Experimental result for the heat exchange coefficient of the jet–plate compared to the Tawfek relation (Equation 4.3.3). For close distances, the water flow is hindered and consequently the heat exchange coefficient lowered in average. An optimum position is found near 3.5 mm distance between the jet–plate and the cooled surface.

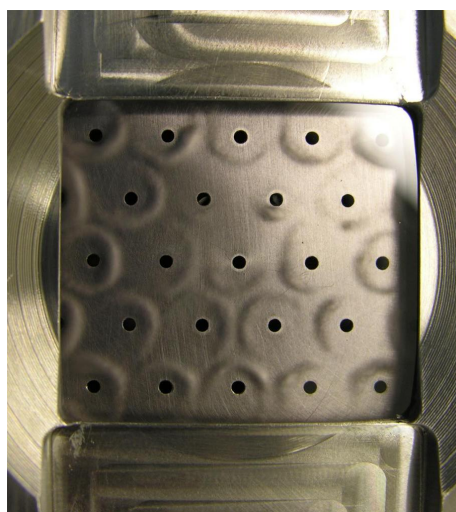


**Figure 4.13.:** Visualization of the cross flow introduced by neighboring water jets with the JP of the main laser head. Air is injected into the laser head and appears as small bubbles caught in the cross flow regions. As the arrangement is hexagonal, a similar pattern is found in the visualization. Under standard operation, no such turbulences are visible to the naked eye, as no air is within the laser head.

A question arises then: if the lateral cross flow of the water significantly impacts the heat exchange coefficient, will an important surface temperature variation be observed? To answer, we set up an experiment whose results are presented in Figure 4.14. An IR camera images the surface temperature distribution of a pumped rectangular Yb<sup>3+</sup>:YAG crystal of high doping concentration. A crystal with a doping level of 20 at.% and a thickness of 4.7 mm was used. The gain medium was pumped at up to 10 Hz with an intensity of only  $\approx 1.8 \text{ kW cm}^{-2}$ . The transverse temperature variation is in the order of  $\sim 0.2 \text{ K}$  and does not change with a variation of  $H$ .

Consequently the inhomogeneity of the JP flow will not seriously impact the laser head performance. It is sufficient for the following calculations to consider a spatially averaged  $h$ , which will be taken from now on to be  $h = 15.000 \text{ W m}^{-2} \text{ K}^{-1}$ .

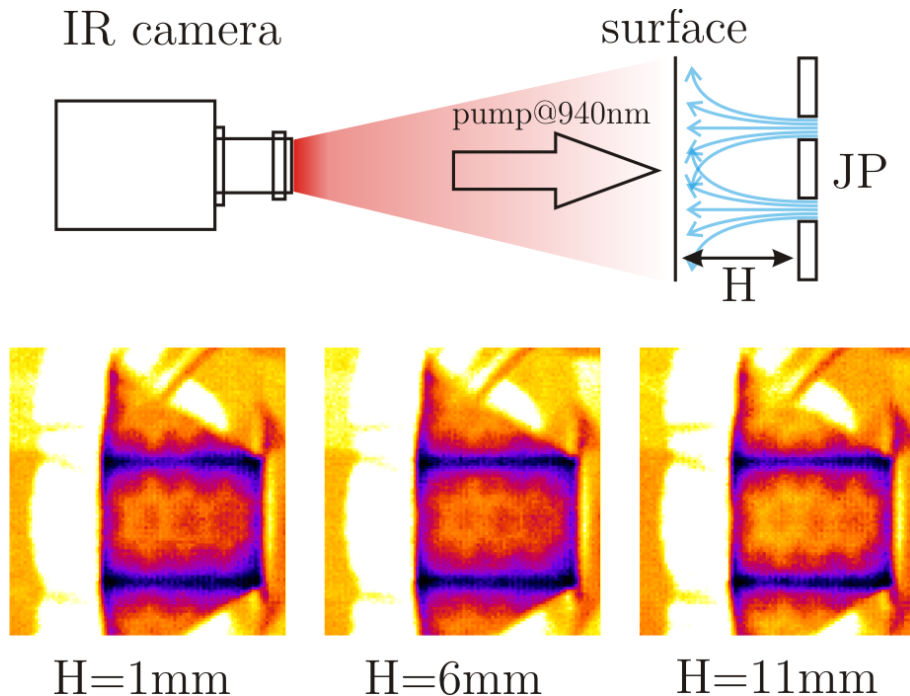


**Figure 4.14.:** Visualization of the surface temperature modulations introduced by the jet–plate for different distances jet–plate – cooled surface  $H$ . A highly doped (20 at.%) Yb<sup>3+</sup>:YAG crystal with a thickness of 4.7 mm thickness is mounted into the laser head and pumped at  $2 \text{ kW cm}^{-2}$  using the MPA. The surface temperature distribution is recorded with an IR camera at an angle of observation of  $25^\circ$  with respect to the surface normal. A variation of the distance  $H$  does not reveal any qualitative change. A hexagonal temperature variation is visible. It must be noted that the image color scale is adapted to augment the contrast, as the temperature variation is small.

## 4.4. Thermally induced wavefront deformation

While the last section was dedicated to the generation of heat, the resulting temperature distribution within the laser gain medium and consequently the use of a specific cooling technique for the active mirror case, we now discuss the impact of this temperature distribution on the opto-mechanical properties of the pumped laser gain medium.

A laser beam traveling through a pumped laser gain medium will experience unavoidable wavefront deformations. The deformation has three origins:

- deformations of the surfaces – mechanical lens effect
- bulk nonuniform temperature distribution – thermal lens effect
- nonuniform pump profile – “electronic” lens effect

The first effect is mechanically connected to the temperature, as a nonuniform temperature distribution leads to different elongations at different positions within the crystal – the medium is deformed and by this its surfaces. This leads, as we will see, to a “bi-metal” deformation in the case of thin disks and to a bulging of the surfaces.

The thermal lens effect can be split up into several contributions. At first, a temperature variation leads to a profile of the index of refraction. This impacts the phase of the transmitted laser beam. With the thermal expansion, stress and strain are applied to the material and changes consequently the optical indicatrix [140]. Polarization dependent effects, like bi-focusing, birefringence, etc. appear. A thorough discussion can be found in [141].

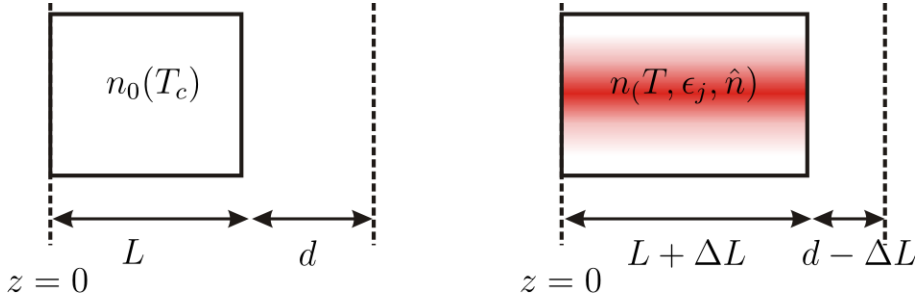
The third effect (electronic lens effect) is more subtle, as an excitation within the electronic level system changes the polarizability within the material [142, 143].

Figure 4.15 illustrates schematically the case of a gain medium in the not pumped and the pumped case. We consider a rod-like geometry with cylindrical coordinates  $r, \theta$  and a coordinate  $z$  along the (straight) propagation direction. The extend of the gain medium is  $L$  and the free space traveled  $d$ . For the optical path in the not pumped case one can write:

$$\delta^{off} = n_0(T_c)L + d \quad (4.4.1)$$

where  $T_c$  is the initial (cold) temperature. Being pumped (on), this changes to:

$$\delta_{r,\theta}^{on} = \int_0^{L+\Delta L} n_{r,\theta}(T, \epsilon_j, \hat{n}) dz + d - \Delta L(r). \quad (4.4.2)$$



**Figure 4.15.:** The thermal index variations of a pumped gain medium depends on the temperature  $T$ , the strain/stress  $\epsilon_j$  and the inversion  $\hat{n}$ , after [141].

where the index strain is  $\epsilon_j$ , the coordinates are  $r, \theta, z$  and  $\Delta L(r)$  corresponds to the (mechanical) deformation of the material. Expanding this equation into a Taylor series and neglecting terms higher than the first order, yields for a pump light distribution depending only on  $r$  and  $z$ :

$$\delta_{r,\theta}^{on} = \int_0^{L+\Delta L} \left[ n_0(T_c) + \left( \frac{\partial n_{r,\theta}}{\partial T} \right) (T(r,z) - T_c) + \sum_{j=r,\theta,z} \left( \frac{\partial n_{r,\theta}}{\partial \epsilon_j} \right) \epsilon_j(r,z) + \left( \frac{\partial n_{r,\theta}}{\partial \hat{n}} \right) \hat{n}(r,z) \right] dz + d - \Delta L(r). \quad (4.4.3)$$

where we estimated the electronic lens effect to be independent from temperature and strain. It should be noted, that  $\hat{n}$  corresponds to the excitation of the upper laser state.

Equation 4.4.3 is discussed partially in [141]. Let us estimate the order of magnitude for the electronic lens. For the sake of simplicity, all effects are taken to be isotropic. The corresponding change in the refractive index due to a temperature change  $\Delta T$  (at constant strain) is thus:

$$\Delta n_T = \frac{\partial n}{\partial T} \Delta T \quad (4.4.4)$$

The change in the refractive index due to the change in polarizability  $\Delta p$  is given as [142, 143]:

$$\Delta n_e = 2\pi F_L^2 \Delta p \Delta \hat{n} / n_0 \quad (4.4.5)$$

where  $F_L = (n_0^2 + 2)/3$  is the Lorenz factor and  $\Delta \hat{n}$  the population inversion difference across the extraction beam profile. The change in polarizability is in the order of  $\Delta p \approx 2 \times 10^{-26} \text{ cm}^3$  for  $\text{Yb}^{3+}:\text{YAG}$  in the visible (633 nm) [143] and near infrared (1030 nm) [144] spectral region. Data for other gain media are also available [145, 146]. On the other hand, the refractive index is dependent from the temperature as well. At ambient temperature  $\partial n / \partial T \approx 8 \times 10^{-6} \text{ K}^{-1}$  for YAG, while it drops down to  $3 \times 10^{-6} \text{ K}^{-1}$  at 150 K [130].

At room temperature  $\Delta T$  is typically in the order of 10 K, whereas  $\Delta \hat{n} \approx 0.2 \times \hat{n}_{tot}$ . With a doping of 2 at.%, we get  $\Delta n_T \approx 8 \times 10^{-5}$  while  $\Delta n_e \approx 10.8 \times 2 \cdot 10^{-26} \times 0.2 \times 2 \times 1.39 \cdot 10^{20} \approx 1.2 \times 10^{-6}$ . The electronic lens effect is approximately one order of magnitude less important than the refractive index change due to the temperature variation. At cryogenic conditions however, they might get comparable. However, as the desired pump light distribution is usually as homogeneously as possible, an electronic lens effect might be suppressed.

In the case of a rod-like geometry, the thermal lens dominates over the surface deformation [10]. Considering the Lucia main amplifier head, where the gain medium is close to the shape of the thin disc geometry, a strong thermal variation perpendicular to the extraction direction is not expected. The mechanical lens effect will be consequently stronger than the thermal lens effect.

#### 4.4.1. Basic Model

In order to estimate, in first order, the deformation for the thin disk case, we consider the deformation to be small and the bulging between the surfaces to be negligible. With the definitions as shown in Figure 4.16 we get:

$$\frac{L}{L + \Delta L} = \frac{R}{R + D} \quad (4.4.6)$$

The elongation with the temperature is  $\Delta L = \alpha_T \Delta T L$  with  $\Delta T$  the temperature difference between surfaces and  $\alpha_T$  the thermal expansion coefficient. We get by this:

$$R = \frac{D}{\alpha_T \Delta T} \quad (4.4.7)$$

Using Equation 4.2.14 to determine the temperature difference between the two large surfaces in the single-side cooled, active mirror case:

$$\Delta T = \frac{\dot{q} D^2}{2k} \quad (4.4.8)$$

The volumetric heat generation  $\dot{q}$  is expressed using Equation 4.2.5 as

$$\dot{q} = \eta_h \eta_{abs} P_{inj} / V \quad (4.4.9)$$

where the factor  $\eta_{abs}$  describes the fraction of the absorbed total injected average power  $P_{inj}$  within the volume  $V$ . As  $\dot{q}$  was assumed to be uniform, the volume  $V$  is by this defined as  $V = A_{beam} D$  where  $A_{beam}$  is the beam section. Finally, the radius

of curvature of the deformed gain medium is given by

$$R = \frac{2kA_{beam}}{\alpha_T\eta_h\eta_{abs}P_{inj}} \quad (4.4.10)$$

The active mirror scheme applied at the main amplifier head uses an extraction beam passing the front surface (bent to a radius  $R + D$ ) then experiencing a reflection on the surface with a curvature  $R$  and finally again a transmission through the first surface. Under the estimation of  $D \ll R$  a reflection on the front surface gives  $f_{front} = R/2$ , which is the same in the case of the described internal reflection  $f = f_{int} = f_{front} = R/2$  [147]. As  $P_{inj}/A_{beam}$  corresponds to the average intensity (in space and time)  $I_{avg}$ , the focal length is in these approximations:

$$|f| = \frac{k}{\alpha_T\eta_h\eta_{abs}I_{avg}} \quad (4.4.11)$$

Interestingly the focal length does not depend on the thickness of the laser gain medium. A higher thermal conductivity  $k$  and smaller thermal expansion  $\alpha_T$  will lead to longer focal lengths on ones side, while a higher dissipated power per area  $\eta_h\eta_{abs}I_{avg}$  will shorten the focal length.

Another information which can be directly drawn out of Figure 4.16 is that in the case of the Lucia main amplifier, we get preferably a negative focal length. Extraction and pump direction are coincident. This is contrary to the rod-like geometries, where the positive lens from the thermal lens and the bulged back side most likely generate a positive focal length.

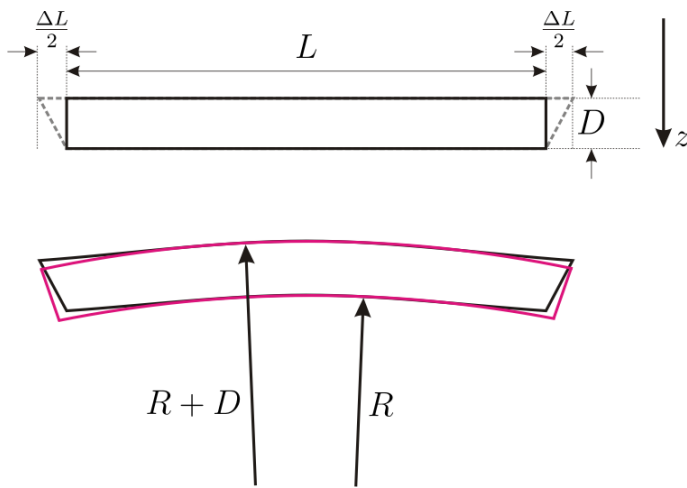


**Figure 4.16.:** Sketch for the estimation of the deformation of an active medium in the thin disc case. The transverse size of the gain medium is  $L$  while its thickness is  $D$ . The temperature induced deformation leads to a different transverse elongation perpendicular to the large surfaces and by this to a bending. In first order the radii are  $R$  and  $R + D$ . The pump direction is in  $z$ .

#### 4.4.2. Thermal performance of the laser head

Three separate cases are depicted in Figure 4.17. An  $\text{Yb}^{3+}$ :YAG crystal doped at 2 at.% at ambient temperature (300 K) is characterized by  $\alpha_T \approx 6 \times 10^{-6} \text{ K}^{-1}$  and  $k = 9 \text{ W m}^{-1} \text{ K}^{-1}$ , while at 150 K the thermal focal length increases by almost a factor of 4, since  $\alpha_T \approx 3.5 \times 10^{-6} \text{ K}^{-1}$  and  $k = 20 \text{ W m}^{-1} \text{ K}^{-1}$  ( $\eta_h = 0.1$ ,  $\eta_{abs} = 0.9$ ).

The third case is a thick, highly doped crystal (20 at.%). As discussed before, for such high doping concentrations the heat generation is strongly increased. Values reported are in the order of up to 30 % [148].

The crystal is thick compared to the reabsorption-length (1/e) and consequently, strong reabsorption introduces an additional heating rate. As the spontaneous emission is isotropic, the spontaneously emitted photons near the surface have a chance of  $\sim 50\%$  to escape the crystal, otherwise they are reabsorbed and generate additional heat. A photon traveling from one surface to the other will consequently increase the heat generation by  $\approx 0.5 \cdot 0.3 / (1 - 0.5 \cdot 0.3) \approx 18\%$ .

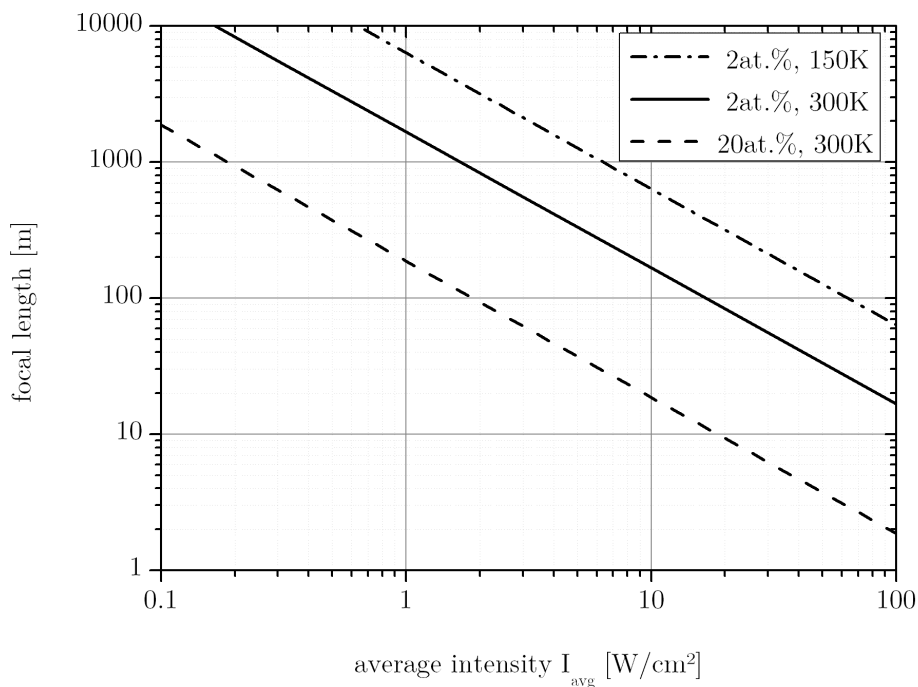


**Figure 4.17.:** Estimations for the thermally induced focal length in three cases as a function of the average incident intensity  $I_{avg}$ . Plotted curves stand for 2 at.% doped  $\text{Yb}^{3+}$ :YAG crystal at 300 K and 150 K with  $\eta_h = 0.1$ ,  $\eta_{abs} = 0.9$  and a highly doped case (20 at.%), where  $\eta_h = 0.5$  and  $\eta_{abs} = 1$  are estimated.

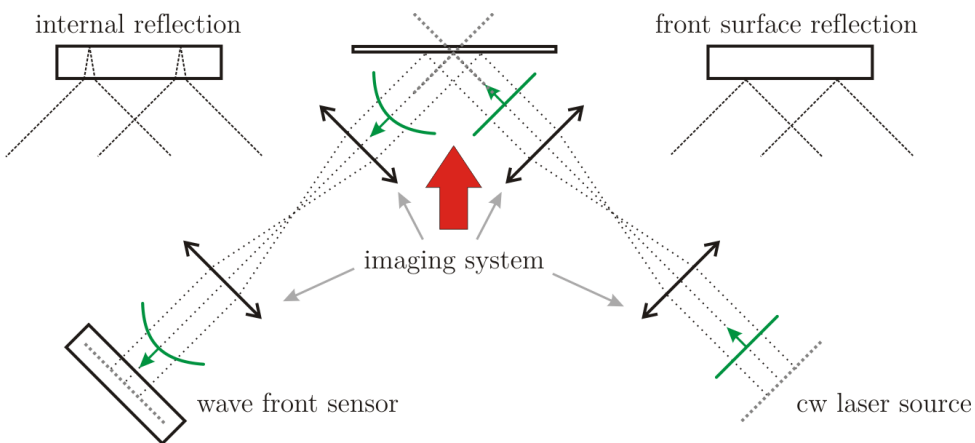
Overall for a thick, highly doped crystal, we get  $\eta_h \approx 0.5$ . Considering also a twice lower thermal conductivity, it is expected, that such a crystal will generate a one order of magnitude shorter thermally induced focal length compared to its low doped counterpart.

Figure 4.18 illustrates the experimental setup to measure the wavefront deformation on the main laser amplifier head. A collimated cw laser source (633 nm and 1064 nm) is imaged on the laser head, reflected on/within the pumped gain medium wavefront and finally imaged onto a wavefront sensor (SID4, Phasics). The laser head is pumped using the LDA (red arrow) with intensities of up to  $18 \text{ kW cm}^{-2}$  and repetition rates of up to 10 Hz in a circular area with a diameter of 30 mm. The pulse length is 1 ms. The angle of incidence is  $25^\circ$ , corresponding to an internal reflection angle of  $13^\circ$ .

Three different crystals were studied:

- 2 at.%, rectangular crystal,  $40 \text{ mm} \times 35.8 \text{ mm} \times 8.4 \text{ mm}$
- 20 at.%, rectangular crystal,  $41 \text{ mm} \times 37 \text{ mm} \times 4.7 \text{ mm}$
- 2 at.%, circular crystal, 60 mm diameter, 7 mm thickness

where the first two crystals served as calculation testbed, while the 60 mm circular disc corresponds to the actual gain medium used on the Lucia laser amplifier.



**Figure 4.18.:** Sketch of the experimental setup measuring the wavefront deformation on the Lucia main amplifier laser head. A well collimated cw laser source is imaged onto the crystal to be tested. The analyzed reflection might be coming from the front surface or from the rear surface (internal reflection). The reflected wavefront is imaged onto a wavefront sensor. The reference wavefront is recorded, when no incident pump light illuminates the crystals.

The rectangular crystals are coated in such a way, that both large surfaces have a low reflectivity for the pump wavelength (i.e. 940 nm AR). For the test wavelength (in this case 633 nm) one side is HR coated, while the opposite side is AR coated. With this feature, the crystals can be flipped, to either measure the wavefront distortion introduced by only the front surface or the whole distortion as it is seen by the extraction beam under internal reflection (see Figure 4.18).

The circular crystal is coated according to Lucia nominal pump/extraction requirements, i.e. one surface is anti-reflection coated for both the pump wavelength and extraction/test wavelength and the other surface is highly reflective for both wavelengths as well. As the designed extraction wavelength is 1030 nm, a sufficiently good performance for the test wavelength at 1064 nm is ensured.

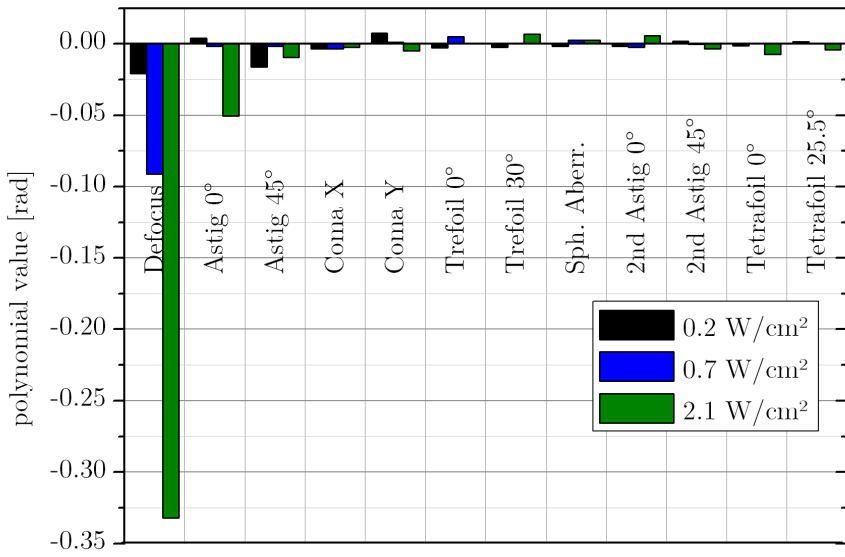
The phase arriving at the wavefront sensor is expanded on Zernike polynomials. One of those polynomial describes the parabolic deformation (defocus) of the wavefront, its amplitude is  $Z_{def}$ . The corresponding focal length  $f$  can be calculated with the pupil radius  $r_p$  and the measurement wavelength  $\lambda$ :

$$|f| = \frac{r_p^2}{4\sqrt{3}\lambda Z_{def}}. \quad (4.4.12)$$

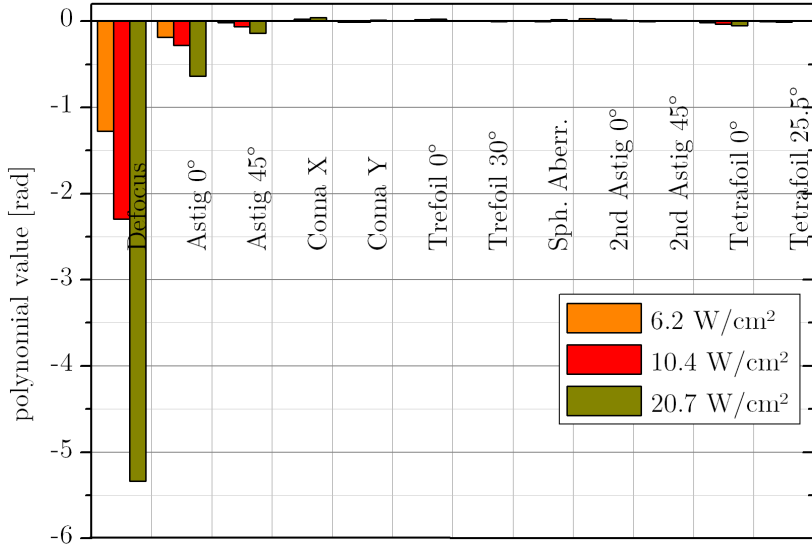
The first crystal to be tested is the highly doped (20 at.%, 4.7 mm thickness) sample, as it is expected to exhibit the strongest deformation for a given  $I_{avg}$ . Figure 4.19 shows the first twelve Zernike polynomials for six different average intensities varying between  $0.2 \text{ W cm}^{-2}$  and  $20.7 \text{ W cm}^{-2}$ . Ten successive shots were averaged for repetition rates ranging from 0.1 Hz to 10 Hz. The measurement was performed on the front surface reflection only.

Figures 4.19(a) and 4.19(b) show clearly that the defocus and the  $0^\circ$  astigmatism polynomials are the most important, where  $Z_{def}$  is approximately six times stronger than  $Z_{ast0^\circ}$ . We will mainly face a parabolic wavefront distortion. On these graphs only the steady state wavefront deformation is considered. Let us now examine the temporal behavior of the two most important Zernike polynomials between two successive pump pulses as it gives information about the heat generation and transport. Figure 4.21(a) depicts, in double logarithmic scale, the temporal evolution of the absolute values for the first Zernike Polynominal ( $Z_{def}$ ) and the corresponding information for  $Z_{ast0^\circ}$ .

The peak power of the pump pulse was  $\approx 2.1 \text{ kW cm}^{-2}$  with a pulse length of 1 ms. Two successive pump pulses are separated by their repetition rate ranging from 0.1 s (10 Hz) to 10 s (0.1 Hz). This fixed pump power combined with a repetition rate varying over two decades allow to explore a range of average power from 0.2



**(a)** The first 12 Zernike polynomials as a function of the average incident intensity  $I_{avg}$  for a highly doped  $\text{Yb}^{3+}\text{:YAG}$  slab (20 at.%). The intensities were  $0.2 \text{ W cm}^{-2}$ ,  $0.7 \text{ W cm}^{-2}$  and  $2.1 \text{ W cm}^{-2}$ .



**(b)** The first 12 Zernike polynomials as a function of the average incident intensity  $I_{avg}$  for a highly doped  $\text{Yb}^{3+}\text{:YAG}$  slab (20 at.%). The intensities were  $6.2 \text{ W cm}^{-2}$ ,  $10.4 \text{ W cm}^{-2}$  and  $20.7 \text{ W cm}^{-2}$ .

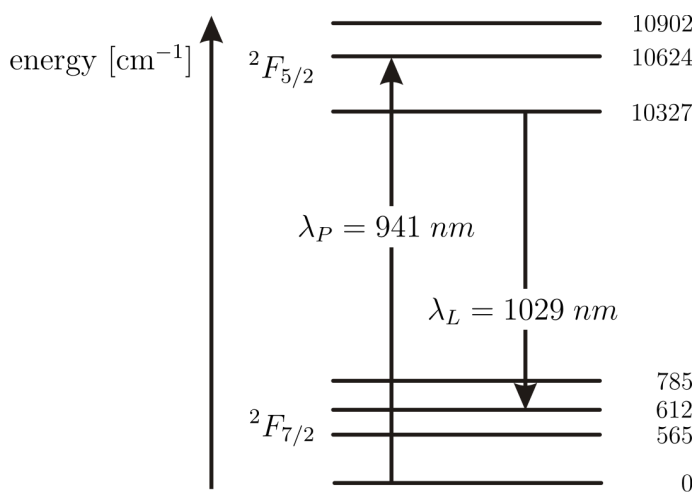
**Figure 4.19.:** The first 12 Zernike polynomials in the case of the highly doped 20 at.%  $\text{Yb}^{3+}\text{:YAG}$  slab. The polynomial describing the defocus,  $Z_{def}$ , is approximately one order of magnitude stronger than the second, the  $0^\circ$  astigmatism  $Z_{ast0^\circ}$ .

to  $20 \text{ W cm}^{-2}$ . We observe that, even as the pump pulse stops after 1 ms, the deformation is still growing, until at 3 ms the maximum is reached. From this (temporal) point on, a slow relaxation sets in.

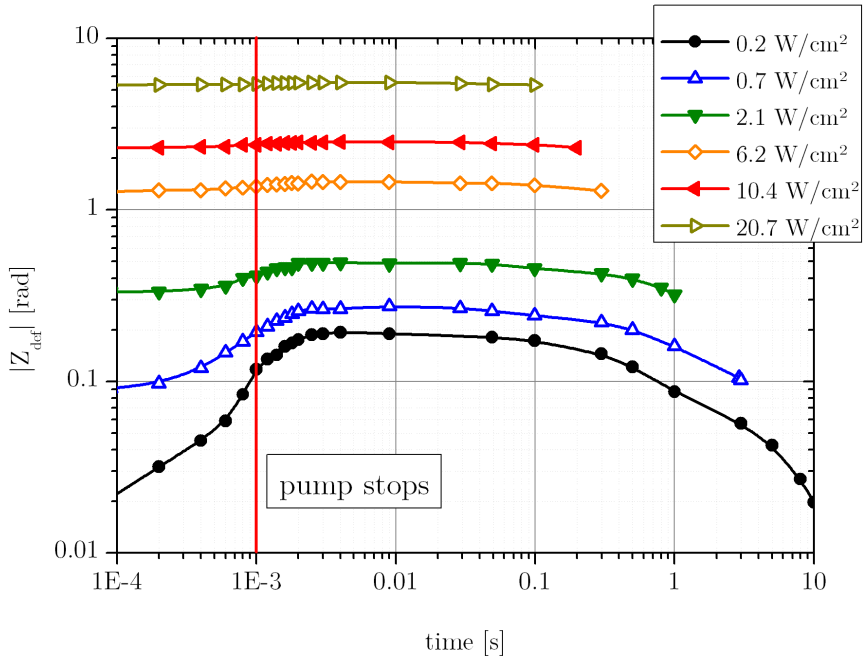
These observations are related to heat generation and heat transport processes within the gain medium. Due to high doping level (20 at.%) and thickness (4.7 mm) compared to the  $1/e$  absorption length for the pump wavelength ( $\approx 0.5 \text{ mm}$ ), significant population  $\hat{n}$  will only be generated within a thin surface layer during the 1 ms long pump pulse.

Figure 4.20 illustrates the simplified electronic structure of  $\text{Yb}^{3+}\text{:YAG}$ . During pumping, electrons rise from the lower  $^2F_{7/2}$  multiplet into the upper  $^2F_{5/2}$  multiplet. The relaxations within the multiplets are fast compared to the typical time scale of the experimental observation ( $\sim 10 \text{ ps}$  [149] vs.  $\sim 100 \mu\text{s}$ ). For the following considerations we take no other decay branches (due to impurities, etc.) into account. The intraband energy transfers are considered to be radiationless and therefore each excited electron generates  $\approx 300 \text{ cm}^{-1}$  of energy transformed into heat. After depopulating of the upper laser state towards the lower laser state, again  $\approx 610 \text{ cm}^{-1}$  are generated from each transition.

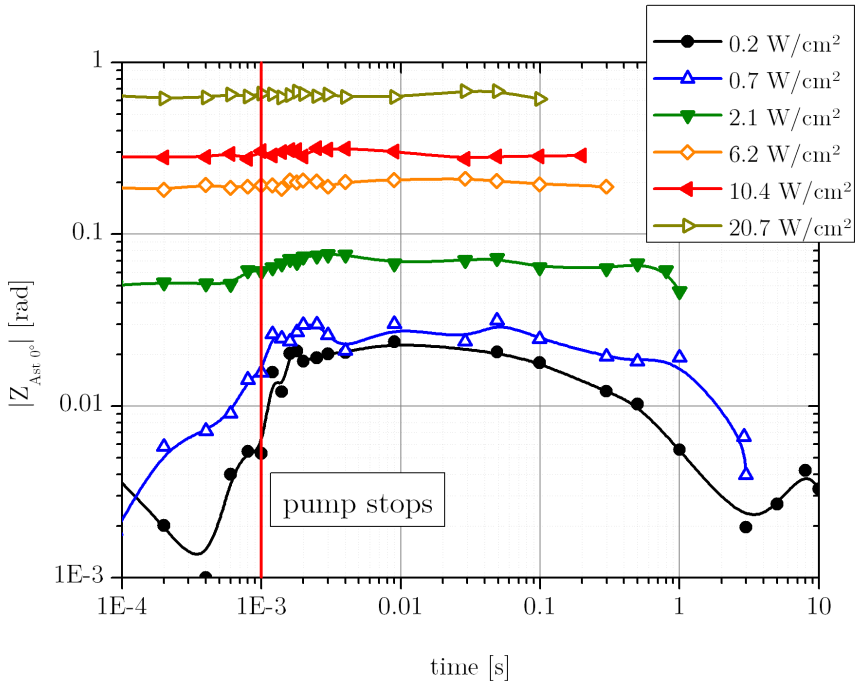
Consequently, heat generation will only stop, if the upper laser state is depleted. After approximately one to two times the lifetime, i.e. after  $\approx 1 - 2 \text{ ms}$  after the pulse pump stopped, this effect will become such weak, that the rise in deformation is stopped. Indeed, this corresponds to the maximums for polynomials shown in Figure 4.21(a) and (b). A similar effect can be understood for the successive reabsorption of the spontaneous emission.



**Figure 4.20.:** Simplified quasi–three level level scheme for  $\text{Yb}^{3+}\text{:YAG}$ , after [10].



(a) Time resolved measurement of the absolute value of the defocus Zernike polynomial.



(b) Time resolved measurement of the absolute value of the 0° astigmatism Zernike polynomial.

**Figure 4.21.:** The time resolved measurement of the wavefront deformation yields the temporal evolution of the Zernike polynomials, of which the absolute values of the defocus  $Z_{def}$  and the 0° astigmatism are shown. The variation of the repetition rate generates the different average intensities. The pump duration was 1 ms.

At  $\approx 2$  ms after the end of the pump pulse, the deformation starts to decrease until the next pulse sets in. For large deformations such transient thermal effects become small and can consequently be neglected. Therefore only the steady state thermal deformation is of interest for the following discussion.

Since  $Z_{def}$  is dominant against the other wavefront distortions, we will concentrate from this point on the focal length calculated using Equation 4.4.12.

For several average incident intensities  $I_{avg}$ , we have measured the wavefront deformation and extracted the corresponding focal length with Equation 4.4.12, using the polynomial  $Z_{def}$  derived out of the static deformation. Figure 4.22 shows the calculated focal length as the function of the average Intensity  $I_{avg}$  for the three studied cases. Figure 4.22(a) illustrates the steady state focal length for the highly doped gain medium case.

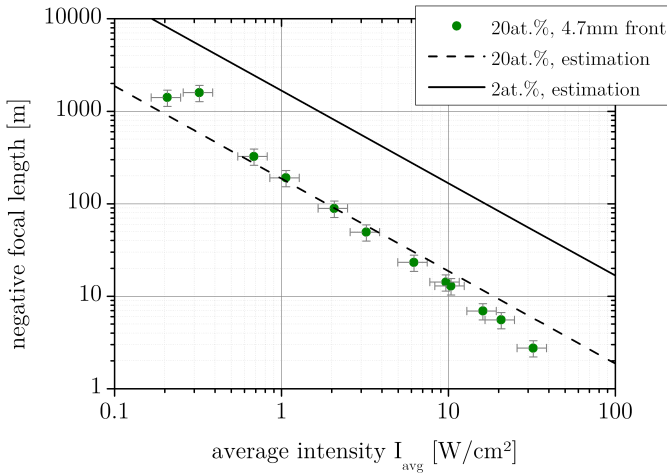
As references, both estimated performances are shown in Figure 4.17 for 300 K are added. A good accordance to the  $1/I_{avg}$  relation is found (see Equation 4.4.11). For high average intensities (above  $10 \text{ W cm}^{-2}$ ), the gain medium properties (especially the thermal conductivity and thermal expansion) dependency from the temperature have to be taken into account. As this is not the case for the modeling, deviations from the experimental results occur.

The fracture limit of the gain medium under such conditions was reached at  $\approx 30 \text{ W cm}^{-2}$ , while the experimental arrangement was set up for front-surface reflection analysis. Therefore no measurement for the internal reflection could be performed on this crystal for the internal reflection case.

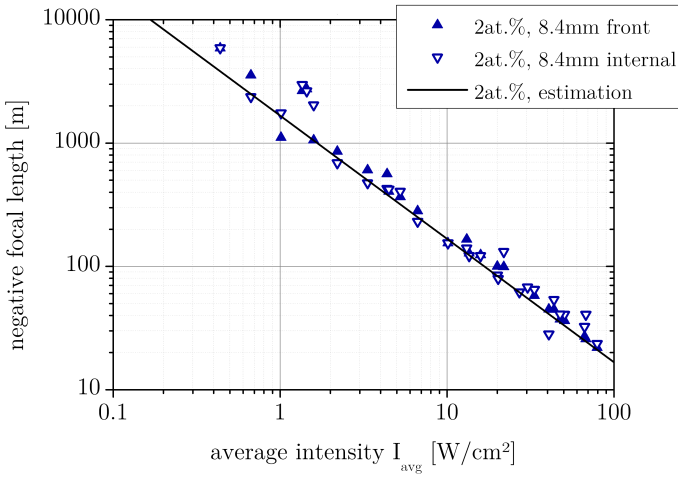
Figure 4.22(b) shows the case of the 8.4 mm thick, rectangular crystal doped at 2 at.% and compares the result to the simple model derived in Section 4.4.1. Both, for the reflection on the front surface (solid triangles) and the reflection on the inner HR coating (open triangles), a very good agreement between the measurement results and the prediction is found.

The same evaluation in the case of the 60 mm diameter circular disk brings an obvious mismatch from the model as shown in Figure 4.22(c). The measurement shows a significantly better performance as it could be expected. The model expressed in Equation 4.4.11 is not capable anymore to predict such a behavior. Indeed, as stated in Section 4.2.4, a temperature distribution cannot be neglected anymore.

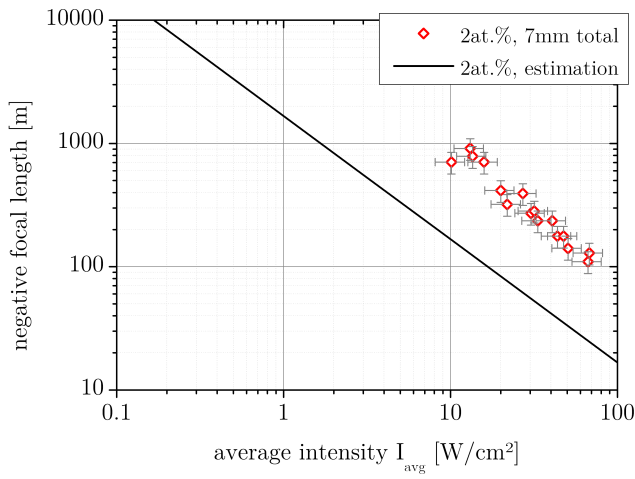
In the cases of the rectangular crystal, the typical size was 40 mm, while a 30 mm pump diameter was used. This corresponds to 75 % of occupation ( $a' = 0.75$  in Figure 4.7). In the circular case (Lucia), this value dropped to 50 % ( $a' = 0.5$  in Figure 4.7). Therefore a more complex, three dimensional analysis is necessary and will be described in the following section.



(a) Focal length in the 20 at.% doped, rect. crystal case



(b) Focal lengths in the 2 at.% doped, rect. crystal case



(c) Focal length in the 2 at.% doped, circular crystal case

**Figure 4.22.:** Comparison between the experimentally observed static deformation and predictions for three different crystals. While (a) and (b) can be explained with the simplified derived model, a complete model for (c) is necessary.

#### 4.4.3. Numerical estimation of the gain medium deformation

As we have seen in the previous section, a simple analytical model can describe, under certain approximations, the thermally induced wavefront deformations.

The model developed in Section 4.4.1 took only the lateral deformation into account, but not the bulging of the surfaces and thermal lens due to a non-homogeneous lateral temperature profile. Therefore a three dimensional numerical calculation is required.

A Finite-Element-Analysis (FEA) is performed using CAST3M<sup>2</sup> in order to calculate the wavefront deformation of a plane wave traveling through the gain medium.

In the model we consider the material properties ( $\rho, c, k, \alpha_T$ ) as constant. If a significant rise in temperature is observed, we will consequently underestimate the temperature and deformation.

The calculation for the three individual gain medium configurations (described on page 145) is performed in three steps:

- Calculation of the temperature distribution
- Calculation of the deformation
- Estimation of the wavefront deformation

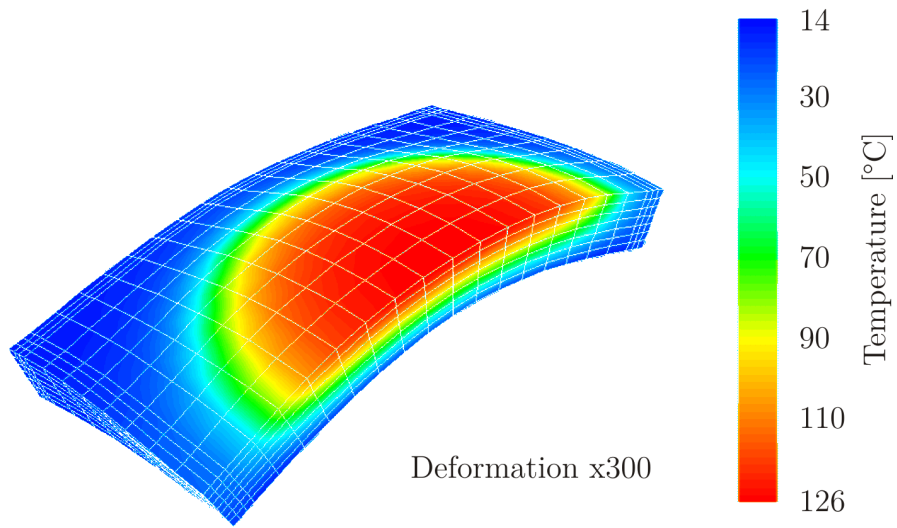
Figure 4.23 illustrates the result of the steady state heat transport equation by displaying the resulting temperature map and the steady state deformation for the rectangular highly doped crystal (20 at.%, 4.7 mm thickness) pumped with  $I_{avg} = 30 \text{ W cm}^{-2}$  and the Lucia laser head relevant case of a circular, 7 mm thick, 2 at.% doped crystal pumped with  $I_{avg} = 75 \text{ W cm}^{-2}$ .

It should be noted, that the calculated temperature for the highly doped crystal exceeds 120 °C at a pump intensity of  $I_{avg} = 30 \text{ W cm}^{-2}$ , while in the case shown in Figure 4.23(b) only 41 °C are reached for  $I_{avg} = 75 \text{ W cm}^{-2}$ . Consequently, as already mentioned, the interpretation of the values derived for the highly doped case must be taken with caution due to the temperature dependent material properties.

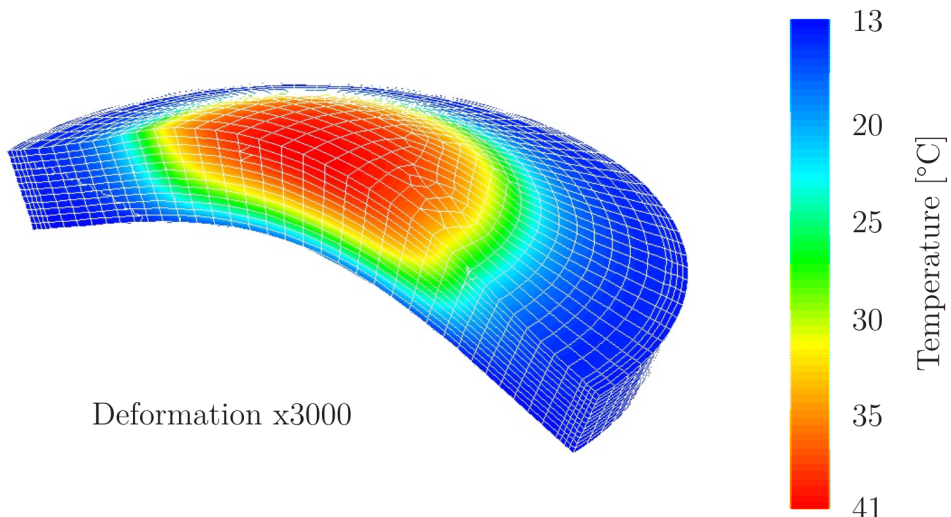
Figure 4.24 shows the predicted distorted wavefronts (with a 24 mm observation pupil) after exiting the crystal with an internal reflection for the circular (a) rectangular (b) crystals doped at 2 at.%. The average pump intensity was

---

<sup>2</sup>CAST3M is available at <http://www-cast3m.cea.fr/cast3m/index.jsp>

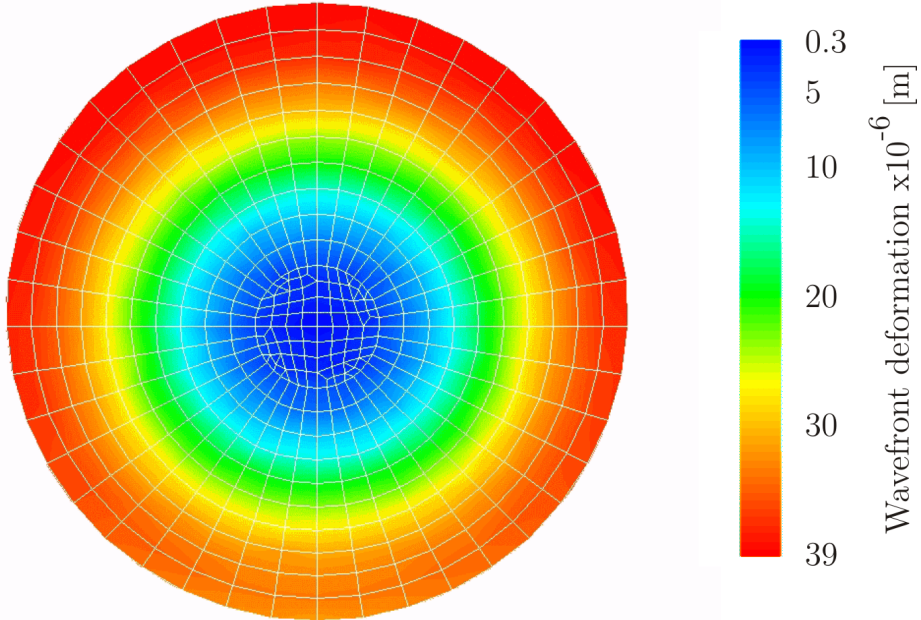


(a) Deformation and temperature map (colorbar in °C) for the 20 at.% doped, rectangular crystal,  $I_{avg} = 30 \text{ W cm}^{-2}$ , deformation is  $\times 300$  magnified.

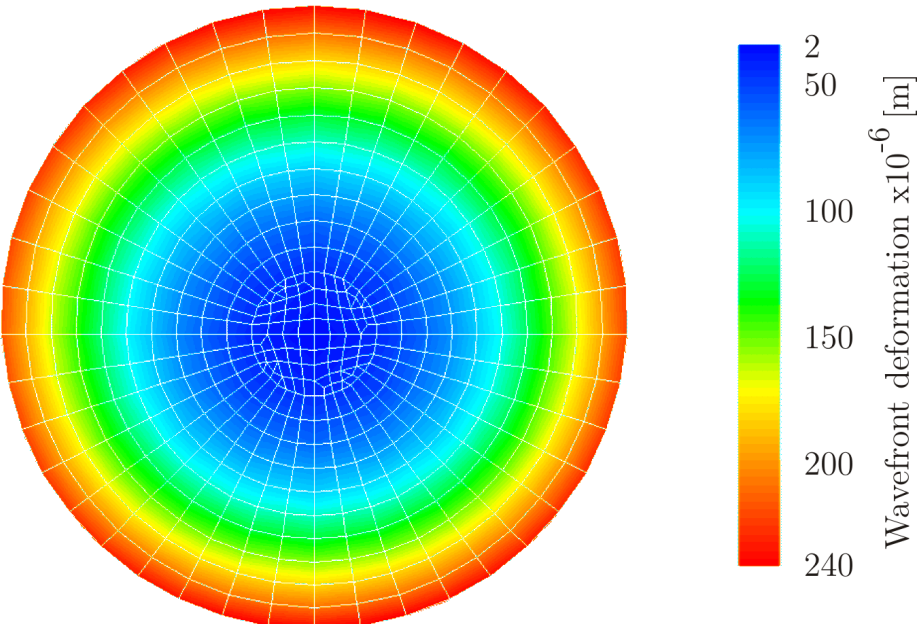


(b) Deformation and temperature map (colorbar in °C) for the 2 at.% doped, cylindrical crystal,  $I_{avg} = 75 \text{ W cm}^{-2}$ , deformation is  $\times 3000$  magnified.

**Figure 4.23.:** Deformation and temperature map for the 20 at.% doped, rect. crystal pumped at  $I_{avg} = 30 \text{ W cm}^{-2}$  (a) and the 2 at.% doped, circ. crystal pumped at  $I_{avg} = 75 \text{ W cm}^{-2}$  (b). The deformation in (a) is magnified 300 $\times$ , while in (b) it is 3000 $\times$ .



(a) Wavefront deformation (colorbar in  $m$ ) as seen by a plane wave experiencing an internal reflection on the 2 at.% doped, 7 mm thick, cyl. crystal,  $I_{avg} = 75 \text{ W cm}^{-2}$ . The maximum deformation is  $\sim 0.4\lambda$ .



(b) Wavefront deformation (colorbar in  $m$ ) as seen by a plane wave experiencing an internal reflection on the 2 at.% doped, 8.4 mm thick, rect. crystal,  $I_{avg} = 75 \text{ W cm}^{-2}$ . The maximum deformation is  $\sim 2.4\lambda$ .

**Figure 4.24.:** Wavefront deformation as seen by a plane wave after an internal reflection on the 2 at.% doped, 7 mm thick, cyl. crystal (a) and the 2 at.% doped, 8.4 mm thick, rect. crystal. Both cases are pumped at  $I_{avg} = 75 \text{ W cm}^{-2}$ . A six times less important wavefront distortion is found in the cylindrical case.

$I_{avg} = 75 \text{ W cm}^{-2}$ . For the case of the circular, 2 at.% doped crystal (Figure 4.24(a)) we get a  $\sim 6 \times$  lower maximum deformation compared to the rectangular case (see Figure 4.24(b)).

Horizontal lineouts of the predicted wavefronts obtained for the 20 at.% doped crystal exposed to  $I_{avg} = 30 \text{ W cm}^{-2}$  and for both 2 at.% doped crystals at  $I_{avg} = 75 \text{ W cm}^{-2}$  are shown in Figure 4.25. The experimental observation pupil was  $\approx 22 \text{ mm}$  over which the peak-to-peak surface deformations are approximately  $15 \mu\text{m}$ ,  $1.1 \mu\text{m}$  and  $0.6 \mu\text{m}$ .

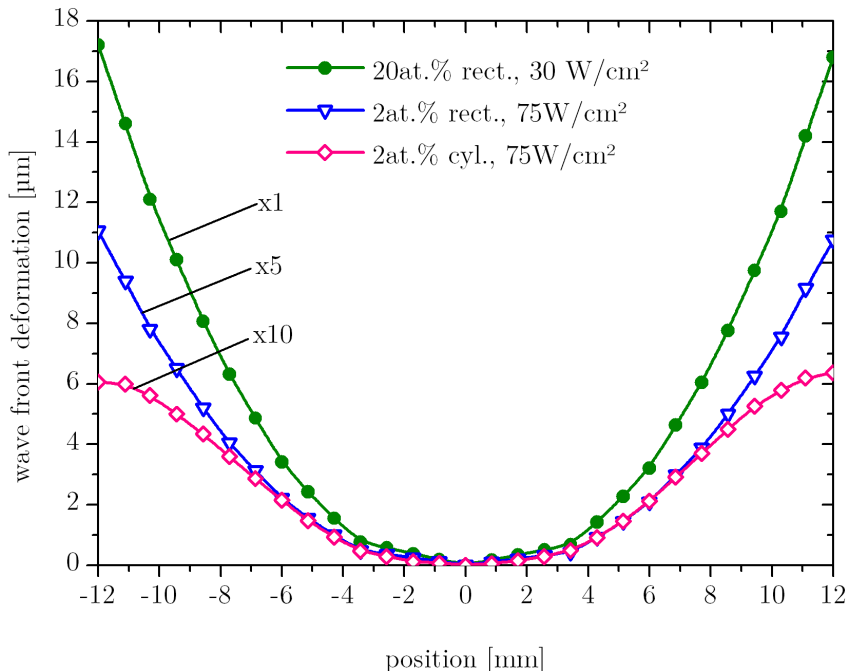


**Figure 4.25.:** Horizontal lineouts of the predicted wavefront deformation in the case of the highly doped, rectangular (20 at.%, 4.7 mm thick) (red diamonds), the 2 at.% doped rectangular crystal (8.4 mm thick) (orange triangles, magnified 5 $\times$ ) and the crystal with the geometry of the Lucia laser head (2 at.%, 7 mm thick, 60 mm diameter) (green circles, magnified 10 $\times$ ).

For each of the three modeled crystals similar lineouts are computed and a parabolic polynomial fit is applied to the central part (for intensities ranging from below  $1 \text{ W cm}^{-2}$  up to  $100 \text{ W cm}^{-2}$ ). Out of this fit, the focal lengths are derived. A comparison between the calculated (using the 3D model) and the experimental results is shown in Figure 4.26.

We see a very good agreement between the numerical predictions and the experimental results even for the cylindrical crystal pumped over only half of its diameter. Whereas the pure bi-metal model used in the previous section was not able to explain the rise in focal length, the full three-dimensional model is now capable to do so.

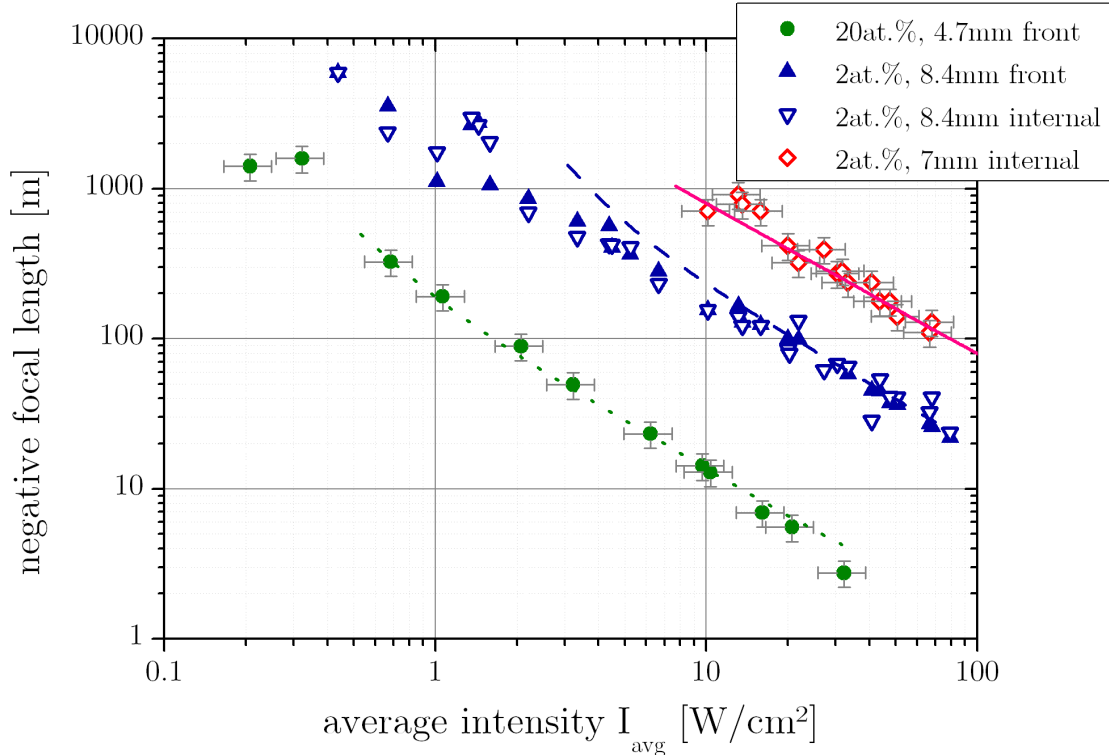


**Figure 4.26.:** Deformation compilation of the experiments done on the main amplifier head. The symbols show measured values for a highly doped crystal (green full circles), a rectangular, 8.4 mm thick crystal doped at 2 at.% where the test beam is reflected on the front surface (blue full triangles) or under internal reflection (blue open triangles) and the crystal used in the main laser head (circular, 7 mm thick, red open diamonds). The computed negative focal length is plotted as a function of the injected average laser intensity. The lines indicate simulated focal lengths retrieved from the three dimensional model. The error bars in the case of the highly doped case and for the circular crystal indicate the order of magnitude for the measurement error.

## 4.5. Thermally induced depolarization

### 4.5.1. Stress induced birefringence

A well known problem related to high-average power operation of lasers is the depolarization of the incoming polarized light when passing through a pumped gain medium. Indeed, while being pumped, the gain medium is subject to temperature induced stress. This results in a change in the index of refraction due to the photo-elastic effect.

Stress changes in an anisotropic manner the dielectric permittivity  $\epsilon$  and impermeability  $B$ , where both second-rank symmetric tensors are connected by [150, 140]:

$$B\epsilon = I \quad (4.5.1)$$

where  $I$  is the corresponding identity tensor. Those quantities are described as quadric

$$\epsilon_{ij}x_i x_j = 1 \quad (4.5.2)$$

$$B_{ij}x_i x_j = 1 \quad (4.5.3)$$

where  $i, j = 1, 2, 3$  and Einsteins sums convention is used. They can be represented in the principle axis coordinate system as follows:

$$\epsilon_{ii}x_i^2 = 1 \quad (4.5.4)$$

$$B_{ii}x_i^2 = 1. \quad (4.5.5)$$

The index of refraction can also be represented as an ellipsoid in the principal axis coordinate system. However, the index of refraction is not a tensor quantity. If  $x_1$ ,  $x_2$  and  $x_3$  are the principal axis we get the indicatrix for the index of refraction:

$$\frac{x_i^2}{n_i^2} = 1 \quad (4.5.6)$$

which can be related to the tensor values of Equation 4.5.4 and 4.5.5 as:

$$B_{ii} = \frac{1}{\epsilon_{ii}} = \frac{1}{n_i^2}. \quad (4.5.7)$$

In the most general case, a change in index of refraction is expressed as a change of the coefficients  $B_{ij}$ , whereas this change results from an applied electric field  $\mathfrak{E}_k$  or an applied stress  $\sigma_{kl}$

$$\Delta B_{ij} = z_{ijk}\mathfrak{E}_k + \pi_{ijkl}\sigma_{kl}. \quad (4.5.8)$$

The first component complies to the electro-optical effect (third rank tensor  $z_{ijk}$ ) and the second to the (fourth-rank tensor) photo-elastic effect with the piezo-optical coefficients  $\pi_{ijkl}$ .

In the absence of stress, the refractive index indicatrix for a cubic crystal is a sphere

$$\mathbf{B}_0(x_1^2 + x_2^2 + x_3^2) = 1. \quad (4.5.9)$$

With stress applied, the dielectric impermeability tensor writes as

$$\mathbf{B}_{ij} = \Delta \mathbf{B}_{ij} + \mathbf{B}_0. \quad (4.5.10)$$

Consequently, even cubic crystals can become uni- or biaxial, depending on crystal geometry, and the direction along which the stress is applied. A more detailed discussion how the dielectric impermeability tensor is expressed for different conditions is given in [150, 140].

Under propagation through the pumped crystal (i.e. along the z-axis), we have to know the submatrix  $\mathbf{B}_\perp$  [150] which describes the electric field polarization in the plane perpendicular to the propagation direction.

$$\mathbf{B}_\perp = \begin{pmatrix} \mathbf{B}_{11} & \mathbf{B}_{12} \\ \mathbf{B}_{21} & \mathbf{B}_{22} \end{pmatrix} \quad (4.5.11)$$

with its eigenvalues  $\mathbf{B}_\pm = 1/(n_\pm^2)$ . The angle of rotation of the principle axes is:

$$\tan(2\theta) = \frac{2\mathbf{B}_{12}}{\mathbf{B}_{11} - \mathbf{B}_{22}} \quad (4.5.12)$$

and the polarization phase shift  $\Delta\delta$

$$\Delta\delta = \frac{2\pi}{\lambda} D(n_+ - n_-) \quad (4.5.13)$$

where  $\lambda$  is the wavelength and  $D$  the length of the gain medium. The depolarization losses  $\mathfrak{L}$  are given as [150, 10]:

$$\mathfrak{L} = \frac{2\pi}{\lambda} \sin^2(2\theta) \sin^2\left(\frac{\Delta\delta}{2}\right). \quad (4.5.14)$$

In summary we see, that an applied stress changes the indicatrix and will consequently alter the polarization of an incident laser beam. Figure 4.27 illustrates the impact on a linear polarized beam traveling through a crystal under stress. In a circular geometry the stress might be decomposed into a radial stress  $\boldsymbol{\sigma}_r$  and a tangential stress  $\boldsymbol{\sigma}_t$ . As the projection of the direction of polarization and the stresses  $\boldsymbol{\sigma}_r$  and  $\boldsymbol{\sigma}_t$  depend on the position within the crystal, a spatial dependency is found. In this case the major axis of polarization along the  $x$  and  $y$ -axis is not altered in Figure 4.27, since only one of the stresses ( $\boldsymbol{\sigma}_r$  and  $\boldsymbol{\sigma}_t$ ) has a non-zero

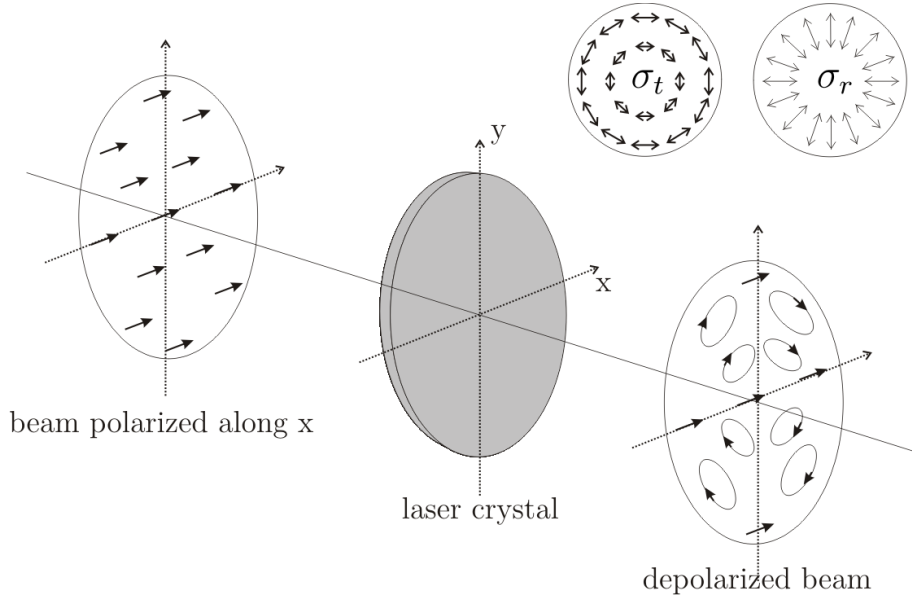


**Figure 4.27.:** Depolarization sketch for a linearly polarized beam traveling through a laser crystal under stress. The beam is initially polarized along the x-axis and gets transversely depolarized.

component.

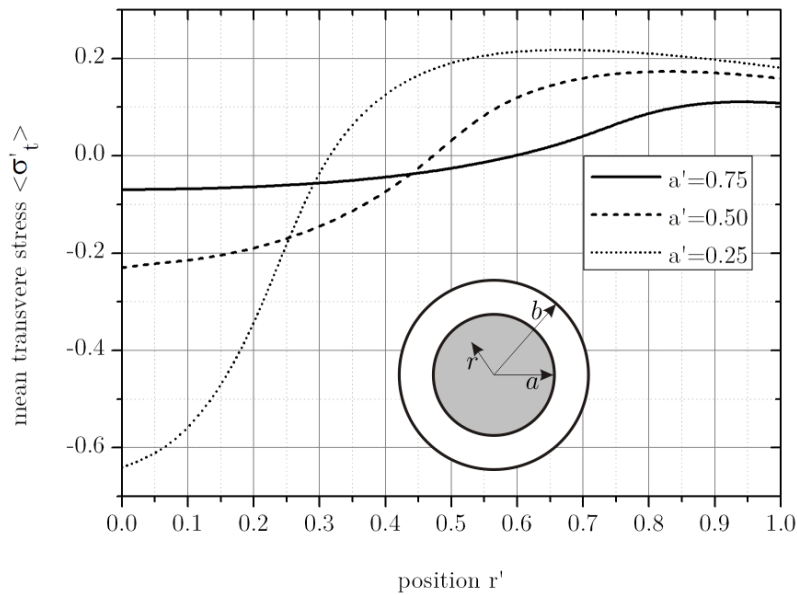
The model introduced in Section 4.2.4 allows the calculation of the mean radial  $\langle \boldsymbol{\sigma}'_r \rangle$  and tangential stress  $\langle \boldsymbol{\sigma}'_t \rangle$  as a function of the normalized radius  $r'$  [134]:

$$\langle \boldsymbol{\sigma}'_r \rangle = - \sum_{n=1}^{\infty} \frac{C_n}{\beta_n r'} J_1(\beta_n r') \quad (4.5.15)$$

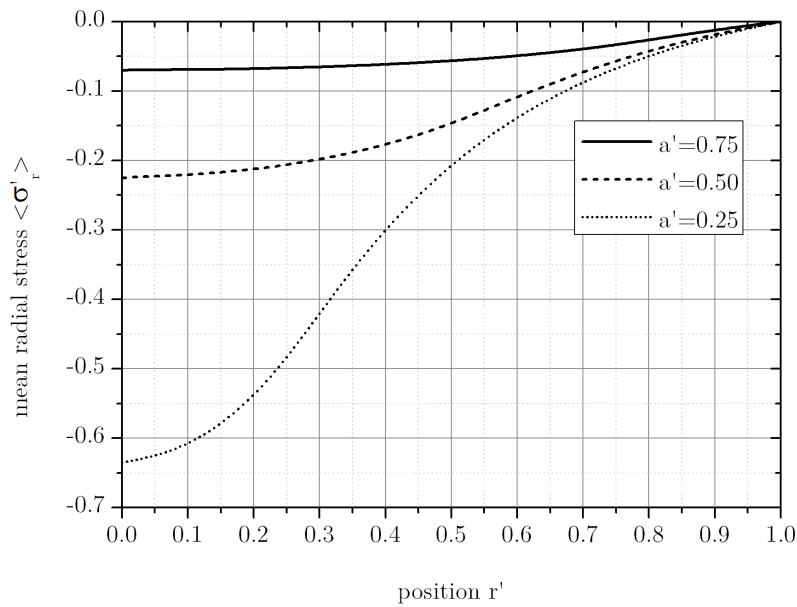
$$\langle \boldsymbol{\sigma}'_t \rangle = \sum_{n=1}^{\infty} \frac{C_n}{\beta_n r'} [J_1(\beta_n r') - (\beta_n r') J_0(\beta_n r')] \quad (4.5.16)$$

Resulting stresses for  $D' = 0.2$  and for the occupation factor  $a'$  varying between 0.25 and 0.75 are depicted in Figure 4.28(a) and (b).

Like for the temperature distribution (Figure 4.7), we observe that, in the case of an almost fully pumped surface, the stress get less important. For a fully pumped surface, the stress will vanish ( $a' \rightarrow 1$ ).



(a) Mean tangential stress  $\langle \sigma'_t \rangle$  integrated along the propagation direction as a function of the normalized radial position  $r' = r/b$  for  $D' = 0.2$  and  $a' = a/b$  varying between 0.25 and 0.75.



(b) Mean radial stress  $\langle \sigma'_r \rangle$  integrated along the propagation direction as a function of the normalized radial position  $r'$  for  $D' = 0.2$  and  $a'$  varying between 0.25 and 0.75.

**Figure 4.28.:** Mean tangential (a) and radial (b) stress distribution as a function of the normalized radial position  $r'$  for  $D' = 0.2$ .

#### 4.5.2. Intrinsic birefringence

Besides the externally introduced birefringence, each material carries its own intrinsic birefringence related to internal stress. This is especially true for laser crystals. Figure 4.29(a) and 4.29(c) show two samples of  $\text{Yb}^{3+}\text{:YAG}$  crystals observed between crossed polarizers. Depending on the growth and cutting direction, after growths treatment etc., different patterns for the intrinsic depolarization can be observed.

Simply using a crossed polarizer assembly is not sufficient to find out if initially linearly polarized light becomes spherically polarized and whether the principle axis is turned clockwise or counter-clockwise. The use of polarization dependent elements can help at this point.

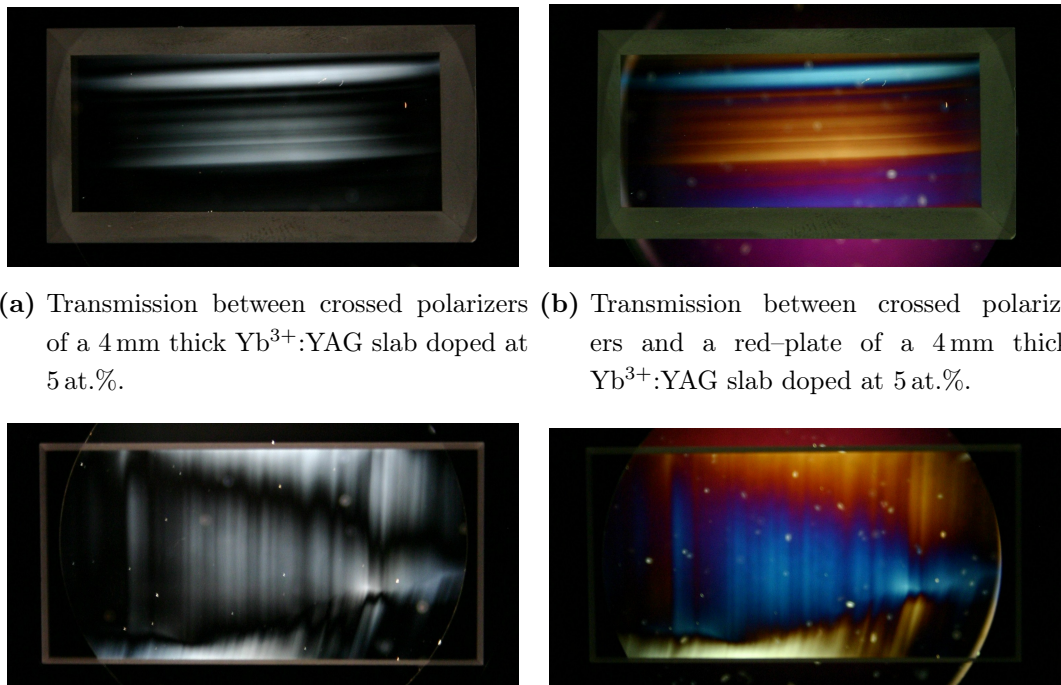
Figure 4.29(b) and (d) are obtained between crossed polarizers and a red-plate<sup>3</sup>[147]. A fraction of the transmitted lights polarization is turned clockwise (e.g. the blue parts), while the complementary colors indicate a counter-clockwise rotation.

Different areas of the crystal under stress turn the polarization in different directions. Also, zeroing (dark areas) in transmitted intensity between crossed polarizers does not necessarily introduce a change in the direction of rotation of the principle axis.

Let us mention that at this stage no effort was undertaken to further quantify the amount of depolarization due to intrinsic birefringence on the samples shown in Figure 4.29.

---

<sup>3</sup>Sometimes called red-one or gypsum plate. It is a first order retardation plate.



(a) Transmission between crossed polarizers of a 4 mm thick Yb<sup>3+</sup>:YAG slab doped at 5 at.%.

(b) Transmission between crossed polarizers and a red-plate of a 4 mm thick Yb<sup>3+</sup>:YAG slab doped at 5 at.%.

(c) Transmission between crossed polarizers of a 1 mm thick Yb<sup>3+</sup>:YAG slab doped at 10 at.%.

(d) Transmission between crossed polarizers and a red-plate of a 1 mm thick Yb<sup>3+</sup>:YAG slab doped at 10 at.%.

**Figure 4.29.:** Transmission examples set between crossed polarizers of two different Yb<sup>3+</sup>:YAG slabs. Images (a) and (c) are obtained between crossed polarizers, while images (b) and (d) show the corresponding images between crossed polarizers and an additional red-plate visualizing the difference for left end right circular polarization of the transmitted light. The bright spots are dust on the apparatus.

### 4.5.3. Thermally introduced birefringence on the Lucia laser head

The test setup for qualifying the depolarization on the Lucia main amplifier is illustrated in Figure 4.30. A collimated laser beam at 1064 nm is polarized using a beam splitter cube and imaged, using a  $4f$  assembly, onto the laser crystal. The beam has a diameter of 24.5 mm (the beam is cut using an apodizer setup).

The crystal is imaged onto a CCD camera using a magnifying image relay (magnification 1/10). The beam passes an analyzer mounted on a rotation stage, whereas the analyzer can be conveniently turned by  $90^\circ$  or to any other desired angle. The maximum extinction of the crossed polarizer setup was found to be better than 1/500, limited by the polarizer cubes used. The optical densities used for the attenuation were measured with a spectro-photometer (Cary 500).

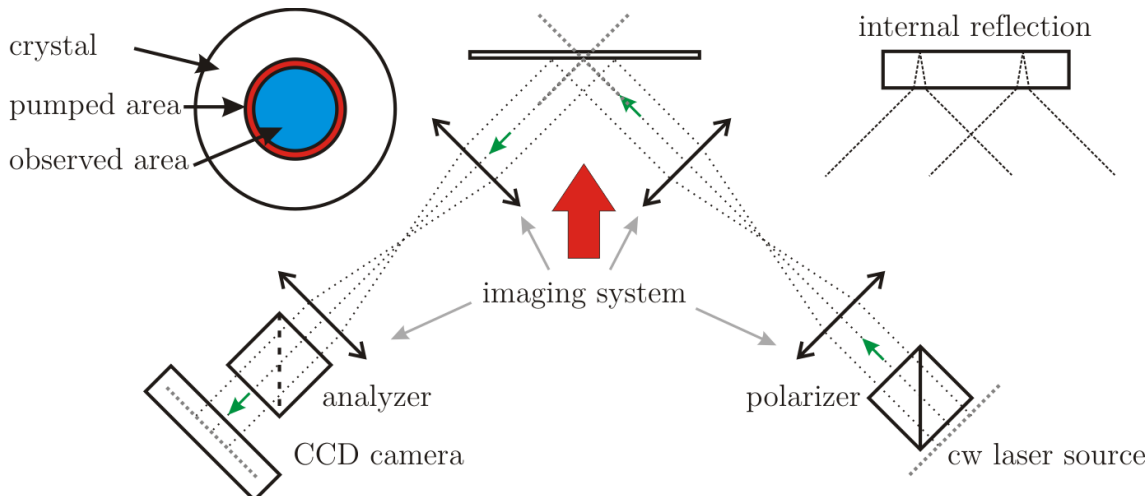


**Figure 4.30.:** Sketch of the experimental setup to measure the thermally induced depolarization. A cw laser source at 1064 nm is imaged onto the gain medium of the laser head. The gain medium is a 60 mm diameter, circular  $\text{Yb}^{3+}\text{:YAG}$  crystal doped at 2 at.% with a thickness of 7 mm. The incoming laser beam is polarized and is reflected from the highly reflective coating on the back side of the crystal. The beam is then imaged onto a CCD camera by passing a rotatable analyzer and optical densities (not shown in sketch).

The general polarization state of light is characterized by the electric field amplitudes in two orthogonal directions ( $\mathfrak{E}_x$  and  $\mathfrak{E}_y$ ) and the relative phase  $\vartheta$  between them.

$$\mathfrak{E} = \begin{pmatrix} \mathfrak{E}_x \\ \mathfrak{E}_y \exp(i\vartheta) \end{pmatrix} \quad (4.5.17)$$

These informations are however not directly accessible. We therefore use three independent measurements to determine corresponding parameters. For simplicity, we consider that the (first) polarizer is oriented along the x-axis.

**Analyzer parallel to x** The analyzer transmits along the x-direction. The intensity seen on the detector is given by:

$$I_1 = \frac{1}{2} c_0 \epsilon_0 |\mathfrak{E}_x|^2 \quad (4.5.18)$$

where  $c_0$  is the velocity of light in vacuum and  $\epsilon_0$  the vacuum permittivity.

**Analyzer parallel to y** The analyzer transmits along the y-direction. The intensity seen on the detector is given by:

$$I_2 = \frac{1}{2} c_0 \epsilon_0 |\mathfrak{E}_y|^2 \quad (4.5.19)$$

**Analyzer set at 45° with respect to x** The direction of the analyzer is rotated to 45° against the x-axis and we get the intensity  $I_3$

$$I_3 = \frac{1}{2} \left( I_1 + I_2 + 2\sqrt{I_1 I_2} \cos \vartheta \right) \quad (4.5.20)$$

Out of these observations we can calculate the phase  $\vartheta$  to be:

$$\vartheta = \arccos \left( \frac{2I_3 - I_2 - I_1}{2\sqrt{I_1 I_2}} \right) \quad (4.5.21)$$

The polarization ellipse itself is rotated by an angle  $\varsigma$  against the x-axis:

$$\varsigma = \arctan \left( \sqrt{I_2/I_1} \right) \quad (4.5.22)$$

This angle is a convenient measure for the depolarization since it corresponds to the angle one must turn the analyzer to achieve extinction on a particular spatial position within the measurement pupil.

$\varsigma$  is measured in [°] and will be used for the following discussion. This method cannot help in identifying if a beam is either unpolarized, circularly or linearly polarized. A fourth measurement with a known phase shift would be necessary to further characterize the nature of the transmitted light.

However, as usually polarizing/polarization sensitive elements are placed within the laser cavity, or at the end of the laser amplifier chain, a depolarization loss corresponding to  $\varsigma$  of  $\sin^2 \varsigma$  would appear. We restrict ourself to the measurement of  $\varsigma$  from now on.

Figure 4.31 shows the measured angle  $\varsigma$  for three different incident average intensity  $I_{avg}$  within a 24.5 mm diameter pupil on the Lucia main laser head. The  $\text{Yb}^{3+}\text{:YAG}$  crystal is oriented with its crystallographic [111]-axis perpendicular to the pumped surface. Ceramics, which are of particular interest for large surface amplifiers, will behave in the same way [151, 152]. Other orientations, like [110] are envisionable for crystals to even further decrease the depolarization in an active mirror extraction layout [150, 153].

The phase shift measured was in every case very close to 0, consequently we omit the discussion for  $\vartheta$ .

Image 4.31(a) gives the map of depolarization when no pump is applied. This intrinsic depolarization exhibits a maximum  $\varsigma$  of  $\approx 0.8^\circ$ . An increase of the pump intensity (b) starts partially to compensate the intrinsic depolarization. For  $I_{avg} \approx 30 \text{ W cm}^{-2}$  a minimum depolarization of  $\varsigma < 0.6^\circ$  is found.

While increasing the pump intensity even further, thermally introduced depolarization overwhelms the intrinsic depolarization and appears in the typical shape illustrated in Figure 4.31(d) and which is subject to textbook explanations [10]. The maximum depolarization angle is  $\varsigma < 3.5^\circ$ .

Figure 4.32 shows the average depolarization angle  $\varsigma$  and  $\varsigma$  in the center of the observation pupil. Within the observed range for  $I_{avg}$ , the average depolarization finds a minimum around  $20 - 30 \text{ W cm}^{-2}$  and starts increasing afterwards again. Intensities below such values are dominated by the intrinsic birefringence. The angle  $\varsigma$  rises approximately linear with increasing incident intensities for observation points close to the center of the crystal.

Further increasing the incident intensity  $I_{avg}$  leads to a higher dissipated power per cross sectional area and consequently increases the thermally induced depolarization loss far beyond the intrinsic value. For higher repetition rates, a compensation becomes necessary.

The most common method comprises a  $90^\circ$  rotator between two identical amplifiers which can compensate the whole thermally introduced birefringence [10]. Both amplifiers have to be identically pumped. It is however somewhat difficult to

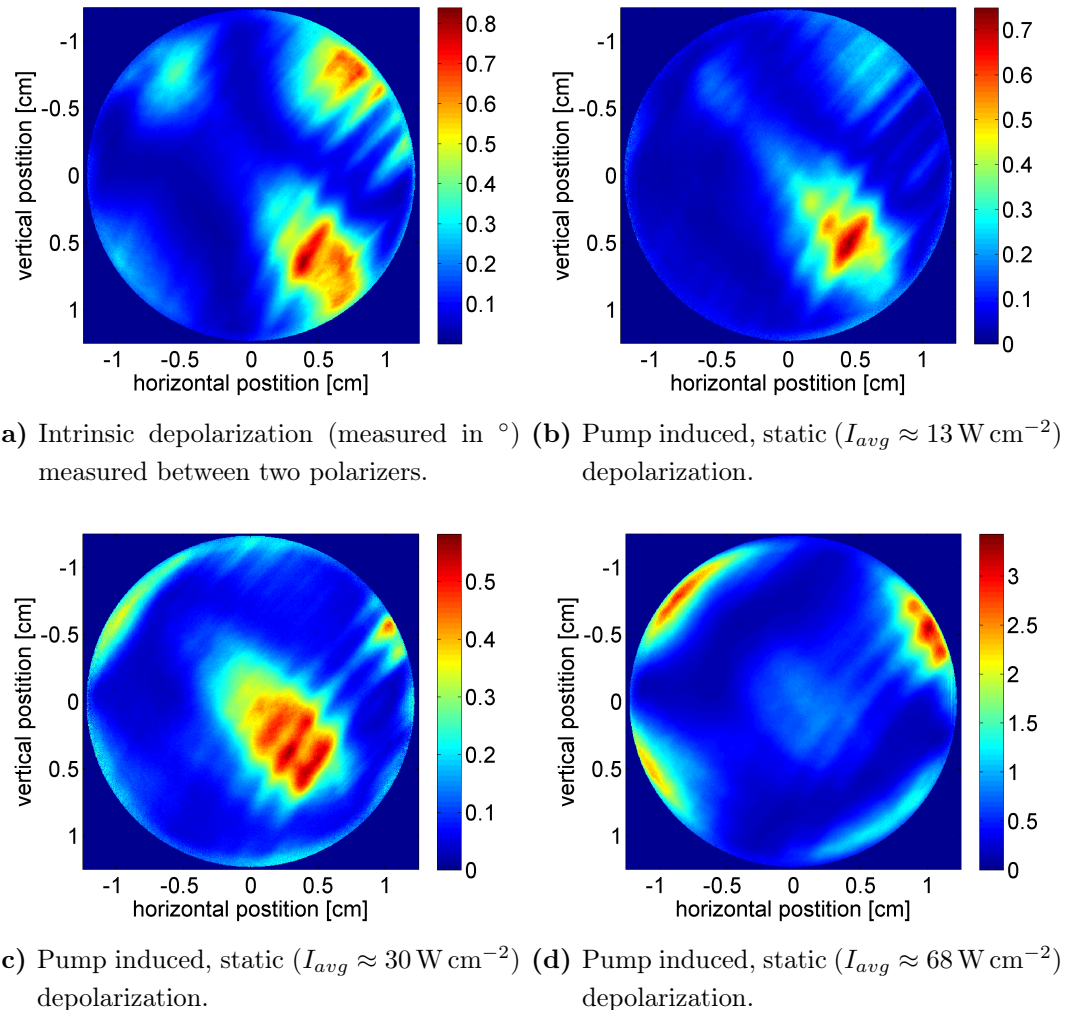


**Figure 4.31.:** Intrinsic and pump induced polarization (colorbar in  $^{\circ}$ ) on the Lucia amplifier head for four different average pump intensities measured at 1064 nm between crossed polarizers as sketched in Figure 4.30.

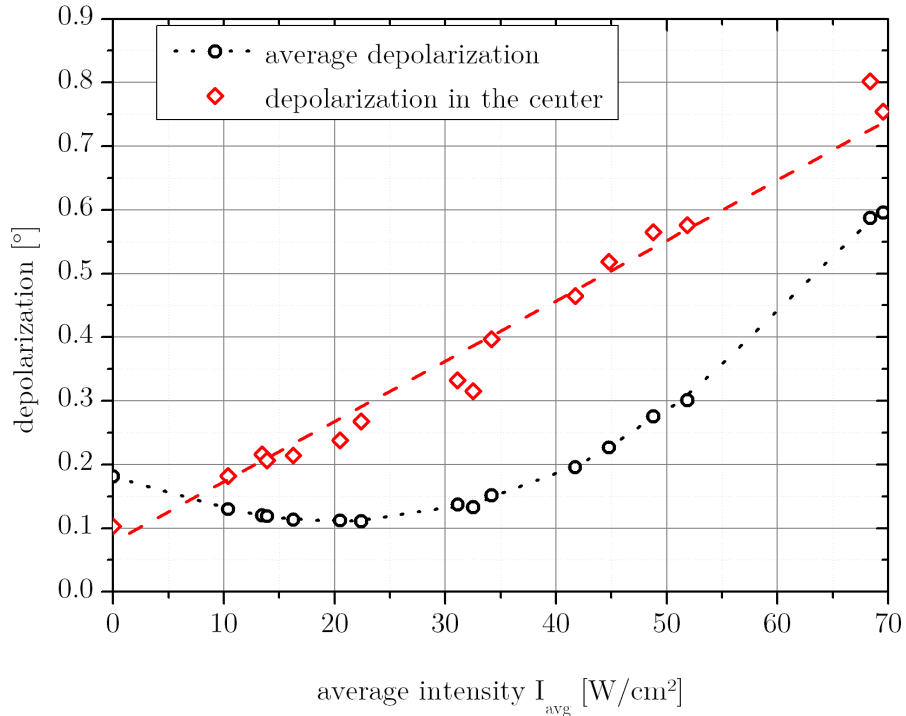


**Figure 4.32.:** Measured depolarization in the center and as the average over the pupil.

produce large rotators.

To circumvent the necessity of large rotators, a similar method uses a quarter-wave plate [154]. Such large wave plates show a better compatibility with large size, high-power laser systems. This method cannot completely compensate the thermally induced birefringence, but at least strongly reduce it [155]. Both methods can be extended to a single amplifier setup [156].

## 4.6. Conclusion

The laser gain medium performance can be severely affected by thermally induced effects ranging from wavefront deformation, birefringence and ultimately catastrophic damage of the gain medium itself.

We discussed in detail the origin of the heat generation, the physical basis of the thermal conductivity and heat transport through the laser gain medium. A one-dimensional steady state and transient model was presented for the active mirror scheme.

We showed that, if the observed transverse position is far away from the edge of the pumped area and the pumped surface is large compared to the thickness, a one-dimensional analysis might be satisfying. This is similar to the thin-disk approximations in heat flow. The resulting heat distribution is of parabolic shape. However, for a partially pumped surface, considering a transverse temperature variation is of importance.

The required cooling capacity of the Lucia amplifier head was estimated to be satisfied with a heat exchange coefficient varying between  $h \approx 10.000 \text{ W m}^{-2} \text{ K}^{-1}$  and  $h \approx 20.000 \text{ W m}^{-2} \text{ K}^{-1}$ . Higher values do not significantly increase the cooling capacity.

A cooling solution (jet-plate setup)<sup>4</sup> was realized and experimentally assessed. The heat exchange coefficient  $h$  estimated to be  $h \approx (16,500 \pm 1000) \text{ W m}^{-2} \text{ K}^{-1}$ .

The general origin of the wavefront deformation is discussed. For the case of an active mirror, a simplified model is derived. The deformation is mainly attributed to the mechanical deformation of the gain medium. The resulting focal length is negative and the scaling law given by:

$$|f| = \frac{k}{\alpha_T \eta_h \eta_{abs} I_{avg}}. \quad (4.6.1)$$

Consequently, the thermally induced lens gets shorter with an increasing absorbed (temporally averaged) intensity  $\eta_{abs} I_{avg}$ . Knowledge about the heat generation is of great significance, as  $f \sim 1/\eta_h$ .

Evidence of the temporally dependent in-pulse heat generation due to the lifetime of the upper laser state is found on the millisecond timescale.

---

<sup>4</sup>This solution was selected for Lucia after fruitful discussions with A. Giesen while he was working at the IFSW, Stuttgart, Germany.

The simplified, one-dimensional model describes the steady state deformation appropriately in the thin-disk approximation. A three dimensional model is nevertheless necessary to explain the deformations observed in the case of the Lucia amplifier head. The results drawn out of this model gives full access to the understanding of the deformation, including the thermal lens effect and bulging of the surfaces.

The thermally induced birefringence is found to be small and comparable with the intrinsic depolarization. Further increase in average intensity brings up the necessity to evaluate the depolarization with a more refined model.

It can be concluded, that the laser head developed and validated here satisfies thermal management requirements imposed by the high average power operation of the Lucia laser system in the context of the first Lucia milestone.

An efficient cooling is crucial for high average power applications. Its optimization is one of the central task for such system.



# 5. Lucia Amplifier Performance

## 5.1. Motivation

After assessing energy storage limitations using a three dimensional ASE-code in chapter Chapter 3, observing the thermal behavior for a repetition rate of up to 2 Hz in terms of wave front deformation as well as depolarization of the laser beam traveling through the laser gain medium in Chapter 4, we will discuss the energy performance of the Lucia main amplifier in this Chapter.

The first part is dedicated to the energy extraction on the main amplifier head and a second part of this Chapter discusses ameliorations and foreseen developments within the context of the Lucia laser system.

## 5.2. Lucia amplifier performance estimation

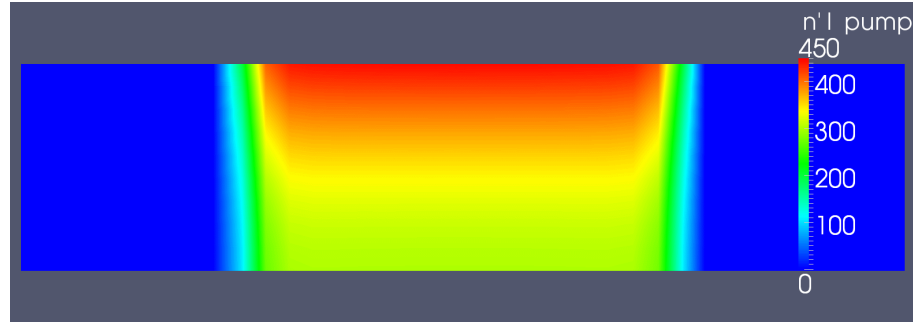
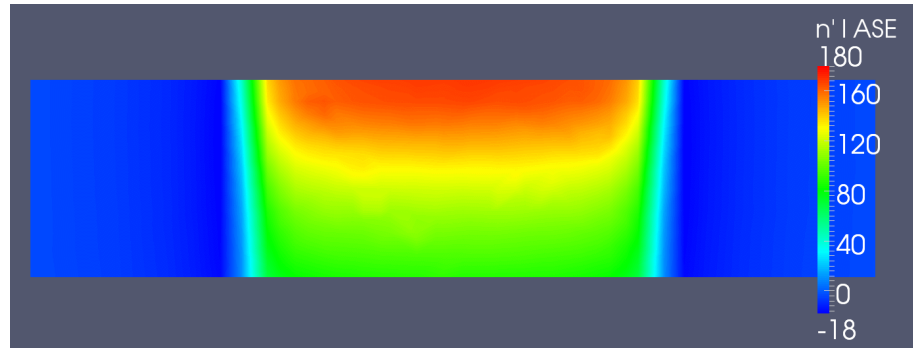
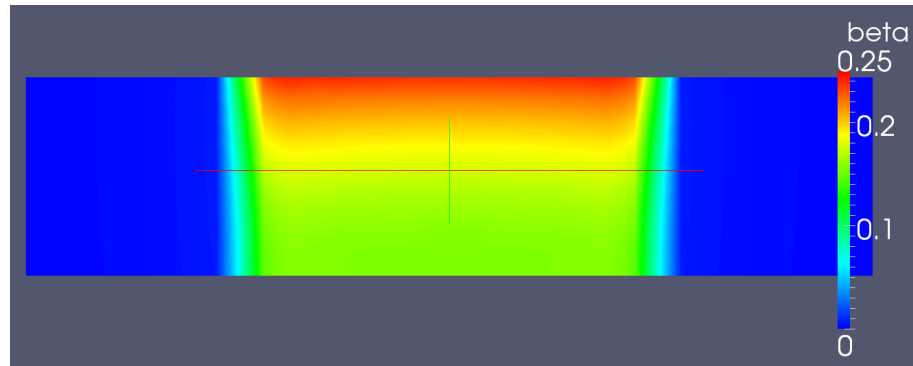
The three dimensional model considering ASE introduced in Chapter 3 is the basis for the following stored energy estimation. It should be recalled, that the surfaces are taken perfectly absorbing, therefore no reflections of ASE are taken into account in the model.

Parasitic oscillation are supposed to be suppressed, which is in good accordance to the results shown in Figure 3.31 (page 118).

Let us recall that the gain medium is a 2 at.% doped  $\text{Yb}^{3+}$ :YAG crystal with a diameter of 60 mm and a thickness of 7 mm. The pumped area is approximated to a circular, super-Gaussian (order 20) shaped pump profile with a peak intensity of  $16 \text{ kW cm}^{-2}$ . The pump pulse duration is set to be 1 ms.

Figure 5.1 shows the numerical result for  $d\beta/dt$  due to the pump (a), due to ASE (b) and the distribution of  $\beta$  (c) at the end of the 1 ms long pump pulse. ASE is clearly of importance, as the maximum value for the ASE depopulation in (b) is only a factor of  $450/180 = 2.5$  below that of the population increase due to the pump action (b).

We consider, in a good approximation, the spatial profile perpendicular to the pump axis to be uniformly distributed over the surface, where extraction takes place. The distribution of  $\beta$  along the pump direction is illustrated in Figure 5.2.

(a)  $d\beta/dt|_P$  after 1 ms pumping at  $16 \text{ kW cm}^{-2}$ (b)  $d\beta/dt|_{ASE}$  after 1 ms pumping at  $16 \text{ kW cm}^{-2}$ (c)  $\beta$  after 1 ms pumping at  $16 \text{ kW cm}^{-2}$ 

**Figure 5.1.:** Simulation results for the Lucia main amplifier 2 at.% doped, 7 mm thick Yb<sup>3+</sup>:YAG crystal pumped at an intensity of  $16 \text{ kW cm}^{-2}$  for 1 ms at 940 nm. The three cuts are performed along the 60 mm long diameter of the crystal (horizontal dimension). The relative excitation is defined as  $\beta = \hat{n}/\hat{n}_{tot}$ . The pump pulse arrives from the top. The thickness (vertical axis) is stretched by a factor of 2 for visualization.

Even with the use of an active mirror concept, we see a difference of a factor 1.5 between the population on the front surface and the back surface.

While, within the pump duration,  $F_{inj} = 16 \text{ J cm}^{-2}$  are injected and 90 % of the energy is absorbed ( $14.4 \text{ J cm}^{-2}$ ),  $F_{st,ideal} = 9 \text{ J cm}^{-2}$  are stored without the additional ASE-losses. This would correspond to the immediate results out of a simple ASE-less code. Using the developed 3D code, the energy density distribution along the z-axis is computed (see Figure 5.2). An integration along the z-axis shows that only  $F_{st} = 6.8 \text{ J cm}^{-2}$  are predicted to be stored in the central part, when considering ASE action. In total  $2.2 \text{ J cm}^{-2}$  are lost to ASE. This signifies an important impact of ASE action.

As Yb<sup>3+</sup>:YAG is a quasi-three level system, a minimum relative population  $\beta_{min} = \sigma_a / (\sigma_a + \sigma_e)$  is necessary to overcome the reabsorption at the laser emission wavelength. For room temperature, this values is  $\beta_{min} \approx 4.4\%$  for Yb<sup>3+</sup>:YAG. The calculated average  $\bar{\beta}$  is 18.1 % leaving, after the consideration of  $\beta_{min}$ , a  $\bar{\beta}' = 13.7\%$ . This corresponds to an extractable energy density of  $F_{extr} = 5.1 \text{ J cm}^{-2}$ . Consequently, the maximum achievable optical-optical efficiency is  $\eta_{o-o} = 31.8\%$ . Table 5.1 summarizes the results with an overview over the energy densities and the optical-optical efficiency.

We can now estimate the energy extraction for the four passes within the gain medium. A one dimensional model uses the retrieved  $\beta$ -distribution along the extraction direction shown in Figure 5.2 to compute the output energy density as a function of the input energy density and the amplifier round trip losses. The result is shown in Figure 5.3.

variable		value
injected energy density	$F_{inj}$	$16 \text{ J cm}^{-2}$
absorbed energy density	$F_{abs}$	$14.4 \text{ J cm}^{-2}$
stored energy density without ASE	$F_{st,ideal}$	$9 \text{ J cm}^{-2}$
stored energy density with ASE	$F_{st}$	$6.8 \text{ J cm}^{-2}$
non-extractable energy density	$F_{non-extr}$	$1.7 \text{ J cm}^{-2}$
extractable energy density	$F_{extr}$	$5.1 \text{ J cm}^{-2}$
maximum o-o efficiency	$\eta_{o-o}$	31.8 %

**Table 5.1.:** Energy storage and extractable energy for the Lucia main amplifier head pumped at  $16 \text{ kW cm}^{-2}$  for 1 ms.

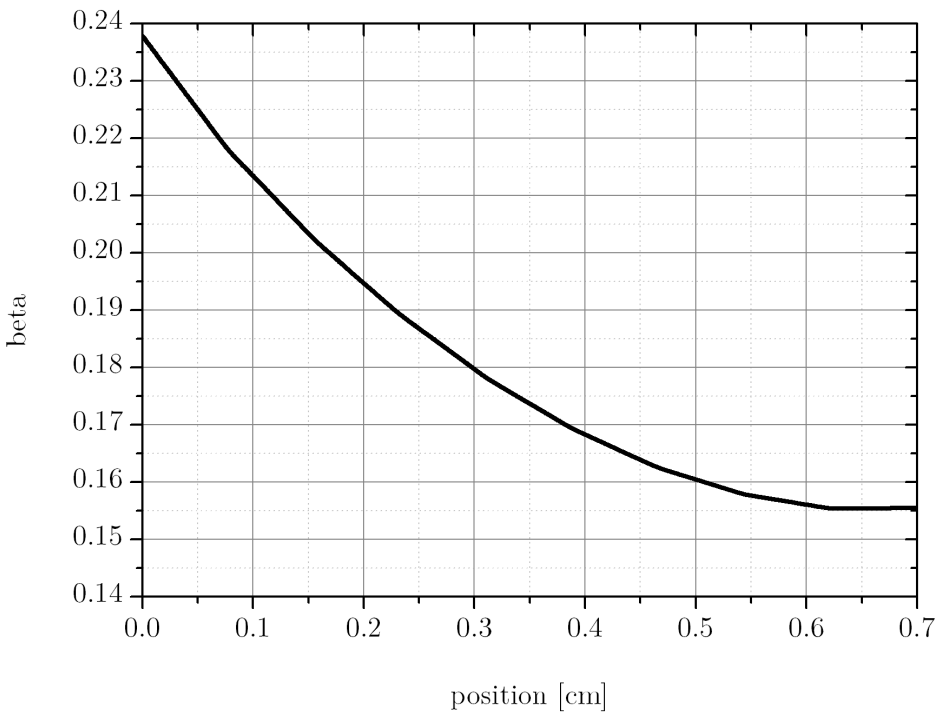


**Figure 5.2.:**  $\beta$ -distribution in the center along the pump axis of Figure 5.1(c).

Typical input energy densities provided by the Lucia front-end are in the order of  $20 \text{ mJ cm}^{-2}$  to  $50 \text{ mJ cm}^{-2}$ . Without considering any losses, energy densities between  $2.2 \text{ J cm}^{-2}$  and  $3.4 \text{ J cm}^{-2}$  are expected. For single pass losses of 10 %, these values are reduced to  $1.6 \text{ J cm}^{-2}$  and  $2.5 \text{ J cm}^{-2}$  respectively.

As an example, considering an input energy of  $110 \text{ mJ}$  within a  $22 \text{ mm}$  diameter circular beam incident under  $25^\circ$  to the surface normal, we get an input energy density of  $\approx 26 \text{ mJ cm}^{-2}$ . In the case of a lossless beam transport, an output energy density of  $2.55 \text{ J cm}^{-2}$  is found, while in the case of 10 % losses this value is reduced to  $1.85 \text{ J cm}^{-2}$ . This corresponds to energies between  $10.8 \text{ J}$  and  $7.8 \text{ J}$ .

Figure 5.4 shows the gain  $G$  for the four passes as a function of the input energy density in the case of a lossless beam transport. Input energy densities above  $0.1 \text{ J cm}^{-2}$  will bring a strong depletion for the last pass.

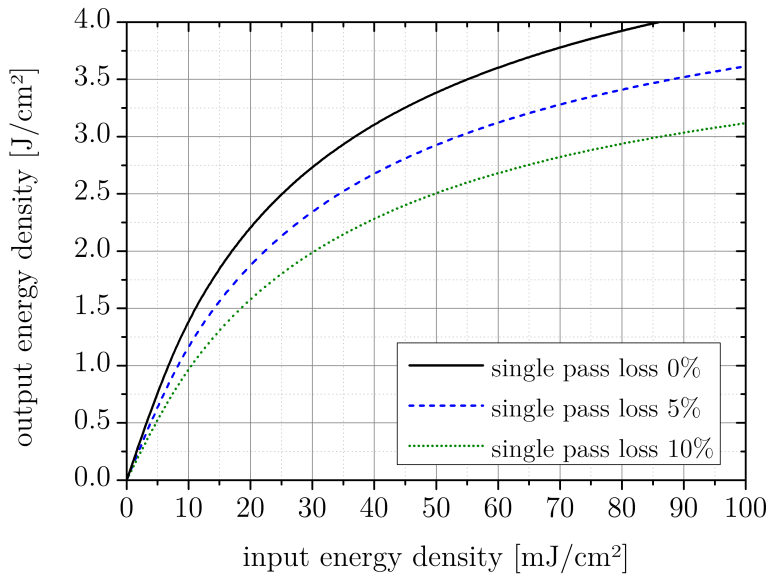


**Figure 5.3.:** Estimation of the output energy density (vertical axis) as a function of the input energy density of the extraction beam (horizontal axis) for the Lucia main amplifier after four passes. The loss is given as a loss per pass in the amplifier.

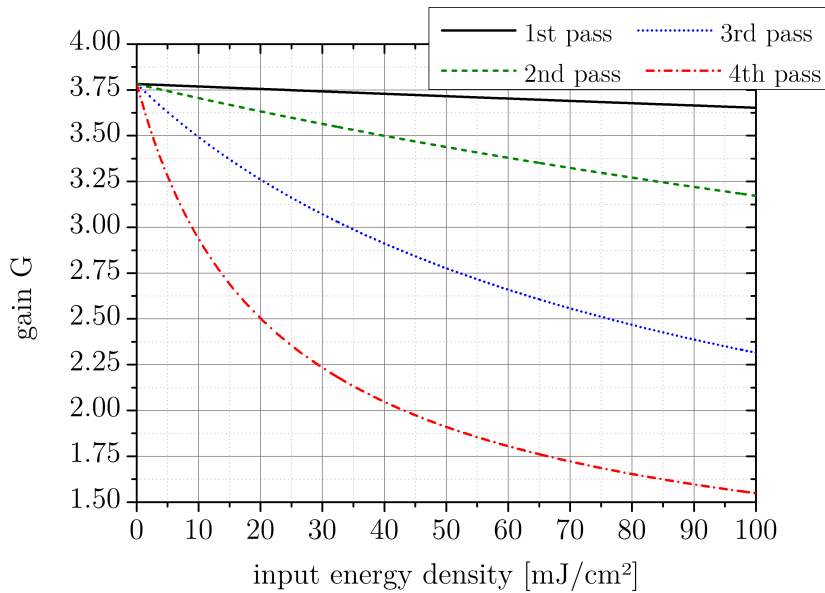


**Figure 5.4.:** Estimated gain  $G$  (vertical axis) for the first four passes in the main amplifier as a function of the input energy density (horizontal axis).

### 5.3. Energy extraction

Let us recall how energy build-up is realized in the Lucia laser system. The oscillator generates pulses at a repetition rate of 2 Hz and energies in the order of 340  $\mu\text{J}$ . Those pulses are amplified in two pre-amplification stages. The energy output of the second stage is in the order of  $\sim 140 \text{ mJ}$ . Finally the beam periphery is apodized through the beam shaping stage, where the apodizer, combined with the spatial filtering, allows, for the experimentally used beam shape, a transmission of 80 %. This results in an energy of  $\sim 110 \text{ mJ}$  available at the entry of the first pass of the Lucia main amplifier.

The angular-multiplexed four-pass extraction architecture of the Lucia final amplification stage is sketched in Figure 5.5. A first amplification pass is realized by imaging the apodizer using an imaging telescope (not depicted) onto the pumped gain medium. The gain medium plane is then imaged onto itself after propagating twice the imaging telescope (4f-assembly with  $f = 1 \text{ m}$ ) shown in Figure 5.5.

To this point, the apodizer plane is strictly imaged. The transition from the second to the third pass occurs under free propagation with a total distance of 4.5 m since no image relay telescope is used. Consequently all the wavefront deformations introduced by the foregoing propagation will impact the intensity distribution arriving on the amplifying medium. The fourth and final pass takes place after traveling through the imaging telescope again.

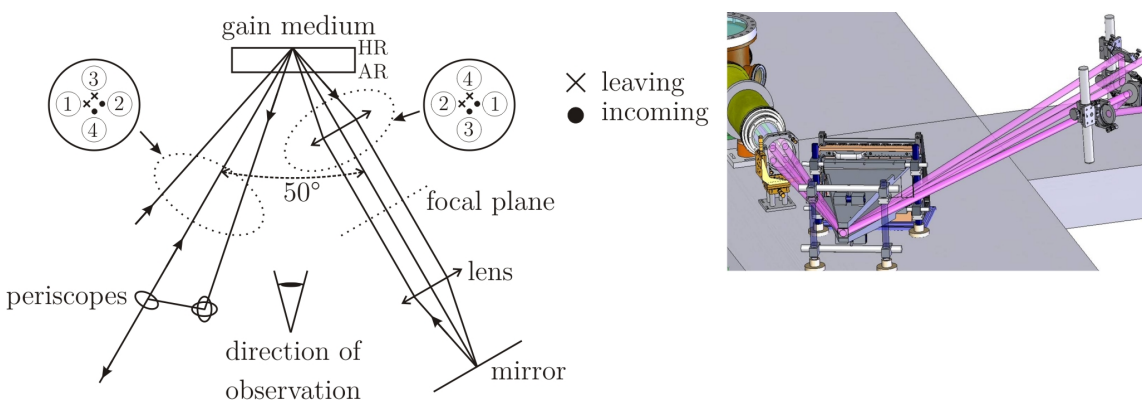


**Figure 5.5.:** The Lucia final amplification stage bases on two arms – an image-relayed arm (right arm) and free propagation (left arm). Both are separated by 50°. The dotted circles indicate the positions of the observation planes explaining the beam sequence. The direction the corresponding beam is traveling through these planes is indicated by crosses (moving towards crystal) and dots (coming from it). The passes are labeled from 1 to 4. The picture on the right gives an illustrative image of the experimental setup.

Figure 5.6 depicts the intensity distributions after the first and second pass in the Lucia main amplifier. While the image (a) is recorded after the first pass without any pump action, (b) shows the same beam shape, but amplified at a repetition rate of 2 Hz. After the second pass, the image is consequently flipped, which is shown for an amplification with 2 Hz in (c).

The images for the first and second pass were gathered separately and exhibit therefore a different input intensity distribution. Nevertheless, as the beam shape was imaged from one plane to the next, no distortion in the intensity distribution is observed.

The energy evolution with respect to the driving current of the Laser Diode Array (LDA) is shown in Figure 5.7 for the first (a) and the second pass (b) for repetition rates of 2 Hz and 0.1 Hz. The injected energy was  $\approx 110$  mJ for both cases.

The change in repetition rate affects the amplifier performance, as the gain depends on the temperature. The difference in the first pass is 10 % – the maximum energy found is 500 mJ for 0.1 Hz, while 440 mJ were obtained at a repetition rate of 2 Hz for an input energy of 110 mJ.

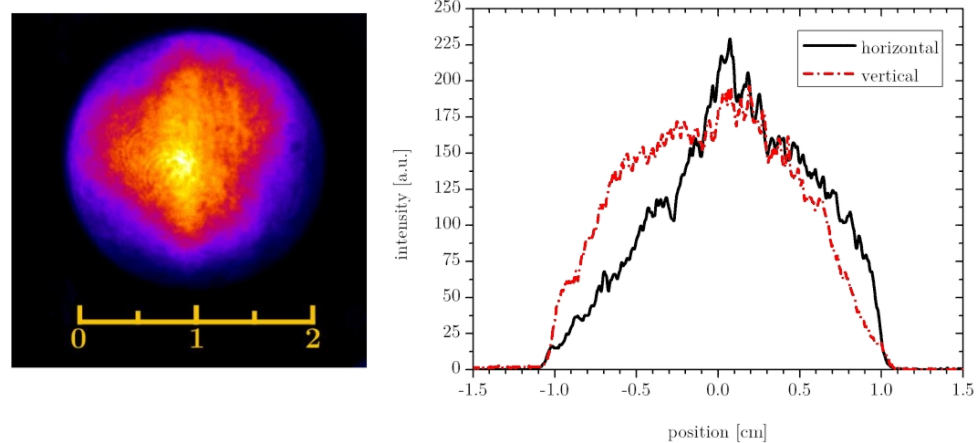
For the second pass, the difference of obtained energy is  $\approx 150$  mJ (1.5 J vs. 1.35 J) for a driving current of 150 A, which corresponds again to the 10 % difference found in the preceding pass.

The energy measurement uncertainty is  $\approx 5$  %. Figure 5.8 shows the beam shape after four passes in the main amplifier without amplification (a), fully amplified at 0.1 Hz (b) and at 2 Hz (c). The main difference to the preceding passes is the 4.5 m long free propagation between the second and third pass.

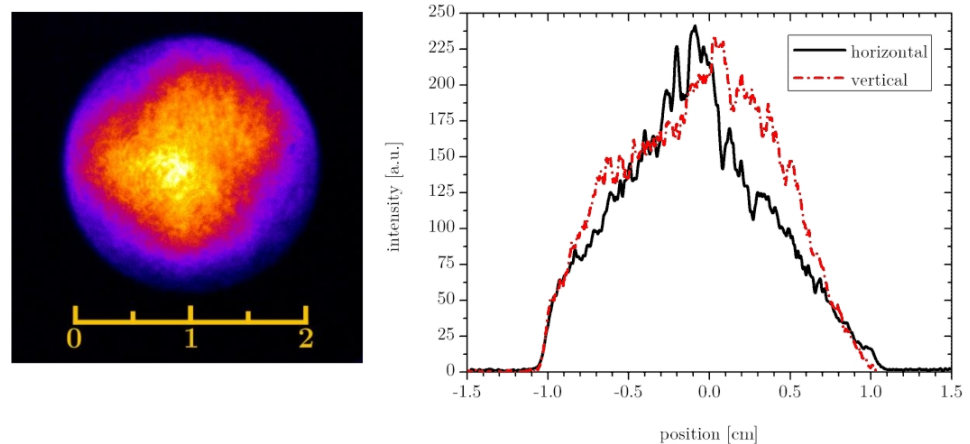
While comparing Figure 5.6(a) and 5.8(a), it appears that the extraction surface is reduced from  $\sim 4.2$  cm<sup>2</sup> to  $\sim 2.8$  cm<sup>2</sup>. This makes it somehow more difficult to extract energy, as the usable stored energy is reduced by a factor of 1.5 too. Gain depletion sets slowly in for the last two passes (see Section 5.2).

The resulting energy (after four passes) as a function of the driving current of the laser diodes on the LDA is shown in Figure 5.9 for repetition rates of 2 Hz and 0.1 Hz.

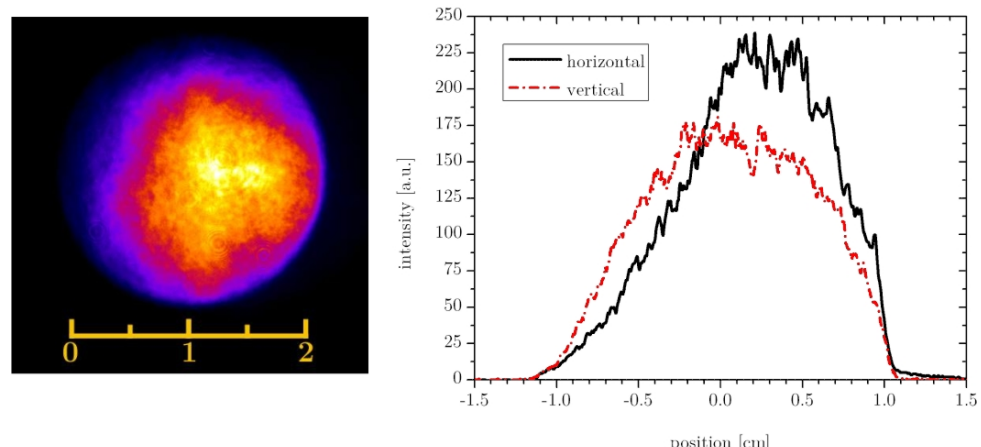
The injected energy of  $\approx 110$  mJ is amplified in four passes to 7 J at 0.1 Hz and to 6.6 J at 2 Hz respectively. Again, the difference is related to the thermal performance of the laser system. However as it is seen at the end of the trail, both curves start to close up. This is related to the saturation of the laser gain medium.



(a) 1st pass, no pump applied, horizontal and vertical lineouts are shown on the right

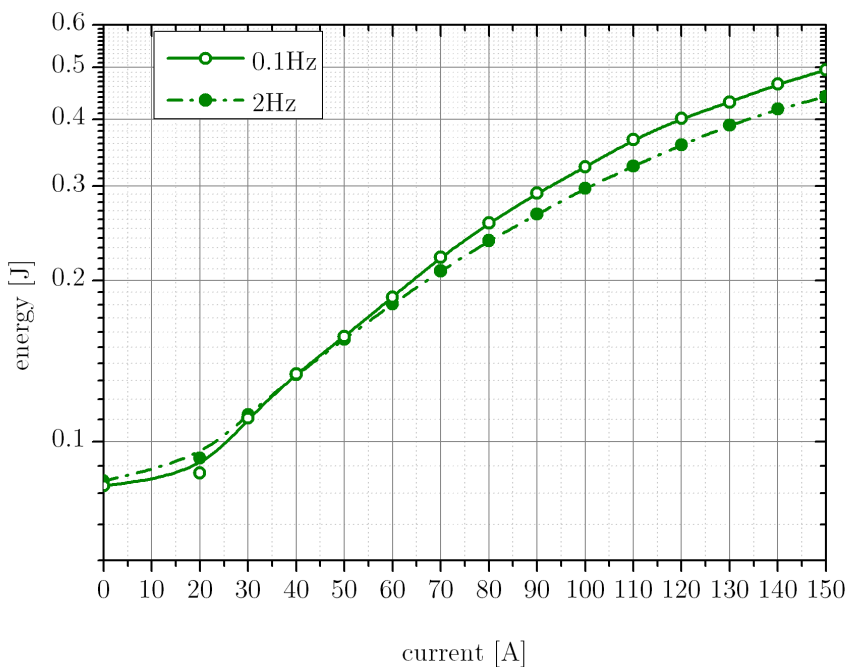


(b) 1st pass, 150 A, 2 Hz, horizontal and vertical lineouts are shown on the right

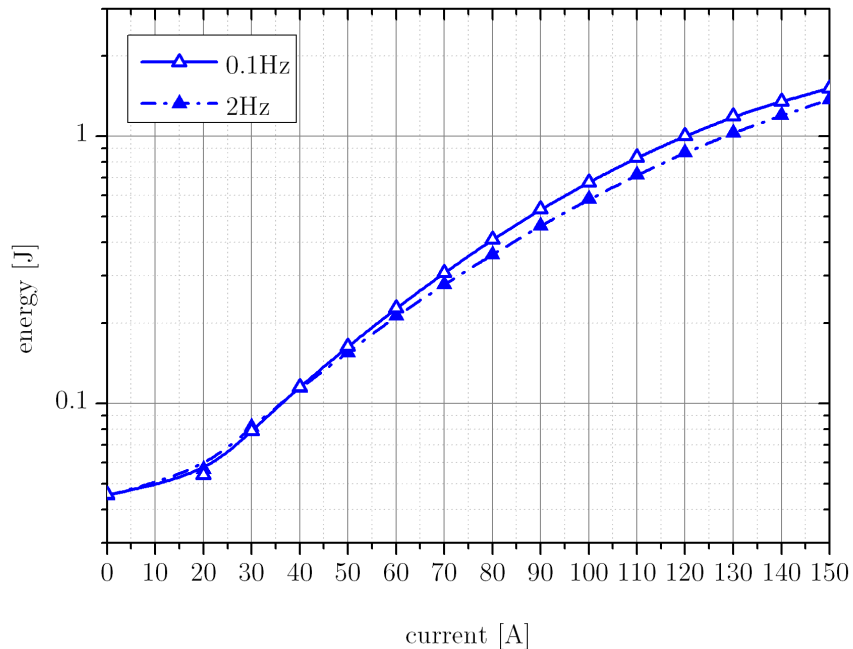


(c) 2nd pass, 150 A, 2 Hz, horizontal and vertical lineouts are shown on the right

**Figure 5.6.:** Beam shape in the image relay plane after one pass without amplification (a) and with maximum laser diode current applied to the LDA (150 A) (b). Subfigure (c) illustrates the beam shape after the 2nd pass with maximum amplification. The repetition rate for (b) and (c) is 2 Hz. The scale is in [cm].

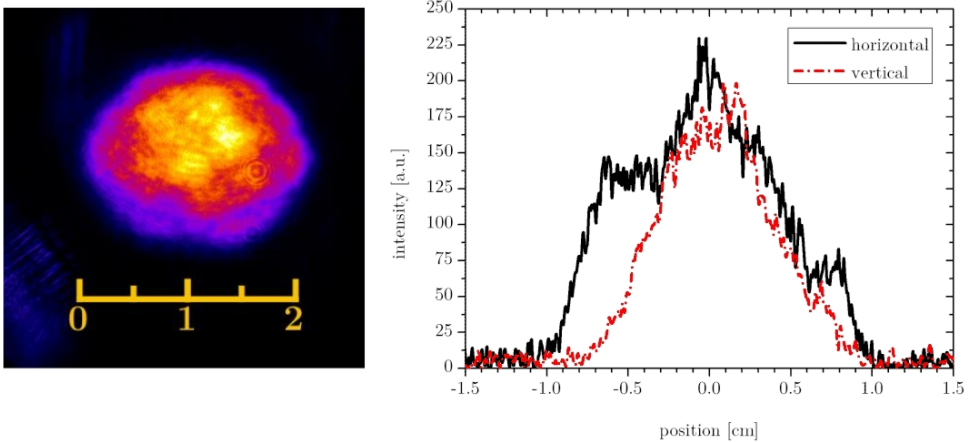


(a) 1st pass for 2 Hz and 0.1 Hz repetition rate

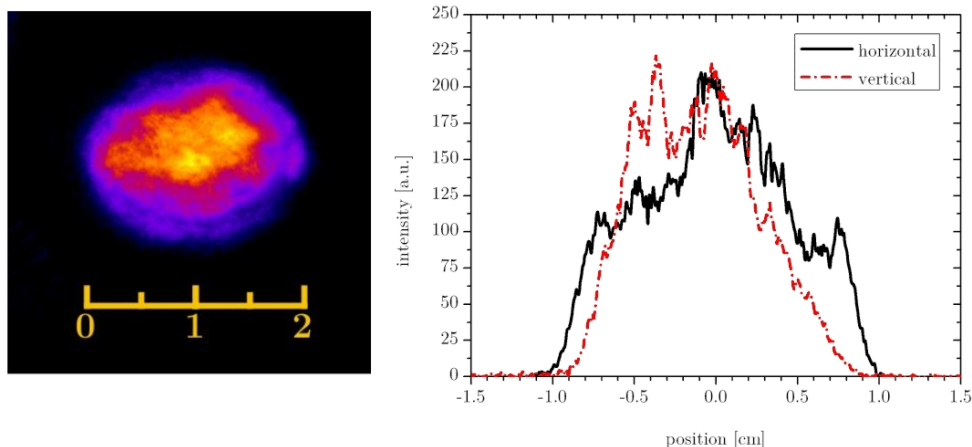


(b) 2nd pass for 2 Hz and 0.1 Hz repetition rate

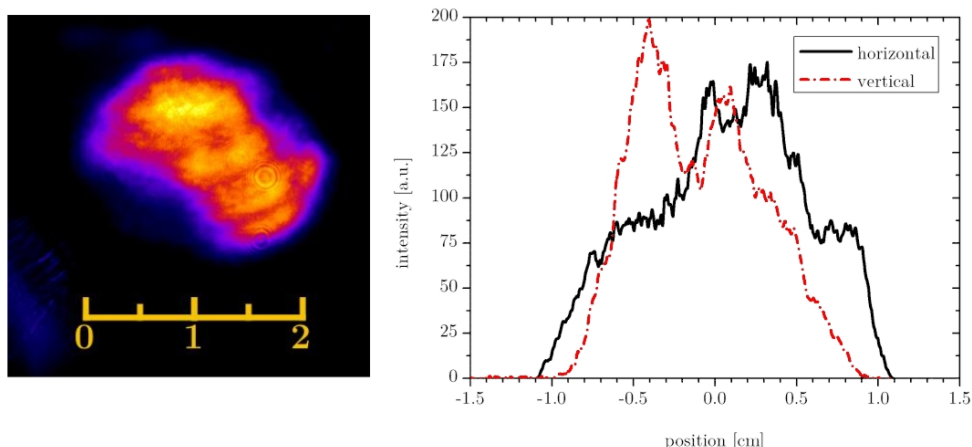
**Figure 5.7.:** Main amplifier performance for 0.1 and 2 Hz in one pass (a) and two passes (b) for 110 mJ injection.



(a) 4th pass, no pump, horizontal and vertical lineouts are shown on the right



(b) 4th pass, 150 A, 0.1 Hz, horizontal and vertical lineouts are shown on the right



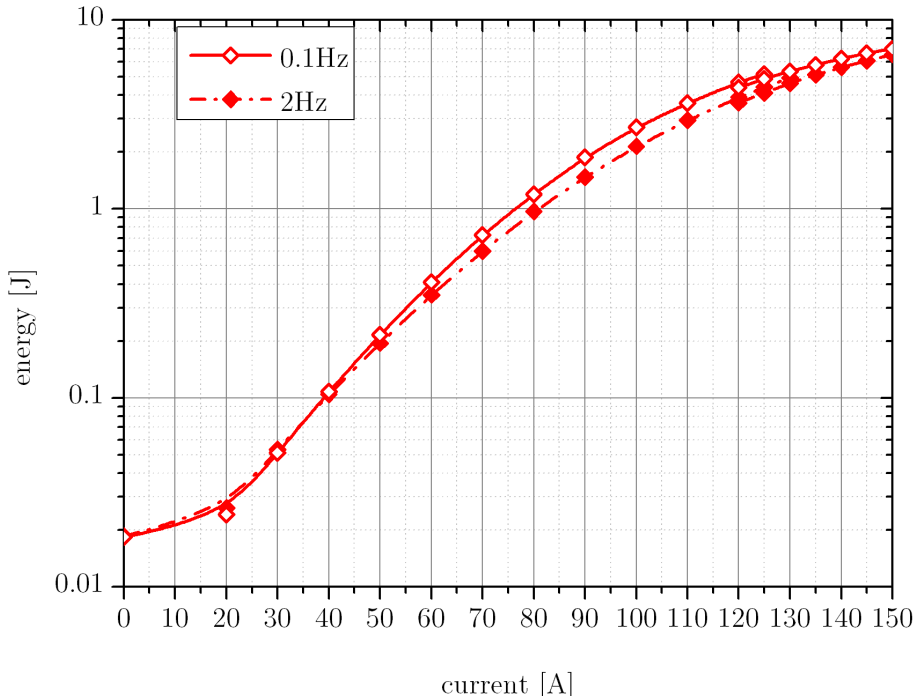
(c) 4th pass, 150 A, 2 Hz, horizontal and vertical lineouts are shown on the right

**Figure 5.8.:** Beam shape in the image relay plane after four passes without amplification (a) and with maximum laser diode current applied to the LDA (150 A) (b) at 0.1 Hz (b) and 2 Hz (c). The shown scale is in [cm].

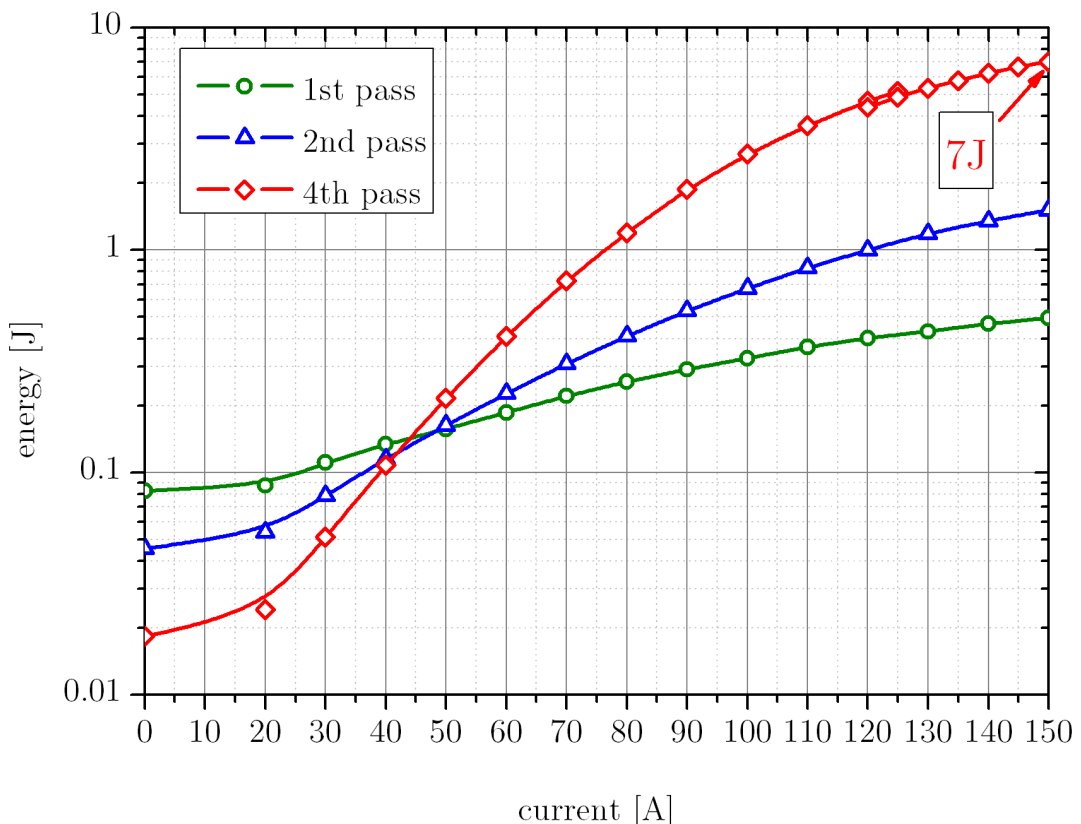
The available energy is efficiently extracted ( $7/2.8 \times 5.1 \approx 49\%$ ), but the optical-optical efficiency (total emitted energy of the LDA) is considerably small ( $\eta_{o-o} \approx 7\text{ J}/123\text{ J} \approx 5.7\%$ ).

Figure 5.10 shows a compilation for the four passes within the amplifier for a repetition rate of 0.1 Hz. It should be recalled, that the three curves were recorded independently. This is the origin of the absence of a shared crossing around 45 A of laser diode driving current.

A future increase in energy demands an improvement in spatial beam quality which might be achieved by correcting the beam deformation or an application of the image relay technique to the second arm of the laser amplifier as well.



**Figure 5.9.:** Fourth pass in the main amplifier for a repetition rate of 2 Hz and 0.1 Hz. The drop at currents around 120 A is related to a filter change during which the output power of the pre-amplified laser pulse dropped by  $\approx 6\%$ .



**Figure 5.10.:** Performance of the Lucia main amplifier in one (green circles), two (blue triangles) and four passes (red diamonds) for a repetition rate of 0.1 Hz. 500 mJ are achieved for one pass, 1.5 J for two passes and finally 7 J after four passes.

## 5.4. Perspectives

### 5.4.1. Static Astigmatism Correction

The correction of accumulated wavefront deformations is an important step towards beam quality improvement. As it is shown in the foregoing section such wave front deformation can severely impact the intensity distribution when the beam experiences free propagation. But, even if the beam is image relayed, wavefront aberrations alter the intensity distribution on the imaging optics (i.e. lenses), potentially leading to LIDT issues.

An aberrated wavefront can be represented as a projection on the Zernike polynomials and its dynamic correction can be achieved with a closed-loop counter-reaction system. For static wave front deformations, low order Zernike polynomials can be compensated using static devices, e.g. a parabolic wave front deformation is compensated using an appropriately bent mirror or lens. Static astigmatism can be addressed in a similar way [157].

We developed a correction apparatus based on a reflective, free standing surface (i.e. a mirror) is deformed using four actuators, as shown in Figure 5.11. The mechanical deformation is transferred into a wave front deformation by reflection on the surface of the mirror. Figure 5.12 shows the experimental setup of the static astigmatism corrector we have developed.

In order to evaluate the performance of the static corrector, a wave front analysis (similar to the measurement setup shown in Section 4.4.2) of the reflected wave front was performed. As a first test, a 10 mm thick highly reflective mirror (under  $0^\circ$ ) is bent (Figure 5.12(a)) and generates a strong Zernike polynomial for  $0^\circ$  astigmatism (Figure 5.12(b)).

Such a compensation technique and its impact on the energy extraction is currently under observation.

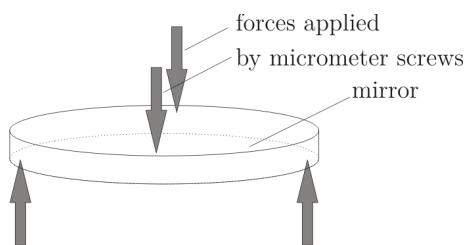
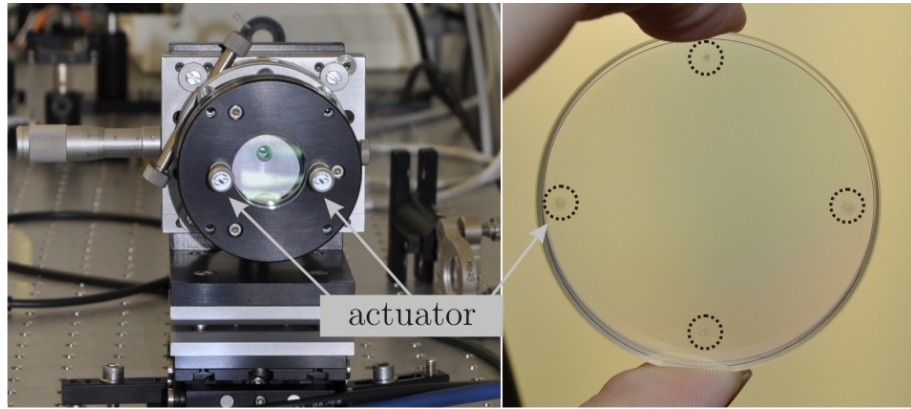
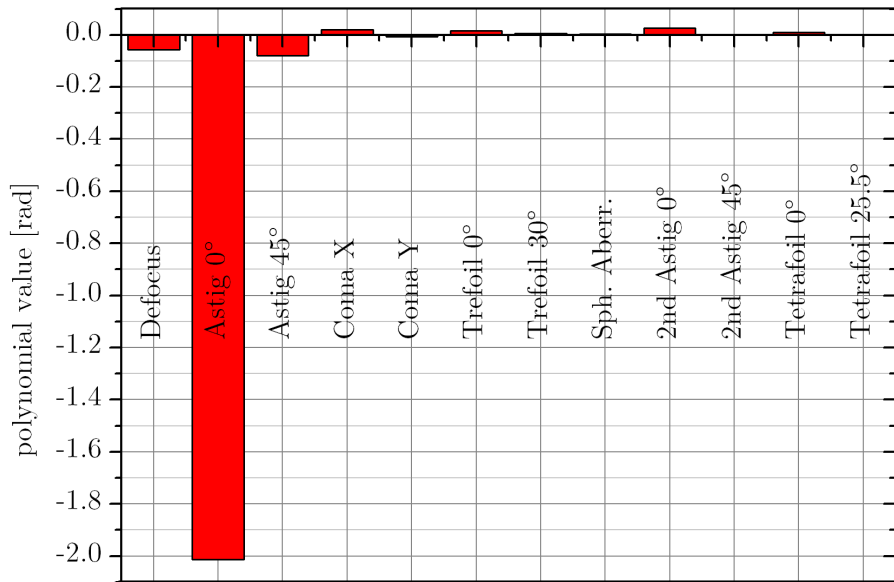


**Figure 5.11.:** Four micrometer screws apply forces on a free standing mirror. Its surface is deformed to statically compensate the astigmatism of an incident wave front.



(a) Static deformable mirror for astigmatism correction. The assembly is shown on the left and a mirror used for testing with the imprints of the micrometer crews on the right.



(b) The first twelve Zernike polynomials retrieved from a measurement of the reflected wavefront.

**Figure 5.12.:** A typical example decomposition of a measured wavefront deformation introduced by the bent mirror (a) shows a strong astigmatism (b). The test wavelength was 1064 nm and the observed surface 20 mm in diameter.

### 5.4.2. Doping variation along the pump axis

Until now we considered a homogeneously doped laser gain medium. As it was discussed in the context of ASE (Chapter 3) and thermal management (Chapter 4), such gain media show a rather unfavorable aspect: the (in first order) exponential absorption of the pump light results in an longitudinal exponential energy deposition. This is unfavorable in two ways:

- The energy deposition, thus the heat load, along the pump direction is inhomogeneous.
- The gain distribution along the pump direction is inhomogeneous.

In the case of an end-pumped radially cooled rod the first point is the most serious. In this particular case, the gain medium temperature varies with the position along the pump axis. The probability of reaching the thermal fracture limit is therefore strongly dependent from the position within the gain medium.

For a disk amplifier, the second point is more important. An inhomogeneous longitudinal energy deposition leads to a localized (in the vicinity of the pumped surface) gain depopulation due to ASE and, potentially, to parasitic oscillations. It is therefore of interest to get a uniform gain distribution.

As the intention is to store the same amount of energy with a uniform gain distribution, a smaller volume is required. This reduces the thickness (extend along the pump direction) for disk amplifiers. The average temperature as well as the temperature difference between the surfaces are also reduced.

This is of special interest for a quasi-three level system, like  $\text{Yb}^{3+}\text{:YAG}$ , as it exhibits a temperature dependent reabsorption at the laser emission wavelength. Also, it ensures, that each position within the gain medium shows a significantly higher relative population density  $\beta$  compared to the minimum  $\beta_{min}$ . This guarantees a maximum extractable energy density.

It may be asked, how this uniformly gain distribution may be achieved. One possibility would be to use multiple passes of the pump light in order to flatten the absorption profile (beam recycling). This can be improved by the use of counter-propagating pump pulses or in combination with the active mirror concept. This method requires a high brightness of the pump beam.

A different approach is to adapt the absorption profile in such a way, that the resulting gain profile will be uniform. However, such a profile will be fixed to one pump condition only.

The most obvious solution is to split the gain medium into several steps with varying doping concentrations. This approach is intensively discussed for longitudinal pumped rods in [24]. It is found, that the most sensitive part is the first doping step, as every following absorption is dependent on it. For cooling, it is even more interesting for those doped slices to be separated from each other and cooled in between (e.g. using a gas jet) allowing a significant decrease in temperature. However, conditions for internal reflections must be seriously considered to avoid parasitic lasing (see Section 3.5). Bonding several doping steps is possible, but becomes, with an increasing number of doping steps, more and more complicated.

The more fine the doping steps are, the more uniform will be the gain distribution. This leads to the transition from discrete doping steps to a continuous doping distribution.

Let us consider a monochromatic, constant pump incident from one side (without backreflection). The geometry shall be one dimensional.

In order to achieve a constant longitudinal gain distribution, the necessary doping distribution will be, in first order, hyperbolic (see Annex, Equation A.1.15):

$$\hat{n}_{tot}(z) = \frac{\hat{n}_{tot}(0)}{1 - z/z_{crit}} \quad (5.4.1)$$

where  $\hat{n}_{tot}(z)$  is the longitudinal doping density distribution,  $z_{crit} = (\hat{n}_{tot}(0) \sigma_{a_P})^{-1}$  the critical thickness,  $\sigma_{a_P}$  the absorption cross section at pump wavelength and  $z$  the pump direction.

The more the pump penetrates the gain medium, the higher the absorbed fraction of the remaining energy must be. The pump efficiency  $\eta_P$  (Equation A.1.18) is given as:

$$\eta_P(z) = \frac{z}{z_{crit}}. \quad (5.4.2)$$

In the active mirror case, an internal (perfect) reflection happens at the backside, modifying the requested doping profile (Equation A.1.35) to:

$$\hat{n}_{tot}(z) = \sigma_{a_P}^{-1} \left[ (z - D)^2 + \left( \frac{D}{\sinh(a)} \right)^2 \right]^{-1/2} \quad (5.4.3)$$

where  $D$  is the thickness of the gain medium and  $a = \ln(1 - \eta_P)/2$ . The ratio  $\hat{n}_{tot}(D)/\hat{n}_{tot}(0)$  between the doping demand on the front and backside is an important factor to be considered in terms of feasibility. This value depends only on the

pump efficiency (Equation A.1.37):

$$\frac{\hat{n}_{tot}(D)}{\hat{n}_{tot}(0)} = \frac{1 - \eta_P/2}{\sqrt{1 - \eta_P}}. \quad (5.4.4)$$

For a 90% pump efficiency Equation 5.4.4 gives  $\approx 1.74$ , for  $\eta_P = 0.95$ ,  $\hat{n}_{tot}(D)/\hat{n}_{tot}(0) \approx 2.35$  and for an absorption of 99 %, a ratio of  $\approx 5$  is necessary.

Figure 5.13 shows the plots of Equation 5.4.1 and 5.4.3 for a unit-length  $D = 1$ ,  $\sigma_{a_P} = 1$  and  $\eta_P = 0.95$ .

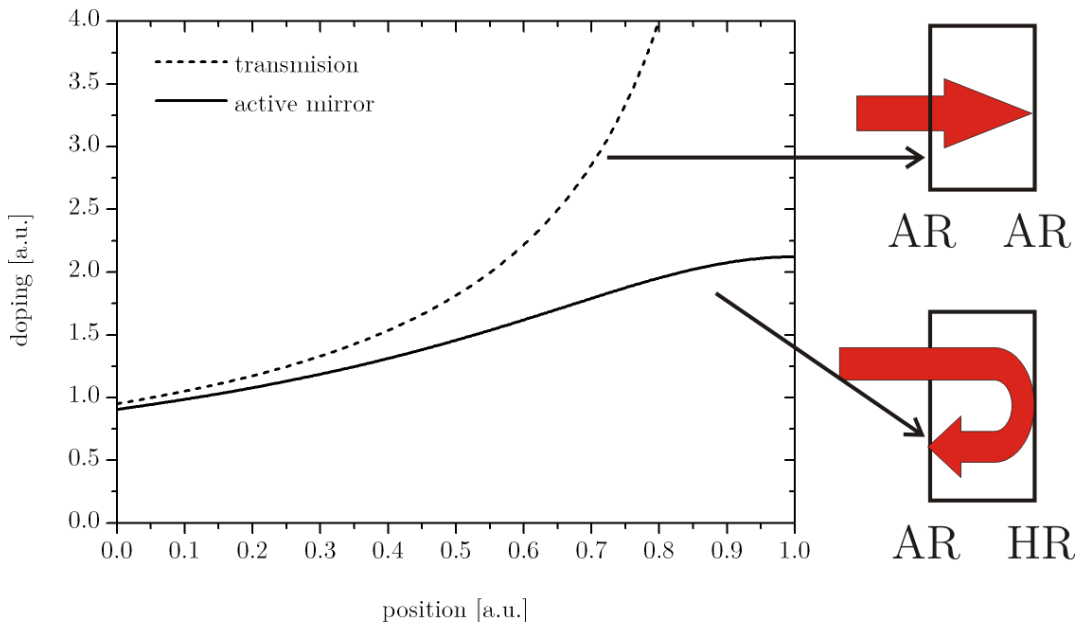


**Figure 5.13.:** Comparison of doping gradient in transmission and internal reflection. Both curves are a unit-length long and have an absorption of  $\eta = 0.95$ .

It may be noted, that Equation 5.4.1 and 5.4.3 do not depend on the incident pump intensity explicitly. A numerical analysis including saturation, reabsorption, spectral behavior and ASE is however necessary to evaluate a more realistic doping gradient. Nevertheless, the relations derived above give a rather good indication for the requested doping profile.

The production of such doping gradients within a gain medium has been demonstrated with ceramic gain media [158] and an exploration whether such controlled gradients are feasible for crystals is currently a field of research within the context of the Lucia laser program.

### 5.4.3. Ceramic laser gain media

The major drawback of crystals is their limited availability in large sizes and good quality. Glasses are available in large sizes and good optical quality but do not offer the required thermal properties for high average powers. Recent years showed a significant improvement for a third kind of gain media host matrices: ceramics.

Ceramic laser gain media have a poly-crystalline structure. They can be brought to complex shapes and large sizes [159, 158], which would be difficult to achieve otherwise.

Due to their crystallite nature, ceramics can show a somewhat lower transmission related to surface, inter- and intra-crystalline pores and grain boundaries [23]. A thorough discussion of fabrication process and the role of additives can be found in [23, 159].

Currently, only laser gain media relying on a cubic system are available in large sizes and in laser grade quality (especially YAG). As the small crystallites are randomly oriented, such ceramic laser gain media show an average orientation similar to a crystal observed in the crystalline [111]-axis [152, 151].

Another important feature of ceramic laser gain media is the possibility to achieve specific doping distributions along defined directions. Small size laser ceramics exhibiting such a doping gradient were demonstrated [158].

Let us now concentrate on the Lucia laser system to present another possibility offered by ceramics. As it is discussed in Chapter 3, parasitic oscillations are one of the major obstacles met. Cosintered ceramics offer the possibility to surround the gain medium with an absorbing cladding. Figure 5.14 shows a YAG ceramic



**Figure 5.14.:** 2 at.% doped Yb<sup>3+</sup>:YAG (35 mm diameter, transparent) ceramic with 5 mm thick Cr<sup>4+</sup>:YAG periphery (black). The thickness is 7 mm. A 50 Euro-Cent coin is given for size comparison.

with an exterior diameter of 45 mm. The 35 mm diameter central part (optically transparent) is doped with 2 at.%  $\text{Yb}^{3+}$ . The outer periphery (5 mm thick) is doped with 0.25 at.%  $\text{Cr}^{4+}$ .

The measured absorption coefficient for both parts is depicted in Figure 5.15.  $\text{Cr}^{4+}$  doped YAG shows a strong broadband absorption between 800 nm and 1200 nm which is in good accordance to the literature [160].

The zero-phonon line for  $\text{Cr}^{4+}$ :YAG is situated at 1280 nm, therefore the SE does not affect the population density of the  $\text{Yb}^{3+}$  doped part. The lifetime of the upper laser state is short compared to  $\text{Yb}^{3+}$ :YAG (at room temperature  $\sim 3 \mu\text{s}$ ) [161].

As the transverse extend of the periphery is 5 mm, a photon will travel (including the reflection on the external surface) a total length of 1 cm, which corresponds to an absorption of  $\sim \exp(-5.5) \approx 1/245$ . This is comparable to the reflection loss achieved with most of the index matching liquids (see Table 3.2 on p. 116), but without the necessity of a specially absorbing gain medium mount preventing a retro-reflection into the gain medium again.

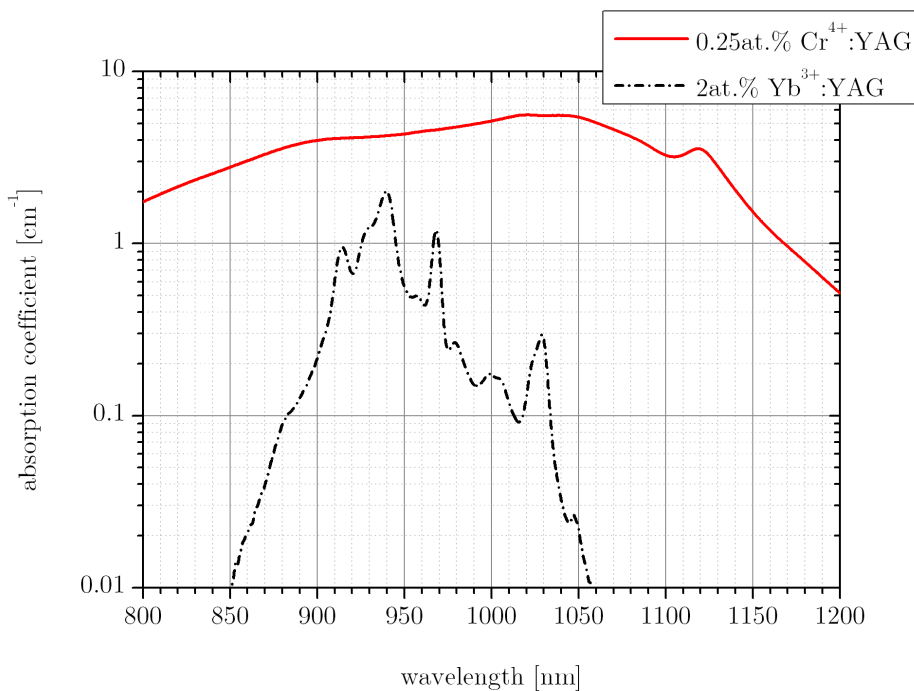


**Figure 5.15.:** Absorption coefficient of 2 at.% doped  $\text{Yb}^{3+}$ :YAG ceramic and 0.25 at.% doped  $\text{Cr}^{4+}$ :YAG ceramic at room temperature. The spectra were recorded using a Cary 500 spectrophotometer.



## 6. Conclusion

This thesis describes the three years of research performed within the framework of the Lucia program at the LULI laboratory. Amplified spontaneous emission and thermal management were the two main subjects for the theoretical and experimental work.

Both issues were explored while keeping in mind the first energetic milestone of the Lucia program, i.e.  $\sim 10\text{ J}$  at a repetition-rate of  $2\text{ Hz}$ . This objective can be considered close to achievement with the very first extraction run, leading to  $7\text{ J}/0.3\text{ Hz}$  and  $6.6\text{ J}/2\text{ Hz}$ . The potential to surpass the  $10\text{ J}$  objective is clearly present when considering the available extractable fluence. Wavefront quality improvement is the main approach being currently explored in foreseen experimental campaigns.

Thermo-mechanical analytical and numerical models of increasing complexity have been developed in order to accurately match experimental data collected on the Lucia amplifier head. The ability of its cooling architecture to allow a satisfying operation was validated to a level of several hundreds of Watts of incident average power.

ASE models were developed and benchmarked with a set of specifically shaped crystals as described in [49]. The pump duration of both preamplifier and amplifier stages was initially limited to  $0.7\text{ ms}$  due to transverse laser oscillations. Numerous solutions were proposed and experimentally explored to finally allow a full use of the laser diode investment ( $1\text{ ms}$  pumping). In addition to the implemented solution (internally absorbing mask coupled to a circulating peripheral liquid) which has been proven to be extremely satisfying, an alternative all-solid-state approach with cosintered ceramics will soon be explored on the Lucia amplifier head.

Extensive use of this two families of modeling codes (thermo-mechanical and ASE) ultimately reveals the great potential offered by doping engineering [162] on laser gain media, not only in terms of thermal and ASE management, but also with respect to the global amount of requested gain medium.

Whereas this last aspect is far from being critical for the Lucia program, it gains dramatically in importance when considering the foreseen multi-kilojoule DPSSL programs. Lucia, like the Mercury, Halna and Polaris laser programs, is one of the first precursor prototypes of high average-power DPSSLs designed to operate in the

kW range. Across the world, Inertial Fusion Energy (IFE) proposals like Life (USA), Koyo-F (Japan) or HiPER (Europe) will require to operate laser beam lines with at least a one or two order of magnitude higher average power (10 kW to 100 kW). In Europe, the HiLASE (multiple kW average power DPSSL program to be located in Dolni Brezany, Czech Republic) program was recently approved by the Czech authorities.

At the moment, the Mercury program owns the world record for a long-run 10 Hz operation at 600 W. Although much higher average powers ( $>10$  kW) have been demonstrated on short time scale (minutes) using heat-capacity DPSSLs, such technology is very unlikely to ever satisfy inertial fusion requirements of continuous (24/7), efficient operation. Within the context of Lucia, the next step will be to engineer a second laser head exploring a working point with a higher repetition rate and extracted energy. This probably requires a cryogenically cooled approach. On the other hand, even higher average power operation will require gain medium of larger volume ( $\sim 100$  cm<sup>3</sup> compared to  $\sim 10$  cm<sup>3</sup>). If we consider laser systems relying on an active mirror scheme, two distinctive scaling approaches can be envisioned. Let  $\gamma$  be the scaling parameter of the typical transverse size of the active mirror.

At first, a pure surface scaling can be considered. Surface, stored energy (at a constant pump intensity) and volume are three parameters scaling with  $\gamma^2$ . As the thickness of the gain medium remains constant, so does the small-signal gain  $g_0 = \text{const.}$  as well as the overall gain  $G$ .

With a larger surface, the aspect ratio will decrease,  $AR_L \sim 1/\gamma$ . Considering a cooling from the large surface(s), the maximum temperature as well as the related thermally induced deformation stays constant in first order constant. The injected power limited by the allowable temperature difference  $P_{\Delta T_{max}}$  (Equation 1.4.29) and due to the thermal shock parameter  $P_{R_S}$  (Equation 1.4.28) scale linear with the surface ( $\sim \gamma^2$ ). As it is discussed in Chapter 3, ASE and parasitic lasing will increase exponentially and can quickly outrun the other parameters. This is the main drawback for such surface scaling approach.

The second options to scale active mirrors is to keep the aspect ration  $AR_L = \text{const.}$  and consequently scaling the volume instead of the surface. Since a constant gain  $G$  is of interest, the doping concentration needs to decrease with the lateral size ( $\sim 1/\gamma$ ).

This approach sacrifices the temperature in order to overcome the limitation introduced by ASE and parasitic lasing. This severely restricts the acceptable

injected power ( $P_{\Delta T_{max}} = \text{const.}$  etc.) and repetition rate ( $\sim 1/\gamma$ ). Thermally induced effects might be avoided by splitting the gain medium into several slices and apply an intermediate cooling. However, this changes the aspect ratio, and the discussion concerning the onset of parasitic lasing, deformation etc. must then be reevaluated.

Table 6.1 summarizes the first order dependencies for the surface and volume scaling approaches for the active mirror scheme. Combining high repetition rate, high energy storage and extraction efficiency will obviously limit the thermal scaling parameters, as well as the parameters for ASE/parasitic lasing, to a tight interval. A further increase in extracted energy is only possible if the number of laser amplifiers is increased.

variable	surface scaling	volume scaling
Surface	$\gamma^2$	$\gamma^2$
Energy	$\gamma^2$	$\gamma^2$
Volume	$\gamma^2$	$\gamma^3$
Doping	1	$\gamma^{-1}$
$g_0$	1	$\gamma^{-1}$
G	1	1
ASE	$\exp(\gamma)$	1
Parasitic Lasing	$\exp(\gamma)$	1
Aspect Ratio $AR_L$	$\gamma^{-1}$	1
$T_{max}$	1	$\gamma$
Repetition rate	1	$\gamma^{-1}$
Deformation	1	1
$P_{\Delta T_{max}}$	$\gamma^2$	1
$P_{R_S}$	$\gamma^2$	$\gamma$
B-Integral	1	$\gamma$

**Table 6.1.:** Scaling parameters for surface and volume scaling of laser materials. The parameter  $\gamma$  scales the characteristic lateral size of the gain medium.

We might state, that thermal effects can be reduced by applying an appropriate cooling solution, and parasitic lasing can be suppressed if limits for the gain medium size, gain, surface reflectivity and external feedback are respected. However, as ASE is a fundamental process inseparably connected to the nature of lasers, its impact can only be minimized but not suppressed completely.



# A. Annex

## A.1. Variable Doping Distribution

In order to obtain the optimum doping distribution inside a gain medium, we have at first to derive a relation between the incident pump intensity and the local excitation. We will explore the two main pumping configurations – the single-side pumped gain medium case (with AR coated surfaces) in Section A.1.2 and the active mirror scheme in Section A.1.3.

### A.1.1. Pump $\leftrightarrow$ Excitation Relationship

The relationship between the absorbed pump  $I_P$  and the relative excitation value  $\beta$  is given by the following set of coupled differential equations:

$$\frac{dI_P}{dz} = g_0(z)I_P(z) \quad (\text{A.1.1})$$

$$\frac{d\beta}{dt} = -g_0 \frac{I_P(z)}{\hbar\nu_P \hat{n}_{tot}} - \frac{\beta}{\tau} \quad (\text{A.1.2})$$

where we used the known expression for the small signal gain  $g_0$ . In the case of a simple transmission, without saturation, backreflection of the pump and without ASE we get the simple evolution for the pump intensity  $I_P$ :

$$\frac{dI_P}{I_P} = g_0 dz \quad (\text{A.1.3})$$

The very well known solution can be written as:

$$I_P = I_0 \exp \left\{ \int_0^D g_0(z) dz \right\} \quad (\text{A.1.4})$$

where  $D$  is the thickness of the gain medium. Beside the use of the unified variable  $\beta$ , one can go back to the use of the (more useful) density of ions in the upper laser state  $\hat{n}$ . Therefore we write may express the differential equation for  $\beta$  in terms of

$\hat{n}$  as:

$$\frac{d\hat{n}}{dt} = -g_0 \frac{I_P(z)}{h\nu_P} - \frac{\hat{n}}{\tau} \quad (\text{A.1.5})$$

Given the relationship for the small signal gain  $g_0 = -[\sigma_a \cdot \hat{n}_{tot} - \hat{n}(\sigma_a + \sigma_e)]$  (Equation 3.2.19) we can write:

$$\frac{d\hat{n}}{dt} = \hat{n}_{tot}\sigma_a \frac{I_P}{h\nu_P} - \hat{n}(\sigma_a + \sigma_e) \frac{I_P}{h\nu_P} - \frac{\hat{n}}{\tau} = \gamma - \hat{n}\kappa \quad (\text{A.1.6})$$

This differential equation can easily be solved and giving the boundary condition ( $\hat{n}(t = 0) = 0$ ) finally yields:

$$\hat{n} = \frac{\gamma}{\kappa} - \frac{\gamma}{\kappa} \exp\{-\kappa t\} \quad (\text{A.1.7})$$

$$\hat{n} \approx \hat{n}_{tot} \frac{I_P}{I_P + I_{Sat}} \left( 1 - \exp\left\{-\frac{I_P + I_{Sat}}{I_{Sat}} \frac{t}{\tau}\right\} \right) \quad (\text{A.1.8})$$

### A.1.2. Doping distribution in transmission case

With the relationship between the pump intensity  $I_P$  and the density of the excitation  $\hat{n}$  derived above we can calculate the doping variation along the z-axis without saturation for our first case, where the pump light is not recycled.

We have to satisfy  $dg_0(\lambda_L)/dz = 0$  to get a constant small signal distribution. Achieving this is performed by introducing a longitudinal dependence  $\hat{n}_{tot}(z)$  to the doping concentration.

In our simplified case we approximate the pump to be small compared to the saturation intensity  $I_p \ll I_{Sat}$  in Equation A.1.8 and we get:

$$\hat{n} \approx \hat{n}_{tot} \frac{I_P}{I_{Sat}} \cdot \underbrace{\left[ 1 - \exp\left\{-\frac{t}{\tau}\right\} \right]}_{\delta} \quad (\text{A.1.9})$$

The small signal gain  $g_0(\lambda_L)$  (all variables at the emission wavelength ( $\lambda_L$ )) simplified by assuming  $\sigma_a \ll \sigma_e$  (four-level case):

$$g_0 = -\sigma_a \hat{n}_{tot} + (\sigma_a + \sigma_e) \hat{n} \approx \sigma_e \hat{n}_{tot} I_P \cdot \underbrace{\frac{\delta}{I_{Sat}}}_{\kappa} \quad (\text{A.1.10})$$

Finally we have to solve:

$$\frac{dg_0}{dz} = 0 \Rightarrow I_P \frac{d\hat{n}_{tot}}{dz} = -\hat{n}_{tot} \frac{dI_p}{dz} \quad (\text{A.1.11})$$

$$\frac{1}{\hat{n}_{tot}} \frac{d\hat{n}_{tot}}{dz} = -\frac{1}{I_P} \frac{dI_p}{dz} \quad (\text{A.1.12})$$

whereas for the pump the emission cross section is negligible and  $\sigma_a(\lambda_L) = \sigma_{a_P}$ :

$$\frac{dI_P}{dz} \approx -\sigma_{a_P} \hat{n}_{tot} I_P \quad (\text{A.1.13})$$

results in the differential equation

$$\frac{d\hat{n}_{tot}}{dz} = \sigma_{a_P} \hat{n}_{tot}^2 \quad (\text{A.1.14})$$

As boundary condition we set  $\hat{n}_{tot}(z = 0) = \hat{n}_0$  and get:

$$\hat{n}_{tot}(z) = \frac{\hat{n}_0}{1 - \hat{n}_0 \sigma_{a_P} z} \quad (\text{A.1.15})$$

Obviously we get a critical length  $z_{crit} = (\hat{n}_0 \sigma_{a_P})^{-1}$ , where the doping concentration will diverge. The reason is simple: the deeper the pump penetrates the gain medium, the weaker it gets and the stronger the absorption has to be.

$$\hat{n}_{tot}(z) = \frac{\hat{n}_0}{1 - z/z_{crit}} \quad (\text{A.1.16})$$

The pump intensity as a function of the penetration depth  $z$  is:

$$\frac{dI_P}{dz} \approx -\sigma_{a_P} \hat{n}_{tot} I_P = -\frac{1}{z_{crit} - z} I_P \quad (\text{A.1.17})$$

$$I_P(z) = I_0 \left( 1 - \frac{z}{z_{crit}} \right) \quad (\text{A.1.18})$$

If one wants to absorb almost all the energy and still achieves a uniform gain profile, one has to come very close to the critical length  $z_{crit}$ .

### A.1.3. Gain profile for internal reflection

After the transmission case, which was quite straight-forward, let us now consider a more interesting case with respect to the Lucia relevant active mirror concept. How should the doping distribution look like, to get a uniform gain in the case of a backreflected pump? As one might expect, the solution will follow at the beginning the hyperbolic result of the previous case, as long as the optical thickness of the gain medium at pump wavelength is high enough. Assuming the pump to be non-coherent, we can estimate the pump intensity  $I_P$  at every position as the

superposition of the forward and backwards traveling intensity, thus

$$I_P(z) = I_P^+(z) + I_P^-(z) \quad (\text{A.1.19})$$

We write the evolution of the intensity again in the form

$$\frac{dI_P^\pm}{dz} = g_{0P} dz \quad (\text{A.1.20})$$

We can formally write this, considering a perfect reflection as:

$$I_P^+(z) = I_0 \exp \left\{ \int_0^z g_{0P}(z') dz' \right\} \quad (\text{A.1.21})$$

$$I_P^-(z) = I_0 \exp \left\{ \int_0^D g_{0P}(z') dz' + \int_z^D g_{0P}(z') dz' \right\}. \quad (\text{A.1.22})$$

Therefore we write using equation A.1.10:

$$g_{0L} = \sigma_{eL} \hat{n}_{tot} \kappa (I_P^+ + I_P^-). \quad (\text{A.1.23})$$

We impose the same demands on the small signal gain  $g_0$ :

$$\frac{dg_{0L}}{dz} = \kappa \sigma_{eL} \cdot \left[ \frac{d\hat{n}_{tot}}{dz} (I_P^+ + I_P^-) + \hat{n}_{tot} \left( \frac{dI_P^+}{dz} + \frac{dI_P^-}{dz} \right) \right]. \quad (\text{A.1.24})$$

Unfortunately it is not as easy to obtain an expression similar to equation A.1.14. We will use an approach as described in [24]. We can imply, that A.1.23 yields the same small-signal gain for  $z = 0$  and for an arbitrary position  $z$ . For simplicity, we abbreviate the expression  $g_{0P}(z') dz' = *$

$$g_{0l}(z) \propto \hat{n}_{tot} I_0 \left[ \exp \left\{ \int_0^z * \right\} + \exp \left\{ \int_0^D * + \int_z^D * \right\} \right] \quad (\text{A.1.25})$$

$$g_{0l}(0) = g_{0l}(z) \quad (\text{A.1.26})$$

$$\hat{n}_{tot}(0) \left[ 1 + \exp \left\{ \int_0^D * + \int_0^D * \right\} \right] = \hat{n}_{tot}(z) \left[ \exp \left\{ \int_0^z * \right\} + \exp \left\{ \int_0^D * + \int_z^D * \right\} \right] \quad (\text{A.1.27})$$

We now multiply both sides with  $\exp \left\{ - \int_0^D * \right\}$ ,  $-\sigma_{aP}$  and use the relation for the hyperbolic cosine  $\cosh(x) = 1/2 \cdot (e^x + e^{-x})$ . As the the exponent of the integral between 0 and  $D$  is the absorption efficiency in one pass (or the square root of the pump absorption efficiency in the active mirror case), we abbreviate  $\int_0^D * = -a$ ,

$\int_0^z * = b$  and  $g_{0P}(0) = G$  yielding:

$$G \cosh(a) = g_{0P}(z) \cosh(a+b) \quad (\text{A.1.28})$$

Therefore we can eliminate the integral  $b$  using the function  $g_{0P}(z)$ :

$$\cosh(a+b) = \frac{G \cosh(a)}{g_{0P}(z)} \quad (\text{A.1.29})$$

$$\frac{dg_{0P}(z)}{dz} = G g_{0P}(z) \frac{\cosh(a) \sinh(a+b)}{\cosh^2(a+b)} \quad (\text{A.1.30})$$

$$\frac{dg_{0P}(z)}{dz} = \frac{g_{0P}^2(z) \sqrt{[G \cosh(a)]^2 - g_{0P}^2(z)}}{G \cosh(a)} \quad (\text{A.1.31})$$

The solution can be found (using Mathematica e.g.) to be

$$g_{0P}(z) = \pm \frac{G \cosh(a)}{\sqrt{1 + (G \cosh(a))^2 z^2 + 2(G \cosh(a))^3 z C_1 + (G \cosh(a))^4 C_1^2}} \quad (\text{A.1.32})$$

The integration constant  $C_1$  can be deduced by the boundary condition  $g_{0P}(0) = G$ . Completing the square in the lower square root finally gives:

$$g_{0P}(z) = \pm \left[ \left( z - \frac{\tanh(a)}{G} \right)^2 + \frac{1}{(G \cosh(a))^2} \right]^{-1/2} \quad (\text{A.1.33})$$

We have to remember, that  $G$  and  $g_{0P}(z)$  are negative. There is still the undetermined absorption on the front surface  $G$ . Considering the previously mentioned approximations we directly get:

$$G = \frac{\tanh(a)}{D} \text{ and } \hat{n}_{tot}(0) = -\frac{\tanh(a)}{\sigma_{aP} D} \quad (\text{A.1.34})$$

Together with equation A.1.33 we get:

$$\hat{n}_{tot}(z) = \sigma_{aP}^{-1} \left[ (z - D)^2 + \left( \frac{D}{\sinh(a)} \right)^2 \right]^{-1/2} \quad (\text{A.1.35})$$

The constant  $a$  can be interpreted to be the absorbed fraction of the pump in single-pass, there for it is in direct connection to the overall pump efficiency  $\eta_P$ .

$$a = \frac{\ln(1 - \eta_P)}{2} \quad (\text{A.1.36})$$

An interesting feature is the ratio  $\Delta_{tot}$  between the doping concentration on the reflective and the front surface:

$$\Delta_{tot} = \frac{\hat{n}_{tot}(D)}{\hat{n}_{tot}(0)} = \cosh(a) = \frac{1 - \eta_P/2}{\sqrt{1 - \eta_P}}. \quad (\text{A.1.37})$$

Interestingly is the ratio only dependent on the pump efficiency. The higher the pump efficiency, the stronger will be the doping requested gradient between both extremities of the gain medium.

## A.2. Linford's Formula

We start from the problem given in Section 3.2.2 in Equation 3.2.8:

$$d^3\Phi_{ASE} = \frac{\hat{n}}{\tau_f} \frac{d\Omega}{4\pi} g(\nu) G d\nu dx \quad (\text{A.2.1})$$

Considering the system as a four-level system, one can use  $G \approx \exp \left[ \int_x^z \sigma_{st} \hat{n}(x') dx' \right]$ . The ASE flux can be expressed as:

$$\Phi_{ASE}(z) = \frac{1}{\tau_f} \frac{\Omega}{4\pi} \int_{-\infty}^{\infty} \int_0^z \hat{n}g(\nu) \exp \left[ \int_x^z \sigma_{st} \hat{n}(x') dx' \right] d\nu dx \quad (\text{A.2.2})$$

The line shape function  $g(\nu)$  and the emission cross section  $\sigma(\nu)$  is approximated with a Gaussian function with the FWHM values of  $\Delta\nu_{st}$  and  $\Delta\nu_{sp}$ . The corresponding expressions are:

$$\sigma(\nu) = \sigma(\nu_0) \exp \left[ -\ln(2) \frac{(\nu - \nu_0)^2}{\Delta\nu_{st}^2} \right] \quad (\text{A.2.3})$$

$$g(\nu) = \frac{\sqrt{\ln(2)/\pi}}{\Delta\nu_{sp}} \exp \left[ -\ln(2) \frac{(\nu - \nu_{sp})^2}{\Delta\nu_{sp}^2} \right] \quad (\text{A.2.4})$$

Equation A.2.2 becomes then [115]:

$$\Phi_{ASE}(z) = \frac{\sqrt{\ln(2)/\pi}}{\Delta\nu_{sp}\tau_f} \frac{\Omega}{4\pi} \int_{-\infty}^{\infty} \exp \left[ -\ln(2) \frac{(\nu - \nu_0)^2}{\Delta\nu_{st}^2} \right] F(\nu, z) d\nu \quad (\text{A.2.5})$$

where  $F(\nu, z)$  is:

$$F(\nu, z) = \int_0^z \hat{n}(x) \exp \left[ \int_x^z \sigma(\nu_0) \exp \left\{ -\ln(2) \frac{(\nu - \nu_0)^2}{\Delta\nu_{st}^2} \right\} \hat{n}(x') dx' \right] dx \quad (\text{A.2.6})$$

The function  $F(\nu, z)$  is approximated by a Gaussian function  $H(\nu, z)$  in the form of:

$$H(\nu, z) = q(z) \exp \left[ -\ln(2) \frac{(\nu - \nu_0)^2}{\Delta\nu_{ASE}^2(z)} \right] \quad (\text{A.2.7})$$

with

$$q(z) = \int_0^z \hat{n}(x) \exp \left[ \int_x^z \sigma(\nu_0) \hat{n}(x') dx' \right] dx \quad (\text{A.2.8})$$

Within this approximation a FWHM value for the Gaussian distribution of the ASE  $\Delta\nu_{ASE}$  is introduced. The functions  $H$  and  $F$  have to show their maximum at the

same position.

$$H(\nu_0, z) = F(\nu_0, z) \quad (\text{A.2.9})$$

$H$  and  $F$  have to show the same curvature at their maximum frequency  $\nu = \nu_0$ .

$$\frac{\partial^2 H(\nu_0, z)}{\partial \nu^2} = \frac{\partial^2 F(\nu_0, z)}{\partial \nu^2} + h(z) \quad (\text{A.2.10})$$

The differentiation gives:

$$\begin{aligned} \frac{q(z)}{\Delta\nu_{ASE}^2(z)} &= \frac{1}{\Delta\nu_{st}^2(z)} \int_0^z \exp \left\{ \int_x^z \sigma(\nu_0) \hat{n}(x') dx' \right\} \\ &\times \left( \int_x^z \sigma(\nu_0) \hat{n}(x') dx' \right) \hat{n}(x) dx - \frac{1}{2 \ln(2)} h(z) \end{aligned} \quad (\text{A.2.11})$$

The auxiliary function  $h$  is indeed necessary to ensure, that the ASE line width tends towards the stimulated emission line width, even for very thin gain media. We have to ensure:

$$\lim_{z \rightarrow 0} \Delta\nu_{ASE}(z) = \Delta\nu_{st} \quad (\text{A.2.12})$$

and to demand consequently:

$$h(z) = -\frac{2 \ln(2)}{\Delta\nu_{st}^2} q(z) \quad (\text{A.2.13})$$

Using Equation A.2.9 together with A.2.11 and A.2.13 results in an expression for the ASE line width:

$$\frac{\Delta\nu_{ASE}^2(z)}{\Delta\nu_{st}^2} = \frac{\int_0^z \hat{n}(x) e^{\int_x^z \sigma(\nu_0) \hat{n}(x') dx'} dx}{\int_0^z \hat{n}(x) e^{\int_x^z \sigma(\nu_0) \hat{n}(x') dx'} dx + \int_0^z e^{\int_x^z \sigma(\nu_0) \hat{n}(x') dx'} \left( \int_x^z \sigma(\nu_0) \hat{n}(x') dx' \right) \hat{n}(x) dx} \quad (\text{A.2.14})$$

Finally the integral for the ASE flux  $\Phi_{ASE}$  is expressed as:

$$\Phi_{ASE}(z) = \frac{1}{\tau_f} \frac{\Omega}{4\pi} \frac{\Delta\nu_{ASE}(z)}{\sqrt{\Delta\nu_{sp}^2 + \Delta\nu_{ASE}^2(z)}} \int_0^z \hat{n}(x) e^{\int_x^z \sigma(\nu_0) \hat{n}(x') dx'} dx \quad (\text{A.2.15})$$

The only information which has to be given is the distribution of the population inversion  $\hat{n}$  along the propagation axis. Estimating the distribution  $\hat{n}$  to be constant, Equation A.2.14 yields:

$$\frac{\Delta\nu_{ASE}(z)}{\Delta\nu_{st}} = \left( \frac{e^{g_0 z} - 1}{g_0 z e^{g_0 z}} \right)^{1/2} \quad (\text{A.2.16})$$

where  $g_0$  is the small-signal gain coefficient in the four-level case. Defining the saturation intensity of the gain medium used as  $I_{sat} = h\nu_0 / [\tau_f \sigma(\nu_0)]$ , we get for the

ASE intensity  $I_{ASE}$

$$I_{ASE} = I_{sat} \frac{\Omega}{4\pi} \frac{\Delta\nu_{ASE}(z)}{\sqrt{\Delta\nu_{sp}^2 + \Delta\nu_{ASE}^2(z)}} (e^{g_0 z} - 1) \quad (\text{A.2.17})$$

In Linfords model implies a strong spectral narrowing ( $\Delta\nu_{ASE}(z) \ll \Delta\nu_{sp}$ ), therefore:

$$I_{ASE} = I_{sat} \frac{\Omega}{4\pi} \frac{\Delta\nu_{st}}{\Delta\nu_{sp}} \frac{(e^{g_0 z} - 1)^{3/2}}{(g_0 z e^{g_0 z})^{1/2}}. \quad (\text{A.2.18})$$

Furthermore, the overall gain  $G$  is very high and the widths of the spontaneous and stimulated emission cross section to be equal, we can write:

$$I_{ASE} = I_{sat} \frac{\Omega}{4\pi} \frac{G(z)}{\sqrt{\ln G(z)}}. \quad (\text{A.2.19})$$

This relation is very convenient to estimate the intensity of ASE at the end of a laser chain.

### A.3. The Quasi–Three–Level–System $\text{Yb}^{3+}\text{:YAG}$

Conventional laser system classifications cook down to the description of three–level and four-level systems. The quasi-three-level-system of  $\text{Yb}^{3+}\text{:YAG}$  is somewhere in between. While the terminal laser level is not the ground level, it is close enough to it, to be considerably populated by the Boltzmann–distribution. Simplifying the situation, we consider 2 level–systems, with four levels in total, where the relative distribution therein is distributed thermally. The term schemata, however, are more complicated.

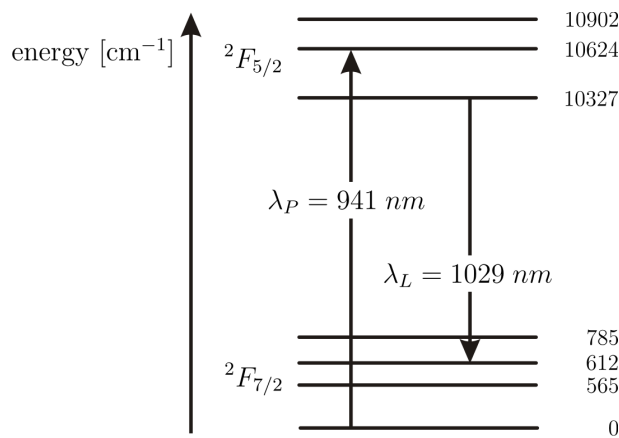


**Figure A.1.:** Quasi–three–level system of  $\text{Yb}^{3+}\text{:YAG}$ . Values for the energy levels after [149, 10]

According to the Einstein coefficients [163], we can write the absorption and emission cross–section at a frequency  $\nu$  between two energetic levels  $i$  and  $j$  with the respective degeneracies  $g_i$  and  $g_j$ , where the index  $j$  marks the higher lying one, as follows:

$$g_0(\nu) = -\alpha(\nu) = \sigma (g_i \hat{n}_j - g_j \hat{n}_i) \quad (\text{A.3.1})$$

$$\sigma = \frac{c^2}{8\pi\nu^2} \frac{A_{ij}}{g_i} \Phi(\nu) \text{ and } \sigma = \frac{\sigma_{ji}}{g_i} = \frac{\sigma_{ij}}{g_j} \quad (\text{A.3.2})$$

hereby we used the sums convention. In the case, that the energy levels correspond to Stark levels ( $i$  for the ground state manifold and  $j$  for the excited state manifold), the respective levels are thermally populated according to the Boltzmann distribution. The fractional thermal occupation is given against the whole occupation in the corresponding manifold. we have therefore:

$$f_{low_i} = \frac{\hat{n}_i}{\hat{n}_{low}} \quad \text{and} \quad f_{up_j} = \frac{\hat{n}_j}{\hat{n}_{up}} \quad (\text{A.3.3})$$

Due to the Boltzman distribution the following equations govern the population

distributions of the lower and upper levels in the manifolds:

$$f_{low_i} = g_i \exp(-E_{low_i}/kT) / \sum_i g_i \exp(-E_{low_i}/kT) \quad (\text{A.3.4})$$

$$f_{up_j} = g_j \exp(-E_{up_j}/kT) / \sum_j g_j \exp(-E_{up_j}/kT) \quad (\text{A.3.5})$$

We can therefore write the emission and absorption cross sections in the following way:

$$\sigma_e(\lambda) = \sum_{i,j} f_{up_j} \sigma_{up_j, low_i} \quad (\text{A.3.6})$$

$$\sigma_a(\lambda) = \sum_{i,j} f_{low_i} \sigma_{low_i, up_j} \quad (\text{A.3.7})$$

In the case of Yb-doped YAG, the relative occupation factor  $f_{low_i}$  is assigned to the occupation factor of sublevel  $low_i$  within the manifold  $^2F_{7/2}$  and  $f_{up_j}$  to the sublevel  $up_j$  within the manifold  $^2F_{5/2}$ .

In the case that only one Stark sublevel contributes to a transition at a specific wavelength  $\lambda$ , the equations lead to:

$$\frac{\sigma_e}{\sigma_a} = \frac{f_{up_j}}{f_{low_i}} \frac{g_i}{g_j} \quad (\text{A.3.8})$$

The total doping density is  $\hat{n}_{tot}$ :

$$\hat{n}_{tot} = \hat{n}_{up} + \hat{n}_{low}. \quad (\text{A.3.9})$$

The small-signal gain  $g_0$  is:

$$g_0 = \sigma_e \hat{n}_{up} - \sigma_e \hat{n}_{down} = -\sigma [g_j f_i \hat{n}_{tot} - (g_j f_i + g_i f_j) \hat{n}_{up}] \quad (\text{A.3.10})$$

At this point we change the variable names to be conform with the definitions found in Chapter 1:

$$\hat{n} = \hat{n}_{up}. \quad (\text{A.3.11})$$

Of special interest is the minimum excitation necessary to bleach out the gain medium  $\beta_{min}$  in this case (Equation A.3.10):

$$\beta_{min} = \frac{\hat{n}}{\hat{n}_{tot}} = \frac{\sigma_a}{\sigma_a + \sigma_e} = \frac{g_j f_{low_i}}{g_j f_{low_i} + g_i f_{up_j}}. \quad (\text{A.3.12})$$

Assuming the degeneracies  $g_i = g_j$ , this relation simplifies to

$$\beta_{min} = \frac{f_{low_i}}{f_{low_i} + f_{up_j}}. \quad (\text{A.3.13})$$

Consequently will the minimum excitation needed, to achieve gain in such a material, dependent from the temperature and decreases with a decreasing temperature.

## B. Tables

variable	Yb <sup>3+</sup> :YAG (2 at.%)	Yb <sup>3+</sup> :YAG (20 at.%)	silicone	steel
$k$ [W m <sup>-1</sup> K <sup>-1</sup> ]	9	6	0.16	16.2
$\rho$ [g cm <sup>-3</sup> ]	4.56	4.56	2	8
$\mathbf{Y}$ [N m <sup>-2</sup> ]	$3 \times 10^{11}$	$3 \times 10^{11}$	$1 \times 10^8$	$2 \times 10^{11}$
$\alpha_T$ [K <sup>-1</sup> ]	$6 \times 10^{-6}$	$6 \times 10^{-6}$	$7 \times 10^{-4}$	$1.6 \times 10^{-5}$
$\alpha$ [m <sup>-1</sup> ]	209.8	2098	—	—

**Table B.1.:** Parameters used within the three dimensional thermo-mechanical analysis.

## B. Tables

Material	$n_0$	$n_2$	$k$	$\alpha_T$	$R_S$	$F_{sat}$	$\Delta\lambda$	$\tau_f$	Ref.
YAG	1.82	7	10.7	6	10.4(55)	9.6(0.6)	9(0.8)	0.95(0.27)	[164, 165, 166, 56, 71]
SFAP	1.62	4.1	2	27	1.1	3(0.35)	4	1.1(0.3)	[164, 166, 71]
FP20	1.51	2.1	0.9	–	0.8	43	48	1.6	[167, 71]
CaF <sub>2</sub>	1.43	1.3	9.7	-18	1.7	86	53	2.4	[21, 95, 71]
SrF <sub>2</sub>	1.43	1.5	8.3	-20	2.2	102	53	2.9	[21, 95, 71]
CaAlGO	–	–	6.9	35	6.4	23	80	0.4	[166, 71]
KYW	2	8.7	2.7	–	–	6.5	16	0.6	[165, 130, 71]
KGW	2	–	3.8	16	4	8.9	20	0.6	[165, 166, 71]
YVO <sub>4</sub>	1.96	1.9	7	–	11.3	2.8(0.18)	–(1)	0.3(0.1)	[165, 166, 71]
YCOB	1.7	9	–	–	–	–	–	3	[165, 71]
GCOB	1.7	10	2	33.5	1	55	44	2.6	[165, 168, 166, 71]
BOYS	1.74	6.6	–	–	–	96	60	1.1	[165, 71]
YSO	1.78	–	5	18	4.7	48	–	0.7	[168, 166, 71]
Sc <sub>2</sub> O <sub>3</sub>	1.93	11.5	16.5	27	13	13	–	–	[164, 166, 71]
Lu <sub>2</sub> O <sub>3</sub>	1.93	8.6	12.2	24	12	15	–	–	[164, 166, 71]
Y <sub>2</sub> O <sub>3</sub>	1.92	11.6	12.8	25.5	12	18	–	–	[164, 165, 166, 71]
YLF	1.45	1.7	5	42	1.8	–	–(1.5)	–(0.5)	[165, 166]
YAlO	1.93	7.3	8.5	25	7.8	–(0.74)	–(2.5)	–(0.16)	[21, 166, 71]
GGG	1.95	12.5	8.2	24	7.6	–(1)	–	–	[21, 166, 71]
GSGG	1.94	12	6	22.5	6.2(64)	–(0.6)	–	–	[21, 166, 53, 56, 71]
LHG-5	1.54	–	1	9.8	1	–	–	–	[53]
LHG-8	1.52	3.1	0.58	12.7	0.5	–(5.2)	–(26.5)	–(0.36)	[72, 169]
LG-750	–	–	0.62	11.4	0.7	–	–(25.4)	–	[53]
LG-770	1.5	2.8	0.57	13.5	0.4	–(4.8)	–	–(0.36)	[72]
fused silica	1.45	2.5	1.4	–	1.5	–	–	–	[21, 71]
Ti:Sa	1.75	3	28	–	34	0.6	230	0.0032	[21, 53, 71]
Cr:LiSAF	–	–	3.1	19	1.6	4.9	180	0.067	[170, 71]
Cr:YAG	1.82	7	10.7	6	10.4	0.3	–	0.004	[164, 165, 71]
Cr:MgSiO	1.67	4.3	–	–	–	1.1	30	0.0025	[21, 71]
Cr:BeAlO	1.73	3.5	23	8	23.5	26	100	0.0026	[21, 53, 71]
Cr:Al <sub>2</sub> O <sub>3</sub>	1.75	3	28	–	34	11	0.5	3	[21, 71]

**Table B.2.:** Characteristics of selected gain media. The upper part of the table shows materials doped with Yb<sup>3+</sup> or Nd<sup>3+</sup>. The lower part shows fused silica and transition metal doped gain media. The nonlinear index of refraction  $n_2$  in  $\times 10^{-16} \text{ cm}^2 \text{ W}^{-1}$ , the thermal conductivity  $k$  in  $\text{W m}^{-1} \text{ K}^{-1}$ , thermal expansion  $\alpha_T$  in  $\times 10^{-6} \text{ K}^{-1}$  and the thermal shock parameter  $R_S$  in  $\text{W cm}^{-1}$  are given for pure materials. Values in brackets for  $R_S$  signify strengthened materials. Saturation fluence at extraction wavelength  $F_{sat}$  in  $\text{J cm}^{-2}$ , the bandwidth  $\Delta\lambda$  in nm and the lifetime  $\tau_f$  in ms are given for Yb<sup>3+</sup>(Nd<sup>3+</sup>) doping.

# List of Figures

1.1.	Three-level-laser and four-level-laser schemata . . . . .	8
1.2.	Storage efficiency as a function of time and ASE . . . . .	21
1.3.	Critical volume for different geometries and the critical radius for a disk as a function of the surface reflectivity. . . . .	23
1.4.	Necessary bandwidths . . . . .	32
1.5.	Fluorescence lifetime and saturation fluence for selected solid state laser gain media . . . . .	33
1.6.	Bandwidth of laser gain materials . . . . .	34
1.7.	Thermal shock parameter $R_S$ for various laser materials. . . . .	35
1.8.	B-Integral susceptibility (vertical axis) and critical power $P_{crit}$ (horizontal axis) for selected solid state laser gain media . . . . .	35
2.1.	Schematic overview over the Lucia laser system. . . . .	45
2.2.	Oscillator setup sketches . . . . .	46
2.3.	Oscillator spectra . . . . .	48
2.4.	Oscillator energy characteristics . . . . .	50
2.5.	Oscillator near and far field . . . . .	51
2.6.	Preamplifier sketch . . . . .	52
2.7.	1st preamplifier setup . . . . .	53
2.8.	2nd preamplifier setup . . . . .	54
2.9.	Performance of the first pre-amplifier. . . . .	55
2.10.	Description of the three major pumping schemes. . . . .	56
2.11.	View from extraction direction at the main amplifier. . . . .	57
2.12.	Lucia apodizer example . . . . .	58
2.13.	General Apodizer setup using a serrated aperture . . . . .	59
2.14.	Serrated aperture tooth design . . . . .	60
2.15.	Triangular teeth pattern example and its FFT . . . . .	61
2.16.	Simulation of the serrated aperture . . . . .	63
2.17.	Impact of the serrated aperture, experiment. . . . .	64
2.18.	Comparison between the calculated and experimental intensity distribution in the focus introduced by the serrated aperture . . . . .	64
2.19.	Overview of the main amplifier setup . . . . .	65

2.20. Water distribution and cooling of the laser diode array . . . . .	66
2.21. Impact of the bias current . . . . .	67
2.22. Schematic setup of the main power amplifier . . . . .	68
2.23. Effect of the prisms . . . . .	69
2.24. Impact of light concentration system on the pump light distribution .	70
2.25. Transmission of the large concentration mirrors . . . . .	71
2.26. Beam trajectory in a gain medium pumped with a modulated gain profile. . . . .	72
2.27. Example calculations of the exiting beam modulation as a function of the gain medium thickness. . . . .	73
2.28. Impact of the gain medium thickness on the modulation of an amplified beam in the active mirror scheme. . . . .	74
2.29. Comparison of the different cooling setups . . . . .	76
2.30. Cooling head assembly . . . . .	77
2.31. Manufactured jet–plate . . . . .	77
2.32. Laser head assembly . . . . .	78
3.1. ASE in 1D sketch . . . . .	80
3.2. Distribution of the ASE–flux in a 1D gain medium . . . . .	81
3.3. Sketches for the 2D and quasi–3D ASE estimations . . . . .	86
3.4. $M_{ASE}$ distribution for different homogeneous $g_0$ . . . . .	88
3.5. $g_0$ (a) and $M_{ASE}$ (b) evolution during the pumping process . . . . .	90
3.6. ASE 2at% Yb:YAG 7mm scaling example . . . . .	91
3.7. Delaunay prism with a random distribution example . . . . .	92
3.8. 3D model example Paraview . . . . .	93
3.9. Pump spectra in the single shot experiment . . . . .	94
3.10. ASE experiment setup . . . . .	95
3.11. ASE experiment examples simulation . . . . .	96
3.12. Experimentally found gain distributions for a weak and strong ASE impact. . . . .	97
3.13. Temporal evolutions during pumping for 1 at.%, 5 mm and 10 at.%, 3 mm. . . . .	99
3.14. Overall comparison between simulation and experiment for the impact of ASE . . . . .	101
3.15. Internal reflection in a slab . . . . .	102
3.16. Impact of the aspect ratio . . . . .	103
3.17. Gain for SE neglecting ASE for a 7 mm thick Yb:YAG crystal pumped at $10 \text{ kW cm}^{-2}$ . . . . .	104

3.18. Closed paths within a circle . . . . .	105
3.19. Circle in circle sketch . . . . .	106
3.20. Circle in a circle calculation examples . . . . .	108
3.21. Sketch of the coatings applied on the 60 mm active mirrors. . . . .	110
3.22. Mount for the 60 mm crystals, open design . . . . .	110
3.23. Pump profile at 130A . . . . .	111
3.24. Comparison between the simulation and measurement rectangular pump zone in a 60 mm crystal, $11.5 \text{ kW cm}^{-2}$ . . . . .	112
3.25. Gain for rays passing through the gain medium, rectangular pump $12 \text{ kW cm}^{-2}$ . . . . .	113
3.26. Light concentration optimizations, theory . . . . .	114
3.27. Light concentration optimizations, realized . . . . .	115
3.28. Temporal gain evolution observed for three experimental pump distributions . . . . .	115
3.29. Impact of the index matching liquid on the gain in the central region, $16 \text{ kW cm}^{-2}$ . . . . .	117
3.30. Redesigned gain mount with incorporated mask and blackening . . . . .	118
3.31. Impact of the new mount and comparison to the simulation results . . . . .	118
4.1. Thermal conductivity of YAG as a function of grain size and temperature . . . . .	124
4.2. Thermal conductivity of $\text{Yb}^{3+}\text{:YAG}$ as a function of doping and temperature . . . . .	125
4.3. Variation of the thermal conductivity of $\text{Yb}^{3+}\text{:YAG}$ as a function of substitution, after [127] . . . . .	126
4.4. Cooling scheme for a rod and for a disc . . . . .	128
4.5. Heat distribution examples for a one-sided and two-sided cooling . . . . .	129
4.6. Definitions for the variables used for the radial temperature distribution estimation . . . . .	131
4.7. Radial distribution of the mean temperature for different relative pump diameters. . . . .	132
4.8. JP working principle sketch . . . . .	133
4.9. Estimation of the heat exchange coefficient for a single jet . . . . .	135
4.10. Scheme of measuring the heat exchange coefficient of the Lucia laser head . . . . .	136
4.11. Setup sketch for the estimation of $h$ with its components. . . . .	137
4.12. Experimental result for the heat exchange coefficient of the jet-plate compared to the Tawfek relation (Equation 4.3.3) . . . . .	138

4.13. Visualization of the cross flow introduced by neighboring jets . . . . .	138
4.14. Visualization of the surface temperature modulations introduced by the jet–plate for different distances jet–plate – cooled surface. . . . .	139
4.15. Sketch of the dependence of the refractive index in a pumped gain medium. . . . .	141
4.16. Sketch for the estimation of the deformation of an active medium in the thin disc case. . . . .	143
4.17. Estimations for the thermally induced focal length. . . . .	144
4.18. Sketch of the experimental setup measuring the wavefront deformation on the Lucia main amplifier laser head. . . . .	145
4.19. The first 12 Zernike polynomials in the case of the highly doped 20 at.% Yb <sup>3+</sup> :YAG slab. . . . .	147
4.20. Simplified quasi–three level level scheme for Yb <sup>3+</sup> :YAG. . . . .	148
4.21. Time resolved measurement of the wavefront deformation . . . . .	149
4.22. Comparison between the experimentally observed static deformation and predictions for three different crystals. . . . .	151
4.23. Deformation and temperature for the 20 at.% doped, rect. crystal, $I_{avg} = 30 \text{ W cm}^{-2}$ and the 2 at.% doped, circ. crystal, $I_{avg} = 75 \text{ W cm}^{-2}$ . . . . .	153
4.24. Wavefront deformation for the 7 mm and 8.4 mm thick laser crystals under internal reflection at $I_{avg} = 75 \text{ W cm}^{-2}$ . . . . .	154
4.25. Horizontal lineouts of the wavefront deformation. . . . .	155
4.26. Deformation compilation of the experiments done on the main amplifier head. . . . .	156
4.27. Depolarization sketch for a linearly polarized beam traveling through a laser crystal under stress. . . . .	159
4.28. Mean radial and tangential stress distribution for $D' = 0.2$ . . . . .	160
4.29. Transmission examples set between crossed polarizers of two different Yb <sup>3+</sup> :YAG slabs . . . . .	162
4.30. Sketch of the experimental setup to measure the thermally induced depolarization. . . . .	163
4.31. Intrinsic and pump induced polarization on the Lucia laser head. . . . .	166
4.32. Measured depolarization in the center and as the average over the pupil. . . . .	167
5.1. Simulation results for the Lucia main amplifier Yb <sup>3+</sup> :YAG crystal . .	172
5.2. $\beta$ –distribution in the center along the pump axis . . . . .	174
5.3. Estimation of the output energy density as a function of the input energy density for the Lucia main amplifier after four passes . . . . .	175

5.4. Estimated gain per pass for the first four passes in the main amplifier as a function of the input energy density. . . . .	175
5.5. Layout of the extraction setup. . . . .	176
5.6. Beam shape in the image relay plane after one and two passes in the main amplifier. . . . .	178
5.7. Main amplifier performance for 0.1 and 2 Hz. . . . .	179
5.8. Beam shape in the image relay plane after four passes in the main amplifier. . . . .	180
5.9. 4th pass for 2 Hz and 0.1 Hz repetition rate . . . . .	181
5.10. Performance of the Lucia main amplifier . . . . .	182
5.11. Static astigmatism correction sketch. . . . .	183
5.12. Astigmatism corrector setup. . . . .	184
5.13. Comparison of doping gradient in transmission and internal reflection	187
5.14. 2 at.% doped $\text{Yb}^{3+}$ :YAG ceramic with $\text{Cr}^{4+}$ :YAG periphery . . . . .	188
5.15. Absorption coefficient of $\text{Yb}^{3+}$ :YAG and $\text{Cr}^{4+}$ :YAG ceramic . . . . .	189
A.1. Quasi-three-level system of $\text{Yb}^{+3}$ :YAG. Values for the energy levels after [149, 10] . . . . .	203



# List of Tables

1.1.	Properties of selected laser materials . . . . .	14
1.2.	Comparison of efficiencies flash lamp and diode pumped systems . . . . .	17
1.3.	Comparison between the different laser DPSSL systems . . . . .	41
3.1.	Maximum $g_0L$ for the benchmark crystals. . . . .	95
3.2.	Used index matching media . . . . .	116
3.3.	Values for $g_0L$ and $\kappa$ for different aspect ratios . . . . .	120
4.1.	Ionic radius and molar mass of trivalent rare earths and Yttrium . . .	125
5.1.	Energy storage and extractable energy for the Lucia main amplifier head. . . . .	173
6.1.	Scaling parameters for surface and volume scaling of laser materials. .	193
B.1.	Data for the 3D model . . . . .	205
B.2.	Gain medium data . . . . .	206



# Bibliography

- [1] Einstein A. ‘Zur Quantentheorie der Strahlung.’ *Physikalische Zeitschrift*, **18**(6):(1917) pp. 121–128.
- [2] Kopfermann H and Ladenburg R. ‘Untersuchungen über die anomale Dispersion angeregter Gase.’ *Zeitschrift für Physik*, **48**(1–2):(1928) pp. 26–50.
- [3] Lewis G. ‘The conservation of Photons.’ *Nature*, **118**(2981):(1926) pp. 874–875.
- [4] Kastler A. ‘Quelques suggestions concernant la production optique et la détection optique d’une inégalité de population des niveaux de quantification spatiale des atomes. Application à l’expérience de Stern et Gerlach et à la résonance magnétique.’ *Journal de Physique et Le Radium*, **11**:(1950) pp. 255–265.
- [5] Purcell EM and Pound RV. ‘A Nuclear Spin System at Negative Temperature.’ *Phys. Rev.*, **81**(2):(1951) pp. 279–280.
- [6] Gordon JP, Zeiger HJ, and Townes CH. ‘Molecular Microwave Oscillator and New Hyperfine Structure in the Microwave Spectrum of NH<sub>3</sub>.’ *Phys. Rev.*, **95**(1):(1954) pp. 282–284.
- [7] Schawlow AL and Townes CH. ‘Infrared and Optical Masers.’ *Physical Review*, **112**(6):(1958) pp. 1940–1949.
- [8] Maiman TH. ‘Stimulated Optical Radiation In Ruby.’ *Nature*, **187**(4736):(1960) pp. 493–494.
- [9] Scully MO, Zhu SY, and Gavrielides A. ‘Degenerate Quantum-beat Laser - Lasing Without Inversion and Inversion Without Lasing.’ *Physical Review Letters*, **62**(24):(1989) pp. 2813–2816.
- [10] Koechner W. *Solid-State Laser Engineering*. Springer, 1999.
- [11] Weber M. *Handbook of Lasers*. CRC Press LLC, 2001.
- [12] Endo M. *Gas Lasers*. CRC Press, 2007.

- [13] Patel CKN. ‘Continuous-Wave Laser Action on Vibrational-Rotational Transitions of CO<sub>2</sub>.’ *Phys. Rev.*, **136**(5A):(1964) pp. A1187–A1193.
- [14] Javan A, Herriott DR, and Bennett WR. ‘Population Inversion and Continuous Optical Maser Oscillation In A Gas Discharge Containing A He-ne Mixture.’ *Physical Review Letters*, **6**(1):(1961) pp. 106–110.
- [15] Sorokin P and Lankard J. ‘Stimulated emission observed from an organic dye, chloro-aluminium phtalocyanine.’ *IBM Journal of Research and Development*, **10**:(1966) p. 162.
- [16] Schafer FP, Schmidt W, and Volze J. ‘Organic Dye Solution Laser.’ *Applied Physics Letters*, **9**(8):(1966) pp. 306–309.
- [17] Johnston TF, Brady RH, and Profitt W. ‘Powerful Single-frequency Ring Dye-laser Spanning the Visible Spectrum.’ *Applied Optics*, **21**(13):(1982) pp. 2307–2316.
- [18] Bornemann R, Lemmer U, and Thiel E. ‘Continuous-wave solid-state dye laser.’ *Opt. Lett.*, **31**(11):(2006) pp. 1669–1671. URL <http://ol.osa.org/abstract.cfm?URI=ol-31-11-1669>.
- [19] Khader MA. ‘Lasing characteristics of Rhodamine B and Rhodamine 6G as a sensitizer in sol-gel silica.’ *Optics and Laser Technology*, **40**(3):(2008) pp. 445–452.
- [20] Boling N, Glass A, and Owyong A. ‘Empirical relationships for predicting nonlinear refractive index changes in optical solids.’ *Quantum Electronics, IEEE Journal of*, **14**(8):(1978) pp. 601–608.
- [21] Adair R, Chase LL, and Payne SA. ‘Nonlinear Refractive-Index Of Optical Crystals.’ *Physical Review B*, **39**(5):(1989) pp. 3337–3350.
- [22] Bloembergen N and Pershan PS. ‘Light waves at the boundary of nonlinear media.’ *Physical Review*, **128**(2):(1962) pp. 606–622.
- [23] Belyakov AV and Sukhozhak AN. ‘Production of Transparent Ceramics (review).’ *Glass and Ceramics*, **52**(1-2):(1995) pp. 14–19.
- [24] Wilhelm R, Frede M, and Kracht D. ‘Power scaling of end-pumped solid-state rod lasers by longitudinal dopant concentration gradients.’ *Ieee Journal Of Quantum Electronics*, **44**(3-4):(2008) pp. 232–244.

- [25] Sorokin PP and Stevenson MJ. ‘Stimulated Infrared Emission from Trivalent Uranium.’ *Phys. Rev. Lett.*, **5**(12):(1960) pp. 557–559.
- [26] Keyes RJ and Quist TM. ‘Injection Luminescent Pumping of Ca F<sub>2</sub>-u3+ With GaAs Diode Lasers.’ *Applied Physics Letters*, **4**(3):(1964) pp. 50–&.
- [27] Sorokin E, Naumov S, and Sorokina I. ‘Ultrabroadband infrared solid-state lasers.’ *Selected Topics in Quantum Electronics, IEEE Journal of*, **11**(3):(2005) pp. 690–712.
- [28] Moulton PF. ‘Spectroscopic and laser characteristics of Ti:Al<sub>2</sub>O<sub>3</sub>.’ *J. Opt. Soc. Am. B*, **3**(1):(1986) pp. 125–133. URL <http://josab.osa.org/abstract.cfm?URI=josab-3-1-125>.
- [29] Spence DE, Kean PN, and Sibbett W. ‘60-fsec pulse generation from a self-mode-locked Ti:sapphire laser.’ *Opt. Lett.*, **16**(1):(1991) pp. 42–44. URL <http://ol.osa.org/abstract.cfm?URI=ol-16-1-42>.
- [30] Milonni PW, Gibson RB, and Taylor AJ. ‘Ultrashort Pulse-propagation In KrF Laser-amplifiers.’ *Journal of the Optical Society of America B-optical Physics*, **5**(7):(1988) pp. 1360–1368.
- [31] Nagy T, Simon P, and Szatmari S. ‘Spectral development of short pulses in KrF gain modules.’ *Applied Physics B-lasers and Optics*, **71**(4):(2000) pp. 495–501.
- [32] Träger F, ed. *Springer Handbook of Lasers and Optics*. Springer, 2007.
- [33] Lin QB and Zhang FG. ‘Coumarin-120 Laser-pulses Close To the Fourier-transform Limit From A Simplified Resonant Cavity.’ *Applied Optics*, **26**(13):(1987) pp. 2572–2574.
- [34] Raju BB and Varadarajan TS. ‘Photophysical properties and energy transfer dye laser characteristics of 7-diethylamino-3-heteroaryl coumarin in solution.’ *Laser Chemistry*, **16**(2):(1995) pp. 109–120.
- [35] Geusic JE, Marcos HM, and Uitert LGV. ‘Laser Oscillations in Nd-doped Yttrium Aluminum, Yttrium Gallium and Gadolinium Garnets.’ *Applied Physics Letters*, **4**(10):(1964) pp. 182–184. URL <http://link.aip.org/link/?APL/4/182/1>.
- [36] Fan TY and Byer RL. ‘Diode Laser-Pumped Solid-State Lasers.’ *Ieee Journal Of Quantum Electronics*, **24**(6):(1988) pp. 895–912.

- [37] Giesen A, Hugel H, Voss A, Wittig K, Brauch U, and Opower H. ‘Scalable Concept For Diode-pumped High-power Solid-state Lasers.’ *Applied Physics B-lasers and Optics*, **58**(5):(1994) pp. 365–372.
- [38] Hall RN, Fenner GE, Kingsley JD, Soltys TJ, and Carlson RO. ‘Coherent Light Emission From GaAs Junctions.’ *Phys. Rev. Lett.*, **9**(9):(1962) pp. 366–368. URL <http://link.aps.org/doi/10.1103/PhysRevLett.9.366>.
- [39] Chow W and Koch S. *Semiconductor-Laser Fundamentals*. Springer, 1999.
- [40] Vanderziel J, Dingle R, Miller R, Wiegmann W, and Nordland W. ‘Laser oscillation from quantum states in very thin GaAs-Al<sub>0.2</sub>Ga<sub>0.8</sub>As multilayer structures.’ *Applied Physics Letters*, **26**(8):(1975) pp. 463–465.
- [41] Klopp P, Petrov V, Griebner U, and Erbert G. ‘Passively mode-locked Yb:KYWlaser pumped by a tapered diode laser.’ *Opt. Express*, **10**(2):(2002) pp. 108–113. URL <http://www.opticsexpress.org/abstract.cfm?URI=oe-10-2-108>.
- [42] Volodin BL, Dolgy SV, Melnik ED, Downs E, Shaw J, and Ban VS. ‘Wavelength stabilization and spectrum narrowing of high-power multimode laser diodes and arrays by use of volume Bragg gratings.’ *Opt. Lett.*, **29**(16):(2004) pp. 1891–1893. URL <http://ol.osa.org/abstract.cfm?URI=ol-29-16-1891>.
- [43] Iga K. ‘Surface-emitting laser-its birth and generation of new optoelectronics field.’ *Selected Topics in Quantum Electronics, IEEE Journal of*, **6**(6):(2000) pp. 1201–1215.
- [44] Frantz LM and Nodvik JS. ‘Theory of Pulse Propagation In A Laser Amplifier.’ *Journal of Applied Physics*, **34**(8):(1963) pp. 2346–2349.
- [45] Allen L and Peters GI. ‘Amplified Spontaneous Emission .3. Intensity And Saturation.’ *Journal Of Physics Part A General*, **4**(4):(1971) p. 564.
- [46] Linford GJ, PeressinER, Sooy WR, and Spaeth ML. ‘Very long lasers.’ *Applied Optics*, **13**(2):(1974) pp. 379–390.
- [47] Ertel K, Hooker C, Hawkes SJ, Parry BT, and Collier JL. ‘ASE suppression in a high energy Titanium sapphire amplifier.’ *Optics Express*, **16**(11):(2008) pp. 8039–8049.

- [48] Speiser J. ‘Scaling of thin-disk lasers-influence of amplified spontaneous emission.’ *Journal Of The Optical Society Of America B-Optical Physics*, **26**(1):(2009) pp. 26–35.
- [49] Albach D, Chanteloup JC, and le Touzé G. ‘Influence of ASE on the gain distribution in large size, high gain Yb<sup>3+</sup>:YAG slabs.’ *Opt. Express*, **17**(5):(2009) pp. 3792–3801. URL <http://www.opticsexpress.org/abstract.cfm?URI=oe-17-5-3792>.
- [50] Potemkin AK, Barmashova TV, Kirsanov AV, Martyanov MA, Khazanov EA, and Shaykin AA. ‘Spatial filters for high-peak-power multistage laser amplifiers.’ *Applied Optics*, **46**(20):(2007) pp. 4423–4430.
- [51] Makarov AI and Potemkin AK. ‘Maximum gain of a mutlistage laser amplifier.’ *Soviet journal of Quantum Electronics*, **15**(5):(1985) pp. 692–694.
- [52] Ross IN, Matousek P, Towrie M, Langley AJ, and Collier JL. ‘The prospects for ultrashort pulse duration and ultrahigh intensity using optical parametric chirped pulse amplifiers.’ *Optics Communications*, **144**(1-3):(1997) pp. 125–133.
- [53] Krupke WF, Shinn MD, Marion JE, Caird JA, and Stokowski SE. ‘Spectroscopic, optical, and thermomechanical properties of neodymium- and chromium-doped gadolinium scandium gallium garnet.’ *J. Opt. Soc. Am. B*, **3**(1):(1986) pp. 102–114. URL <http://josab.osa.org/abstract.cfm?URI=josab-3-1-102>.
- [54] Marion JE. ‘Fracture of Solid-state Laser Slabs.’ *Journal of Applied Physics*, **60**(1):(1986) pp. 69–77.
- [55] Suratwala T, Steele R, Feit M, Wong L, Miller P, Menapace J, and Davis P. ‘Effect of rogue particles on the sub-surface damage of fused silica during grinding/polishing.’ *Journal of Non-Crystalline Solids*, **354**(18):(2008) pp. 2023 – 2037. URL <http://www.sciencedirect.com/science/article/B6TXM-4RR86XG-1/2/e8677e2afe123b1621c6700cf6a93227>.
- [56] Marion J. ‘Strengthened solid-state laser materials.’ *Applied Physics Letters*, **47**(7):(1985) pp. 694–696. URL <http://link.aip.org/link/?APL/47/694/1>.

- [57] Feldman R, Shimony Y, Jackel S, Levy I, and Golan Y. ‘Thermochemical strengthening of Nd:YAG laser rods.’ In Sennaroglu A, ed., ‘Proceedings of SPIE,’ vol. 6190. SPIE, 2006, p. 619019. URL <http://link.aip.org/link/?PSI/6190/619019/1>.
- [58] Cerqua KA, Shoup MJ, Smith DL, Jacobs SD, and Kally JH. ‘Strengthened Phosphate-glass In A High Rep Rate Active-mirror Amplifier Geometry.’ *Applied Optics*, **27**(12):(1988) pp. 2567–2572.
- [59] Fan TY. ‘Heat-Generation In Nd-Yag And Yb-Yag.’ *Ieee Journal Of Quantum Electronics*, **29**(6):(1993) pp. 1457–1459.
- [60] Kouznetsov D, Bisson JF, Dong J, and Ueda KI. ‘Surface loss limit of the power scaling of a thin-disk laser.’ *Journal of the Optical Society of America B-optical Physics*, **23**(6):(2006) pp. 1074–1082.
- [61] Naito K, Yamanaka M, Nakatsuka M, Kanabe T, Mima K, Yamanaka C, and Nakai S. ‘Conceptual Design Studies of A Laser Diode Pumped Solid-state Laser System For the Laser Fusion-reactor Driver.’ *Japanese Journal of Applied Physics Part 1-regular Papers Short Notes & Review Papers*, **31**(2A):(1992) pp. 259–273.
- [62] Stuart BC, Feit MD, Herman S, Rubenchik AM, Shore BW, and Perry MD. ‘Optical ablation by high-power short-pulse lasers.’ *J. Opt. Soc. Am. B*, **13**(2):(1996) pp. 459–468. URL <http://josab.osa.org/abstract.cfm?URI=josab-13-2-459>.
- [63] Bloembergen N. ‘Laser-Induced Electric Breakdown In Solids.’ *Ieee Journal Of Quantum Electronics*, **QE10**(3):(1974) pp. 375–386.
- [64] Hack H and Neuroth N. ‘Resistance of optical and colored glasses to 3-nsec laser pulses.’ *Appl. Opt.*, **21**(18):(1982) pp. 3239–3248. URL <http://ao.osa.org/abstract.cfm?URI=ao-21-18-3239>.
- [65] Bertussi B, Natoli JY, and Commandre M. ‘Effect of polishing process on silica surface laser-induced damage threshold at 355 nm.’ *Optics Communications*, **242**(1-3):(2004) pp. 227 – 231. URL <http://www.sciencedirect.com/science/article/B6TVF-4D4CWW4-5/2/f65f9406557fe47c815bf9ff5dfbc170>.
- [66] Chiao RY, Garmire E, and Townes CH. ‘Self-trapping of Optical Beams.’ *Physical Review Letters*, **13**(15):(1964) pp. 479–482.

- [67] Boyd RW. *Nonlinear Optics*. Academic Press, 3 ed., 2008.
- [68] Bespalov VI and Talanov VI. ‘Filamentary Structure of Light Beams In Nonlinear Liquids.’ *Jetp Letters-ussr*, **3**(12):(1966) pp. 307–310.
- [69] Lukishova SG and Shen YR. *Self-focusing: Past and Present, Fundamentals and Prospects*, vol. 114 of *Topics in Applied Physics*. Springer, 2009.
- [70] Strickland D and Mourou G. ‘Compression of amplified chirped optical pulses.’ *Optics Communications*, **56**(3):(1985) pp. 219–221.
- [71] Siebold M, Hein J, Hornung M, Podleska S, Kaluza MC, Bock S, and Sauerbrey R. ‘Diode-pumped lasers for ultra-high peak power.’ *Applied Physics B-Lasers And Optics*, **90**(3-4):(2008) pp. 431–437.
- [72] Ficini G and Campbell J. ‘Development of Large Scale Production of Nd-doped Phosphate Glasses for Megajoule-Scale Laser Systems.’ Tech. rep., Lawrence Livermore National Laboratory, 1996.
- [73] Druon F, Chériaux G, Faure J, Nees J, Nantel M, Maksimchuk A, Mourou G, Chanteloup JC, and Vdovin G. ‘Wave-front correction of femtosecond terawatt lasers by deformable mirrors.’ *Opt. Lett.*, **23**(13):(1998) pp. 1043–1045. URL <http://ol.osa.org/abstract.cfm?URI=ol-23-13-1043>.
- [74] Wattellier B, Fuchs J, Zou JP, Chanteloup JC, Bandulet H, Michel P, Labaune C, Depierreux S, Kudryashov A, and Aleksandrov A. ‘Generation of a single hot spot by use of a deformable mirror and study of its propagation in an underdense plasma.’ *J. Opt. Soc. Am. B*, **20**(8):(2003) pp. 1632–1642. URL <http://josab.osa.org/abstract.cfm?URI=josab-20-8-1632>.
- [75] Walmsley I, Waxer L, and Dorrer C. ‘The role of dispersion in ultrafast optics.’ *Review Of Scientific Instruments*, **72**(1):(2001) pp. 1–29.
- [76] Baumgartner RA and Byer RL. ‘Optical Parametric Amplification.’ *Ieee Journal Of Quantum Electronics*, **15**(6):(1979) pp. 432–444.
- [77] Ishii N, Turi L, Yakovlev VS, Fuji T, Krausz F, Baltuska A, Butkus R, Veitas G, Smilgevicius V, Danielius R, and Piskarskas A. ‘Multimillijoule chirped parametric amplification of few-cycle pulses.’ *Optics Letters*, **30**(5):(2005) pp. 567–569.
- [78] Kleinman DA. ‘Theory Of Optical Parametric Noise.’ *Physical Review*, **174**(3):(1968) pp. 1027–1041.

- [79] Waxer LJ, Bagnoud V, Begishev IA, Guardalben MJ, Puth J, and Zuegel JD. ‘High-conversion-efficiency optical parametric chirped-pulse amplification system using spatiotemporally shaped pump pulses.’ *Optics Letters*, **28**(14):(2003) pp. 1245–1247.
- [80] Lozhkarev VV, Freidman GI, Ginzburg VN, Katin EV, Khazanov EA, Kirsanov AV, Luchinin GA, Mal’shakov AN, Martyanov MA, Palashov OV, Poteomkin AK, Sergeev AM, Shaykin AA, Yakovlev IV, Garanin SG, Sukharev SA, Rukavishnikov NN, Charukhchev AV, Gerke RR, and Yashin VE. ‘200 TW 45 fs laser based on optical parametric chirped pulse amplification.’ *Optics Express*, **14**(1):(2006) pp. 446–454.
- [81] Esarey E, Schroeder CB, and Leemans WP. ‘Physics of laser-driven plasma-based electron accelerators.’ *Reviews of Modern Physics*, **81**(3):(2009) pp. 1229–1285.
- [82] Leemans WP, Nagler B, Gonsalves AJ, Toth C, Nakamura K, Geddes CGR, Esarey E, Schroeder CB, and Hooker SM. ‘GeV electron beams from a centimetre-scale accelerator.’ *Nat Phys*, **2**(10):(2006) pp. 696–699. URL <http://dx.doi.org/10.1038/nphys418>.
- [83] Malka V, Faure J, Gauduel YA, Lefebvre E, Rousse A, and Phuoc KT. ‘Principles and applications of compact laser-plasma accelerators.’ *Nat Phys*, **4**(6):(2008) pp. 447–453. URL <http://dx.doi.org/10.1038/nphys966>.
- [84] Fuchs J, Audebert P, Borghesi M, Pépin H, and Willi O. ‘Laser acceleration of low emittance, high energy ions and applications.’ *Comptes Rendus Physique*, **10**(2-3):(2009) pp. 176 – 187. URL <http://www.sciencedirect.com/science/article/B6X19-4W75RTF-1/2/6c361458f44a064bea30d40ae3294c94>. Laser acceleration of particles in plasma.
- [85] Schwoerer H, Pfotenhauer S, Jackel O, Amthor KU, Liesfeld B, Ziegler W, Sauerbrey R, Ledingham KWD, and Esirkepov T. ‘Laser-plasma acceleration of quasi-monoenergetic protons from microstructured targets.’ *Nature*, **439**(7075):(2006) pp. 445–448. URL <http://dx.doi.org/10.1038/nature04492>.
- [86] Lawson JD. ‘Some Criteria for a Power Producing Thermonuclear Reactor.’ *Proceedings of the Physical Society. Section B*, **70**(1):(1957) pp. 6–10. URL <http://stacks.iop.org/0370-1301/70/6>.

- [87] Nuckolls J, Thiessen A, Wood L, and Zimmerma G. ‘Laser Compression of Matter to Super-High Densities - Thermonuclear (CTR) Applications.’ *Nature*, **239**(5368):(1972) pp. 139–142.
- [88] Meyer-ter Vehn J. ‘From laser fusion to laser accelerators: basic studies into high power laser plasmas.’ *Plasma Physics and Controlled Fusion*, **51**(12):(2009) p. 124001.
- [89] Tabak M, Hammer J, Glinsky M, Kruer W, Wilks S, Woodworth J, Campbell E, Perry M, and Mason R. ‘Ignition and High-Gain with Ultrapowerful Lasers.’ *Physics of Plasmas*, **1**(5, Part 2):(1994) pp. 1626–1634. 35th Annual Meeting of the Division-of-Plasma-Physics of the American-Physical-Society, ST LOUIS, MO, NOV 01-05, 1993.
- [90] Atzeni S. ‘Laser driven inertial fusion: the physical basis of current and recently proposed ignition experiments.’ *Plasma Physics and Controlled Fusion*, **51**(12):(2009) p. 124029.
- [91] Atzeni S, Schiavi A, Honrubia JJ, Ribeyre X, Schurtz G, Nicolai P, Olazabal-Loume M, Bellei C, Evans RG, and Davies JR. ‘Fast ignitor target studies for the HiPER project.’ *Physics of Plasmas*, **15**(5):(2008) p. 056311.
- [92] Treacy EB. ‘Optical pulse compression with diffraction gratings.’ *Ieee Journal Of Quantum Electronics*, **QE 5**(9):(1969) pp. 454–458.
- [93] Betti R, Zhou CD, Anderson KS, Perkins LJ, Theobald W, and Solodov AA. ‘Shock ignition of thermonuclear fuel with high areal density.’ *Physical Review Letters*, **98**(15):(2007) p. 155001.
- [94] Ribeyre X, Schurtz G, Lafon M, Galera S, and Weber S. ‘Shock ignition: an alternative scheme for HiPER.’ *Plasma Physics and Controlled Fusion*, **51**(1):(2009) p. 015013.
- [95] Siebold M, Bock S, Schramm U, Xu B, Doualan J, Camy P, and Moncorgé R. ‘Yb:CaF<sub>2</sub> – a new old laser crystal.’ *Applied Physics B*, **97**(2):(2009) pp. 147–158.
- [96] Hein J, Kaluza MC, Bödefeld R, Siebold M, Podleska S, and Sauerbrey R. ‘POLARIS: An All Diode-Pumped Ultrahigh Peak Power Laser for High Repetition Rates.’ *Lasers and Nuclei*, **694**:(2006) pp. 47–66. URL [http://dx.doi.org/10.1007/3-540-30272-7\\_4](http://dx.doi.org/10.1007/3-540-30272-7_4).

- [97] Karsch S, Major Z, Fülöp J, Ahmad I, Wang TJ, Henig A, Kruber S, Weingartner R, Siebold M, Hein J, Wandt C, Klingebiel S, Osterhoff J, Hörlein R, and Krausz F. ‘The Petawatt Field Synthesizer: A New Approach to Ultrahigh Field Generation.’ In ‘OSA Technical Digest Series (CD),’ Optical Society of America, Jan. 2008, pp. WF1–. URL <http://www.opticsinfobase.org/abstract.cfm?URI=ASSP-2008-WF1>.
- [98] Siebold M, Klingebiel S, Wandt C, Major Z, Popp A, Ahmad I, Wang TJ, Hein J, Krausz F, and Karsch S. ‘High Energy Diode-Pumped Yb:YAG Laser for ns-Pulses.’ *Optics Express*, **16**:(2008) pp. 3674–3679. URL <http://www.opticsinfobase.org/abstract.cfm?URI=ASSP-2008-MF3>.
- [99] Bayramian A, Armstrong P, Ault E, Beach R, Bibeau C, Caird J, Campbell R, Chai B, Dawson J, Ebbers C, Erlandson A, Fei Y, Freitas B, Kent R, Liao Z, Ladran T, Menapace J, Molander B, Payne S, Peterson N, Randles M, Schaffers K, Sutton S, Tassano J, Telford S, and Utterback E. ‘The mercury project: A high average power, gas-cooled laser for inertial fusion energy development.’ *Fusion Science and Technology*, **52**(3):(2007) pp. 383–387.
- [100] Bibeau C, Bayramian A, Armstrong P, Ault E, Beach R, Benapfl M, Campbell R, Dawson J, Ebbers C, Freitas B, Kent R, Liao Z, Ladran T, Menapace J, Molander B, Moses E, Oberhelman S, Payne S, Peterson N, Schaffers K, Stolz C, Sutton S, Tassano J, Telford S, Utterback E, Randles M, Chai B, and Fei Y. ‘The mercury laser system - An average power, gas-cooled, Yb : S-FAP based system with frequency conversion and wavefront correction.’ *Journal De Physique Iv*, **133**:(2006) pp. 797–803.
- [101] Schaffers KI. ‘Yb:S-FAP lasers.’ *Optical Materials*, **26**(4):(2004) pp. 391–394. URL <http://www.sciencedirect.com/science/article/B6TXP-4BY3XHM-4/2/c027bcdd62fc944d0d3a2ba7bbb74dd0>.
- [102] Kawashima T, Ikegawa T, Kawanaka J, Miyanaga N, Nakatsuka M, Izawa Y, Matsumoto O, Yasuhara R, Kurita T, Sekine T, Miyamoto M, Kan H, Furukawa H, Motokoshi S, and Kanabe T. ‘The HALNA project: Diode-pumped solid-state laser for inertial fusion energy.’ *Journal De Physique Iv*, **133**:(2006) pp. 615–620.
- [103] Yasuhara R, Kawashima T, Sekine T, Kurita T, Ikegawa T, Matsumoto O, Miyamoto M, Kan H, Yoshida H, Kawanaka J, Nakatsuka M, Miyanaga N, Izawa Y, and Kanabe T. ‘213 W average power of 2.4 GW pulsed thermally

- controlled Nd : glass zigzag slab laser with a stimulated Brillouin scattering mirror.' *Optics Letters*, **33**(15):(2008) pp. 1711–1713.
- [104] Kawanaka J, Yamakawa K, Tsubakimoto K, Kanabe T, Kawshima T, Nakano H, Yoshida M, Yanagitani T, Yamamura F, Fujita M, Suzuki Y, Mianaga N, and Izawa Y. 'Generation of ENergetic Beam Ultimate (GENBU) Laser - Main Laser.' *The Review of Laser Engineering*, **36**(APLS):(2008) pp. 1056–1058.
- [105] Yasuhara R, Katai R, Kawanaka J, Kawashima T, Miyajima H, and Kan H. '1J x 100 Hz Cryogenic Yb:YAG Laser Development for Feasibility Demonstration of GENBU Main Laser.' *The Review of Laser Engineering*, **36**(APLS):(2008) pp. 1092–1093.
- [106] Wandt C, Klingebiel S, Siebold M, Major Z, Hein J, Krausz F, and Karsch S. 'Generation of 220 mJ nanosecond pulses at a 10 Hz repetition rate with excellent beam quality in a diode-pumped Yb:YAG MOPA system.' *Opt. Lett.*, **33**(10):(2008) pp. 1111–1113. URL <http://ol.osa.org/abstract.cfm?URI=ol-33-10-1111>.
- [107] Hoffnagle JA and Jefferson CM. 'Design and performance of a refractive optical system that converts a Gaussian to a flattop beam.' *Applied Optics*, **39**(30):(2000) pp. 5488–5499.
- [108] Gao XM, Fei Z, Xu WD, and Gan FX. 'Tunable three-dimensional intensity distribution by a pure phase-shifting apodizer.' *Applied Optics*, **44**(23):(2005) pp. 4870–4873.
- [109] Saucedo A, Ramirez PJG, Garcia-Gonzalez L, Martinez-Castillo J, Herrera-May L, and Castro A. 'Imaging properties of phase-shifting apodizers.' *Revista Mexicana De Fisica*, **52**(4):(2006) pp. 336–341.
- [110] Auerbach JM and Karpenko VP. 'Serrated-Aperture Apodizers For High-Energy Laser Systems.' *Applied Optics*, **33**(15):(1994) pp. 3179–3183.
- [111] Rambo PK, Schwarz J, Kimmel M, Atherton BW, Bergstrom A, and Flusche B. 'Development of High Damage Threshold Apodizers for Laser Applications.,' In 'CLEO,' 2008.
- [112] Palmer KF and Williams D. 'Optical properties of water in the near infrared.' *J. Opt. Soc. Am.*, **64**(8):(1974) pp. 1107–1110. URL <http://www.opticsinfobase.org/abstract.cfm?URI=josa-64-8-1107>.

- [113] Goren C, Tzuk Y, Marcus G, and Pearl S. ‘Amplified spontaneous emission in slab amplifiers.’ *Ieee Journal Of Quantum Electronics*, **42**(11-12):(2006) pp. 1239–1247.
- [114] Tommasini R and Balmer JE. ‘Amplified spontaneous emission and maximum gain-length product revised for general line shapes.’ *Journal Of The Optical Society Of America B-Optical Physics*, **16**(4):(1999) pp. 538–545.
- [115] Tommasini R and Fill EE. ‘Generalized Linford formula.’ *Journal Of The Optical Society Of America B-Optical Physics*, **17**(10):(2000) pp. 1665–1670.
- [116] Lowenthal DD and Eggleston JM. ‘Ase Effects In Small Aspect Ratio Laser-Oscillators And Amplifiers With Nonsaturable Absorption.’ *Ieee Journal Of Quantum Electronics*, **22**(8):(1986) pp. 1165–1173.
- [117] Matsumoto M and Nishimura T. ‘Mersenne twister: a 623-dimensionally equidistributed uniform pseudo-random number generator.’ *ACM Trans. Model. Comput. Simul.*, **8**(1):(1998) pp. 3–30.
- [118] Graham ME, Davis BI, and Keller DV. ‘Immersion Liquids For Ruby Lasers.’ *Applied Optics*, **4**(5):(1965) pp. 613–615.
- [119] Gaworski CL, Haun CC, MacEwen JD, Vernot EH, Bruner RH, Amster RL, and Cowan J M J. ‘A 90-Day Vapor Inhalation Toxicity Study of Decalin.’ *Toxicol. Sci.*, **5**(4):(1985) pp. 785–793. URL <http://toxsci.oxfordjournals.org/cgi/content/abstract/5/4/785>.
- [120] Christophorou L and Hadjiantoniou D. ‘Electron attachment and molecular toxicity.’ *CHEMICAL PHYSICS LETTERS*, **419**(4-6):(2006) pp. 405–410.
- [121] Guch S. ‘Parasitic suppression in large aperture disk lasers employing liquid edge claddings.’ *Applied Optics*, **15**(6):(1976) pp. 1453–1457.
- [122] Fan TY, Ripin DJ, Aggarwal RL, Ochoa JR, Chann B, Tilleman M, and Spitzberg J. ‘Cryogenic Yb<sup>3+</sup>-doped solid-state lasers.’ *Ieee Journal Of Selected Topics In Quantum Electronics*, **13**(3):(2007) pp. 448–459.
- [123] Yin HB, Deng PZ, and Gan FX. ‘Defects in YAG : Yb crystals.’ *Journal of Applied Physics*, **83**(7):(1998) pp. 3825–3828.

- [124] Barnes N and Walsh BM. ‘Quantum efficiency measurements of Nd:YAG, Yb:YAG, and Tm:YAG.’ In ‘Advanced Solid-State Lasers,’ Optical Society of America, 2002, p. TuB15. URL <http://www.opticsinfobase.org/abstract.cfm?URI=ASSL-2002-TuB15>.
- [125] Sato Y, Akiyama J, and Taira T. ‘Effects of rare-earth doping on thermal conductivity in Y<sub>3</sub>Al<sub>5</sub>O<sub>12</sub> crystals.’ *Optical Materials*, **31**(5):(2009) pp. 720–724.
- [126] Ashcroft NW and Mermin ND. *Festkörperphysik*. Oldenbourg, 2001.
- [127] Gaume R, Viana B, Vivien D, Roger JP, and Fournier D. ‘A simple model for the prediction of thermal conductivity in pure and doped insulating crystals.’ *Applied Physics Letters*, **83**(7):(2003) pp. 1355–1357.
- [128] Yagi H, Yanagitani T, Numazawa T, and Ueda K. ‘The physical properties of transparent Y<sub>3</sub>Al<sub>5</sub>O<sub>12</sub> elastic modulus at high temperature and thermal conductivity at low temperature.’ *Ceramics International*, **33**(5):(2007) pp. 711–714.
- [129] Kawanaka J. ‘personal communication.’
- [130] Aggarwal RL, Ripin DJ, Ochoa JR, and Fan TY. ‘Measurement of thermo-optic properties of Y<sub>3</sub>Al<sub>5</sub>O<sub>12</sub>, Lu<sub>3</sub>Al<sub>5</sub>O<sub>12</sub>, YAIO(3), LiYF<sub>4</sub>, LiLuF<sub>4</sub>, BaY<sub>2</sub>F<sub>8</sub>, KGd(WO<sub>4</sub>)(2), and KY(WO<sub>4</sub>)(2) laser crystals in the 80-300 K temperature range.’ *Journal of Applied Physics*, **98**(10):(2005) p. 103514.
- [131] Shannon RD. ‘Revised effective ionic radii and systematic studies of interatomic distances in halides and chalcogenides.’ *Acta Crystallographica Section A*, **32**(5):(1976) pp. 751–767. URL <http://dx.doi.org/10.1107/S0567739476001551>.
- [132] Wieser ME. ‘Atomic weights of the elements 2005.’ *JOURNAL OF PHYSICAL AND CHEMICAL REFERENCE DATA*, **36**(2):(2007) pp. 485–496.
- [133] Polifke W and J K. *Wärmeübertragung*. Pearson Education, 2005.
- [134] Cousins A. ‘Temperature and thermal stress scaling in finite-length end-pumped laser rods.’ *Quantum Electronics, IEEE Journal of*, **28**(4):(1992) pp. 1057 –1069.

- [135] Li CY and Garimella SV. ‘Prandtl-number effects and generalized correlations for confined and submerged jet impingement.’ *International Journal of Heat and Mass Transfer*, **44**(18):(2001) pp. 3471–3480.
- [136] Chang CT, Kojasoy G, and Landis F. ‘Confined Single-jet and Multiple-jet Impingement Heat-transfer .1. Turbulent Submerged Liquid Jets.’ *International Journal of Heat and Mass Transfer*, **38**(5):(1995) pp. 833–842.
- [137] Garimella SV and Schroeder VP. ‘Local heat transfer distributions in confined multiple air jet impingement.’ *Journal of Electronic Packaging*, **123**(3):(2001) pp. 165–172.
- [138] Oliphant K, Webb BW, and McQuay MQ. ‘An experimental comparison of liquid jet array and spray impingement cooling in the non-boiling regime.’ *Experimental Thermal and Fluid Science*, **18**(1):(1998) pp. 1–10.
- [139] Tawfek AA. ‘Heat transfer studies of the oblique impingement of round jets upon a curved surface.’ *Heat and Mass Transfer*, **38**(6):(2002) pp. 467–475.
- [140] Nye J. *Physical Properties of Crystals*. Oxford Science Publications, 1985.
- [141] Chenais S, Druon F, Forget S, Balembois F, and Georges P. ‘On thermal effects in solid-state lasers: The case of ytterbium-doped materials.’ *Progress In Quantum Electronics*, **30**(4):(2006) pp. 89–153.
- [142] Antipov OL, Eremeykin ON, Savikin AP, Vorob’ev VA, Bredikhin DV, and Kuznetsov MS. ‘Electronic changes of refractive index in intensively pumped Nd : YAG laser crystals.’ *Ieee Journal Of Quantum Electronics*, **39**(7):(2003) pp. 910–918.
- [143] Antipov OL, Bredikhin DV, Eremeykin ON, Savikin AP, Ivakin EV, and Sukhadolau AV. ‘Electronic mechanism for refractive-index changes in intensively pumped Yb : YAG laser crystals.’ *Optics Letters*, **31**(6):(2006) pp. 763–765.
- [144] Moncorgé R, Eremeykin O, Doualan J, and Antipov O. ‘Origin of athermal refractive index changes observed in Yb<sup>3+</sup> doped YAG and KGW.’ *Optics Communications*, **281**(9):(2008) pp. 2526–2530. URL <http://www.sciencedirect.com/science/article/B6TVF-4RNJB23-3/2/583e587f48c3dfd3197baa84701b34a7>.

- [145] Soulard R, Zinoviev A, Doualan JL, Ivakin E, Antipov O, and Moncorgé R. ‘Detailed characterization of pump-induced refractive index changes observed in Nd:YVO<sub>4</sub>, Nd:GdVO<sub>4</sub> and Nd:KGW.’ *Opt. Express*, **18**(2):(2010) pp. 1553–1568. URL <http://www.opticsexpress.org/abstract.cfm?URI=oe-18-2-1553>.
- [146] Soulard R, Moncorgé R, Zinoviev A, Petermann K, Antipov O, and Brignon A. ‘Nonlinear spectroscopic properties of Yb<sup>3+</sup>-doped sesquioxides Lu<sub>2</sub>O<sub>3</sub> and Sc<sub>2</sub>O<sub>3</sub>.’ *Opt. Express*, **18**(11):(2010) pp. 11173–11180. URL <http://www.opticsexpress.org/abstract.cfm?URI=oe-18-11-11173>.
- [147] Haferkorn H. *Optik. Hochschulbücher für Physik.* VEB Deutscher Verlag der Wissenschaften, 1980.
- [148] Patel F. ‘Properties of YbAG and highly doped YbYAG.’ In ‘CLEO,’ 1999.
- [149] Krupke WF. ‘Ytterbium solid-state lasers - The first decade.’ *Ieee Journal Of Selected Topics In Quantum Electronics*, **6**(6):(2000) pp. 1287–1296.
- [150] Chen Y, Chen B, Patel MKR, and Bass M. ‘Calculation of thermal-gradient-induced stress birefringence in slab Lasers-I.’ *IEEE Journal of Quantum Electronics*, **40**(7):(2004) pp. 909–916.
- [151] Shoji I, Taira T, Ikesue A, and Yoshida K. ‘Reduction of the thermal load by laser oscillation in highly Nd<sup>3+</sup>-doped ceramic YAG.’ In ‘Advanced Solid-State Photonics (TOPS),’ Optical Society of America, 2004, p. 415. URL <http://www.opticsinfobase.org/abstract.cfm?URI=ASSP-2004-415>.
- [152] Khazanov EA. ‘Thermally induced birefringence in Nd:YAG ceramics.’ *Opt. Lett.*, **27**(9):(2002) pp. 716–718. URL <http://ol.osa.org/abstract.cfm?URI=ol-27-9-716>.
- [153] Chen Y, Chen B, Patel MKR, Kar A, and Bass M. ‘Calculation of thermal-gradient-induced stress birefringence in slab Lasers-II.’ *IEEE Journal of Quantum Electronics*, **40**(7):(2004) pp. 917–928.
- [154] Clarkson WA, Felgate NS, and Hanna DC. ‘Simple method for reducing the depolarization loss resulting from thermally induced birefringence in solid-state lasers.’ *Opt. Lett.*, **24**(12):(1999) pp. 820–822. URL <http://ol.osa.org/abstract.cfm?URI=ol-24-12-820>.

- [155] Kandasamy R, Yamanaka M, Izawa Y, and Nakai S. ‘Analysis of birefringence compensation using a quarter-wave plate in solid-state lasers.’ *Optical Review*, **7**(2):(2000) pp. 149–151.
- [156] Fluck R, Hermann MR, and Hackel LA. ‘Birefringence compensation in single solid-state rods.’ *Applied Physics Letters*, **76**(12):(2000) pp. 1513–1515. URL <http://link.aip.org/link/?APL/76/1513/1>.
- [157] Hernandez-Gomez C, Collier J, and Hawkes S. ‘Vulcan Intensity Increase by Wavefront Quality Improvement.’ Tech. rep., CLRC Rutherford Appleton Laboratory, 1998.
- [158] Ikesue A and Aung YL. ‘Ceramic laser materials.’ *Nature Photonics*, **2**(12):(2008) pp. 721–727.
- [159] Ikesue A, Aung YL, Taira T, Kamimura T, Yoshida K, and Messing GL. ‘Progress in ceramic lasers.’ *Annual Review of Materials Research*, **36**:(2006) pp. 397–429.
- [160] Xu XD, Zhao ZW, Wang HH, Song PX, Zhou GQ, Xu J, and Deng PZ. ‘Spectroscopic and thermal properties of Cr<sub>x</sub>Yb : YAG crystal.’ *Journal Of Crystal Growth*, **262**(1-4):(2004) pp. 317–321.
- [161] Eilers H, Hommerich U, Jacobsen SM, Yen WM, Hoffman KR, and Jia W. ‘Spectroscopy And Dynamics Of Cr<sup>4+</sup> Y<sub>3</sub>Al<sub>5</sub>O<sub>12</sub>.’ *Physical Review B*, **49**(22):(1994) pp. 15505–15513.
- [162] Albach D, Bourdet G, Chanteloup JC, Hollander P, and Vincent B. ‘Dispositif laser de forte énergie à milieu à gain à gradient de dopage.’, 2008.
- [163] Moncorgé R. *Current Topics in Rare-earth Lasers*. Springer, 2005. URL [http://dx.doi.org/10.1007/3-540-28209-2\\_6](http://dx.doi.org/10.1007/3-540-28209-2_6).
- [164] Senatsky Y, Shirakawa A, Sato Y, Hagiwara J, Lu J, Ueda K, Yagi H, and Yanagitani TY. ‘Measurements of nonlinear refractive indices in ceramic laser media.’ *Laser Optics 2003: Solid State Lasers And Nonlinear Frequency Conversion*, **5478**:(2004) pp. 88–97.
- [165] Major A, Aitchison JS, Smith PWE, Druon F, Georges P, Viana B, and Aka GP. ‘Z-scan measurements of the nonlinear refractive indices of novel Yb-doped laser crystal hosts.’ *Applied Physics B-Lasers And Optics*, **80**(2):(2005) pp. 199–201.

- [166] Sennaroglu A. *Solid-State Lasers and Applications*. CRC Press, 2007.
- [167] Topfer T, Hein J, Philipps J, Ehrt D, and Sauerbrey R. ‘Tailoring the nonlinear refractive index of fluoride-phosphate glasses for laser applications.’ *Applied Physics B-lasers and Optics*, **71**(2):(2000) pp. 203–206.
- [168] Haumesser PH, Gaume R, Viana B, and Vivien D. ‘Determination of laser parameters of ytterbium-doped oxide crystalline materials.’ *Journal of the Optical Society of America B-optical Physics*, **19**(10):(2002) pp. 2365–2375.
- [169] Lambropoulos JC. ‘Slow Crack Growth during radiative Cooling of LHG8 and BK7 Plates.’ Tech. Rep. 119, LLE, June 2009.
- [170] Payne SA, Smith LK, Beach RJ, Chai BHT, Tassano JH, DeLoach LD, Kway WL, Solarz RW, and Krupke WF. ‘Properties of Cr:LiSrAlF<sub>6</sub> crystals for laser operation.’ *Appl. Opt.*, **33**(24):(1994) pp. 5526–5536. URL <http://ao.osa.org/abstract.cfm?URI=ao-33-24-5526>.